UNIVERSITY OF SOUTHAMPTON

Investigating the Effect of Ocean Waves on GNSS-R Microwave Remote Sensing Measurements

by

Maria Paola Clarizia

A thesis submitted for the

degree of Doctor of Philosophy

in the

Faculty of Natural and Environmental Sciences

School of Ocean and Earth Science

October 2012

ABSTRACT

Doctor of Philosophy

by Maria Paola Clarizia

Global Navigation Satellite System-Reflectometry (GNSS-R) is an innovative technique for ocean remote sensing. It exploits signals of opportunity from navigation constellations, to look primarily at the ocean surface roughness. This dissertation investigates the capabilities of GNSS-Reflectometry to convey information about sea state, and the response of GPS reflected signals to different wind and wave conditions. This is done through the use of real GPS-R data, as well as through simulations of the scattering of GPS signals from realistic ocean surfaces. A retrieval of ocean roughness parameters is carried out on four GNSS-R datasets, collected onboard the UK-DMC Satellite. Measured Delay-Doppler Maps (DDMs) from GPS-R data are least-square fitted to DDMs simulated using a theoretical (Zavorotny-Voronovich, or Z-V) model. The retrieved parameters are compared and validated against measurements from co-located NDBC buoys, and theoretical calculations, and a reasonable agreement is observed.

A GPS scattering simulator is then presented, that uses explicit 3D ocean surface representations, and an innovative facet-based polarimetric scattering model, called the Facet Approach (FA). The results of the GPS scattering simulator are first analysed in the spatial domain, as 2D maps of normalized radar cross section and polarization ratio. These maps exhibit clear features related to the explicit waves of the underlying sea surface. A detailed analysis of noise-free idealized DDMs of both scattered GPS power and polarization ratio is then carried out for a variety of different ocean surfaces, both linear and non-linear. This analysis stresses in particular the importance of wave directionality as a crucial parameter that influences the DDM sensitivity to sea surface roughness

and wave direction, and the polarization effects on the scattered signal. It is revealed that polarization is another important parameter, as it can convey information on wave direction and directionality, and potentially be used to identify nonlinearities on the sea surface. Finally, an investigation of subsets of noise-free idealized DDMs, computed at a high DD resolution, is presented, and its potentials as a tool for detecting the explicit waves on the sea surface are highlighted.

The research and analyses of this PhD dissertation represent novel contributions to the field of GPR-Reflectometry. In particular, the analysis of satellite GPS-R data is the first one that makes use of the whole DDM, and of data collected onboard a satellite. The results from the GPS scattering simulator provide a comprehensive description of how and to what extent different parameters of the ocean surface, linked to wind and waves, influence the scattering of GPS signals. Furthermore, they identify polarization as a new crucial parameter for future GNSS-R missions, since it provides additional information about sea-state, and might be used as a potential indicator of sea surface nonlinearities.

Contents

List of Figures

List of Tables

Acronyms

BPSK = Binary Phase Shift Keying;

C/A = Coarse/Acquisition;

CDMA = Code Division Multiple Access;

CPU = Central Processing Unit;

DD = Delay-Doppler;

DDM = Delay-Doppler Map;

DMSS = Directional Mean Square Slope;

DW = Delay Waveform;

ECEF = Earth Centered Earth Fixed;

EM = ElectroMagnetic;

FA = Facet Approach;

GNSS = Global Navigation Satellite System;

GNSS-R = Global Navigation Satellite System-Reflectometry;

GNSS-RO = Global Navigation Satellite System-Radio Occultation;

GO = Geometrical Optics;

GPS = Global Positioning System;

GZ = Glistening Zone;

H = Horizontal;

HOSM = Higher Order Spectral Method;

IEEE = Institute of Electrical and Electronics Engineers;

IF = Intermediate Frequency;

IGS = International GNSS Service;

IR-SST = InfraRed-Sea Surface Temperature;

JONSWAP = Joint North Sea Wave Project;

KA = Kirchhoff Approximation;

LHCP = Left Hand Circularly Polarized;

LEO = Low Earth Orbit;

MAD = Median Absolute Deviation;

MSS = Mean Square Slope;

MUSIC = MUltiple SIgnal Classification ;

MWD = Mean Wave Direction;

NDBC = National Data Buoy Center;

NRCS = Normalized Radar Cross Section;

PDF = Probability Density Function;

P-M = Pierson-Moskovitz;

PO = Physical Optics;

PR = Polarization Ratio;

PRN = PseudoRandom Noise;

PWSD = Principal Wave Slope Direction;

RAM = Random Access Memory;

RCS = Radar Cross Section;

RHCP = Right Hand Circularly Polarized;

SAR = Synthetic Aperture Radar;

SCR = Space Collocation Range;

SGR = Space GNSS Receiver;

SIR-C = Spaceborne Imaging Radar-C band;

SMOS = Soil Moisture and Ocean Salinity Mission;

SP = Specular Point;

SPA = Stationary Phase Approximation;

SSA = Small Slope Approximation;

SSTL = Surrey Satellite Technology Ltd;

SWH = Significant Wave Height;

TPA = Tangent Plane Approximation;

TSM = Two-Scale Model;

UK-DMC = United Kingdom-Disaster Monitoring Constellation;

Z-V = Zavorotny-Voronovich;

V = Vertical;

WAF = Woodward Ambiguity Function;

WNL = Weakly Nonlinear Surfaces;

Symbols

Symbol	Parameter represented
θ_i	incidence angle
θ_s	scattering angle
$y(t)$	Coarse/Aquisition (C/A) code
$d(t)$	navigation message code
$p(t)$	Precision (P) code
$\mathbf{v}_t$	transmitter velocity
$\mathbf{v}_r$	receiver velocity
τ	delay
f	frequency
f^D	Doppler frequency
τ_c	chip
T_i	coherent integration time
$r(t)$	received signal
$u\left(\hat{\tau}, \hat{f}^D\right)$	cross-correlation signal
$P\left(\hat{\tau}, \hat{f}^D\right)$	cross-correlation power
$\chi\left(\delta\tau, \delta f^D\right)$	Woodward Ambiguity Function (WAF)
R_0, R	transmitter/receiver range
$D(r)$	receiver antenna gain
c	speed of light
U_{10}	wind speed measured at the height of 10 m
ϕ_{wind}	wind direction
σ_0	Normalized Radar Cross Section

σ^2_{upwind}	mean square slope upwind
$\sigma^2_{crosswind}$	mean square slope crosswind
ϕ_{dir}	principal wave slope direction
k_0	incident wavenumber
λ	incident wavelength
$S(f)$	frequency spectrum
$S(k)$	wavenumber spectrum
g	gravity acceleration
ϵ	permittivity of sea water
μ	permeability of sea water
r_c	radius of curvature
$\mathbf{E}^s$	scattered electric field
$\mathbf{H}^s$	scattered magnetic field
$\hat{n}$	surface normal
ω	angular frequency
η_s	intrinsic impedance of a medium
$R_\perp$	Fresnel reflection coefficient for horizontal polarization
$R_\parallel$	Fresnel reflection coefficient for vertical polarization
$\mathbf{q}$	scattering vector
σ_z	standard deviation of surface heights
B_{eff}	effective Doppler bandwidth
N	directionality parameter for JONSWAP surfaces
	symbol referring to parameters of local replica

Acknowledgements

CHAPTER 1

Introduction

1.1 Ocean Remote Sensing using GNSS Signals

It is widely recognized that signals from Global Navigation Satellite System (GNSS) constellations (GPS, GLONASS, and Galileo) can be used not only for positioning, but also for remote sensing. These signals are already being exploited for a variety of purposes, ranging from the fully operational GNSS-Radio Occultation (GNSS-RO) for atmospheric sounding [Wickert et al. (2004), Luntama et al. (2008)], to remote sensing of the oceans [Zavorotny and Voronovich (2000), Garrison et al. (2002), Komjathy et al. (2004), Germain et al. (2004), Gleason et al. (2005), Thompson et al. (2005), Clarizia et al. (2009b), Marchan-Hernandez et al. (2009), Marchan-Hernandez et al. (2010), Valencia et al. (2011a)], of land [Rodriguez-Alvarez et al. (2009), Rodriguez-Alvarez et al. (2011)], and of sea ice [Gleason (2010), Fabra et al. (2010)]. The ability to investigate properties of the surface of the oceans by means of navigation signals has now been demonstrated with a reasonable level of accuracy [Germain et al. (2004), Clarizia et al. (2009b), Marchan-Hernandez et al. (2010)], and the ongoing improvements and increase of navigation systems and signals contribute to maintain the interest for such topic very high among the scientific community. Ocean remote sensing using navigations signals of opportunity relies on the fact that the reflection of these signals from

the surface of the ocean carry information about the properties and characteristics of the scattering surface. The technique is called GNSS-Reflectometry (GNSS-R), and can be therefore used to look at a variety of ocean geophysical parameters, with a primary focus on ocean surface roughness, for scatterometric applications [Germain et al. (2004), Gleason et al. (2005), Clarizia et al. (2009b), Marchan-Hernandez et al. (2010), Valencia et al. (2011a)]. Other potential ocean remote sensing capabilities of GNSS-R include the retrieval of sea surface heights for altimetric applications [Martin-Neira (1993), Martin-Neira et al. (2001), Ruffini et al. (2004), Rius et al. (2010)], the retrieval of salinity content [Sabia et al. (2007), Marchan-Hernandez et al. (2008), Valencia et al. (2011b)], the measurement of currents and surface pressure over the ocean [Ruffini et al. (2003)], coastal monitoring [Soulat et al. (2004)] and real-time tsunami detection [Stosius et al. (2010), Stosius et al. (2011)]. GNSS-R retrieval of the ocean surface roughness has been demonstrated using airborne receivers [Germain et al. (2004)], and more recently using satellite receivers [Gleason et al. (2005), Clarizia et al. (2009b)]. The latter was possible due to the pioneering GNSS-R experiment onboard UK-Disaster Monitoring Constellation Satellite launched in 2003 by Surrey Satellite Technology Ltd (SSTL). GNSS-R requires ordinary small, cheap and low-power GPS receivers, thus implying small payloads and small satellites to carry these receivers, as well as the possibility of easily piggybacking these receivers on other satellites. The technique has got some limitations, mainly related to the complexity of bistatic geometry, and above all to the signals used, which are not specifically designed and optimised for remote sensing applications. Nevertheless, the improvements in the design and characteristics of navigation signals for future constellations and augmentation/modernization programmes, coupled with the application of advanced signal processing techniques on the reflections of these signals, should ultimately lead to such problems being overcome in the near future.

1.2 The Ocean Monitoring Capabilities of GNSS-R

The characteristics of GNSS signals and their reflections from the oceans make them particularly suitable for sensing the ocean surface roughness, which currently represents

the more developed and well-established information that can be obtained from GNSS-R over the oceans. The roughness of the ocean surface is often described in terms of the so-called Directional Mean Square Slope (DMSS), and this can be directly linked to the sea surface waves, and to the wind speed and direction. The DMSS information from the ocean has an enormous importance, both for operational and scientific uses. High density global measurements of DMSS over the ocean would be of invaluable help to operational weather and ocean forecasting, in particular for the prediction or real-time detection of high winds, dangerous sea states, risk of flooding and storm surges. From a scientific point of view, DMSS is the parameter controlling the air-sea exchanges of gas, energy and momentum at the ocean/atmosphere interface, driving the ocean circulation and water waves [Frew et al. (2004), Drennan et al. (2005)]. Therefore, accurate and ubiquitous maps of DMSS would have an impact on understanding the magnitude and distribution of atmospheric uptake of gases by the ocean, and their influence and response to climate change. Knowledge of DMSS could also help quantify the fluxes of carbon dioxide to understand the ocean acidification, where it is primarily happening and how fast it is occurring. Ocean roughness also plays a supporting role for important climate-relevant Earth Observation techniques, for example InfraRed Sea Surface Temperature (IR-SST) where wind history is used to quantify the degree of vertical stratification in micro layer [Spall (2010)], or surface salinity retrieval with the Soil Moisture and Ocean Salinity (SMOS) mission, to remove the effect of ocean roughness on L-band brightness temperature [Sabia et al. (2007), Marchan-Hernandez et al. (2008), Valencia et al. (2011b)]. As a final consideration, roughness parameters are also extremely useful for climate and weather models, where they are often used as input and validation sources. Global measurements of the ocean surface roughness with high resolution in space and time are still a missing element from the global climate and observations system. In this context, the advantages and potentials of GNSS-R to guarantee a high spatial and temporal sampling of these oceanic variables are much stronger compared to other satellites (i.e. scatterometers, altimeters, SAR). GNSS-R exploits pre-existing signals of opportunity, and their ubiquity in space and time allows a global coverage in all weather conditions, and for long term due to the guaranteed

temporal availability of navigation signals. These features, combined with the possi-bility to capture multiple reflections within the satellite field of view at a given time (from different constellations and different satellites) translate into a dramatic increase in space-time sampling, therefore addressing the requirements for accurate observations of the air-sea interface. As an example, if four GNSS constellations are considered as transmitters, then the spatial sampling is increased by an estimated factor of 16 with respect to conventional radar altimeters [D'Addio et al. (2008)]. A clear representation of such improved spatial sampling is shown in figure 1.1. The illustration at the top of figure 1.1 shows the coverage of 10 GNSS-R receivers, receiving the specular reflections from 4 typical GNSS constellations of satellites.The receiving satellites are Low Earth Orbit (LEO) satellites, with an altitude of 800 km, an inclination of 50° and a swath diameter of 1300 Km, and they capture all the specular reflections from GNSS transmit-ters within their swath. The illustration at the bottom of figure 1.1 represents instead the coverage offered by a constellation of 10 altimeters with the same orbit, altitude and inclination, tracking the point at nadir only (specular point in the altimeter). Both the illustrations refer to a coverage achieved in 4 hours.

1.3   Aims and Motivation of this PhD research

The general objective of this PhD has been to investigate properties of the sea surface using GNSS-R, considering specifically reflections of GPS signals. The aim of the re-search was to assess how and to what extent the scattering of GPS signals is affected by different types of sea surfaces, characterized by a different degree of roughness. This has been done through the use of GPS-R satellite data first, and then through numerical simulations of the electromagnetic scattering of GPS signals from realistic rough sea surfaces. The first part of this PhD research was focused on the use of real GNSS-R data from the UK-DMC experiment to retrieve sea surface roughness. Some of these data have been analyzed in the form of Delay-Doppler Maps (DDMs), to retrieve the optimal Directional Mean Square Slopes (DMSS) from them. This was done through comparisons of the measured DDMs to maps generated from a theoretical Zavorotny-Voronovich (Z-V) model [Zavorotny and Voronovich (2000)]. Results from this analysis
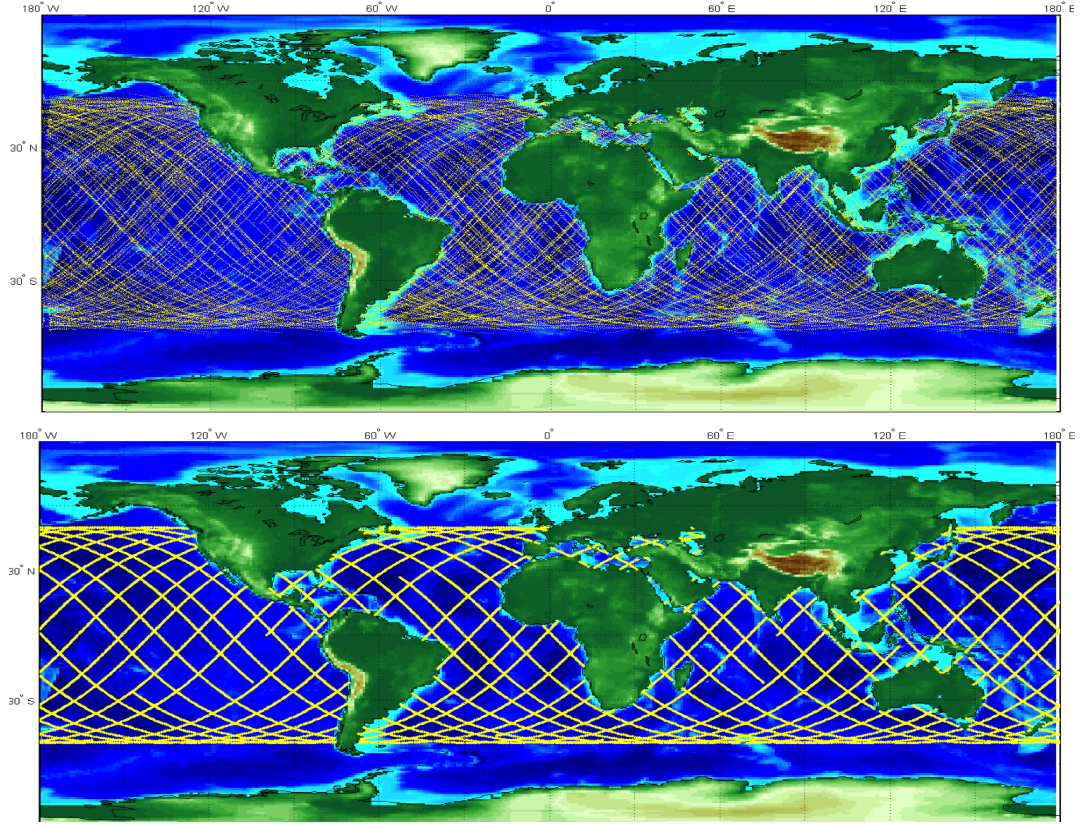
FIGURE 1.1: Comparison between spatial sampling capabilities of GNSS-R versus conventional radar altimetry. The top figure shows the coverage achieved with 10 GNSS-R receivers, The bottom figure shows the coverage from a constellation of 10 radar altimeters. [D'Addio et al. (2008)].

have been published in [Clarizia et al. (2009b)], showing that the retrievals of roughness information from UK-DMC data are in good agreement with in situ measurements. At the same time, the results highlighted some important differences between measurements and simulations. One of the causes of such differences is the theoretical model used, as it is based on the Geometric Optics (GO) limit to describe the scattering, where only the contribution from the specular points of the surface is taken into account. Most importantly, the model assumes *a priori* Gaussian statistics of the sea surface, and therefore simply describes the sea surface through a Gaussian pdf. All these considerations led to the conclusion that accurate retrievals of surface roughness require a more realistic representation of the sea surface itself, and a better description of the scattering of these signals from the sea surface. A way to tackle this problem was identified in the implementation of a GPS scattering simulator. This approach is significantly different from the closed-form statistical model such as the Z-V one: first, explicit simulations of the

sea surface allow us to effectively build the sea surface, with given spectral and statistical properties, and not simply describing it through a pdf; second, it provides the flexibility to create wind wave seas or mixed seas with wind waves and swell, as well as the ability to investigate the response of GPS signals to sea surfaces characterized by nonlinearities, and how different this response is with respect to the linear Gaussian case. The innovative facet-based scattering model developed in the context of this research (Facet Approach) adopts the more general theoretical framework of the Physical Optics (PO) scattering approximation (also known as the Kirchhoff approximation, KA), and allows the computations of an istantaneous scattered power, from explicit sea surface realizations, without being too demanding in terms of computational costs. This approach has provided a more complete picture of the interactions between the microwave GPS radiation and the sea surface than the Z-V model. Finally, the vector formulation adopted for the scattering model allows the investigation of polarization effects, whose importance for GNSS-R has been foreseen in some studies [Zuffada et al. (2004), Thompson et al. (2005)], but cannot be explored when simple GO-based scattering formulations like Z-V are used.

1.4   Organization of PhD Dissertation

The PhD dissertation is organized as follows:

- Chapter 2 presents an overview of the GPS-Reflectometry concept and principles, focusing mainly on the description of the GPS signal structure, and on the GPS-R UK-DMC experiment and data processing to obtain delay-Doppler maps (DDMs).

- Chapter 3 illustrates the retrieval of roughness parameters (in the form of directional mean square slopes) from measured DDMs, using a well-established theoretical model. The estimations of sea surface roughness from GPS-R data are then compared to in-situ measurements provided by buoys, and theoretical calculations using a given surface wave spectrum.

- Chapter 4 presents the novel Facet Approach scattering model adopted for the GPS scattering simulator. An overview of background scattering model is first

presented, followed by the mathematical derivation of the FA, and a discussion on the choice of the size of the facets representing the sea surface.

- Chapter 5 shows the results in the spatial domain of the GPS scattering simulator, n the form of Normalized Radar Cross Section (NRCS) and Polarization Ratio (PR), computed using explicit sea surface realizations, and the FA scattering model.

- Chapter 6 shows the results in Delay-Doppler (DD) domain of the GPS scattering simulator, in the form of DDMs. These are analysed with respect to different sea surfaces with different roughness characteristics. An analysis of DDM subsets computed at high DD resolution is also illustrated.

- Chapter 7 overviews the effect of polarization in DDMs from linear surfaces. DDMs of polarization ratio are illustrated, and the effects of wave parameters like directionality and direction on DDMs is highlighted.

- Chapter 8 is devoted to the investigation of the effect of nonlinear surface waves on the scattering of GPS signals. This effect is analysed in space domain first, and then in DD domain, both for the scattered power and for polarization ratio.

- Chapter 9 presents the conclusions of this research, and outlines some ideas for future work and recommendations for forthcoming GNSS-R missions.

CHAPTER 2

Fundamentals of GPS-Reflectometry

2.1 Introduction

In this chapter we present an overview of the GPS signals, and of the GPS-Reflectometry (GPS-R) technique. Here we focus on the processing and results from the GPS-R experiment onboard the UK-Disaster Monitoring Constellation (UK-DMC) Satellite. We first explain the concept of GNSS-Reflectometry for ocean remote sensing, along with the main characteristics and structure of the GPS signals. Subsequently, we illustrate a brief overview of the GPS-R experiment from the UK-DMC Satellite, and how GPS measurements are processed to produce the so-called delay-Doppler maps (DDMs) and delay waveforms (DWs). We also show examples of measured DWs and DDMs from the data collected through the UK-DMC GPS-R experiment, and how they differ for different sea surface conditions. The present chapter provides some background information, that is fundamental to understand how we extract the sea surface roughness information from GPS-R data (chapter 3), and how we simulate and analyse the scattering of GPS signals from realistic sea surfaces (chapters 4 to 8).

2.2 GNSS-R Principles and Geometry

The term Global Navigation Satellite System (GNSS) designs constellations of satellites which can provide timing and position information to users located on the Earth. Among the GNSS constellations, the most important and widely used so far for GNSS-R is the Global Positioning System (GPS), which is a constellation of up to 32 Medium-Earth orbit Satellites in operation at any given time. GPS satellites are in six different orbital planes, and have a near circular orbit with an inclination angle of 55°, an orbital period of about 12 hours, and an altitude of about 20200 km. GNSS-Reflectometry is based upon scattering in a bistatic geometry, meaning that transmitter and receiver are not collocated on the same platform. The basic principle is that GNSS signals (or more specifically here, GPS signals), transmitted from GNSS satellites, are reflected and scattered off the surface of the ocean, and received by a simple downwards-pointing antenna of a GPS receiver onboard an aircraft or a Low Earth Orbiting (LEO) satellite. These reflections carry information about the surface that has scattered them, in our case the surface of the ocean. The typical configurations of GPS for positioning and of GPS-Reflectometry are illustrated in Figure 2.1.

(a)   (b)
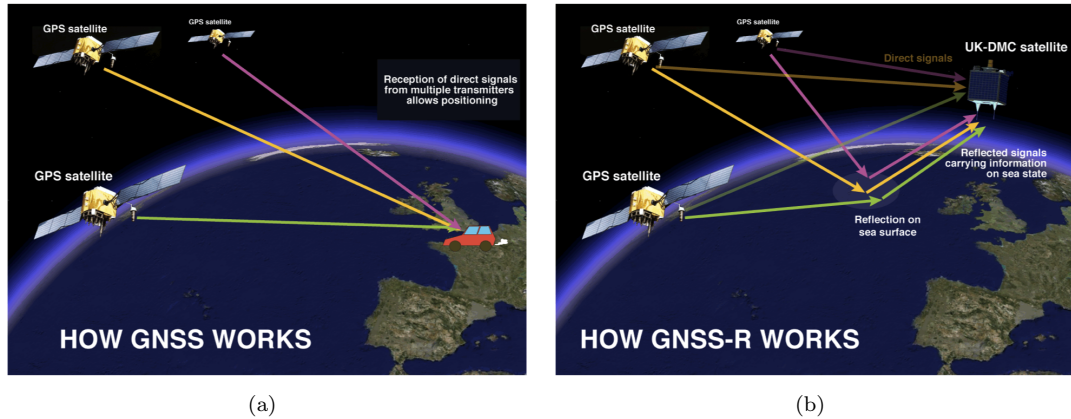
FIGURE 2.1: Illustration of the geometry of the classical GNSS configuration for positioning (a), and of the GNSS-R configuration for Remote Sensing of the ocean (b).

The forward scattering is dominated by specular reflection, and the main scattering contributions to the received signal come from the Specular Point (SP), where a specular reflection occurs, and the area around it called the Glistening Zone (GZ), where power is scattered towards the receiver (Figure 2.2). The SP can be easily located from simple

geometrical considerations, once the transmitter and receiver are known, because it is the point where the incident and scattering angle are equal. Intuitively, the size of the GZ increases with increasing roughness of the sea surface, when power is redirected towards the receiver from points further away from the SP. The scattering is therefore strongly influenced by the roughness characteristics of the scattering surface. This will be demonstrated more formally in chapter 3.
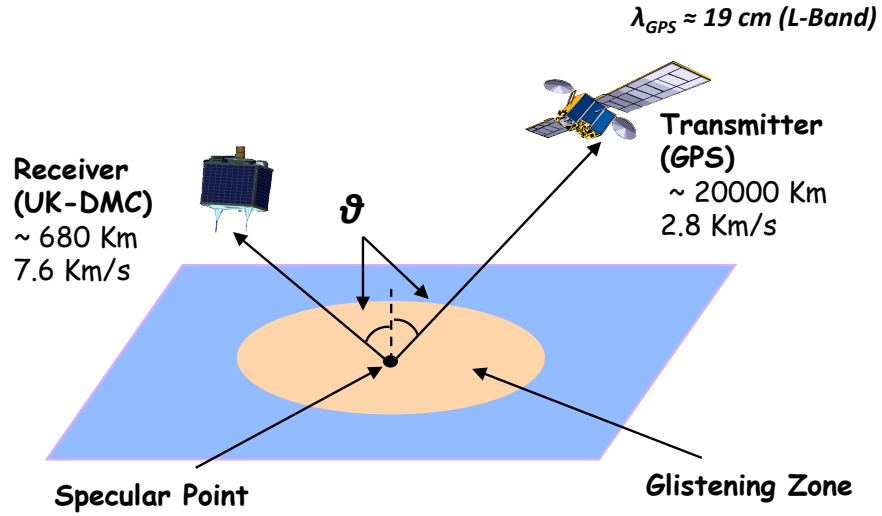
FIGURE 2.2: Illustration of the Specular Point (SP) and the Glistening Zone (GZ) for a typical GPS-R geometry.

The scattered signal can be thought of as a superposition of components scattered from various points on the sea surface. Each component will have a shift in both the time at which the signal arrives at the receiver (delay shift) and the frequency of the signal (Doppler shift). The diversity in delay is due to different paths followed by each scattered signal, while different frequency shifts are caused by the relative motion between transmitter, scattering point on the surface and receiver. Each point of the GZ is therefore characterized by its own delay and Doppler shift, as illustrated in figure 2.3. The pair of delay-Doppler values to which each point in space can be associated represents indeed a new domain in which the GZ can be mapped, and it is known as delay-Doppler domain. Such domain is fundamental for GNSS-R processing since it is the domain in which GNSS-R data are commonly presented and mapped, in the form of the so called delay-Doppler Maps (DDMs). However, different points on the sea surface will

correspond to the same pair of delay-Doppler values. Lines corresponding to constant delays (iso-range) and constant Doppler shifts (iso-Doppler) can be identified on the sea surface (figure 2.3), and they have respectively an elliptical and parabolic shape. Lines of constant delays, also called iso-range lines, are given by concentric ellipses around the SP, and they correspond to increasing delays for increasing distance from the SP, which is the point at minimum delay. Rigorously speaking, the iso-range lines are the intersections of spheroids (equi-range surfaces) having receiver and transmitter as foci, with the sea surface, which causes the ellipses to be not exactly concentric as their centers move towards the transmitter [Zuffada et al. (2004)]. The iso-Doppler lines are parabolic shaped lines cutting through the GZ. They are also asymmetric and characterized by complicated equations, and lines of lower and higher Doppler frequency shifts cannot be predicted, since they strictly depend on the relative velocities among the transmitter, the scattering point and the receiver.
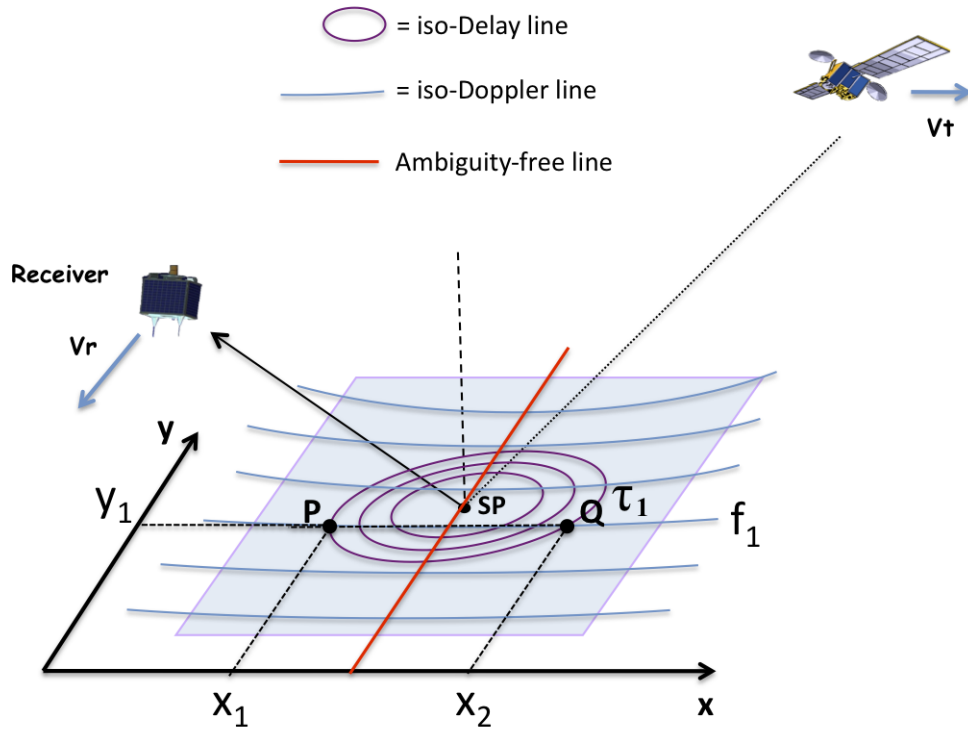
FIGURE 2.3: A Schematic of the GNSS-R geometry, with a Transmitter and Receiver and their velocity vectors (v_t and v_r), iso-range (purple) and iso-Doppler (light blue) lines, and ambiguity-free line (red).

From figure 2.3, we can notice that a generic point P on the GZ can be described by a delay and Doppler coordinate. Such a correspondence is however not biunivocal, and

there is an ambiguity since the intersection between an iso-range and iso-Doppler line is made of two points in space, which will have the same Delay and Doppler frequency, like points P and Q in figure 2.3. Despite that, it is interesting to note that there exists a line free of ambiguity, which can be thought as the transverse axis of the hyperbolic iso-Doppler lines, shown in red in figure 2.3.

2.3   The UK-DMC Experiment

Initially, the possibility of detecting reflected GPS signals from spacecraft altitudes was uncertain, and therefore the way to exploit the information coming from those signals was almost unknown. The Eddy experiment [Germain et al. (2004)] had demonstrated the capability to detect GPS-R signals using airborne receivers at low altitudes, and to retrieve geophysical parameters from those signals. The first GPS-reflection from space was observed in 2000 onboard the space shuttle SIR-C, but at a relatively low altitude of about 200 km [Lowe et al. (2002)]. The GNSS-R experiment carried onboard the UK-DMC satellite represents the first experiment that has successfully measured and processed a number of GPS-Reflections at spaceborne altitudes [Gleason et al. (2005), Gleason (2006), Bian (2007)]. The United Kingdom-Disaster Monitoring Constellation (UK-DMC) is a Low Earth Orbit (LEO) Satellite of the DMC family, built by Surrey Satellite Technology Ltd (SSTL) [Unwin et al. (2003)], with a 680 Km altitude sun-synchronous orbit, intended to image disaster areas and provide images to relief agencies around the globe [Gleason (2006)]. The UK-DMC differs from the other DMC satellites in that it contained several experiments, including a GNSS bistatic radar experiment for ocean, land, snow and ice remote sensing. A picture of the UK-DMC Satellite is shown in figure 2.4a.

The payload for the GNSS bistatic experiment was made up of a GPS receiver, a solid state data recorder and an additional downward pointing antenna, which was added to the two existing space pointing antennas on all the DMC satellites used for time and navigation information. The downward pointing antenna was a medium gain (11.8 dBic of peak gain, where dBic is the gain expressed in decibels relative to an isotropic radiator

(a)   (b)

FIGURE 2.4: (a) UK-DMC Satellite in test status; (b) The UK-DMC GNSS bistatic radar antenna on the Earth facing facet [Gleason (2006)].

that is circularly polarized), Left Hand Circularly Polarized (LHCP), and it pointed $10°$ behind the satellite, opposite to its velocity vector. The medium gain gives a larger footprint, compared a high gain antenna, achieving a $28°$ along track and $70°$ cross track 3 dB beam width, hence covering a large area of about 1000 x 200 km^2. The choice of the polarization was dictated by the scattered signal, which has been demonstrated by [Elfouhaily et al. (2002)] to be mostly LHCP, as the scattering phenomenon causes the transmitted RHCP signal to reverse its polarization when it bounces off the sea surface. An illustration of the UK-DMC downward pointing antenna and its 3 dB footprint is provided in Figure 2.4b and 2.5. The solid state data recorder performs raw data sampling of the down-converted signals from both a single upward looking navigation antenna and the downward pointing antenna, and stores up to 20 seconds of continuous data.
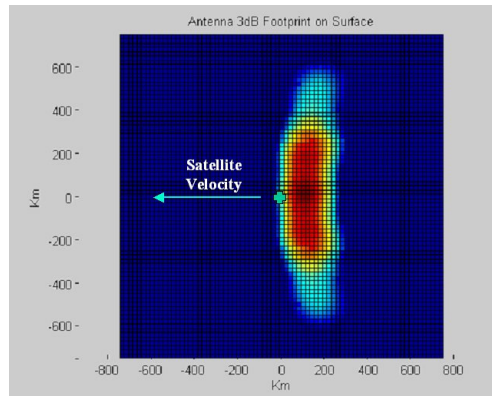
FIGURE 2.5: The 3dB antenna footprint on the surface [Gleason (2006)].

The GPS receiver used was Surrey Satellite Technology Limited Space GPS Receiver

(SGR), based on the Zarlink (formerly GEC Plessey) chipset [Plessey (1996)]. The experiment configuration on-board the UK-DMC allowed both a real-time data processing, including the possibility of performing real-time DD mapping of the reflected GPS signal, and logging and downloading Intermediate Frequency (IF) raw sampled data, through the use of the solid state data recorder, for a more specific post-processing on the ground.[Gleason et al. (2005)]. A block diagram of the UK-DMC GNSS-R bistatic experiment is shown in Figure 2.6.
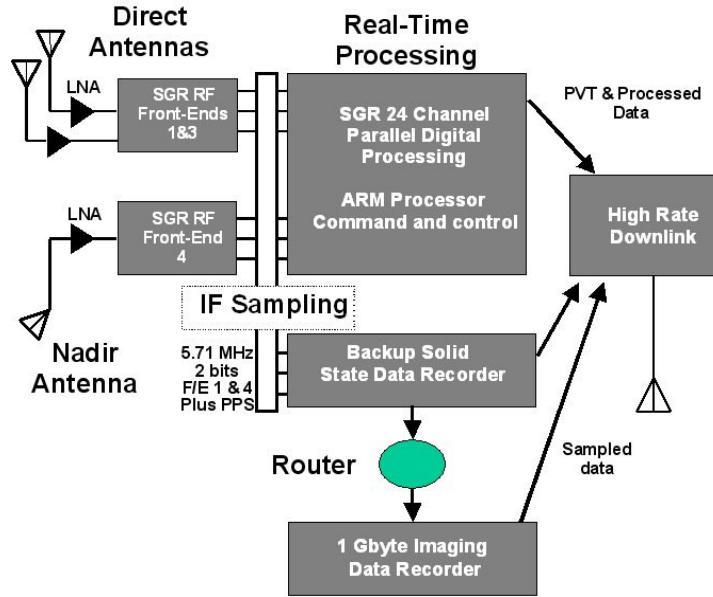
FIGURE 2.6: Block Diagram of the UK-DMC GNSS-R bistatic experiment [Gleason (2006)].

All the UK-DMC datasets are a collection of 20 seconds of GPS reflections over the ocean, acquired at different locations and times during 2004-2005 [Gleason (2006)]. These reflections come from different PRN codes (different GPS Satellites) and are characterized by different scattering geometries. Many of the datasets are co-located with in-situ wind and wave measurements by buoys of the National Data Buoy Center (NDBC). The general rule that was followed regarding the time and space co-location was that the UK-DMC data collection must coincide with the in-situ measurement to within 1 hour and 100 km [Gommenginger et al. (2002)]. Detailed information about each of the UK-DMC GNSS-R datasets can be found in [Gleason (2006)].

2.4 The GPS Signal

Here we present a brief description of the GPS signal, with a focus on its structure and characteristics that are mostly relevant to GPS-Reflectometry, and to the GPS-R processing presented later in section 2.5. We follow closely the GPS signal description contained in [Tsui (2000)], and [Grewal et al. (2001)], to which the reader is referred for more details. The GPS signal contains two frequency components: link 1 (L1) and link 2 (L2). The center frequency of L1 is at 1575.42 MHz (19 cm) and L2 is at 1227.6 MHz (24 cm). They belong to the L-Band, which is the transmission band chosen by navigation signals to limit ionospheric delays and avoid influences by weather phenomena. These carriers are modulated by three different modulation techniques. Two modulations are known as ranging codes, and they are used to measure the distance (range) from the receiver to the transmitting satellite. The ranging codes are the Coarse/Acquisition (C/A) code, which is available for public use, and the Precision (P) code, reserved for military applications. They represent two distinct types of Code Division Multiple Access (CDMA) encodings [Tsui (2000)]. The C/A code modulates the L1 carrier only, while the P-code modulates both the carrier frequencies. The third modulation is known as the navigation message, and it affects both the carriers, for it provides the receiver with information about the time-of-day, the GPS week number, the satellite health, the ephemeris, and finally the almanac. The L1 and L2 signals for the $i-th$ satellite can be written as follows:

$$s_{L_1}^i(t) = A_y y^i(t) d^i(t) \cos\left(2\pi f_1 t + \phi_1\right) + A_p p^i(t) d^i(t) \sin(2\pi f_1 t + \phi_1) \qquad (2.1)$$

$$s_{L_2}^i(t) = A_2 p^i(t) d^i(t) \cos(2\pi f_2 t + \phi_2) \qquad (2.2)$$

where A_y and A_p are respectively the amplitudes of the C/A modulated and P-modulated component of the L1 signal, A_2 is the amplitude for the P-modulated L2 signal, $y^i(t)$ is the C/A code for the $i-th$ satellite, $p^i(t)$ is the P-code and $d^i(t)$ is the navigation message. For GNSS-R purposes we will focus on the C/A code modulation only, and thus on the L1 signal. An illustration of all the components of the transmitted GPS L1 signal is illustrated in figure 2.7.
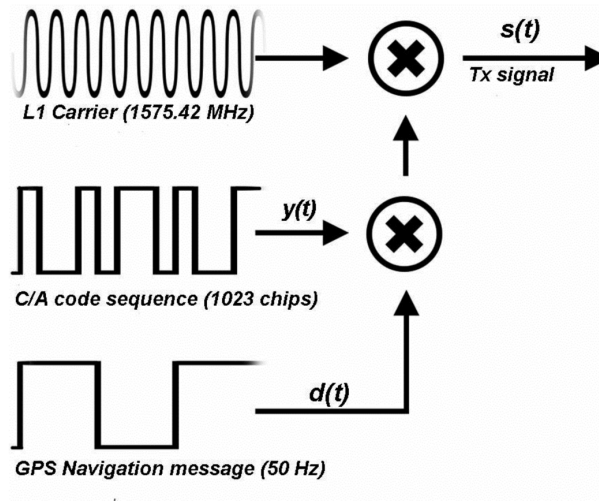
FIGURE 2.7: Illustration of the L1 signal structure.

The signals generated by the satellite transmitting antenna are Right-Hand Circularly Polarized (RHCP). The minimum power levels of the signals must fulfill the values listed in table 2.1 at the receiver. The received power levels at various points on the earth are different, with a maximum difference of about 2.1 dB. In order to generate a uniform power over the surface of the earth, the main beam of the transmitting antenna is slightly weaker at the center to compensate for the user at the edge of the beam [Tsui (2000)].

	P	C/A
L1	-133dBm	-130dBm
L2	-136dBm	-136dBm

TABLE 2.1: Power Levels of GPS Signals.

As we will see in chapter 3, the fact that the GPS power arriving at the receiver is only required to be higher than a threshold, but can vary above that threshold, actually constitutes a limitation for GNSS-R applications. The amplitude information, which would be extremely useful for GNSS-R, cannot be exploited because we lack the information on the exact GPS power level arriving at the sea surface.

2.4.1 The C/A Code

The C/A code belongs to the family of PseudoRandom Noise (PRN) codes known as the Gold codes. The C/A code is a PRN sequence of rectangular pulses of amplitudes 1, working as a Binary Phase Shift Keying (BPSK) modulation for the carrier L1.

These rectangular pulses are also called chips (τ_c), and their duration is about 0.97 μs. Each PRN sequence is made of 1023 chips, such that each sequence lasts about 1 ms for rapid acquisition, and it repeats itself. The shape of the C/A code spectrum is a sinc function, with the null-to-null bandwidth of the main lobe of 2.046 MHz. The transmitting bandwidth of the GPS satellite in the L1 frequency is approximately 20 MHz to accommodate the P code signal; therefore, the C/A code transmitted contains the main lobe and several sidelobes [Tsui (2000)]. A picture of the C/A code spectrum is illustrated in figure 2.8.
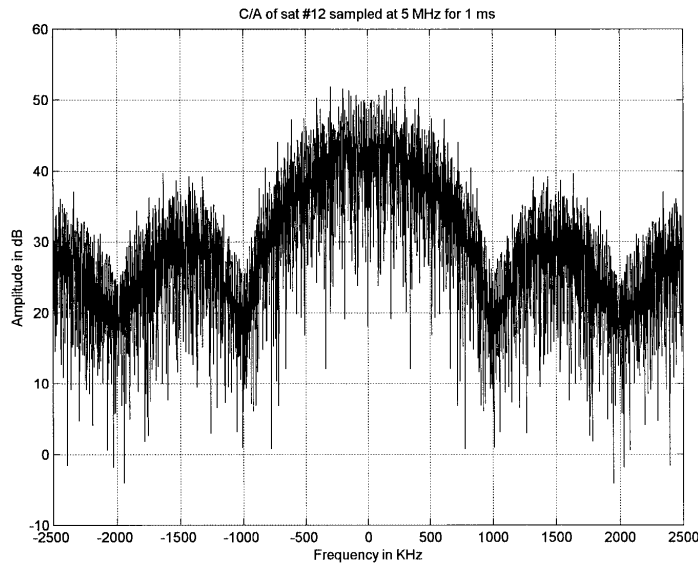
FIGURE 2.8: Spectrum of a C/A code [Tsui (2000)]

The role of the PRN sequence modulation is to reduce the transmitted signal to a noise-like signal, because the C/A code sequence spreads the energy of the original signal into a much wider frequency band. This technique is known as Spread Spectrum technique, and it is conceptually illustrated in Figure 2.9.

The resulting signal has a spectrum similar to that of white noise, making it resistant to jamming and external interferences, as well apparently very hard to detect and to demodulate. However if the PRN sequence, modulating the transmitted signal, is available at the receiver, it can be used to reconstruct exactly the original signal, by multiplying it for the received signal: this operation restores the original bandwidth, and is known as despreading. Each GPS satellite is characterized by its own PRN code, different from those of the other satellites, and the PRN codes are near orthogonal to each other, such
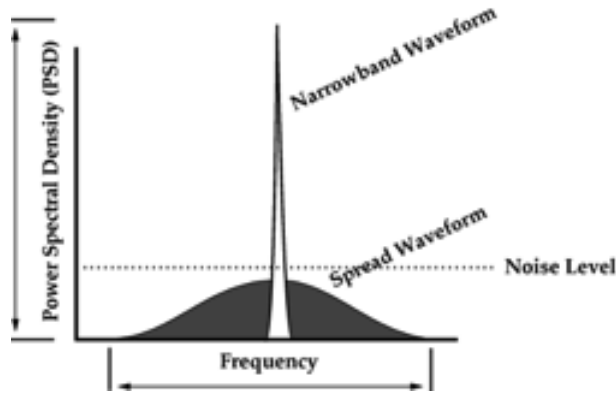
FIGURE 2.9: Illustration of a signal PSD, before and after the application of the spread spectrum technique.

that a PRN code of a certain satellite has got a high autocorrelation peak but low values of cross-correlation with other PRN codes by other satellites (figure 2.10).

(a) Autocorrelation of satellite 19.
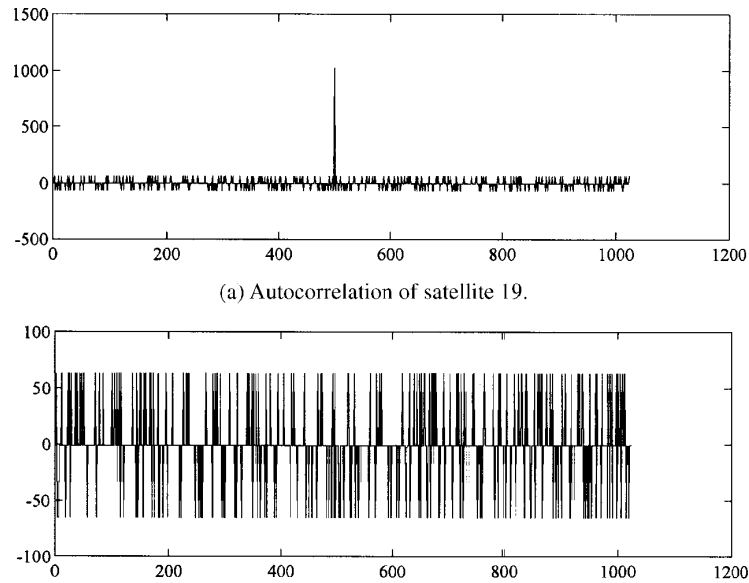
FIGURE 2.10: Auto and cross-correlation of a C/A code [Tsui (2000)].

Therefore, if the codes are known at the receiver for each satellite, the received signal can be correlated with all of them, and the correlation peak will reveal the satellite from which the transmitted signal comes from. For the classical GPS the correlation peak will actually give a delay and thus a range information between the transmitter and the receiver.

2.4.2   The Navigation Message Code

The Navigation message code is also a modulation sequence of rectangular pulses, which in this case are called bits. However its bit rate is of 50 Hz, meaning that each pulse lasts 20 ms. When the navigation message is multiplied to the C/A code, it simply causes a possible change in the amplitude (a 180-degree shift) every 20 ms, thus every 20 PRN sequences. The navigation message contains the following information [Grewal et al. (2001)]:

1. *Satellite Almanac Data*, which enables the user to calculate the approximate location of every satellite in the GPS constellation at any given time;

2. *Satellite Ephemeris Data*, similar to almanac data but able to provide a much more accurate determination of satellite position;

3. *Signal Timing Data*, used to establish the transmission time of specific points on the GPS signal;

4. *Ionospheric Delay Data*, which are ranging errors due to ionospheric effects;

5. *Satellite Health Message*, so that the receiver can ignore that satellite if it is not operating properly.

2.5   GPS-R signal processing and DDM generation

The GPS signal, whose characteristics have been presented in section 2.4, is reflected from the surface of the ocean, and processed to obtain information about the scattering surface. The receiver used to process these reflections essentially performs similar operations to those of an ordinary GPS receiver for positioning. The main difference is that the receiver deals with the signal scattered by the ocean surface, and not with a direct signal. The output of the processing also changes from a pseudorange measurement to a map of scattered power. For classical GPS positioning, the received signal is normally equal to the transmitted one, but delayed and shifted in frequency due to the Doppler

effect. For GNSS-R, the received signal is the result of the reflection of the incident GPS signal from the sea surface, which in principle distorts the incident signal according to its impulse response. However, the sea surface behaves like an ensemble of scatterers, and the scattered signal can be thought as a superposition of components differently attenuated, and differently shifted in delay and Doppler frequency, as follows:

$$r(t) = \sum_{k=1}^{N} A_k \left(y(t - \tau_k) \oplus d(t - \tau_k) \right) \exp \left(j2\pi \left(f_1 + f_k^D \right) t + \phi_1 \right) \tag{2.3}$$

where N is the number of scatterers, A_k, τ_k and f_k^D are respectively the attenuation, the shift in delay and the shift in Doppler frequency associated with the k-th scatterer on the sea surface. Here the attenuation term A_k includes all types of effects, namely the effect of the antenna pattern, the path losses and the electromagnetic scattering. The scattered signal is then received and processed by a GPS-R receiver, whose simplified schematic is illustrated in figure 2.11. Details of the GPS-R processing steps outlined in
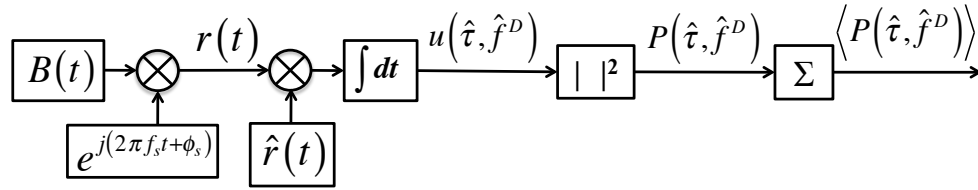
FIGURE 2.11: Schematic of a GPS receiver.

the following sections can be found in [Gleason (2006)].

2.5.1 Coherent Correlation

When the scattered signal arrives at the receiver, it is first amplified and down-converted to to base-band. For our purposes here, we do not present the technical details of these preliminary stages, which can be found in [Gleason (2006)]. We therefore write the received signal directly as:

$$r(t) = \sum_{k=1}^{N} A_k y(t - \tau_k) \exp \left(j2\pi f_k^D t + \phi \right) \tag{2.4}$$

where ϕ is the phase term encompassing the GPS navigation message $d(t)$, because it only produces a phase shift every 20 ms (20 PRN sequences) and we are here interested only in the signal magnitude, and not its phase. The receiver generates a local replica of the transmitted signal, trying to match the incoming signal as better as possible. This replica can be represented as follows:

$$\hat{r}(t) = \hat{y}(t - \hat{\tau}) \exp\left(-j2\pi \hat{f}t - \hat{\phi}\right) \tag{2.5}$$

where:

- $\hat{\tau}$ is the delay matching the one of the incoming signal;

- $\hat{f}^D$ is the Doppler frequency matching those of the incoming signal;

- $\hat{y}(t - \hat{\tau})$ is the locally generated replica of the GPS satellite C/A code.

Similarly to what happens for the classical GPS processing, the replica is cross-correlated with the received signal, and this cross-correlation is performed in 2D along the delay and Doppler dimension. The result is a map of the scattered signal as a function of delay and Doppler frequency, whose mathematical expression is:

$$u\left(\hat{\tau}, \hat{f}^D\right) = \int_0^{T_i} r(t)\,\hat{r}(t)\,dt \tag{2.6}$$

$$= \sum_{k=1}^{N} \int_0^{T_i} A_k y(t - \tau_k) \hat{y}(t - \hat{\tau}) \exp\left(j2\pi f_k^D t + \phi\right) \exp\left(-j2\pi \hat{f}t - \hat{\phi}\right) dt$$

The term T_i is known as the coherent integration time, and it will be considered in greater detail in the next paragraph. Substituting the expression for $\hat{f}$ in (2.6) and rearranging some terms we can write it as:

$$u\left(\hat{\tau}, \hat{f}^D\right) = \sum_{k=1}^{N} A_k \exp\left[j\left(\phi - \hat{\phi}\right)\right] T_i \chi\left(\tau_k - \hat{\tau}, f_k^D - \hat{f}^D\right) \tag{2.7}$$

where we define the function $\chi\left(\tau_k - \hat{\tau}, f_k{}^D - \hat{f}^D\right)$ as:

$$\chi\left(\tau_k - \hat{\tau}, f_k{}^D - \hat{f}^D\right) = \frac{1}{T_i} \int\limits_0^{T_i} y(t - \tau_k)\hat{y}(t - \hat{\tau}) \exp\left(j2\pi\left(f_k{}^D - \hat{f}^D\right)t\right) dt \qquad (2.8)$$

This is commonly known in radar theory as the Woodward Ambiguity Function (WAF) of pseudo-random C/A codes. Details on the WAF and its effect on the DDM will be presented in the context of theoretical modelling of DDMs (paragraph 3.2 in chapter 3). It is worth pointing out that the practical implementation of this is done by cross-correlating the incoming signal with both the in-phase and in-quadrature components of the signal replica separately, and then combining the results as the square root of the sum of the squared results from the correlation [Gleason (2006)]. The mathematical result of the correlation remains the same as for eq. (2.7), but this split in the correlation is commonly found in real receivers as its easier to implement in practice.

2.5.2 The Coherent Integration Time

The integration time T_i is known as the coherent integration time, and it is the time during which the scattering surface does not change significantly, so that the scattered signal also remains unchanged, and the integration is coherent. It is also often defined as the time during which the sea surface appears frozen to the receiver, and it is therefore strictly dependent upon the rapidity with which the scattering surface changes in time. Two different phenomena are responsible for such changes of the scattering surface: one is the moving receiver, which will not be looking at the same area on the Earth after some time, and the other one is the intrinsic temporal variations of the sea surface itself. The coherent integration time can be entirely dictated by the rate of change of the sea surface when the GNSS-R receiver is on a fixed platform [Valencia et al. (2010)], or can be relatively large ($\sim$20 ms) when the receiver is on a slower moving airborne platform [Germain et al. (2004), You et al. (2006)], whereas its usually much lower at spaceborne ($\sim$1 ms), due to the high speed of the moving receiver [Gleason (2006)]. The coherent integration time is difficult to determine from a theoretical point of view. Intuitively, if T_i is chosen to be less than the effective coherence time of the sea surface, then this causes

a decrease in the power gained from the coherent correlation, as well as an increase in the frequency bandwidth, which ultimately translates into a poorer frequency resolution in the DDM. However, if T_i is longer than the coherence time of the sea surface, it means that the surface is no more frozen and will assume different configurations within the time interval T_i, which causes a destructive interference between the scattering from these different configurations and ultimately a reduction in the signal level detected. For spaceborne applications [Gleason (2006)] has performed a coherent correlation between two different received GPS-R signals, corresponding to two different sea state conditions, and their local replica, for varying coherent integration times. This resulted in a correlation peak situated at about 1 ms in both cases. Although such result is empirical, it is in agreement with other studies carried out separately [Lowe et al. (2002)], therefore the conclusion was that the optical coherent integration time for UK-DMC GNSS-R data is 1 ms. In this dissertation, we do not aim at investigating again the optimal coherent integration time, therefore after 1 ms we can assume that the surface decorrelates, and T_i=1 ms will be used thoroughly.

2.5.3 The Fading Problem and the Incoherent Summation

The scattered signal $u\left(\hat{\tau}, \hat{f}^D\right)$ expressed through (2.7) is normally converted into scattered power, by simply taking its square module. The scattered power is therefore given by:

$$P\left(\hat{\tau}, \hat{f}^D\right) = \left|u\left(\hat{\tau}, \hat{f}^D\right)\right|^2 \tag{2.9}$$

This represents the power scattered from a single look, namely from a single temporal observation of the ocean surface. The scattered power from a single look does not produce a useable waveform, as it is strongly affected by the fading noise. Fading or speckle noise is the result of constructive and destructive interferences among reflection contributions from the scattering points on the surface. More precisely, when the ocean roughness is comparable with the 19 cm GPS wavelength, the scattering points on the surface, having different heights and orientations, will shift the phase of the incident wave randomly, causing some of the signal contributions arriving at the receiver to sum constructively, and some others to interfere destructively with each other. Therefore, if

the power from a single temporal look is considered, the probability of recovering the true signal is low due to the random fluctuations of the power level. However, if the sum of power levels from more, uncorrelated looks is considered, then that probability increases, and the fading effect is mitigated. For the looks to be uncorrelated, a certain time is required for the scattering surface to change enough such that the conglomeration of phases arriving a the receiver is different from the one of the previous look. This time can be reasonably given by the coherent integration time, which is about 1 ms for spaceborne GNSS-R configurations. Thus, the final power value will be given by the sum of power levels of consecutive looks:

$$\left\langle P\left(\hat{\tau}, \hat{f}^D\right)\right\rangle = \left\langle \left|u\left(\hat{\tau}, \hat{f}^D\right)\right|^2\right\rangle = T_i \sum_{n=1}^{M}\left|\sum_{k=1}^{N} A_k^n \exp\left[j\left(\phi^n - \hat{\phi}^n\right)\right]\chi\left(\tau_k^n - \hat{\tau}^n, f_k^{Dn} - \hat{f}^{Dn}\right)\right|^2 \tag{2.10}$$

where M is the number of looks accumulated. This multi-look processing is quite similar to the one used in SAR processing to average out speckle noise, and it reduces the speckle noise by a factor of $\sqrt{M}$ [Soulat (2003)]. The number of looks to be accumulated depends quite strongly on the transmitted signal itself and on the noise floor. The aim is to accumulate a sufficient number of looks in order to make the signal shape distinguishable from the noise floor. It has been has empirically found in [Gleason (2006)] that depending on whether the UK-DMC GPS-R signal detected is strong or weak, the minimum number of looks to be accumulated may oscillate between 10 and 200, but usually a good smoothing is achieved when 1000 looks are summed, independently of the strength of the received signal. Therefore, a suitable incoherent accumulation time for UK-DMC data is given by 1 s (1000 looks of 1 ms each). The terms τ_k^n and f_k^{Dn} in the argument of the WAF indicate that a movement respectively along the delay and the Doppler occurs over the integration time. This effect, which is negligible within the coherent integration time, becomes stronger (particularly along the delays) as more and more looks are summed, and it will be shown to cause a sort of blurring effect on the maps of scattered power.

2.5.4 GPS-R Processing Outputs: Delay-Doppler Maps

The final product from the GPS-R receiver is a map of GPS signal power scattered from the sea surface, as a 2D function of delay and Doppler frequency, which is known as a Delay-Doppler Map, or DDM. The generation of DDMs from UK-DMC datasets has been carried out using the Daaxa software, developed by Scott Gleason [Gleason et al. (2005), Gleason (2006)]. The software requires a software receiver script file as input, containing some initialization parameters like GPS PRN number of the GPS reflection to search for, the C/A code movement, representing the shift along the delays, the coherent and incoherent integration times etc., and it produces DDMs in the form of matrices, together with the absolute delay and Doppler axes as output. Details of the software and the way it works can be found in [Gleason (2006)]. It is worth pointing out that this software is not optimized as it requires the user to specify parameters (GPS PRN number of the reflection, range of delays and dopplers where to look for the reflection etc.) that could be in principle estimated or calculated using some a priori information. An example of two DDMs is illustrated in figure 2.12. They are extracted from the same UK-DMC GPS-R dataset, but they have been obtained using 2 different incoherent averaging time of 200 ms and 1 s.
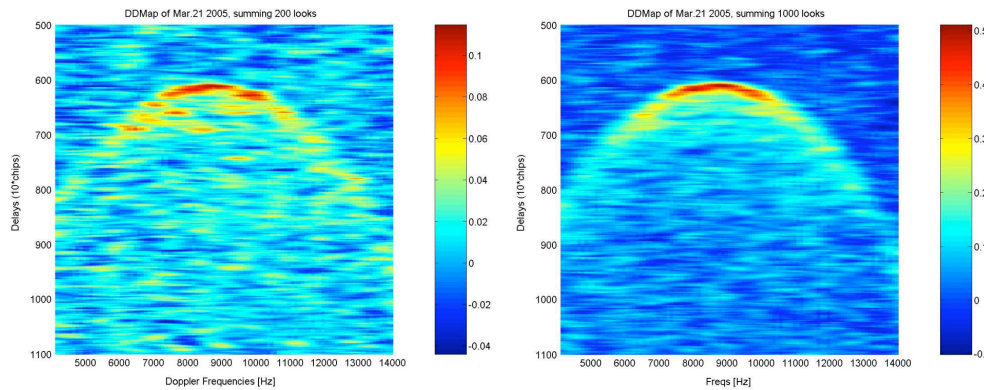
FIGURE 2.12: DDMs obtained using a 200 ms (left) and 1000 ms (right) incoherent accumulation time.

The delay and Doppler axes are expressed respectively in chips (1 chip $\sim 1\mu s$) and in Hz, and the delay and Doppler resolutions are respectively 0.18 chip (which coincides with the sampling step of the incoming signal) and 100 Hz. The delay and Doppler axes, as well as the power values, are in this case expressed in absolute values. The DDM

exhibits a typical horseshoe shape, and exhibits the maximum power on the top of it, for the delay and the Doppler frequency of the SP, and a decreasing power with increasing delays and increasing Doppler frequencies (in absolute value). Such a shape of the DDM is dependent upon the configuration of both the iso-range lines and the iso-Doppler lines (see figure 2.3), and the power distribution is related to the spatial distribution of the scattered power. Details and explanation for the particular shape of the DDM can be found in chapter 3. We now concentrate on the effect of the incoherent summation, and from Figure 2.12 it is clear that the incoherent summation of 1000 looks (on the right) lowers the noise floor with respect to the 200 look summation (on the left) and allows a better recovering of the true signal profile. However, it is important to keep in mind that a non-negligible displacement of the maps occurs after a certain time interval, mostly in the delay direction. This effect already mentioned is due to the receiver travelling at 7.6 km/s, fast enough that the viewing geometry has sufficiently changed after a short time interval. Thus, the number of looks has to be carefully chosen as a trade-off between the need to eliminate the speckle noise and the need to keep the scenario observed by the receiver quite unchanged after the summation time, such that all the accumulated maps reasonably refer to the same observed surface. In this study, a 1 s accumulation time has been constantly used to generate real DDMs, following the approach outlined in [Gleason (2006)]. This choice is also consistent with the averaging normally used in satellite nadir altimetry. A 1 s accumulation time still results in a shift of the single look DDMs along the delay axis, such that the 1000 maps to be accumulated are not aligned with each other. This misalignment would produce a blurring effect in the DDM if not compensated, and it obviously becomes stronger for longer accumulation times. We will see that such effect requires an extra step in DDM processing which is a re-alignment of the single look DDMs, based on an estimation of the DDM shift along the delay direction (called code slide parameter) for each ms.

2.5.5   GPS-R Processing Outputs: Delay Waveforms

A different way to look at GNSS-R data is through the so-called Delay Waveform (DW). This is simply the scattered power as a function of delays only, for a fixed Doppler shift,

which is normally chosen to be the one at the SP. Although it represents a product of lower information content [Germain et al. (2004)], the DWs are historically the most used so far from the GNSS-R community, with numerous studies in literature analysing DWs and trying to link them to wind speed and sea state [Garrison et al. (2002), Cardellach et al. (2003), Komjathy et al. (2004), Gleason et al. (2005), Thompson et al. (2005)]. This is probably because they are easier and more manageable than DDMs, and also because the spreading in Doppler of the scattered signal is actually much lower for ground-based or airborne GNSS-R configuration, which represent most of the GNSS-R experiments conducted so far. At spacecraft altitudes, the Doppler spreading of the scattered signal can no longer be considered negligible, and therefore the DDM represents a much more comprehensive way of analysing the data. An example of two DWs, again obtained for two different incoherent accumulation times, is shown in figure 2.13. Even in this case, we can notice how the signal is smoothed out and the true waveform is recovered as the accumulation time increases.
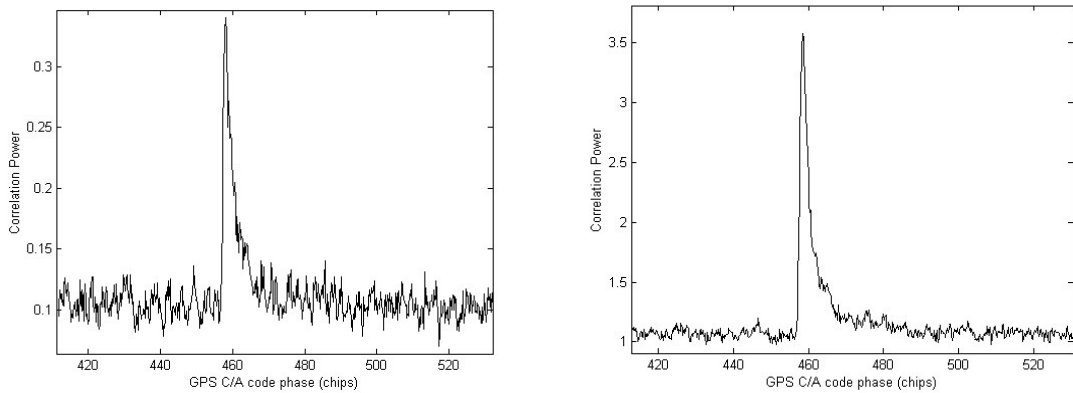
FIGURE 2.13: DWs obtained using a 100 ms (left) and 1000 ms (right) incoherent accumulation time [Gleason (2006)].

The DWs exhibit a peak of the power at the delay corresponding to the SP, where the scattering is maximum, and a tail which represents the combination of the scattering contributions from the other points of the sea surface, with the power decreasing for points at larger delays, thus further away from the SP. The DW has got a distorted triangular-like shape due to the fact that the correlation of the local replica with each of the scattered signal components is triangular. As mentioned before, a DW contains only part of the total scattered signal, whereas a full DD mapping allows instead the exploitation of the whole available scattered signal. An extensive study on DWs and

their variations and sensitivity to sea state has been conducted in [Gleason (2006)]. In this study, we will focus our attention on DDMs, and will investigate how different sea conditions affect them.

2.6 Delay-Doppler maps for different sea conditions

Figure 2.14 shows an example of DDMs from four different UK-DMC datasets. All the maps are normalized with respect to their maximum value. The DDMs have been
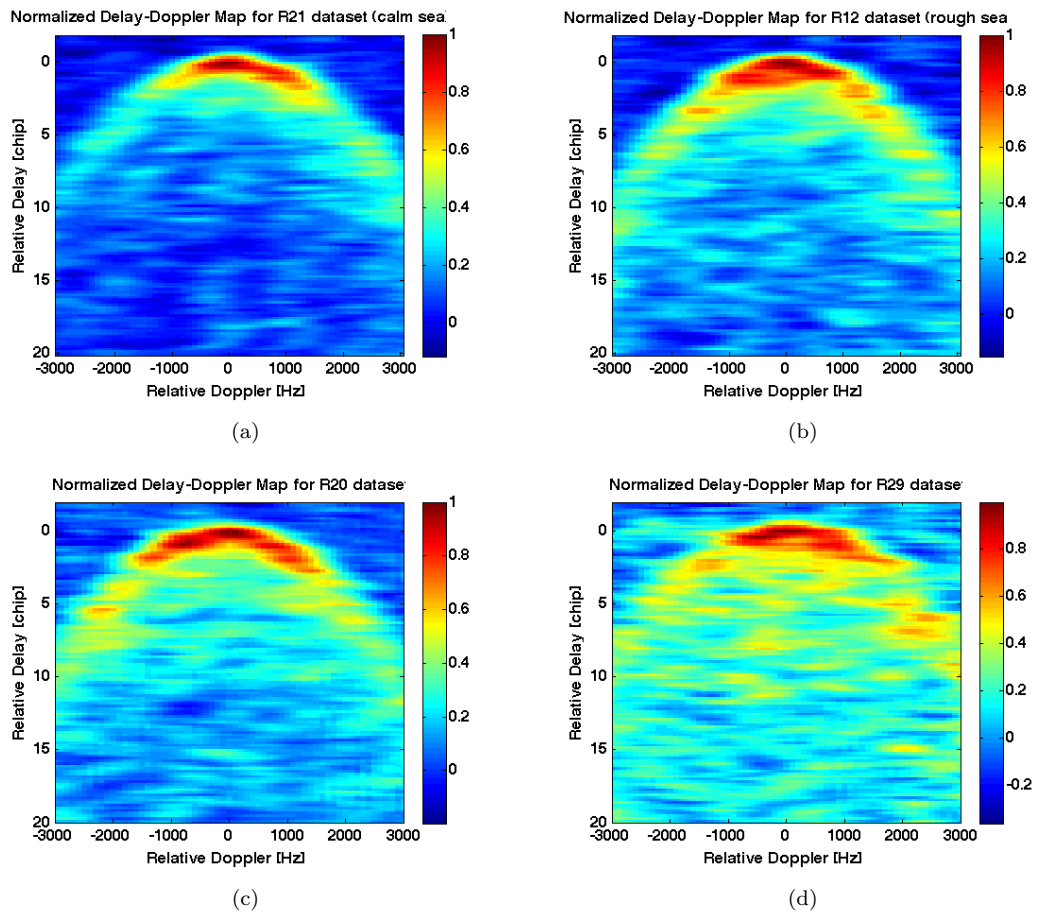
FIGURE 2.14: Normalized DDMs obtained from the four UK-DMC datasets (R21, R12, R20, R29).

obtained using a fixed 1 ms coherent integration time, and a 1 s accumulation time. The DD resolution of the maps is 0.18 chip and 100 Hz, and the delay and Doppler axes are expressed relative to the delay-Doppler value at the SP. A visual comparison between the maps reveals that most of the power is confined within the horseshoe shape, and around

the specular point (zero delay/zero Doppler), for the calm sea case (R21), whereas for the rougher sea case there is more scattered power both between the branches of the horseshoe shape, and along them, for larger delays and Doppler values (R12, R20, R29). The analysis is here restricted to normalized maps, meaning that we cannot exploit any magnitude information, but only the shape of the DDMs. Such limitation is due to the lack of a calibration of the incident GPS signal, as well as unrecorded effects within the receiver (amplifiers, automatic gain control), affecting the amplitude of the received signals. This actually limits also our ability to discriminate different sea states, as the decrease in scattered power values at the SP for rougher sea is neglected when both the maps are normalized. We now focus on DDMs from the R21 and R12 datasets, which are the two datasets with the strongest difference in sea state. Co-located buoy wind and wave measurements indicate a condition of low wind and waves for R21, and medium wind and waves for R12. The wind speed and Significant Wave Height (SWH) registered at the time R21 was collected were respectively 4.5 m/s and 1.98 m, whereas a wind speed of 8.3 m/s and SWH of 2.8 m were registered at the time R12 was collected (see table 2.1). Unfortunately, datasets corresponding to more different sea states (i.e. low wind and waves vs high wind and waves) were not available at the time the GNSS-R processing was performed to obtain DDMs. Nevertheless, the relative DDMs of these two datasets already show some interesting differences. The general behaviour of the DDMs for calm and rougher sea can be predicted based on our knowledge of the scattering for the two cases. A condition of relatively calm sea corresponds to a scattering closer to a quasi-specular regime because the surface is almost flat, and the DDM would be characterized by a strong and sharp peak at the Specular Point (SP), and a rapidly dropping scattered power for points away from the SP. Instead, a certain degree of roughness of the sea surface causes the amount of power scattered from the SP to be lower, and more power being scattered from other points of the GZ, far from the SP. The described power distribution for calmer and rougher sea can be seen in the contour plots of the two DDMs, in figure 2.15. A more pronounced skewness for the calm sea DDM can be also noticed in both figure 2.14(a) and 2.15(b), and when such skewness occurs it is usually due to the antenna pattern. The antenna gain is usually not symmetric over the GZ, and in this particular case the area of the GZ corresponding to positive Doppler

(a)   (b)
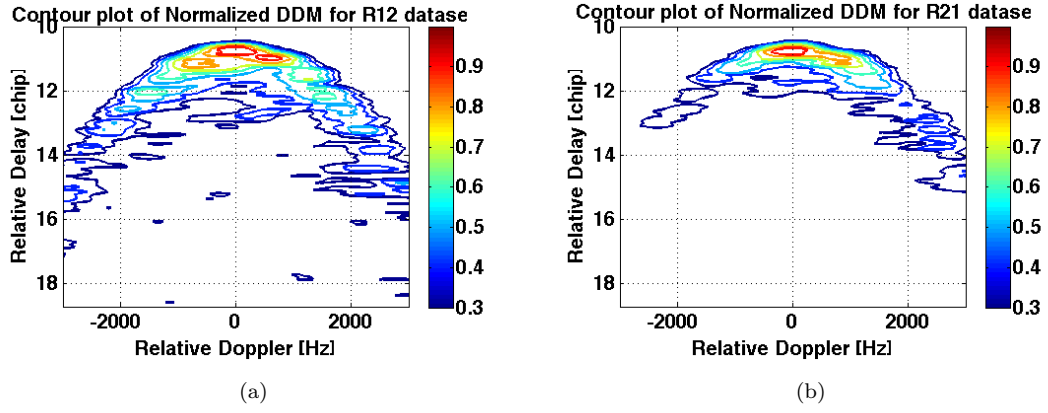
FIGURE 2.15: Contour plots of two of the normalized DDMs shown in figure 2.14.

shifts was characterized by a larger antenna gain than the rest of the GZ, causing an asymmetry of the power distribution of the DDM. The effect of the antenna pattern over a DDM will be explored in chapter 3. Figures 2.16 and 2.17 show slices of the R21 and
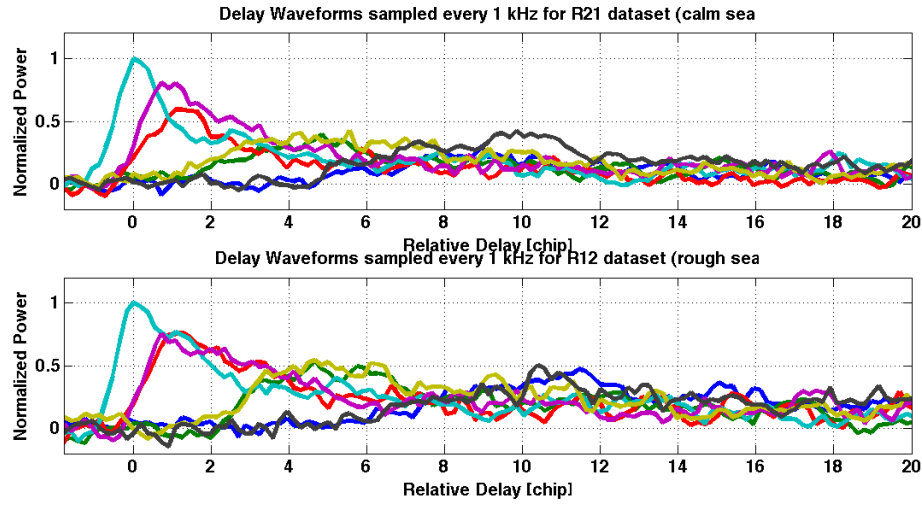
FIGURE 2.16: Delay waveforms obtained as vertical slices (along the delay) of the DDMs for R21 (top) and R12 (bottom) datasets, corresponding a calmer and rougher sea state respectively.

R12 DDMs through the delays and Dopplers respectively, where lines of the same colour indicate a slice of the DDM at the same delay or Doppler frequency. Both the delay and the Doppler waveforms for R21/calm sea case show a more rapid drop-off with respect to the corresponding ones of the R12/rougher sea case, thus confirming once again that the scattered power along the horseshoe shape drops faster in calm sea conditions than rougher seas. The skewness of the R21 DDM translates into a stronger asymmetry of the Doppler waveforms with respect to the R12 case. Finally, a closer look at the DWs
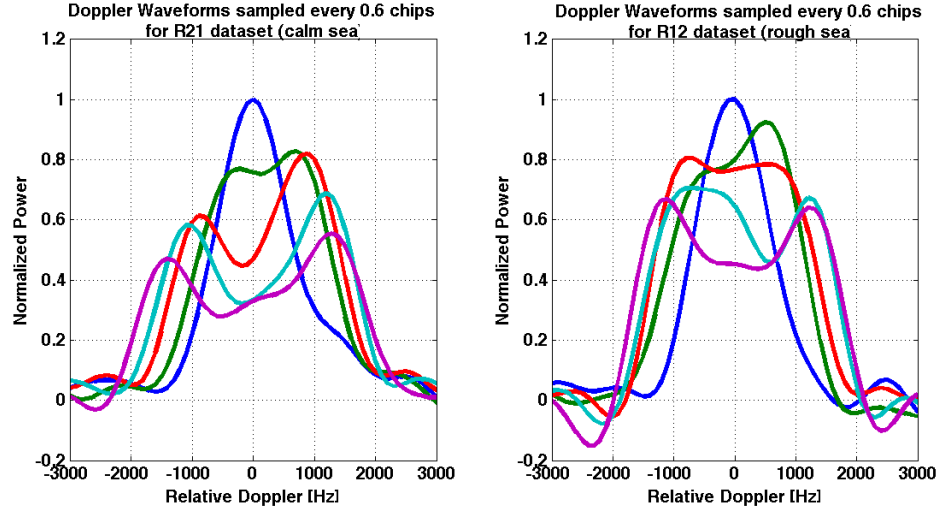
FIGURE 2.17: Doppler waveforms obtained as horizontal slices (along the Doppler) of the DDMs for R21 (left) and R12 (right) datasets, corresponding a calmer and rougher sea state respectively.

at the SP, along with the DWs integrated over all the Doppler values has been carried out for the two DDMs, and they are illustrated in figure 2.18. The DW at the specular point for the R21 case (blue) in figure 2.18a shows a narrower peak with respect to the R12 case (red), as expected from a quasi-specular scattering regime due to a calm sea state. A more rapidly dropping tail of the R21 DWs can also be noticed, although this effect is much stronger when the integrated DWs in figure 2.18b are considered. The integrated DW for R12/rougher sea case shows an interesting shift in the peak towards larger delays, and the reason for that still needs to be investigated.

2.7 Summary

In this chapter we have presented some important background information. We have first provided an overview of the GPS-Reflectometry concept and principles for ocean remote sensing, and of the main characteristics of GPS signals. Then, the GPS-Reflectometry experiment onboard the UK-DMC Satellite has been illustrated, showing briefly the processing chain of the reflected GPS signals, adopted by the GPS-R receiver used for this experiment. We have presented the results of real measurements, in the form of Delay Waveforms (DWs) and delay-Doppler Maps (DDMs), and we have briefly analysed them, and how they vary with respect to different sea conditions. This analysis, which
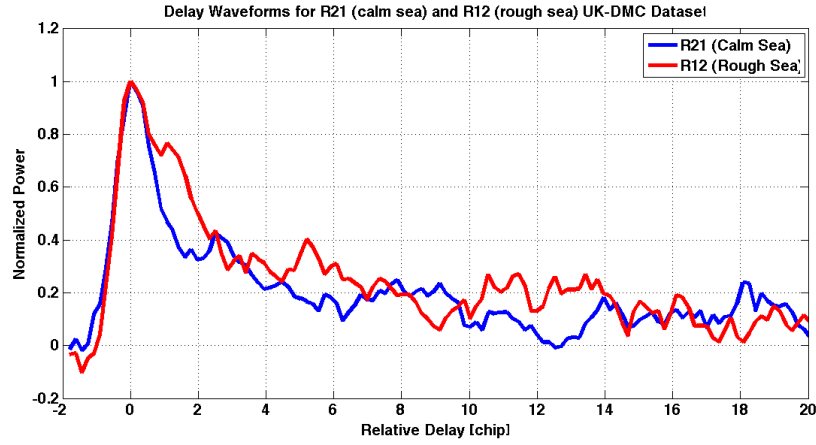
(a)
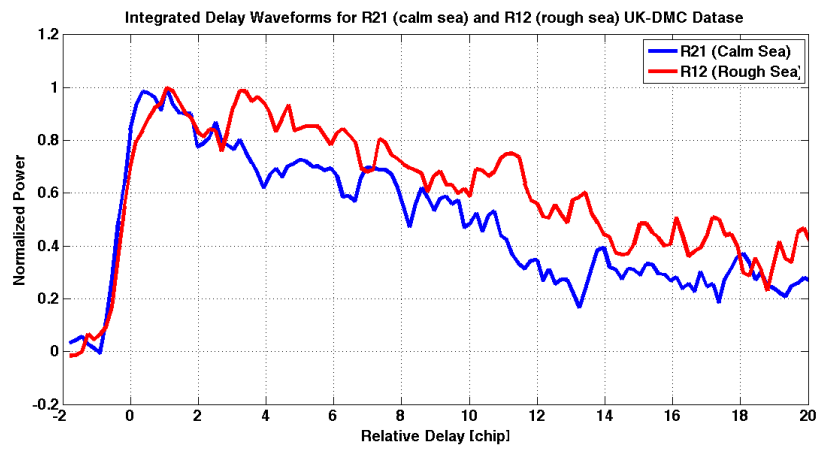
(b)

FIGURE 2.18: Delay waveforms at the SP (top) and integrated over all Doppler frequencies (bottom) for the R21/calm sea case (blue) and R12/rough sea case (red).

has been done here qualitatively, will me extended and improved in chapter 3, where these GPS-R measurements from the UK-DMC satellite will be compared to a theoretical model, to extract a quantitative measure for the roughness of the surfaces from which they have been scattered.

CHAPTER 3

Retrieval of Mean Square Slopes from UK-DMC Delay-Doppler Maps

3.1 Introduction

In this chapter, we present a methodology to extract ocean roughness information from spaceborne GNSS-Reflectometry data, from the UK-Disaster Monitoring Constellation (UK-DMC) satellite. We compare this information with both theoretical calculations and in-situ data from buoys of the National Data Buoy Centre (NDBC). We perform these retrievals through a least-square fitting of GNSS reflections with a theoretical model for such reflections. Here we first give an overview of the theoretical modeling of GNSS-R scattering, and present the Zavorotny-Voronovich (Z-V) model that will be used in this chapter to simulate DDMs. We present the general expression of the average GPS scattered power from a sea surface given by the Z-V model, and numerical simulations of DDMs computed using the Z-V theory. The last section of the chapter is entirely devoted to the detailed presentation and analysis of experimental results to

retrieve sea surface roughness from spaceborne UK-DMC DDMs using the Z-V model, with a comprehensive discussion of the results, and comparisons with theoretical calculations and in-situ measurements. Some of these results were published in [Clarizia et al. (2009b)], which is included in Appendix I.

3.2 The Zavorotny-Voronovich Model for DDM Simulations

Here we present the theoretical model commonly used to simulate DDMs, based on the theory formulated by [Zavorotny and Voronovich (2000)], and hereafter referred to as the Zavorotny-Voronovich (Z-V) model. This model describes the average scattering of GNSS signals from the sea surface, using a specific ElectroMagnetic (EM) approximation called Geometrical Optics (GO). The GO represents the high-frequency limit of the Kirchhoff Approximation (KA), that is an EM model suitable to describe the scattering from large-scale components of the sea surface. Both KA and GO will be presented and illustrated in detail in chapter 4. The expression for the average scattered GPS power as a function of the delay and Doppler frequency, under the GO limit is the following:

$$\left\langle P\left(\hat{\tau}, \hat{f}^D\right)\right\rangle = T_i^2 \iint\limits_{S} \frac{1}{4\pi R_0^2 R^2} D^2\left(\mathbf{r}\right) \Lambda^2\left(\frac{\delta\tau}{\tau_c}\right) sinc^2\left(\frac{\delta f^D}{T_i}\right) \sigma_0\left(\mathbf{r}\right) d^2 r \qquad (3.1)$$

where:

1. S is the scattering surface, and $\mathbf{r}$ is the point on the scattering surface;

2. T_i is the coherent integration time (chosen equal to 1 ms for UK-DMC data);

3. $1/4\pi R_0^2 R^2$ represents the attenuation due to path losses, as R_0 and R are respectively the transmitter and receiver range from the scattering point;

4. $D\left(\mathbf{r}\right)$ is the footprint function of the receiving antenna in terms of complex amplitudes, and $D^2\left(\mathbf{r}\right)$ is the power antenna footprint;

5. $\Lambda\left(...\right) \cdot sinc\left(...\right)$ is the Woodward Ambiguity Function or WAF ($\chi\left(...\right)$) of pseudo-random C/A sequences;

6. $\sigma_0 (\mathbf{r})$ is the bistatic Normalized Radar Cross Section (NRCS).

The full derivation of equation (3.1) can be found in the paper by [Zavorotny and Voronovich (2000)]. However, two terms of this equation, the WAF and NRCS, need to be analysed in greater detail. The NRCS is obtained using the GO approximation, resulting in the following mathematical expression:

$$\sigma_0 (\mathbf{r}) = \frac{\pi |\Re|^2 q^4}{q_z^4} f_{\mathrm{q}} \left(\frac{-\mathbf{q}_\perp}{q_z} \right) \tag{3.2}$$

It depends on the Fresnel reflection coefficient $\Re$, and on the Probability Density Function (PDF) $f_{\mathrm{q}} ()$ of the sea surface slopes, defined as $\mathbf{s} = -\mathbf{q}_\perp/q_z = [-q_x/q_z, -q_y/q_z]$. The vector $\mathbf{q} = [q_x, q_y, q_z]$ is known as the scattering vector, namely the vector obtained as the sum of the unitary vector pointing from the scattering point towards the transmitter, and the unitary vector pointing from the scattering point towards the receiver. This vector plays a crucial role, as it represents the ideal orientation that the tangent to the scattering point considered should have for the power to be scattered exactly towards the receiver. The Woodward Ambiguity Function (WAF), mentioned already in paragraph 2.5.1, is a closed-form mathematical expression that approximates the 2D cross-correlation of pseudo-random C/A sequences, shifted in Doppler frequency. Its original expression is:

$$\chi \left(\tau - \hat{\tau}, f^D - \hat{f}^D \right) = \frac{1}{T_i} \int_0^{T_i} y(t - \tau) \hat{y}(t - \hat{\tau}) \exp \left(j2\pi \left(f^D - \hat{f}^D \right) t \right) dt \tag{3.3}$$

A general analytical expression for the WAF is quite difficult to obtain, due to the pseudo-random sequences $y(t)$ and $\hat{y}(t)$. However a good approximation of this function consists of evaluating the integral of the delay-dependent and Doppler-dependent term separately, that is:

$$\chi \left(\delta\tau, \delta f^D \right) \approx \chi \left(\delta\tau, 0 \right) \cdot \chi \left(0, \delta f^D \right) \tag{3.4}$$

where

$$\chi \left(\delta\tau, 0 \right) = \frac{1}{T_i} \int_0^{T_i} y(t + \tau) \hat{y}(t - \hat{\tau}) dt \approx \Lambda \left(\frac{\delta\tau}{\tau_c} \right) \tag{3.5}$$

$$\chi\left(0, \delta f^D\right) = \frac{1}{T_i} \int_0^{T_i} \exp\left[j2\pi\delta f^D t\right] dt \approx \text{sinc}\left[\delta f^D T_i\right] \exp\left[j2\pi\delta f^D T_i\right] \qquad (3.6)$$

where $\delta\tau = \tau - \hat{\tau}$ and $\delta f^D = f^D - \hat{f}^D$. The first delay-dependent term of the WAF, given by the autocorrelation of PRN sequences, can be well approximated with a triangular function of fixed width equal to the chip duration (τ_c), known as the GPS correlation function. The second Doppler-dependent term of the WAF can be well approximated with a sinc function, called the Doppler correlation function, whose width depends on the integration time T_i . Substituting (3.5) and (3.6) in (3.4) we obtain:

$$\chi\left(\tau_k - \hat{\tau}, f_k^D - \hat{f}^D\right) \approx \Lambda\left(\frac{\tau_k - \hat{\tau}}{\tau_c}\right) \text{sinc}\left[\left(f_k^D - \hat{f}^D\right)T_i\right] \exp\left[j2\pi\left(f_k^D - \hat{f}^D\right)T_i\right] \quad (3.7)$$

that is the expression commonly used to approximate the WAF, already presented in equation (2.8) in chapter 2. The GPS delay correlation function, the Doppler correlation function, and the full 2D WAF are illustrated in figure 3.1 for an integration time of T_i=1 ms.

We will analyse separately the components of equation (3.1) and will show how they affect the final DDM.

3.3 Scattered Power in Space Domain

In this paragraph we analyse the spatial distribution across the GZ of the components of the average GPS scattered power from the Z-V model. Although the ultimate GNSS-R product is a mapping of the power in a different (Delay-Doppler) domain, a look at how such power is distributed in space is very useful to then interpret the power distribution in DD domain and the shape of the DDM. The geometry we consider for our simulations here consists of a transmitter and a receiver lying on the $x - z$ plane, and located respectively on the left (negative x-coordinate) and on the right (positive x-coordinate) side of the SP. A picture of the transmitter, receiver and SP position for the geometry considered is illustrated in figure 3.2. Velocity vectors of both the transmitter and the receiver are also shown.

(a)

(b)

(c)
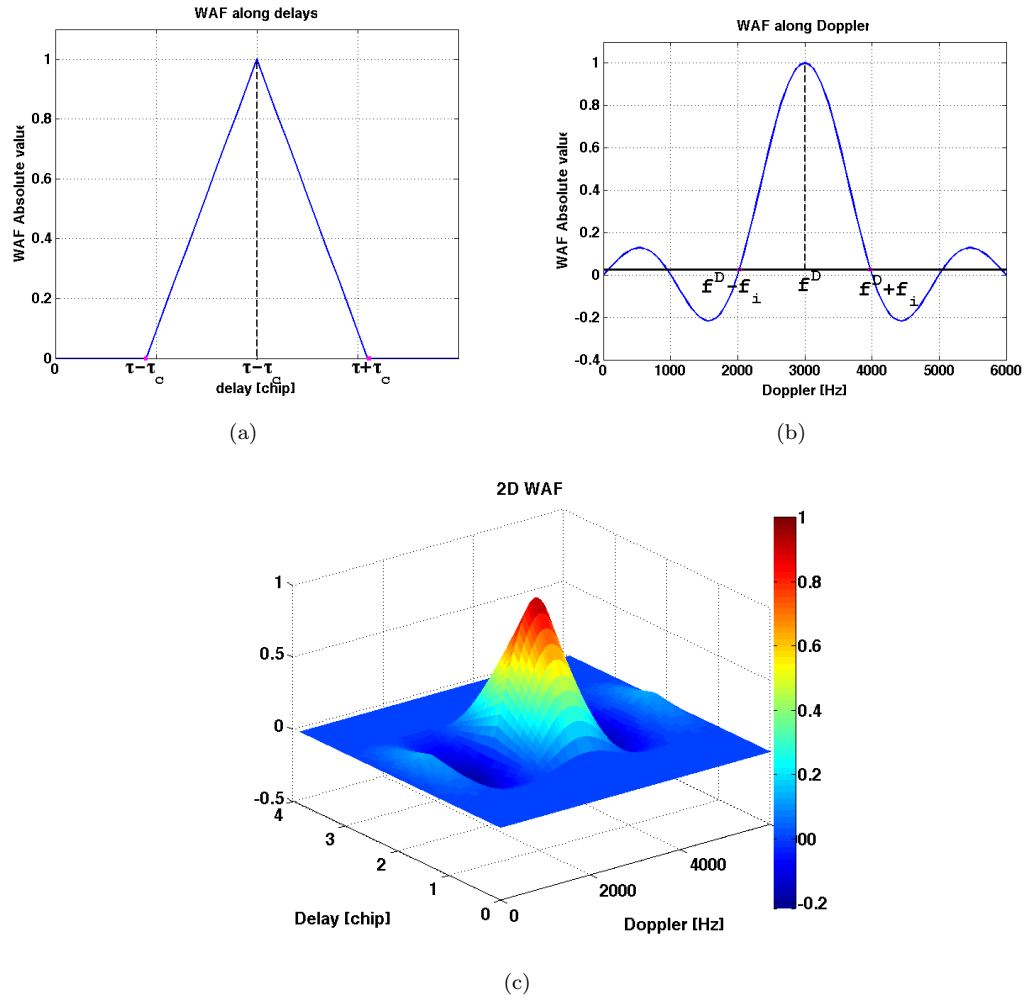
FIGURE 3.1: (a) GPS correlation function (WAF along delays); (b) Doppler correlation function (WAF along Doppler frequencies), where $f_i = 1/T_i$; (c) 2D WAF in delay-Doppler space.
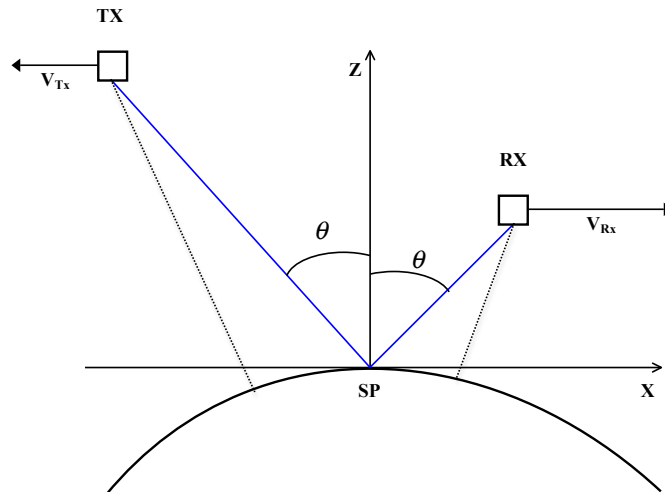
FIGURE 3.2: The geometry considered for the simulations presented in this chapter.

In the following paragraphs, we analyse the spatial distribution of the NRCS, of the path losses and of the receiver antenna pattern. The effect of the WAF is instead illustrated directly in the DD domain.

3.3.1   Spatial NRCS

Equation (3.2) for the NRCS does not specify a PDF of slopes and therefore is valid for any slope statistical distribution [Zavorotny and Voronovich (2000)]. In our case, we consider a gaussian PDF of the sea surface slopes, which also takes into account the wave direction [Germain et al. (2004)]. Its expression is as follows:

$$f_{\mathbf{q}}\left(\frac{-\mathbf{q}_{\perp}}{q_z}\right) = 1/2\pi \det\left(\mathbf{M}\right) \exp\left[-\left(\frac{1}{2}\mathbf{q}^t_{\perp}\mathbf{M}^{-1}\mathbf{q}_{\perp}\right)\right] \tag{3.8}$$

$$\mathbf{M} = \begin{bmatrix} \cos\left(\phi\right) & -\sin\left(\phi\right) \\ \sin\left(\phi\right) & \cos\left(\phi\right) \end{bmatrix} \begin{bmatrix} \sigma^2_{up} & 0 \\ 0 & \sigma^2_{down} \end{bmatrix} \begin{bmatrix} \cos\left(\phi\right) & \sin\left(\phi\right) \\ -\sin\left(\phi\right) & \cos\left(\phi\right) \end{bmatrix} \tag{3.9}$$

where σ^2_{up} and σ^2_{down} are respectively the Directional Mean Square Slopes (DMSS) along the major and minor axes of the 2D gaussian PDF, and ϕ is the Principal Wave Slope Direction (PWSD), namely the angle between the x-axis and the major axis of the PDF, clockwise. For brevity we call these two parameters the DMSS and PWSD. For wind-generated waves, the DMSS can be thought as the MSS upwind and crosswind, and the PWSD as the angle defining the direction of the wind waves. These three parameters are extremely important as they entirely characterize the gaussian PDF of the sea surface slopes, and therefore they represent the sea surface roughness parameters in the Z-V model. Figure 3.3 shows two examples of NRCS, for lower (left) and higher (right) DMSS values, and for waves travelling along the x-direction (3.3a) and 45° clockwise from the x-axis (3.3b).

The 2D elliptical shape characterizing the gaussian PDF reduces in amplitude for larger DMSS, and decreases more slowly when moving away from the SP, consistent with the expected behaviour of the scattered power for rougher seas. A rotation of such elliptical
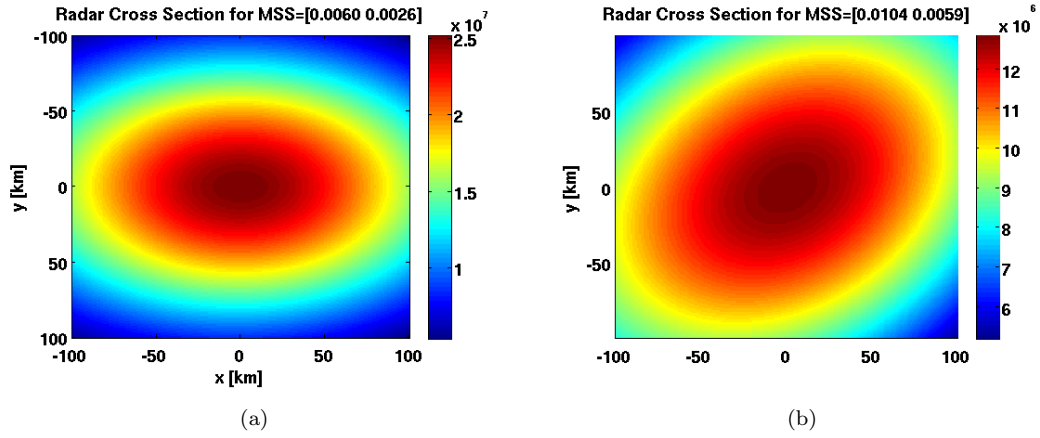
FIGURE 3.3: (a) RCS for lower DMSS and PWSD of 0°.(b) RCS for higher DMSS and PWSD of 45°.

shape can be also noticed for changing ϕ values, indicating a change in the direction the waves are travelling.

3.3.2   Path Losses and Receiver Antenna Gain

Path losses are inversely proportional to the squared product of the range between the transmitter and the surface points, and the receiver and surface points. The GPS-R geometry is asymmetric in all cases, as the GPS satellites are at much higher altitude than the GPS-R receiver, with an even more pronounced asymmetry when such receiver is at airborne than spaceborne. This asymmetry also causes the attenuation due to path losses to be always stronger for those points closer to the receiver (on the right side of the GZ), than for those closer to the transmitter (on the left side of the GZ). This effect also depends on the incidence angle θ, and it strenghtens for increasing values of θ. An illustration of path losses in space for the R12 and R21 geometry is shown in figure 3.4, where the higher asymmetry that characterizes the R12 case is due to a higher incidence angle for this case.

A degree of asymmetry normally affects also the receiver antenna gain. This happens because the Specular point usually does not coincide with the point at maximum gain. As said in paragraph 2.3, the receiver antenna points roughly 10° behind the satellite, so the closer the incidence angle θ (shown in figure 3.2) is to 10°, the higher the chances that the GZ falls exacly within the 3dB antenna lobe. Figure 3.5 shows an example
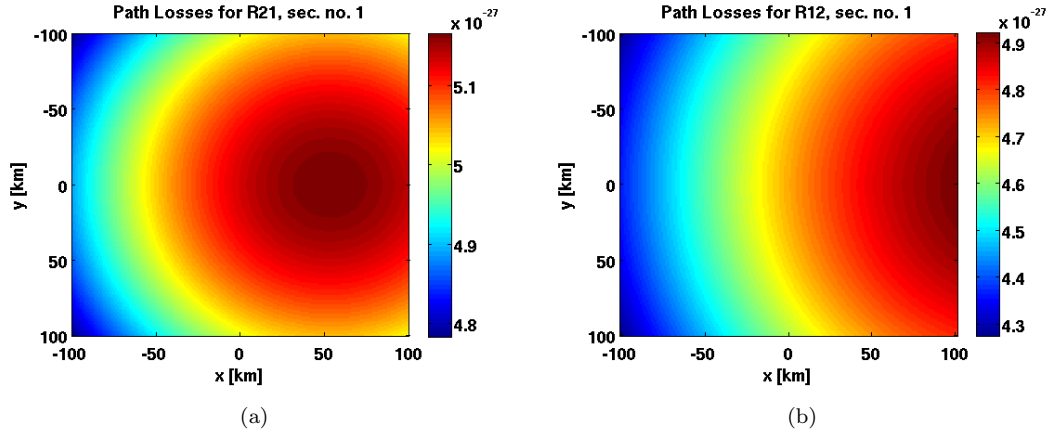
FIGURE 3.4: Path losses in space, for R21 geometry (a), where the incidence angle θ is 5°. and for R12 (b) geometry, where the incidence angle θ is 12°.

of the antenna gain across the GZ for two different incidence/scattering angles. The gain has been computed here taking into account the velocity vectors of the GPS and UK-DMC satellite at the time of the R12 and R21 data acquisitions. An interpolation has also been applied to generate the antenna footprints in figure 3.5, since the spatial resolution chosen for the simulations is finer than the one of the original antenna gain map. As can be noticed in figure 3.5, when the incidence angle is quite different from 10° the 3dB antenna lobe is significantly asymmetric across the GZ.
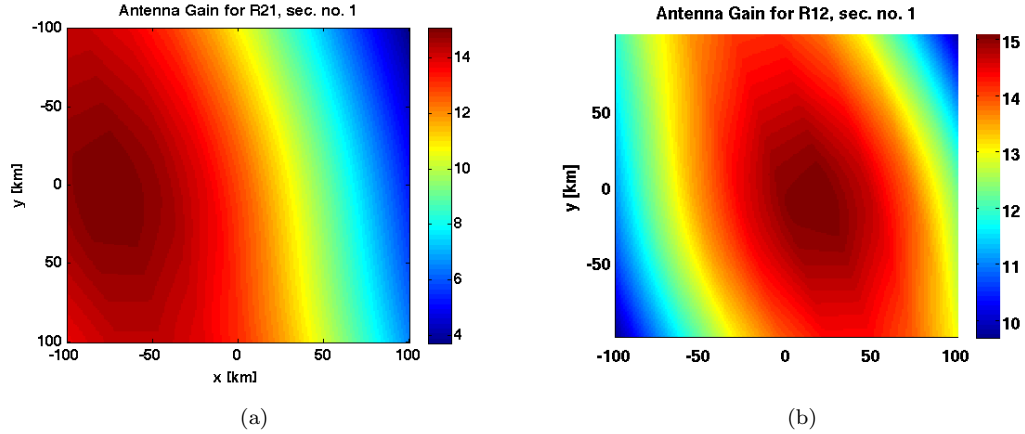
FIGURE 3.5: (a) Antenna gain for R21 geometry, where the incidence angle θ is 5°. (b) Antenna gain for R12 geometry, where θ is 12°.

3.3.3   Total Scattered Power in Space

Figure 3.6 shows two examples of total scattered power obtained by combining altogether the NRCS, the path losses and the antenna gains of figures 3.3-3.5. The final scattered power in space remains quite asymmetric for the R21 case.
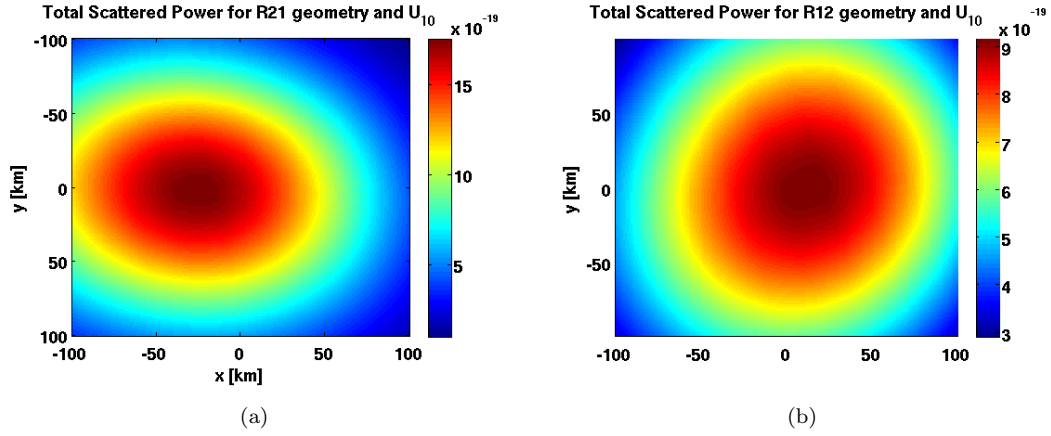
FIGURE 3.6: (a) Total scattered power across the GZ, as combination of all the terms of the Z-V model, for R21 dataset. (b) total scattered power across the GZ, for R12 dataset.

We will show that this effect translates into an asymmetry in the DD domain too, causing a skewness in the final DDM.

3.4   Delay-Doppler Mapping

The spatial mapping of the scattered power is useful to understand how the power is distributed across the GZ, and to help interpret the shape and characteristics of the DDM. However, when GNSS-R data are processed, the result of such processing is directly a map of the scattered power into the delay-Doppler domain. Thus, we now analyse the scattered power in figure 3.6 in delay-Doppler domain. In order to map a spatial pixel in DD domain, we first need to look at how lines of constant delays (iso-delay lines) and constant Doppler shifts (iso-Doppler lines) appear across the GZ. Figure 3.7a shows the RCS shown in figure 3.3a, with overlapped iso-delay (continuous lines) and iso-Doppler lines (dashed lines). It can be noticed that the iso-Doppler lines are for the GPS/UK-DMC geometry almost equally spaced to each other, and since the hyperbolic

curvature is evident only over very big spatial areas, they look almost like straight lines for the GZ we are considering. The iso-delay lines instead tend to become closer and closer to each other for larger delays away from the SP. Figure 3.7b shows how the RCS is mapped into the DD domain, where the delays and Doppler frequency values are expressed relative to those at the SP. Each DD pixel of figure 3.7b will contain the sum of the power scattered from all those spatial pixels that are at the intersection of the iso-delay and iso-Doppler lines corresponding to that pair of delay and Doppler frequency values. A DD mapping of the scattered power naturally produces a horseshoe shape pattern. The center of the horseshoe shape contains the strongest power scattered from the area around the SP. This area, indicated as the central blue rectangle in figure 3.7a, is quite large. The branches of the horseshoe shape represents the power scattered from larger delays and larger Doppler frequencies, namely from points on the sea surface located away from the SP, along and in the vicinity of ambiguity-free line. Here the intersections between iso-delay and iso-Doppler lines that are still quite large, and the scattered power along the horseshoe shape is still considerable. The two small blue areas shown in figure 3.7a correspond instead to DD cells inside the horseshoe shape. These areas in space are small, and they also contain a much weaker scattered power, therefore the DDM values inside the horseshoe shape are much smaller than those along the horseshoe shape.

(a)   (b)
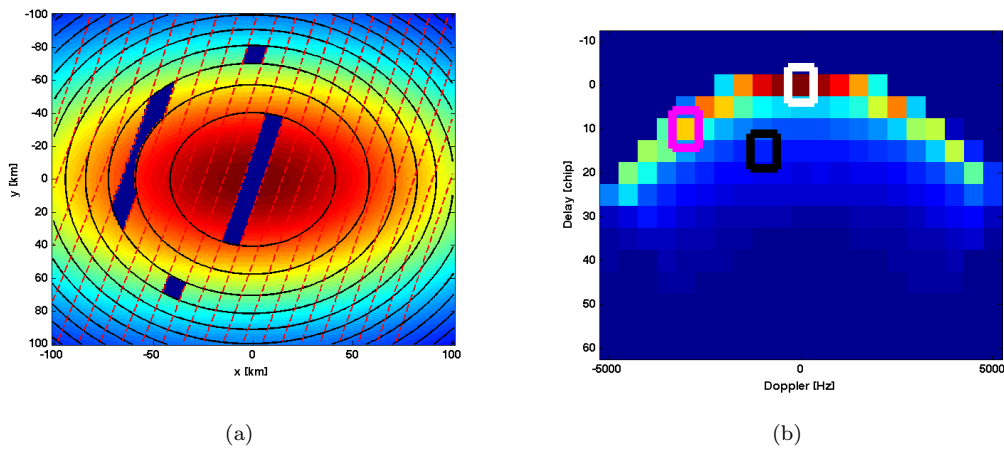
FIGURE 3.7: Illustration of how a DD mapping works. The delay and Doppler resolution have been chosen respectively equal to 5 chips and 500 Hz. The DD cell in the white rectangle in (b) corresponds to the large central blue rectangular shape in (a). The DD cell in the magenta rectangle in (b) corresponds to the large blue area on the left hand side of the SP in (a). Finally, the DD cell in the black rectangle in (b) corresponds to the two small rectangular blue areas in (a).

The power along the horseshoe shape tends to decrease for larger delays and Doppler frequencies, due to a decrease in power for points away from the SP, and also a decrease in the areas of intersection because the iso-delay lines become closer to each other. Figure 3.8 shows two examples of the DD mapping of the maps of scattered power from figure 3.6. Note how the asymmetry in the scattered power translates into a skewness of the horseshoe shape of the DDMs. This effect is important as it affects the sensitivity of the DDMs with respect to different sea state conditions.
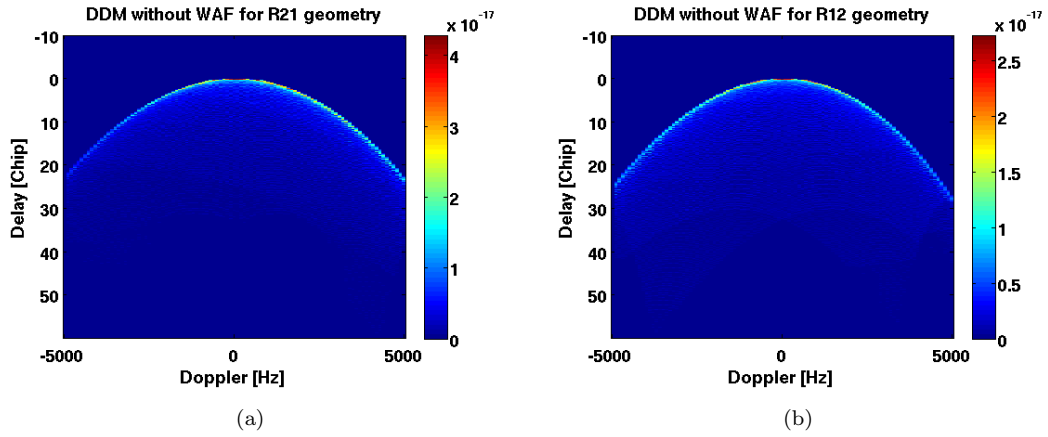
FIGURE 3.8: DD mapping of the maps of scattered power, shown in figure 3.6.

3.5   Effect of WAF

The DDMs illustrated in figure 3.8 have been obtained through a pure space-to-delay-Doppler domain transformation applied to the power scattered across the GZ. This means that the value at a given DD pixel in the DDM is solely determined by the spatial area corresponding to that pair of DD coordinates, which is an ideal case. When the WAF is taken into account, the power value for each DD pixel becomes the weighted summation of the power scattered from the corresponding spatial area, plus that from a number of adjacent areas. This spreading effect is caused by the WAF of pseudorandom GPS sequences. The spreading effect reduces for a narrower WAF, and it would ideally disappear for a 2D delta WAF. An example of the effect of a WAF in space for a generic DD cell is illustrated in figure 3.9. The DD cell chosen here is located at 10 chips, and 2 KHz. The top row shows the range of delays (blue annulus) around 10 chips, and doppler frequencies (red stripe) around 2 KHz, representing the DD cell. The width of

the annulus is two chips, and it coincides with the width of the GPS triangular function, whereas the width of the red stripe is 2 KHz, and it coincides with the width of the Doppler sinc function. The bottom plot of figure 3.9 shows how the WAF filters in space the power contributions in space for the DD cell considered, and the weight that it applies to the selected spatial region.
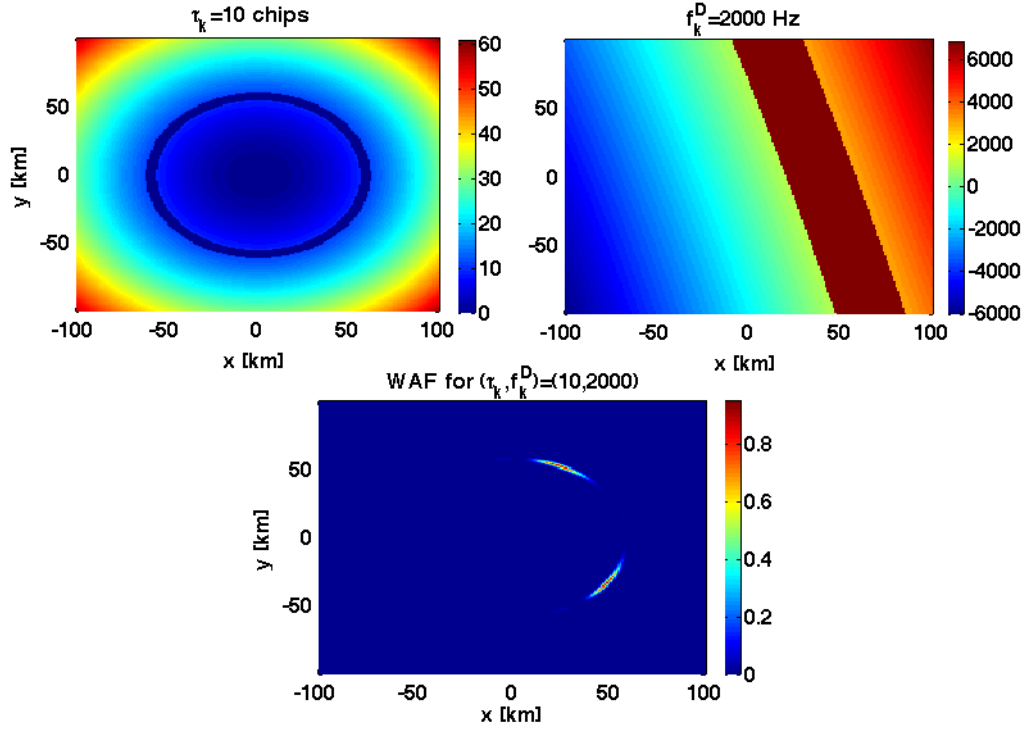
FIGURE 3.9: Illustration of the effect of WAF in space.

As it will be explained in detail in chapter 6, it is mathematically appropriate and computationally convenient to apply the WAF directly in the DD domain, to the DDMs shown in figure 3.8. In this case, the power at each DD pixel of the DDM is given by the sum of the value at that pixel, and the contributions from the neighbouring pixels, weighted by the WAF. This causes a spreading of the power the original DDM in both the delay and the Doppler frequency directions. A plot of the final DDMs, obtained through WAF application to the ideal DDMs in figure 3.8, is shown in figure 3.10.

The DDMs in figure 3.10 represent the expression of the average scattered power in DD domain according to Z-V theory, shown in equation (3.1), and we will call them the Z-V DDMs. A comparison of a measured UK-DMC DDM with a Z-V DDM is shown in figure 3.11. The geometrical (transmitter/receiver positions and velocities) and sea
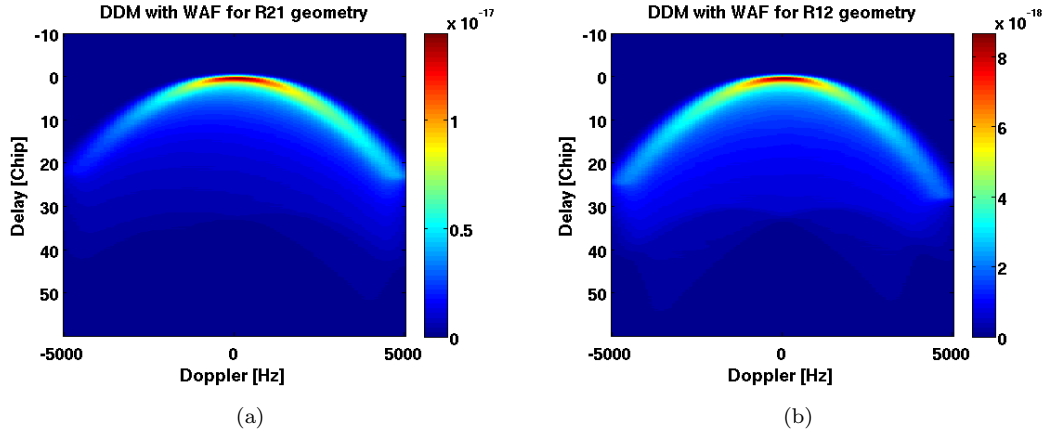
FIGURE 3.10: Final DDMs for R21 (a) and R12 (b) case, obtained through WAF application to the DDMs in figure 3.8.

state parameters (DMSS, PWSD) used to simulate the DDM have been matched in this case to those from the measurements.
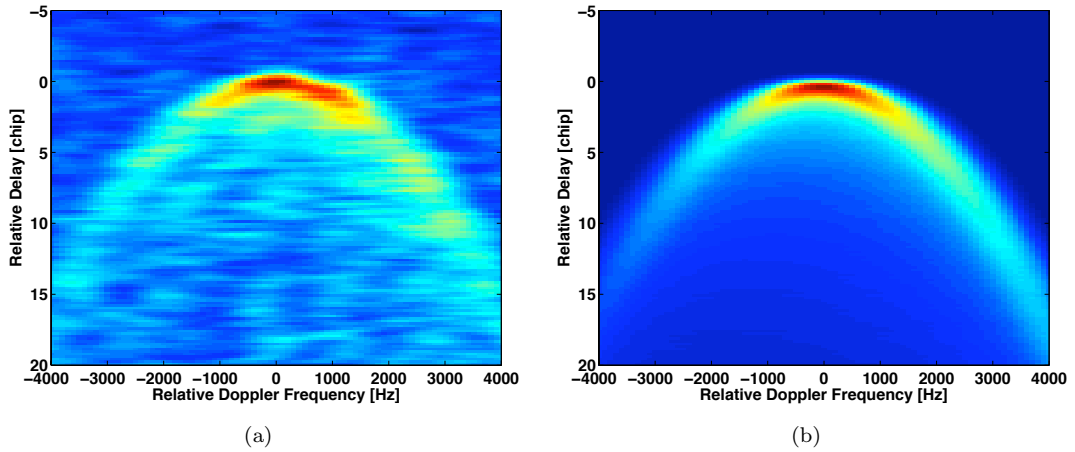
FIGURE 3.11: (a) Measured DDM obtained from the first second of UK-DMC R21 data. (b) simulated DDM using the Zavorotny-Voronovich model.

An overall good agreement can be noticed between measured and Z-V simulated DDMs, but some differences in shape, structure and power distribution can also be detected. These differences are partly due to the strong residual fading noise in the measured DDM, which cause the scattered power to be much more spread across the entire DD domain. However the theoretical model itself, which is based upon several approximations and simplifications, also plays a crucial role. These observed differences between model and data actually constitute one of the reasons for the implementation of a more sophisticated DDM simulator, which will be presented in the following chapters.

3.6   Z-V DDM Sensitivity to Sea State

Having illustrated how to simulate a theoretical DDM using the Z-V model, we now analyse how these maps respond to different sea states. In this paragraph we investigate variations in the DDMs with respect to different DMSS and different PWSD. A good sensitivity of the maps to changing DMSS and PWSD is of course desirable, as it would translate in a better capability to retrieve sea state information from DDMs. In order to characterize the effect of each of them on a DDM, we carry out two separate analyses of DDM sensitivity with respect to DMSS and PWSD.

3.6.1   Sensitivity to DMSS

As regards DMSS, the Z-V maps exhibit some variability in both the range of power values and the shape, when the DMSS change. For rougher seas (larger DMSS) the power peak at the specular point in the DDM tends to decrease, while the power scattered from points away from the SP increases, resulting in an increase of power values along the branches of the horseshoe shape in the DDM. This variability in the power level of the Z-V DDMs is relevant as it could potentially be used to discriminate different sea states. Unfortunately we have not been able to exploit the magnitude information in the measured UK-DMC DDMs, due to the lack of calibration of the incident GPS signal, as well as unrecorded effects within the receiver (amplifiers, automatic gain control), affecting the amplitude of the received signals. A direct comparison between simulated and measured DDMs is therefore feasible only if both of them are normalized. The normalization obviously removes the amplitude information, and leaves the shape of the DDM as the only parameter that can be exploited to retrieve the sea state. For this reason, the analysis of DDM sensitivity to different sea surface roughness conditions is here carried out on normalized DDMs. It is also worth pointing out that the DDMs have been computed in this paragraph using only the NRCS term as the scattered power. All the other terms (path losses, antenna gain) are assumed unitary across the GZ. Figure 3.12 shows contour plots of normalized DDMs for increasing DMSS. The DMSS values are in this case quite low, as this is the range of values where the DDMs exhibit the

strongest variability. In figure 3.12 we notice the effect of extension of the branches of the horseshoe shape, which cover larger delay and Doppler ranges for increasing MSS, demonstrating how power is increasingly scattered from areas away from the SP when the sea gets rougher. However, the DMSS values considered in figure 3.12 correspond to very calm sea conditions.
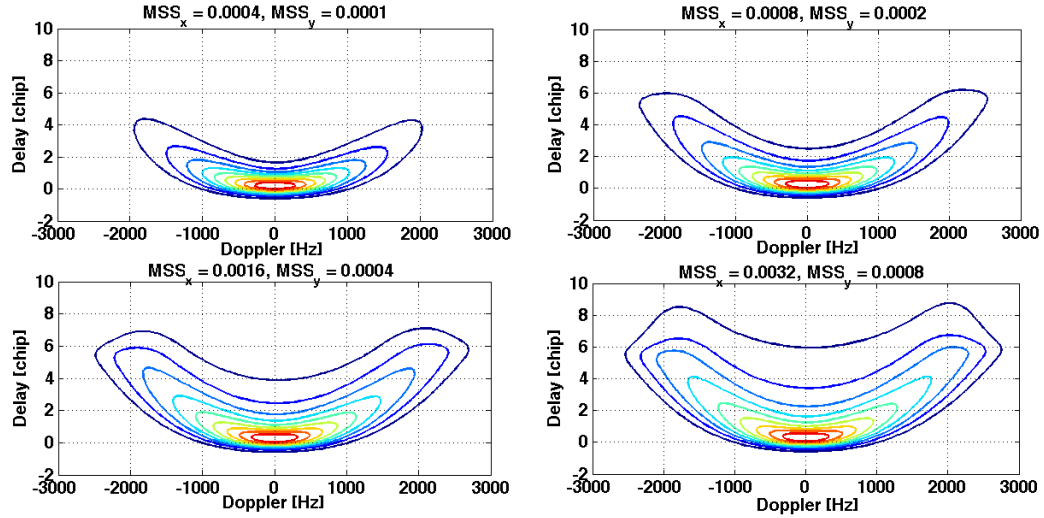
FIGURE 3.12: DDM variability shown as contour plots for small values of DMSS, assuming a zero wave direction. The contour lines correspond to normalized power levels.

DDMs for more realistic DMSS values, corresponding to rough sea conditions where some wind is present, are illustrated in figure 3.13. Compared to figure 3.12, here the DMSS values are already high enough to determine a saturation effect in the variability of the horseshoe shape of the DDM. This is a consequence of the saturation of the 2D gaussian function describing the slope PDF, for high DMSS values. Most of the DDM variability is now concentrated between the branches of the horseshoe shape, where the contour lines corresponding to the lowest power levels expand towards larger delays.

We have also carried out an additional sensitivity analysis for a skewed DDM, as a result of the combination of all the terms of the Z-V model, and found that the DDM sensitivity would increase for one side of the DDM (the one containing most of the scattered power), and decrease for the other side. Another important factor that strongly influences the DDM sensitivity with respect to DMSS is the directionality of the waves, defined as the ratio between the two DMSS. As an example, a highly directional sea surface will have the MSS along the major axis of the PDF much stronger than the other one. A high
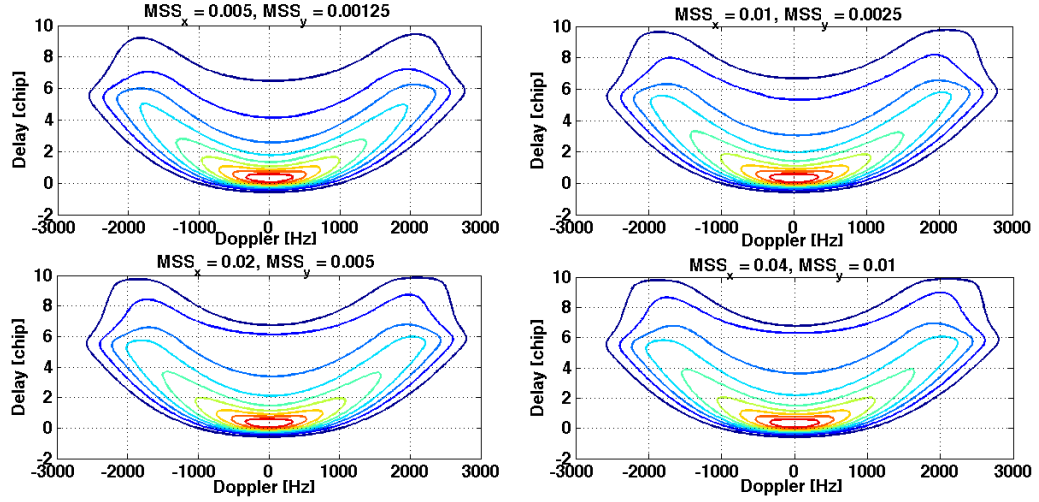
FIGURE 3.13: DDM variability shown as contour plots for larger values of DMSS, assuming a zero wave direction.

directionality of the sea surface translates into a stronger DDM variability with respect to DMSS, and therefore a stronger sensitivity.

3.6.2 Sensitivity to PWSD

The DDM sensitivity with respect to different direction of the waves is slighly more complex than the one relative to DMSS. This sensitivity is influenced by a number of factors, among which the geometry, through the configuration of the iso-delay and iso-Doppler lines, the directionality of the waves, defined by the ratio between the two MSS, that also determines the eccentricity of the gaussian ellipse, and finally the antenna footprint across the GZ. For simplicity here we fix both the geometry (shown in figure 3.2) and the directionality of the waves, and we analyse the DDM sensitivity with respect to different wave directions, with both a symmetric (unitary) and a skewed antenna. The directionality chosen for this analysis is reasonably high (MSS_x= 0.0138, MSS_y= 0.0011), to improve the DDM sensitivity with respect to different wave directions. This is intuitive, since when the two MSS are increasingly similar to each other the slope PDF ellipse collapses into a circle, preventing any retrieval of wave direction because the PDF would become rotationally symmetric. The sensitivity of DDMs with respect to 4 different directions of the major axis of the slope PDF, indicated as ϕ, is shown in figure 3.14. As in paragraph 3.5.1, here the DDMs have been obtained by mapping in

delay-Doppler domain the spatial map of NRCS, assuming a unitary symmetric antenna pattern across the GZ. The slope direction ϕ is only analysed between $0°$ and $180°$, as this is the only range of directions that we can retrieve, due to the symmetry of the slope PDF itself, for which a rotation of the NRCS of ϕ or of $\phi + 180°$ would produce exactly the same result. It is worth mentioning that such limitation would actually be eliminated if one considers a skewed PDF, having the two semi-axes of the 2D PDF ellipse not equal to each other. This is a non-linear effect that has been observed in real data [Cardellach and Rius (2008)], and that could be easily caused by the wind blowing in a given direction, and introducing an up-down asymmetry in the slope PDF. However, we do not use this assumption in the Z-V model.
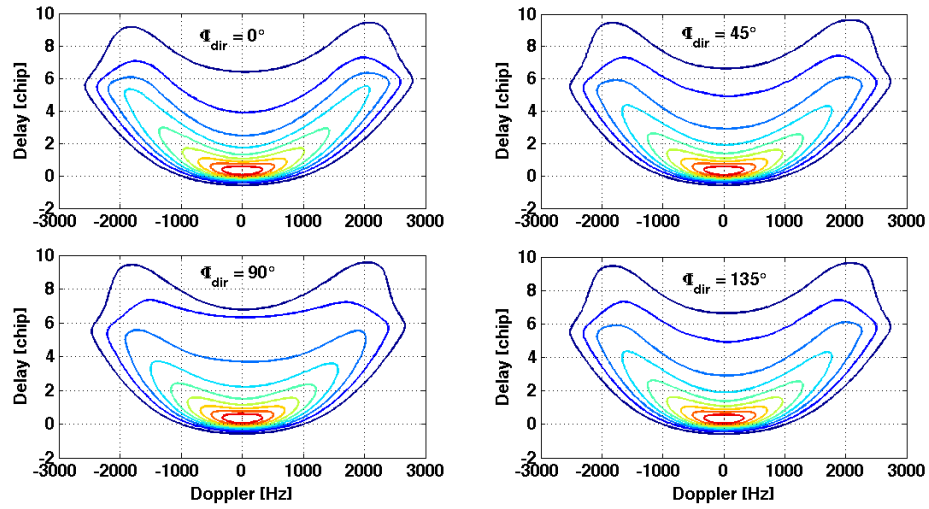
FIGURE 3.14: DDM variability as contour plots with respect to four different PWSD values (indicated as ϕ). The DDMs are here obtained through DD mapping of the NRCS only.

In figure 3.14, we can notice a progressive change in the power distribution, which is mostly concentrated along the horseshoe shape for $\phi = 0°$, while it reduces along the branches of the horseshoe shape and increases in the DD space between these branches for increasing values of ϕ , up to $90°$. For $\phi > 90°$ the trend reverses and goes back to the original one, as the DDM for $\phi = 180°$ is the same as that for $\phi = 0°$. The changes we observe in the DDM power distribution between $\phi = 0°$ and $\phi = 90°$ (or $\phi = 90°$ and $\phi = 180°$) can be justified by looking at the configuration of the iso-delay and iso-Doppler lines with respect to the NRCS map on the sea surface. Figure 3.15 shows the iso-delay and iso-Doppler lines for the considered geometry, along with the

NRCS map in space, whose major axis is oriented along x (a) or $60°$ counterclockwise from x (b). It is not difficult to see that most of the power in 3.15a is distributed along the horseshoe shape, when the major axis of the slope PDF almost coincides with the transverse axis of the iso-Doppler lines. When this happens, the biggest DD intersections in space, that correspond to points along the horseshoe shape, contain the highest part (the areas in red) of the power. In figure 3.15b, the NRCS rotation causes the same DD cells along the horseshoe shape to contain less power compared to figure 3.15a, while there is more scattered power for the smaller DD cells, away from the iso-Doppler axis, which correspond to points between the branches of the horseshoe shape. According to figure 3.14, when ϕ reaches approximately $90°$ the horseshoe shape should therefore reach its minimum extension.
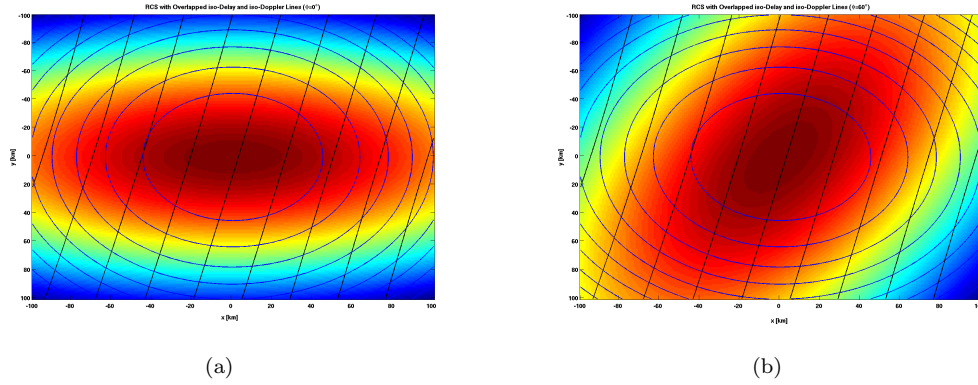
FIGURE 3.15: NRCS with overlapped iso-Delay and iso-Doppler lines, taken from a real GPS/UK-DMC geometry (R21 dataset, sec. no. 1). The PWSD is $0°$ in (a), and $60°$ in (b).

The DDMs in figure 3.14 for $\phi = 45°$ and $\phi = 135°$ appear instead almost identical to each other. This is not surprising, since the NRCS symmetry with respect to the y-axis results in a $90°$ ambiguity in the DDM , producing the same DDM when the rotation angle is either ϕ or $180° - \phi$. When the symmetry of the total scattered power is removed, through for example the addition of an asymmetric antenna pattern to the NRCS, then this $90°$ ambiguity is eliminated. Figure 3.16 shows DDMs for the same values of ϕ as in figure 3.14, but where the scattered power mapped in DD domain is now the combination of the same NRCS with an antenna pattern that is strongly asymmetric across the GZ, which can correspond to a realistic case. This time we notice that the DDMs for $\phi = 45°$ and $\phi = 135°$ are no longer identical, and the ambiguity disappears.

This is interesting, as it leads to the conclusion that a perfectly symmetric scattering across the GZ is indeed not desirable at all, as it makes the directions of the waves less distinguishable from each other and more difficult to retrieve unambiguously.
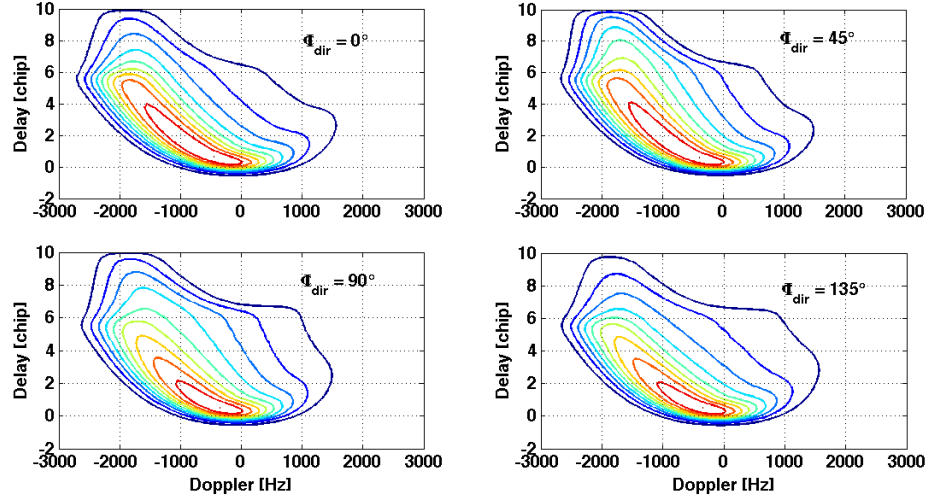
FIGURE 3.16: DDM variability as contour plots with respect to four different PWSD values (indicated as ϕ). The DDMs are here obtained through DD mapping of the NRCS multiplied by a strongly asymmetric antenna gain.

3.7   Least-Square Fitting of Simulated and Measured DDMs

Once theoretical DDMs are available from the Z-V model, a natural step forward would be to perform a direct comparison between real and simulated DDMs, and retrieve sea state geophysical parameters from such comparison. The approach we have used is to retrieve optimal values of DMSS and PWSD from the theoretical map that best matches the data map, in a least-square sense. Those values of DMSS and PWSD should be ideally representative of the sea surface conditions at that time. In practice, a direct comparison is made difficult by two factors: the first one is the noise, which is present in the measured DDMs; the second one is the need to normalize both the measured and the simulated DDMs, and the consequent loss of part of the DDM sensitivity with respect to roughness parameters. Despite these limitations, a Least-Square fitting procedure has been carried out for DDMs from four available UK-DMC datasets, each corresponding to sea states reasonably different from each other. The results obtained will be shown to be in good agreement with both theoretical calculations and in-situ measurements.

3.7.1 The Z-V delay-Doppler Map simulator

A simulator that uses the Zavorotny-Voronovich theory illustrated in paragraph 3.2 has been implemented to generate delay-Doppler maps. Results of this DDM simulator, first as spatial maps of the different components of the Z-V model (antenna gain, NRCS, path losses) and as final DDM (with and without WAF) have been extensively shown in sections 3.3-3.5. The Z-V simulator requires some input parameters which can be grouped into:

1. Geometry parameters: these are transmitter and receiver positions and velocities, in ECEF coordinate system, available from the IGS GPS satellite files and the UK-DMC telemetry files, respectively [Gleason (2006)];

2. Dimension and resolution of the Glistening Zone;

3. Antenna parameters: the simulator requires the original UK-DMC downward antenna 3dB footprint map;

4. Sea state parameters: these are the DMSS and the PWSD, defining the PDF of the sea surface wave slopes;

5. Delay-Doppler parameters: these are the delay range and resolution, expressed in chips, and the Doppler range and resolution, expressed in Hz.

The Z-V simulator first finds the SP by scanning the transmitter-receiver line, projected onto the Earth surface, and choosing the point for which the incident angle is equal to the reflected one, satisfying Snells law. Then, it converts the ECEF positions and velocities of the transmitter and receiver into a new coordinate system, with its origin into the SP, the z-axis orthogonal to the sea surface, and the transmitter and receiver lying on the $x - z$ plane, with a negative and positive x-coordinate respectively (illustrated in figure 3.2). The method to find the SP is graphically illustrated in figure 3.17.
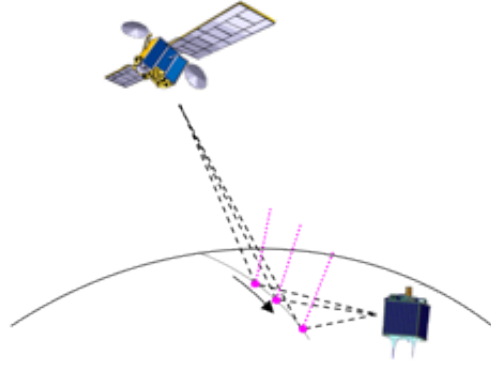
FIGURE 3.17: An illustration of the method used to find the specular point. The transmitter-receiver line, projected onto the Earth surface is scanned, and the incidence and scattering angles or each point of it are calculated and compared to each other.

3.7.2 DDM Fitting Procedure

The purpose of the DDM fitting procedure is to find the DMSS and PWSD values of the simulated DDM that best matches the measured DDM, in a least square sense. These values should be representative of the roughness of the sea surface where the GNSS reflection comes from. Mathematically this means:

$$[DMSS, PWSD]_{opt} = \underset{\substack{DMSS \\ PWSD}}{argmin} \left\{ \left[\left\langle P_{DATA}\left(\hat{\tau}, \hat{f}_D\right) \right\rangle - \left\langle P_{Z-V}\left(\hat{\tau}, \hat{f}_D\right) \right\rangle \right]^2 \right. \tag{3.10}$$

The least-square fitting has been accomplished using the lsqcurvefit optimization routine of the MATLAB *Optimization Toolbox*. A large-scale optimization algorithm has been chosen, based on the interior-reflective Newton method. This type of algorithm has been preferred over the medium-scale algorithms because it allows to set an upper and lower bound for both DMSS and PWSD. The upper and lower bounds for PWSD have been chosen equal to 0 and π respectively, given the 180° ambiguity in the direction retrieval, discussed in 3.6.2. The upper and lower bounds for DMSS have been chosen empirically, looking at extreme values of DMSS for very calm and very rough seas (0.0005 and 0.4 respectively). The fitting procedure was applied to the four UK-DMC datasets only, which were the only data available at the time the processing was performed. These data are a collection of 20-second of GPS reflections, acquired at different times, for different PRN codes (GPS satellites) and different sea conditions. Given that the incoherent

accumulation time for each DDM is chosen to be 1 s, each dataset can be thought as a collection of 20 DDMs. For each dataset, the fitting has been only applied the first 12 seconds of data collections, therefore to the first 12 DDMs. The processing was not applied to the whole 20 seconds of data collection because the generation of each single 1-s DDM using the Daaxa software was very time consuming. The fitting routine has also been applied to the average DDM, namely the DDM obtained by averaging altogether the 12 1-second DDMs for each dataset. A 12 s average was a good compromise between the need to smooth out the DDM to mitigate the fading noise, and the need to keep such temporal average restrained due to changing geometry of the satellite and viewing of the sea surface. All the UK-DMC datasets were collocated with in situ measurements of wind and waves by NDBC buoys. Table 3.1 shows for each data collection the co-located buoy data for Wind Speed (SW), Wind Direction (WD), Significant Wave Height (SWH), and Mean Wave Direction (MWD), the latter available for one dataset only. It also shows the so-called space collocation range (SCR), namely the distance of the buoy from the closest to fathest SP within the 12-second interval. The 1 hour/100 km

Label	Date/ Time	Region	NDBC Buoy Id	Buoy WS [m/s]	Buoy WD [Deg.]	Buoy MWD [Deg.]	Buoy SWH [m]	SCR [km]
R12	16/11/04 07:54	NW Pacific	46006	8.3	253	N/A	2.80	[38-56]
R20	21/03/05 07:29	NW Pacific	46002	3.6	297	N/A	4.30	[32-58]
R21	02/05/05 09:16	Hawaii	51001	4.5	23	N/A	1.98	[1-44]
R29	29/10/05 14:40	Virginia	44014	9.4	326	341	1.68	[70-79]

TABLE 3.1: Available UK-DMC GPS-R Data Collections, Together With Collocated in Situ Measurements by NDBC Buoys [from Clarizia et al. (2009b)].

time/space co-location criterion [Gommenginger et al. (2002)] ensures that all the 12-second measurements are fully collocated. We have carried out an examination of the buoy wind/wave measurements preceding and following in time the GNSS reflection, in order to characterize more accurately the wind/wave conditions at the time the signal was acquired. This examination is shown in figure 3.18, and it indicates that the four situations are atypical seas.
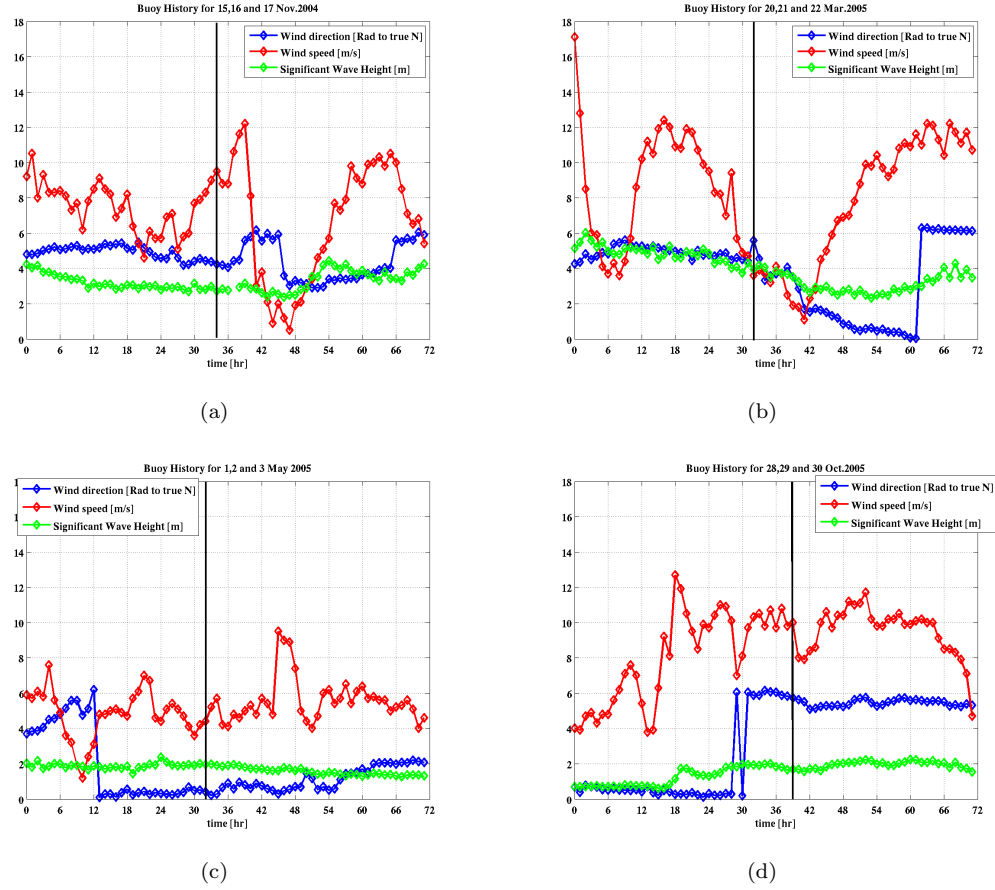
FIGURE 3.18: Analysis of wind speed, wind direction and SWH from the buoys collocated with the four GNSS-R acquisitions, from the day before to the day after the acquisition was made. The black line indicates the time the GNSS-R signal was acquired.

The wind/wave conditions for each case can be described as follows:

- A moderately rough sea characterizes the R12 dataset, with high wind speed variability and some swell;

- A decaying sea characterizes the R20 dataset, with a rapidly decaying wind speed (from 12 m/s to 4 m/s in 12 hours). In this case, the high SWH (see table 3.1) has been generated by the wind previously blowing at 12 m/s, and it is therefore not related to the instantaneous wind speed. Some swell is also present;

- Steady wind/wave conditions were present for R21 dataset, with a wind blowing at about 5 m/s, and with some swell;

- A growing sea condition was registered for R29 dataset. As opposed to R20, this time we have a moderately high wind speed, but a low swell. This means that the wind has been blowing at a quite low speed, leaving behind a calm sea state, and it is increasing at the time the acquisition is made. This is also the only case where the swell is likely to be absent.

It is worth mentioning that the presence of swell is normally established through well-known empirical relationships between wind speed and SWH, like the Pierson-Moskowitz (P-M) relationship [Pierson and Moskowitz (1964)], such that a SWH higher than that predicted by the P-M relationship, calculated using the local wind speed, would normally indicate a swell superimposed on wind waves. Before presenting and discussing the results, some extra DDM manipulations are needed prior to the least-square fitting, and they will be explained in the next two paragraphs.

3.7.3   DDM Alignment

Two types of alignment between DDMs must be carried out prior to the least-square fitting procedure. The first one is the alignment between the 12 DDMs from the same UK-DMC datasets, to construct the single average DDM. This is due to the shift, mostly along the delay, and marginally along the Doppler, that the measured DDMs exhibit from one second to the other [Gleason (2006)], due to the movements of transmitter and receiver and changing geometry in time. This effect requires a re-alignment of the 12 maps, to avoid a blurring effect in the final DDM. Figure 3.19 shows the DDM displacement at different seconds, along with the average DDM obtained through alignment of all the 12 DDMs.

The second alignment required is instead between the data DDMs (either 1-second or average DDM) and the theoretical DDM from the Z-V model. This is mainly due to the fact that the delay-Doppler location of the SP is not known with high accuracy in the measured DDMs. The SP is usually difficult to identify mainly due to the residual speckle noise in the maps, which obscures the power peak at the SP. Moreover, the exact SP location in a measured DDM could be calculated through knowledge of the
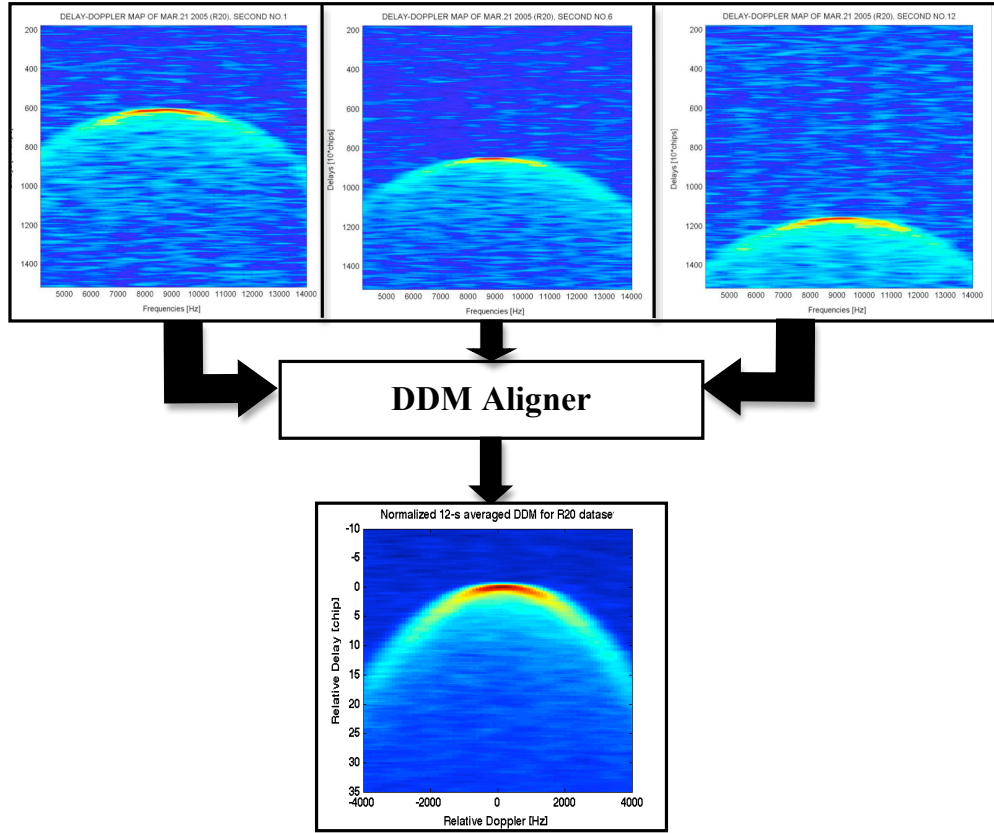
FIGURE 3.19: Illustration of DDMs for R20 dataset , from the 1st (left), 6th (centre) and 12th (right) second of acquisition. The delay and Doppler axes are in absolute values. The shift of the horseshoe shape, along the vertical (delay) axis, is clearly visible. These DDMs are the input to the DDM aligner that produces the 12-s average DDM as output. The delay and Doppler axes of the 12-s average DDM are relative to that at the SP.

transmitter and receiver positions and velocities, but a small residual error in such calculation remains, due to a bias in the clock receiver [Gleason (2006)]. Because we did not have access to all the necessary information to estimate such bias, we chose a different approach, which consists of aligning the measured and simulated DDM through a 2D cross-correlation. The criterion is to maximise the 2D correlation between maps, and then to select a subset of the measured DDM (usually much larger than the theoretical DDM) using the horizontal and vertical position of the peak of the 2D correlation map. A schematic of this procedure is illustrated in figure 3.20.

In principle the alignment procedure should be repeated every time the DMSS and PWSD values are changed and a new theoretical map is generated within the fitting procedure. However, we carried out some empirical tests which demonstrate that such
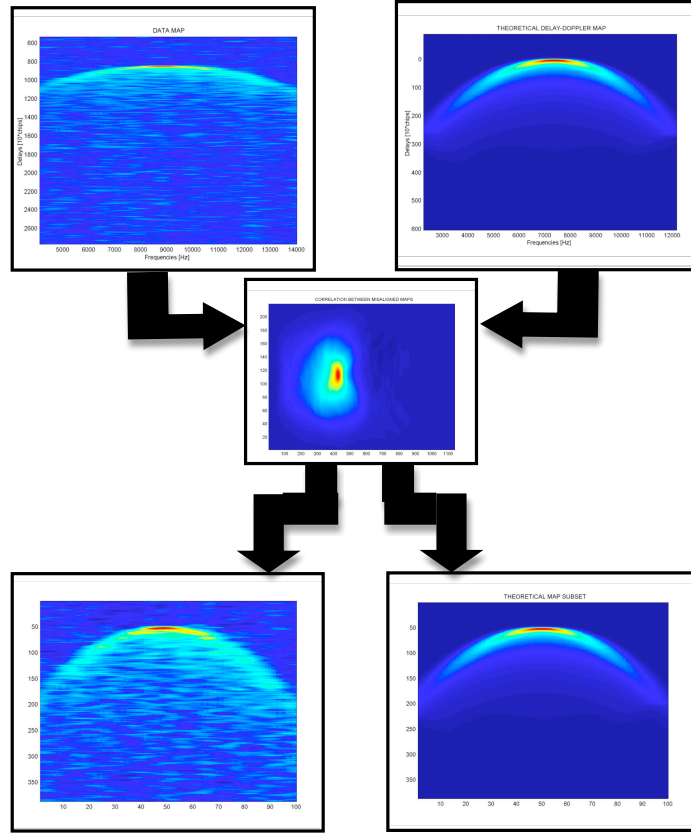
FIGURE 3.20: A schematic of the alignment between the measured and the Z-V DDM. A 2D cross-correlation map is produced from the original measured and simulated DDMs, the x-lag and y-lag of the peak in the correlation map is used to cut the measured DDM, and has now the same delay and Doppler range as the Z-V DDM, and it is aligned with it.

alignment does not change when only the wave slope PDF parameters are changed. This suggests that the alignment is actually influenced only by the particular geometry rather than the sea roughness. Thus, the alignment was carried out only once for each data DDM, prior to the beginning of the fitting procedure.

3.7.4   DDM Normalization

After having aligned the maps, a further problem arises when comparing their power values, which has been shown to be quite different, due to the lack of calibrated data. Therefore, we have added in the fitting procedure a scale and offset factor for the DDM values, to be estimated along with the DMSS and PWSD, in a least-square sense. This has been inspired by the approach outlined in [Germain et al. (2004)], where they jointly

estimate in an iterative manner the roughness parameters measured at airborne, along with some nuisance parameters which contained among others an amplitude and offset factor, too. The least-square procedure can be therefore re-summarized mathematically as follows:

$$[DMSS, PWSD, \alpha, \beta]_{opt} = \underset{\substack{DMSS \\ PWSD \\ \alpha, \beta}}{argmin} \left\{ \left[\left\langle P_{DATA}\left(\hat{\tau}, \hat{f}_D\right) \right\rangle - \left(\alpha \left\langle P_{Z-V}\left(\hat{\tau}, \hat{f}_D\right) \right\rangle + \beta \right) \right]^2 \right\} \quad (3.11)$$

where α and β are now the amplitude and offset parameters to be jointly estimated with the roughness parameters. The inizialization values of the scale and offset parameters of the theoretical maps are chosen such that their minimum amplitude corresponds to the mean of the noise floor in the data maps, and their maximum amplitude is the same as that of the data maps.

3.8 Roughness Parameters from UK-DMC delay-Doppler Maps

Here we illustrate the results derived from the fitting procedure, in terms of DMSS and PWSD for the four UK-DMC datasets under investigation. We then compare our resulting total Mean Square Slope (MSS) with some theoretical MSS calculations, obtained from a given theoretical wind wave slope spectrum, and with MSS from in-situ measurements by NDBC buoys. The total MSS is simply obtained by summing the DMSS, and the comparison is made over total slopes because of the lack of direction information in the buoy data. The PWSD of only a single dataset was compared to the mean wave direction measured by the relative co-located buoy, because that was the only directional buoy available.

3.8.1   Fitting Results

We present the retrievals of DMSS and PWSD, calculated for each UK-DMC data collection. For each dataset, there are 12 retrieved DMSS and MSWD values, obtained from the 12 1-second DDMs, plus a single DMSS and MSWD retrieval, obtained from the

12-second average DDM. The first type of retrieval allows us to estimate the variability of the parameters within a 12-second time interval, but it is clear that part of this variability is dicated by the changing sea state, and part of it is due to the noise in the maps. The second type of retrieval increases the signal-to noise ratio in the DDM and it gives a smoother, almost noise-free map, which is easier to fit, but provides no insight into the variability of the retrieved parameters [Clarizia et al. (2009b)]. We analyse here the results from the first type of retrieval, from 1-second DDMs. Figure 3.21 shows the retrieved DMSS, along the major (upwind) and minor (crosswind) axis of the 2D gaussian PDF, for the four datasets. The ratio of the crosswind MSS and the upwind MSS is also illustrated, as it gives an indication of the directionality of the waves from the sea surface.

The MSS along the minor axis of the gaussian slope PDF, called here MSS crosswind, are considerably smaller than those along the major axis, called upwind. This is also confirmed by the ratio between them illustrated in figure 3.21c, suggesting that the waves on the sea surface from which the MSS were retrieved were reasonably directional. Figure 3.22 shows (a) the total MSS for the four UK-DMC datasets, which is simply the sum of the two DMSS, and (b) the retrieved PWSD. Given that the MSS crosswind are very low, it is not surprising that the trend of the total MSS remains the same as for the upwind MSS. The plotted retrieved PWSD is here the angle between the direction of the major axis of the slope PDF and the true north, that is the direction along the earth's surface towards the geographic north pole. The original PWSD from the fitting procedure are simply the angles between the major axis and the x-axis of the coordinate system shown in figure 3.2, so they have been converted into angles with respect to the true north.

It is interesting to note that the MSSs retrieved from the R21 dataset in figure 3.22a have a much narrower variability than the other cases. Indeed, the R21 case corresponds to probably the easiest and steadiest sea conditions among all the datasets. The results from R12 and R20 do not strong a strong variability either, apart from one or two high values. These values might either be true, or just the result of convergence of the fitting algorithm to local minima. The strongest variation in the retrieved MSS is found instead
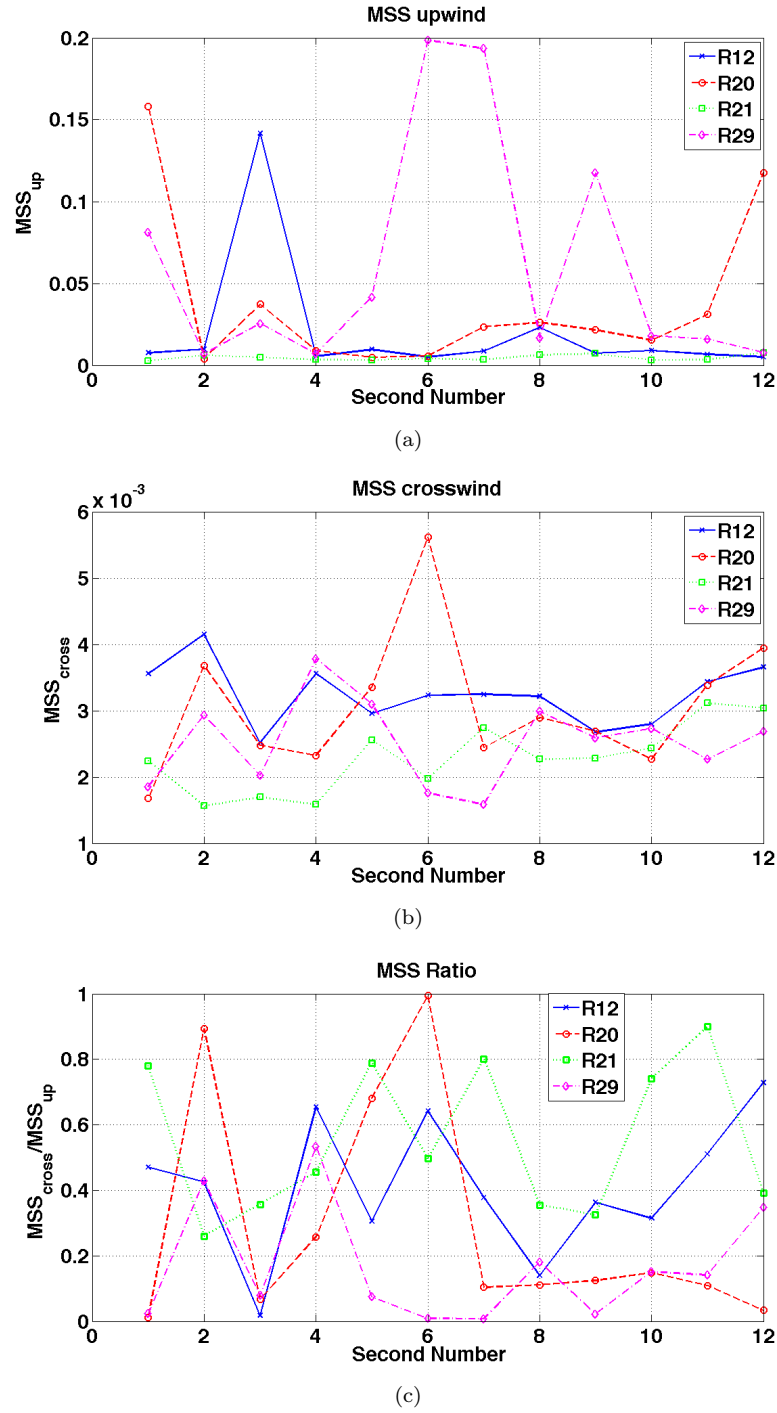
Figure 3.21: Retrieved MSS along the principal (a) and secondary (b) axis of the gaussian slope PDF, and ratio between the MSS crosswind and the MSS upwind (c), for the four UK-DMC datasets. The time axis indicates the second number, and the MSS axis shows the retrieved MSS value from the DDM corresponding to that second. Each color refers to a specific dataset.
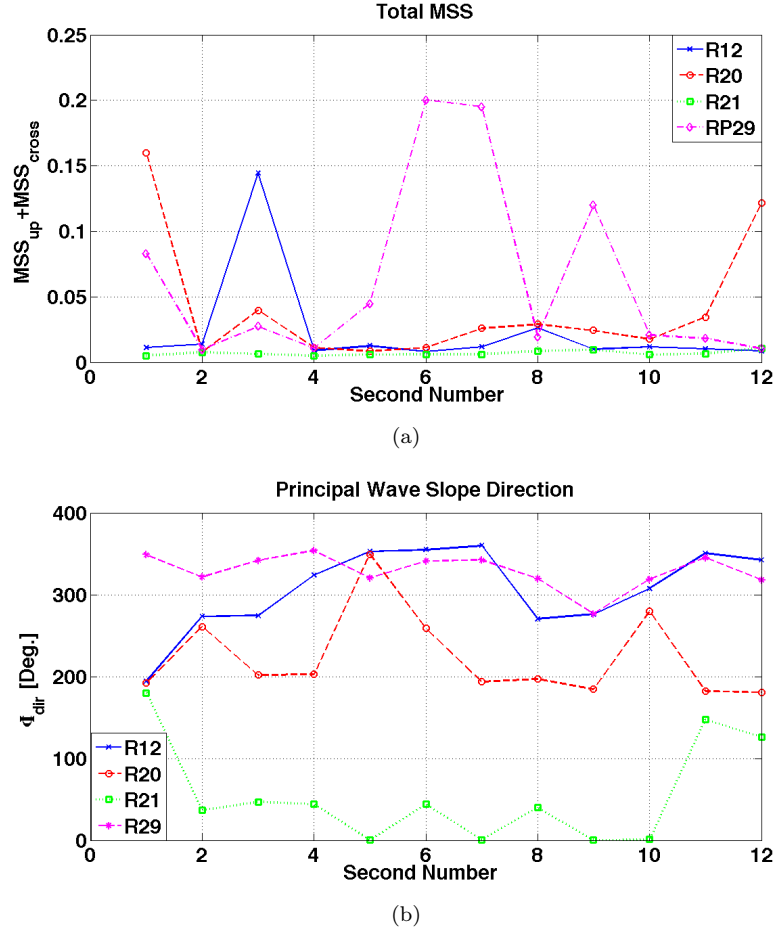
FIGURE 3.22: Retrieved total MSS (a) and PWSD (b), for the four UK-DMC datasets. The time axis indicates the second number, and the MSS axis shows the retrieved MSS value from the DDM corresponding to that second. Each color refers to a specific dataset.

in R29. This was a dataset with quite unusual sea conditions, as it was characterized by a high wind speed but a not very high SWH. It is therefore possible that the local wind affects the short-wave roughness of the sea surface and ultimately the GNSS-R scattering, causing fluctuations in the MSS and in the retrievals. On the other hand, the DDMs for the R29 dataset were also much noisier than the other cases, and this is likely to cause more fluctuations in the results. Figure 3.22b shows a degree of variability for the retrieved PWSD in all cases. Interestingly, the lowest variability is given by R29, as opposed to the MSS case.

3.8.2   MSS from NDBC Buoy Spectra

In order to verify the reliability of the produced results, we have compared our retrievals with some available real data, which should in principle constitute the ground truth. A real source of information is given by buoys of the National Data Buoy Center (NDBC) [www.ndbc.noaa.gov]. These buoys provide a wave spectrum, which they calculate by measuring a vertical displacement during a wave acquisition time, made up of several minutes. This spectrum does not contain any directional information, and it refers to a single spatial point, and a specific temporal interval. The buoy spectrum is therefore a frequency spectrum $S(f)$, and it is quite limited, as it usually contains frequencies from 0.03 Hz up to 0.4 Hz only. Because the DMSS retrievals refer instead to a spatial variability of the slopes, and a single temporal instant, we need to convert the buoy spectrum into a wavenumber spectrum $S(k)$ in order to do the comparison. The wavenumber spectrum and frequency spectrum are linked to each other through the following relation:

$$S(f)\, df = S(k)\, dk \rightarrow S(k) = s(f)\frac{df}{dk} \tag{3.12}$$

Frequency f and wavenumber k are relate through each other through the dispersion relation, whose approximate expression for long waves, assuming a high water depth, becomes [Robinson (2004)]:

$$(2\pi f)^2 = gk \rightarrow \quad \begin{aligned} f &= \frac{\sqrt{gk}}{2\pi} \\ \frac{df}{dk} &= \frac{\sqrt{g}}{4\pi\sqrt{k}} \end{aligned} \tag{3.13}$$

where g is the gravity acceleration. Equations (3.11) and (3.12) allows to obtain both the k-axis from the f-axis, and $S(k)$ from $S(f)$. To this point, the calculation of the Mean Square Slope (MSS) is done through integration of the slope spectrum $S_p(k)$, which is simply given by the height spectrum $S(k)$ multiplied by the squared wavenumber, as follows [Elfouhaily et al. (1997)]:

$$\sigma^2_{p(buoy)} = \int_{k_1}^{k_2} S_p(k)\, dk = \int_{k_1}^{k_2} k^2 S(k)\, dk \tag{3.14}$$

where $k_1 = 0.0036$ rad/m and $k_2 = 0.6439$ rad/m are the minimum and maximum wavenumbers corresponding to the minimum and maximum value of the frequency range 0.03 Hz and 0.4 Hz. In terms of wavelength, the buoy spectra represent the spectral energy of all the wavelengths down to 9.75 m. A plot of the frequency height spectra of the buoys considered for the four GNSS-R data acquisitions is illustrated in figure 3.23.
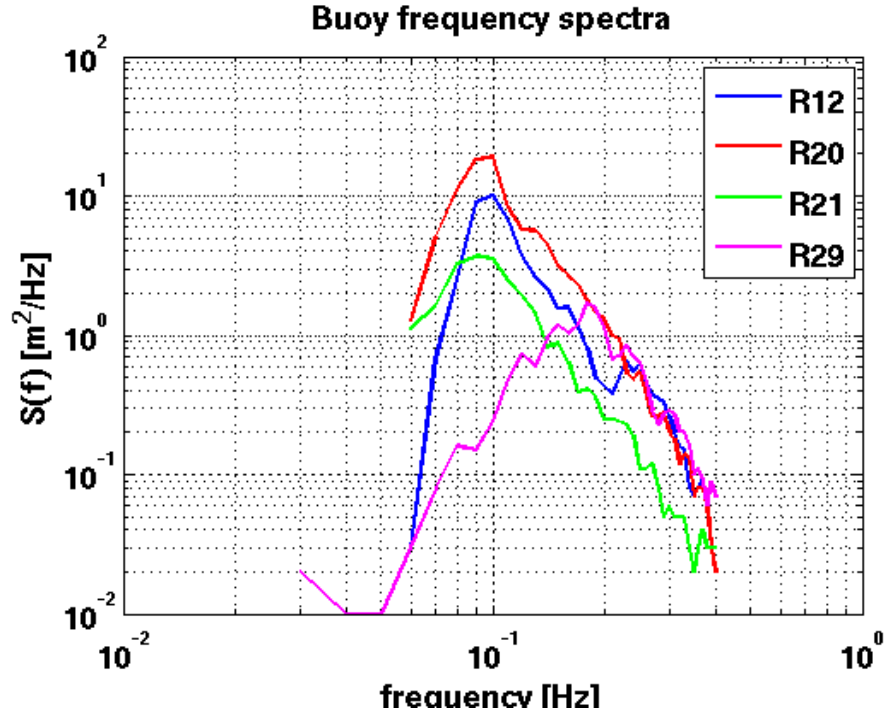
FIGURE 3.23: Frequency spectra of buoys co-located with the four UK-DMC datasets.

3.8.3   MSS from theoretical Spectra

The MSS retrievals have also been compared with MSS calculated from a theoretical wind wave spectrum, illustrated in [Elfouhaily et al. (1997)]. It is a wind-speed dependent wave spectrum, and it also depends on a parameter known as wave fetch, which allows the spectrum to describe both fully developed and young seas. Being a theoretical spectrum, the Elfouhaily spectrum can be calculated and integrated for any range of wavenumbers. This integration range has been matched to that of the buoy spectra, in order to produce results consistent with those obtained from the buoys. Therefore,

the MSS from the Elfouhaily spectrum $S^{Elf}(k)$ are obtained as follows:

$$\sigma^2_{p(Elf)} = \int\limits_{k1}^{k2} k^2 S^{Elf}(k)\, dk \tag{3.15}$$

Figure 3.24 shows a picture of Elfouhaily wave height spectra (dashed lines), calculated using the four buoy-registered wind speeds for each GNSS-R dataset, along with buoy wavenumber spectra of the sea surface height, measured for each dataset (continuous lines), and obtained by converting the buoy frequency spectra shown in figure 3.23. The black vertical dashed lines indicate the minimum and maximum wavenumbers used to integrate the spectra.
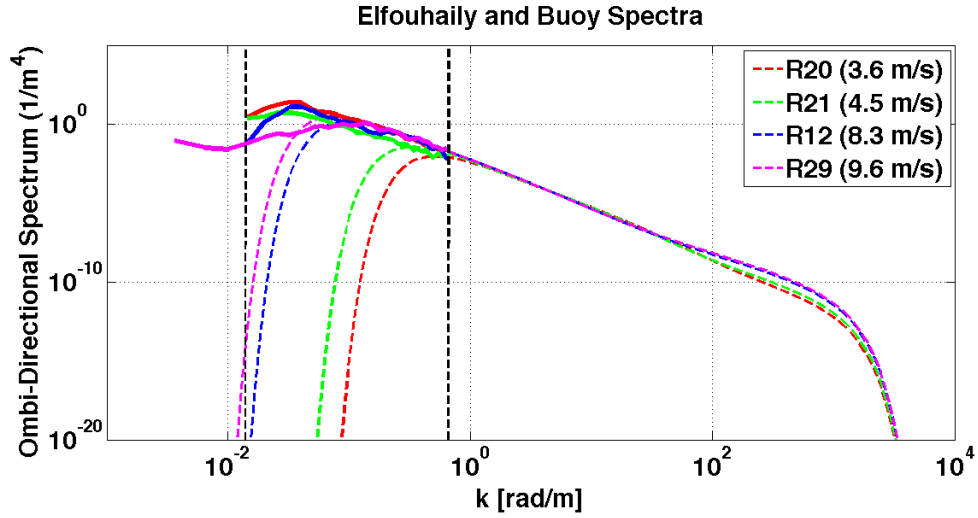
FIGURE 3.24: Buoy (continuous lines) and Elfouhaily spectra (dashed lines) plotted together. The Elfouhaily spectra have been generated using the wind speed measured from the buoy co-located with the acquisitions from the relative dataset.

3.9   Results and Comparison with Buoys and Theoretical Spectra

Figure 3.25 shows a compact representation of the 12 retrieved total MSS illustrated in figure 3.22. They are represented as the median of the retrievals for each dataset (crosses), while the variability of the retrievals is shown as errorbars through the Median Absolute Value (MAD), defined as the median of the absolute residuals from the median of the data. These statistics are more robust with respect to the classical mean and
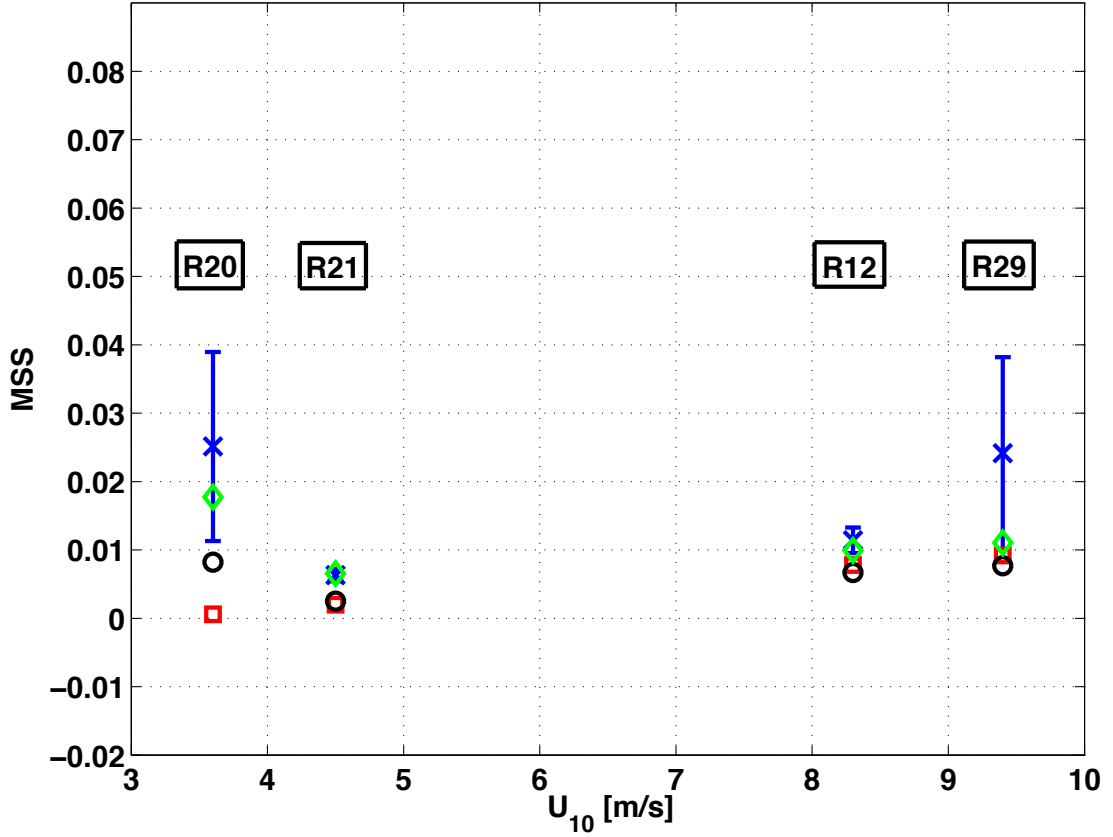
FIGURE 3.25: Median of the total retrieved MSSs from 1- second DDMs over 12 seconds (crosses) with MAD (as error bars) and MSSs estimated from 12-second averaged DDM (diamonds), versus buoy wind speed [Clarizia et al. (2009b)]. Total MSSs from the truncated theoretical Elfouhaily wind wave spectrum (squares) and buoy-derived total MSSs (circles) are also illustrated for comparison.

standard deviation, and they are a preferable choice due the presence of outliers in the retrievals shown in figure 3.22, possibly caused by convergence of the fitting algorithm to local minima in some cases. Figure 3.25 also shows the single MSS retrieval from the 12-second average DDM. All results are plotted versus the buoy wind speed for each data collection.

From Figure 3.25, a lower variability and good agreement can be noticed between the 1-s and 12-s retrievals for the case of R21 (steady conditions with some swell) and R12 (swell, high wind speed variability), compared to the cases of R20 (decaying sea) and R29 (growing sea). The median MSSs for R29 are much higher than the buoy measurements: this could be due to the stronger wind speed, generating higher short waves, not sensed by the buoys, which raises the MSS retrieved from the GPS-R signals. The higher MSS for R20 case might be linked to a higher wind wave component, left behind by the high
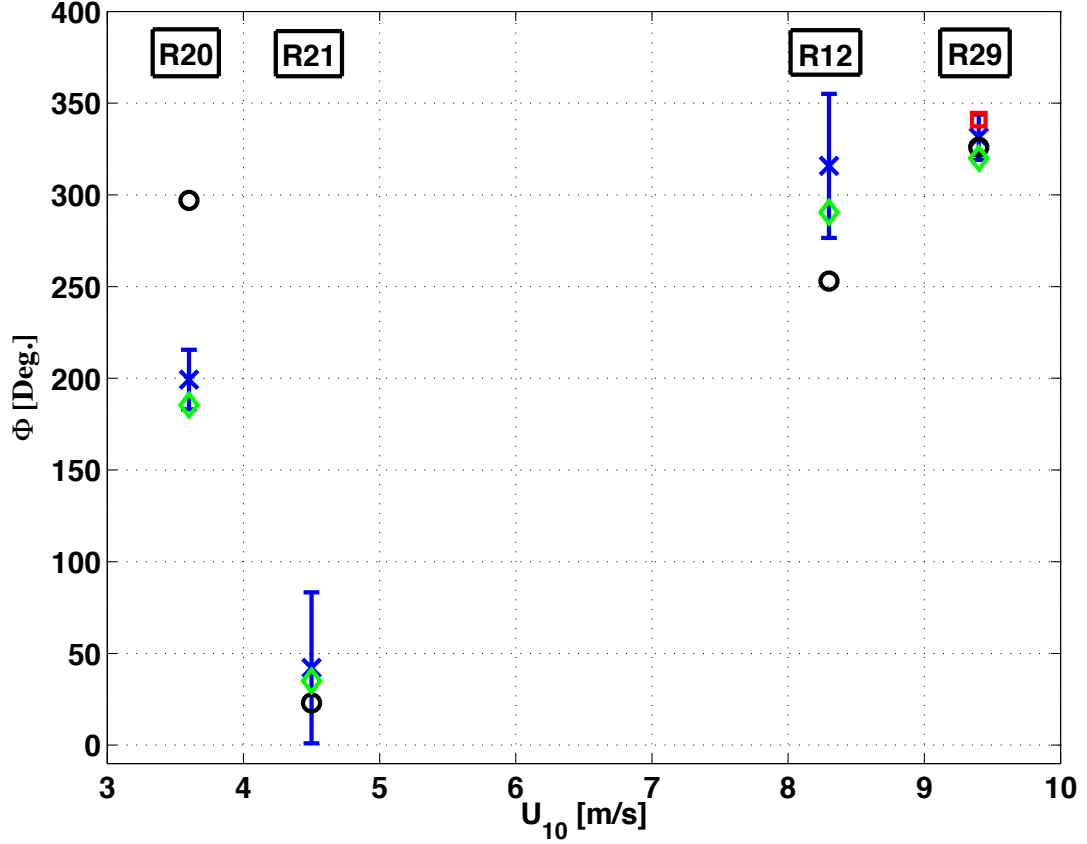
FIGURE 3.26: Median of the retrieved principal slope directions from 1-second DDMs (crosses) with MAD (error bars) and slope directions estimated from 12-second averaged DDM (diamonds), versus buoy wind speed [Clarizia et al. (2009b)]. Buoy wind directions (circles) and MWD (square) are given for comparison.

wind speed that characterized the hours preceding the acquisition, and therefore not related to the low wind speed at the time of the acquisition. Figure 3.25 also highlights that our retrieved MSSs show the same behaviour as the buoy-measured MSSs, and are always higher than them, which might be explained by the sensitivity of the GPS wavelength (19 cm) to shorter waves. Overall good results are obtained for the cases of R21 and R12, as the MAD is quite small, and both the buoy and the theoretical Elfouhaily- truncated MSSs are in good agreement with our estimates. Encouraging results are also obtained for MSSs retrieved from averaged 12-s DDMs, as they appear to be quite close to both the values measured by the buoys and the MSSs obtained from the theoretical spectrum, except at R20. Figure 3.26 shows instead the retrieved PWSD results versus buoy wind speed.

As shown in table 3.1, The Mean Wave Direction (MWD) was available only for R29,

and the MWD value was very close to the wind direction values at the time the acquisition was made, meaning that wind and wave directions were almost aligned. The overall behaviour of the retrieved directions in figure 3.26 follows that of the buoy wind directions. We find good agreement between our 12-second median principal direction from 12 1-second DDMs and the buoy measurements for R21 and R29. As compared to MSS, this time we have a complementary behaviour, as we find a higher variability in the retrieved direction for the cases of R21 and R12, and a lower variability for the cases of R20 and R29. Looking again at the MSS ratio in figure 3.21c, and excluding potential outliers from the plots (which is what the median and MAD do), the PDFs for R20 and R29 are more anisotropic (i.e., the MSS ratio is smaller on average compared to the other two cases), and thus they probably exhibit a predominant slope direction which is retrieved with less ambiguity. Our retrieved slope directions from averaged 12-s DDMs are again in very good agreement with the buoy measurements, and we notice that the worst match is obtained for R20, as in the case of the MSS.

3.10   Summary

In this chapter we have shown how to simulate a DDM using the Z-V theoretical model. We have presented examples of Z-V DDMs, illustrating all the single components that contribute to the DDM generation, and discussing how the DDM is affected by each of them. We have then focused on the variability of the simulated DDMs with respect to changing sea state (MSS and wave direction), as this is the parameter of interest, describing the roughness of the sea surface. We have presented a methodology to retrieve the sea surface roughness from measured UK-DMC DDMs, expressed in the form of DMSS and PWSD. The approach consists of fitting in a least-square sense the data DDMs to those simulated using the Z-V model, in order to extract the optimal DMSS and PWSD values. This approach has been applied to four available UK-DMC datasets, for both single 1-s DDMs, and for the average DDM over 12 seconds of data collection. The results have been compared to mean square slopes measured from co-located NDBC buoys, and to the mean wave slope direction, available for only one dataset. A comparison has also been performed with theoretical calculations of mean square slopes, through

integration of the [Elfouhaily et al. (1997)] wind wave spectrum. Our retrieved values have shown an overall good agreement and general consistency with both buoy measurements and theoretical calculations. This analysis, presented in [Clarizia et al. (2009b)], represents the first one that uses satellite DDMs to retrieve sea surface roughness, complementing previous analyses where satellite delay waveforms [Gleason et al. (2005)], or DDMs from aircraft campaigns [Germain et al. (2004)] were employed. Notably, the exploitation of DDMs allows us to retrieve not only roughness, but also surface slope direction. Even though the analysis has only been applied to four UK-DMC datasets available at the time, the results still offer convincing evidence for using GNSS-R to retrieve wind and wave data using a small passive instrument, that could easily be fitted on more satellites. This study has also highlighted differences between measured and simulated DDMs, that are partly linked to instrumentation and processing, and partly due to geophysical processes not accounted for in the GO-based model. The need for a better understanding and characterization of the interactions between the waves and the GPS scattered signal motivated the implementation of a more sophisticated GPS scattering simulator, which will be presented in the next chapters.

Chapter 4

A New Scattering Model for GNSS-R: the Facet Approach

4.1 Introduction

In the previous chapters, we have shown how to extract roughness information from GNSS-R data (Delay-Doppler maps), through the use of the Zavorotny-Voronovich model for DDM simulation. We now move on to the implementation of a new GNSS-R scattering simulator, different from the Z-V one, which uses realistic explicit representations of the sea surface, and an improved ElectroMagnetic (EM) scattering model. In this chapter, the motivations that lead to the development of such a simulator are first explained, and the overall structure of the simulator is presented, focusing also on the advantages that we gain with respect to the Zavorotny-Voronovich model. Then, we describe in detail the innovative EM scattering model that we use to compute the scattering. This model is based on an approximation of the sea surface through facets, and for this reason we call it the Facet Approach (FA). Before presenting the FA and its details, we provide some background on large-scale scattering theories. These are the Kirchhoff Approximation, and the Geometrical Optics, and they are both fundamental

to a comprehensive understanding of the facet approach. Some results in this chapter were published in [Clarizia et al. (2012)], which is provided in appendix II.

4.2 Motivation and Structure of the GNSS-R Scattering Simulator

In Chapter 3, we have shown how to extract roughness information, in the form of Directional Mean Square Slopes (DMSS) and Principal Wave Slope Direction (PWSD), from spaceborne GNSS-R data. The methodology consisted of fitting in a least-square sense Delay-Doppler Maps from the UK-DMC satellite with DDMs simulated using the Zavorotny-Voronovich model. The study, published in [Clarizia et al. (2009b)], has shown good general agreement between measured and simulated DDMs, and the retrieved DMSS compared favorably against in-situ measurements from buoys and theoretical calculations from the Elfouhaily spectrum. We have also pointed out that this study represented the very first measurement of roughness from spaceborne GNSS-R data, using a more complete source of information, given by the DDMs. However, this study has at the same time highlighted some differences between the UK-DMC measurements and the Z-V model. These differences have been in particular detected away from the specular point in the DDM, where the power drop-off along the horseshoe shape seems slower in the measured DDMs compared to the Z-V DDMs, and patches of power between the horseshoe branches are observed in the measured DDMs only (see figure 3.11). These differences may be due to several factors. Residual speckle noise due to the limited incoherent averaging time in the satellite observations could be partly responsible for the patchiness seen in the measured DDMs, which is not present in the theoretical ones, for which the temporal averaging is effectively infinite. Other elements affecting the measured DDMs could be thermal noise in the receiver, or general limitations or problems in the receiver hardware. Conversely, it is also conceivable that the differences may originate from limitations of the modeling, or from the simplified way of describing complex sea surfaces through a Gaussian PDF of the sea surface heights and slopes. Indeed, the Z-V model is based on Geometrical Optics (GO) limit for the scattering, where only the reflections from specular scatterers of the surface contribute

to the signal. Furthermore, the Z-V model assumes linear statistics of the sea surface, and therefore describes the sea surface simply through a Gaussian PDF. All these considerations led to the conclusion that accurate representation of the GNSS-R scattering may require a more advanced representation of the sea surface itself, and a better model to describe the scattering of these signals from the sea surface. The way to tackle this problem is to use a different approach, which represents the core of this and the following chapters. Instead of using a closed-form analytical model like the one in [Zavorotny and Voronovich (2000)], a simulation of the scattering of GPS signals from the sea surface is implemented. This is done through the use of explicit 3-D representations of the sea surface, and by adopting the more general theoretical framework of the Physical Optics (PO) scattering approximation (also known as the Kirchhoff approximation) in order to simulate the forward scattering of GPS signals from the sea surface. The block diagram shown in figure 4.1 presents the different elements of the simulator we developed:

| 3D Sea Surface Simulation | → | FA Polarimetric Scattering Model | → | DD Processing of the scattered GPS signal | → | WAF Application |
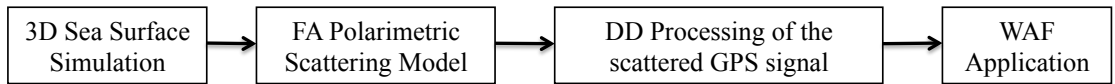
FIGURE 4.1: Block diagram of the GNSS-R scattering simulator.

1. 3D sea surface simulation: the explicit representations of the sea surface allow us to effectively build surfaces, with some given spectral and statistical properties, rather than simply describing them through a Gaussian PDF. This gives more flexibility and leads to a much wider range of sea surface conditions, including complex combinations of wind waves and swell traveling in different directions., or non Gaussian surfaces, characterized by non linear phenomena (i.e. asymmetry in the wave profiles).

2. Facet Approach (FA) polarimetric scattering: the simulator computes the scattering through a novel facet-based implementation of the KA, applied to explicit sea surfaces. We will call this method the Facet Approach (FA). We will show that this approach retains the advantages of the full KA for the representation of the scattering properties (compared with the high-frequency GO approximation used in Z-V) but considerably simplifies the calculation of the KA by applying it to facets approximating the sea surface. As a result, the scattered field can

be calculated directly for the large-scale roughness components present in a sea surface realization, thus depending on the actual features of the simulated sea surface, rather than on a simple statistical description of the wave field. Another important difference of our approach is the use of a vector formulation to model the scattered field, as opposed to scalar formulation used in the Z-V model. This allows us to investigate polarization effects in a much more comprehensive way than the Z-V model. The importance of polarization was previously recognized in [Zuffada et al. (2004)] and the representation of polarization effects in large-scale scattering models was attempted only recently by [Thompson et al. (2005)] using a refined GO model based on a vector formulation.

3. Delay-Doppler Mapping: once a sea surface has been simulated and approximated through facets, and a spatial map of scattered signal using the FA has been computed, it is necessary to perform a delay-Doppler mapping of the spatial map of scattered power, and to apply the WAF as discussed in chapter 3. The delay-Doppler mapping and subsequent WAF applications represent a faster and easier way to numerically implement the full 2D delay-Doppler correlator, and the WAF naturally takes into account the characteristics of the GPS incident signal.

4.3   A brief review of scattering models: KA and GO

In this section, we present an overview of the two most important large-scale scattering models for GNSS-R: the Kirchhoff Approximation (KA), and its high frequency limit, the Geometrical Optics (GO) model. Here we only focus on the scattering from the large-scale components of the sea surface, which is believed to represent the dominant type of GPS signal scattering from sea surfaces [Zavorotny and Voronovich (2000)]. Thus, we do not take into account any small-scale Bragg resonant scattering, which would mainly occur from the periphery of the glistening zone, where diffuse scattering becomes dominant. The importance and effect of small-scale Bragg scattering on GNSS-R remains however an interesting topic that could be investigated in the future. The KA is the general scattering model from which our Facet Approach model is derived. The

GO is the EM model used in the Zavorotny-Voronovich theory, and therefore represents the baseline for comparison with the FA model. In this chapter, an implementation of GO as a vector formulation is presented [Ulaby et al. (1982)], more suitable for vector EM fields, which differs from the scalar GO formulation used in the Z-V model. However, we will also show that for the particular geometry considered for GNSS-R (i.e. transmitter and receiver lying in the $x - z$ plane), the vector formulation of GO reduces to the scalar GO formulation of the Z-V model.

4.3.1   The Kirchhoff Approximation

The Kirchhoff Approximation (KA) [Beckmann and Spizzichino (1963)], [Bass and Fuks (1979)], [Ulaby et al. (1982)], also known as the Tangent Plane Approximation (TPA) or Physical Optics (PO), represents the scattering in a quasi-specular regime, and it is generally applicable to surfaces with gentle undulations, namely with roughness scales much larger than the incident electromagnetic wavelength. This is equivalent to imposing the condition that the local radius of curvature of the surface is much larger than the incident wavelength, as follows [Bass and Fuks (1979)]:

$$\sqrt[3]{k_0 r_c} \cos{(\theta)} \gg 1 \tag{4.1}$$

where k_0 is the wave number of the incident radiation, r_c is the radius of curvature of the surface and θ is the incidence angle. It is worth mentioning that this is not a unique criterion to define the validity of KA. Other, less stringent criteria exist, as in [Beckmann and Spizzichino (1963)], or criteria defined statistically, in terms of correlation length and standard deviation of the heights of the sea surface, as in [Ulaby et al. (1982)]. The KA can be formulated both for scalar fields, and for vector fields. The scalar formulation of KA [Beckmann and Spizzichino (1963); Bass and Fuks (1979)], which is the starting point of the Z-V model, is the most commonly used, for its simplicity, but it does not take into account important effects related to vector fields, primarily polarization. As we deal with ElectroMagnetic (EM) vector fields, we use hereafter the more appropriate vector formulation of KA. The KA in its vector formulation is an approximation of the exact solution of the Stratton-Chu equations [Stratton (1941)] where the electric

($\mathbf{E}^s$) and magnetic ($\mathbf{H}^s$) fields scattered from a surface S are expressed as integrals of their tangential components on S. We use the formulation of the Stratton-Chu equation for the electric field found in [Ulaby et al. (1982)]. The scattered electric field can be expressed accordingly as follows:

$$\mathbf{E}^s\left(\mathbf{r}\right) = \iint\limits_S [j\omega\mu\left(\hat{n}\times\mathbf{H}^s\right)\chi - \left(\hat{n}\times\mathbf{E}^s\right)\times\nabla\chi - \nabla\chi\left(\hat{n}\cdot\mathbf{E}^s\right)]ds - \frac{j}{\omega\varepsilon}\oint\nabla\chi\mathbf{H}^s d\mathbf{l} \quad (4.2)$$

where ω is the radar angular frequency, ϵ and μ are respectively the dielectric constant and permeability of the scattering surface, $\hat{n} = \hat{n}\left(\mathbf{r}\right)$ is the local normal to the surface at the point $\mathbf{r}$, and $\mathbf{E}^s = \mathbf{E}^s\left(\mathbf{r}\right)$ and $\mathbf{H}^s = \mathbf{H}^s\left(\mathbf{r}\right)$ are the electric and magnetic fields on the interface S. The original Stratton-Chu equation, expressed by the first surface integral [Stratton (1941)], is modified through addition of an extra line integral, because the scattering surface S is an open surface. The function χ is known as the scalar Green function, given by:

$$\chi = -\frac{\exp\left(-jk\left|\mathbf{R}_2 - \mathbf{r}\right|\right)}{4\pi\left|\mathbf{R}_2 - \mathbf{r}\right|} \quad (4.3)$$

where the observation point (receiver) is expressed through the vector $\mathbf{R}_2$, and the scattering point on the surface through $\mathbf{r}$ (see figure 4.2). The Far-Zone approximation can be applied to equation (4.3), which allows to write $\left|\mathbf{R}_2 - \mathbf{r}\right| \simeq \left|\mathbf{R}_2\right| = R_2$ at the denominator, and $\left|\mathbf{R}_2 - \mathbf{r}\right| \simeq R_2 - \hat{n}_s \cdot \mathbf{r}$ at the numerator of (4.3) [Ulaby et al. (1982)]. Here $\hat{n}_s$ is the unit vector pointing from the center of the scattering area (the specular point) towards the receiver (figure 4.2). Note that here the Far-Zone approximation is applied with respect to the whole surface S, which therefore should not be too large. Later, for the Facet Approach, we will apply this approximation with respect to each facet, rather than to the entire surface.

This allows to write the Green function and its gradient as follows:

$$\chi = -\frac{\exp\left(-jkR_2 + j\mathbf{k}\cdot\mathbf{r}\right)}{4\pi R_2} \quad (4.4)$$

$$\nabla\chi = -\frac{j\mathbf{k}}{4\pi R_2}\exp\left(-jkR_2 + j\mathbf{k}\cdot\mathbf{r}\right) \quad (4.5)$$
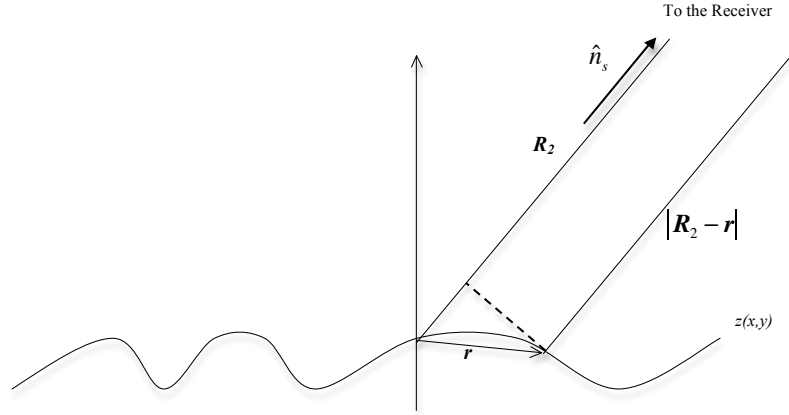
FIGURE 4.2: Illustration of vector $\mathbf{R}_2$ expressing the position of the receiver, vector $\mathbf{r}$ expressing the position of the scattering point on the surface, and the far-field approximation.

where $\mathbf{k} = k_0 \hat{n}_s$. Substitution of (4.4) and (4.5) in (4.2), along with some approximations [Ulaby et al. (1982)], leads to the following final expression for the scattered field:

$$\mathbf{E}^s = -\frac{jk_0}{4\pi R_2} e^{-jk_0 R_2} \iint_S \mathbf{p} \, e^{jk_0 \hat{n}_s \cdot \mathbf{r}} \, dS \tag{4.6}$$

with the vector $\mathbf{p}$ given by

$$\mathbf{p} = \mathbf{p}\left(\mathbf{r}\right) = \hat{n}_s \times [\hat{n} \times \mathbf{E}^s - \eta_s \, \hat{n}_s \times (\hat{n} \times \mathbf{H}^s)] \tag{4.7}$$

and the other quantities defined as:

- $\hat{n}_s$ is the scattered unit vector pointing from the specular point on the sea surface to the receiver;

- $\hat{n} = \hat{n}\left(\mathbf{r}\right)$ is the local normal to the surface at the point $\mathbf{r}$;

- η_s is the intrinsic impedance of the medium in which the electric field is scattered;

- $\mathbf{E}^s = \mathbf{E}^s\left(\mathbf{r}\right)$ and $\mathbf{H}^s = \mathbf{H}^s\left(\mathbf{r}\right)$ are the electric and magnetic fields on the interface S;

- R_2 is the distance from the reflection point on the surface to the receiver.

The geometry of the surface-scattering problem is shown in figure 4.3.
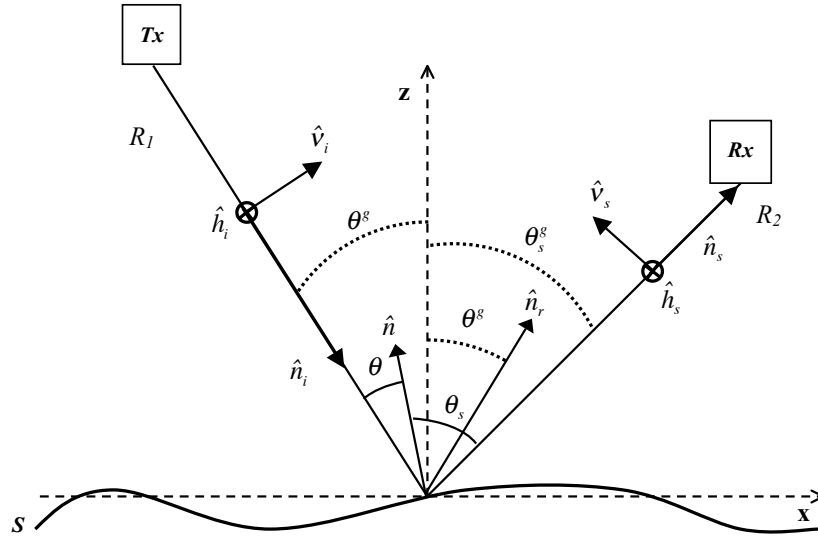
FIGURE 4.3: Geometry of the surface scattering problem. The circled crosses indicate that the horizontal polarization vectors $\hat{h}_i$ and $\hat{h}_s$ are perpendicular to the plane of incidence $x - z$ and directed into the page. Note that the global angles θ^g and θ^g_s are the incident and scattering angles relative to the global normal to the mean sea level (z-axis), whereas θ and θ_s are the local angles relative to the local normal $\hat{n}$ on S.

We now assume that the incident wave on the surface S is a spherical wave expressed as

$$\mathbf{E}^i = \frac{e^{-jk_0 R_1}}{4\pi R_1} \hat{a} \, E_0 \, e^{-jk_0 \, \hat{n}_i \cdot \mathbf{r}} \tag{4.8}$$

where E_0 is the amplitude of the incident signal, and $\hat{a}$ is the incident unit polarization vector. The term R_1 in (4.8) refers to the transmitter range to the specular point, and $\hat{n}_i$ is the unit incident vector pointing from the transmitter towards the specular point on the surface. In (4.8) we assume that the Far-Zone approximation has been applied, in the same way as for the scalar Green function in (4.3). In order to find the tangential fields $\hat{n} \times \mathbf{E}^s$ and $\hat{n} \times \mathbf{H}^s$, it is convenient to work in a local frame of incidence $\left(\hat{n}_i, \hat{t}, \hat{d} \right)$, where $\hat{t}$ and $\hat{d}$ are defined as follows:

$$\hat{t} = \hat{n}_i \times \hat{n} / |\hat{n}_i \times \hat{n}| \tag{4.9a}$$

$$\hat{d} = \hat{n}_i \times \hat{t} \tag{4.9b}$$

Locally, the incident fields $\mathbf{E}^i$ and $\mathbf{H}^i$ can be therefore resolved into a horizontal and vertical component. We rewrite them as:

$$\mathbf{E}^i = E_0 \frac{e^{-jk_0 R_1}}{4\pi R_1} \left(\mathbf{E}^i_\perp + \mathbf{E}^i_\parallel \right) e^{-jk_0 \hat{n}_i \cdot \mathbf{r}} \tag{4.10a}$$

$$\mathbf{H}^i = E_0 \frac{e^{-jk_0 R_1}}{4\pi R_1} \left(\mathbf{H}^i_\perp + \mathbf{H}^i_\parallel \right) e^{-jk_0 \hat{n}_i \cdot \mathbf{r}} \tag{4.10b}$$

where:

$$\mathbf{E}^i_\perp = \left(\hat{a} \cdot \hat{t} \right) \hat{t} \tag{4.11a}$$

$$\mathbf{H}^i_\perp = \frac{1}{\eta_S} \hat{n}_i \times \mathbf{E}^i_\perp = \frac{1}{\eta_S} \left(\hat{a} \cdot \hat{t} \right) \hat{d} \tag{4.11b}$$

$$\mathbf{E}^i_\parallel = \left(\hat{a} \cdot \hat{d} \right) \hat{d} \tag{4.11c}$$

$$\mathbf{H}^i_\parallel = \hat{n}_i \times \mathbf{E}^i_\parallel = - \left(\hat{a} \cdot \hat{d} \right) \hat{t} \tag{4.11d}$$

and the superscripts $\perp$ and $\parallel$ denote the local horizontal and vertical polarization respectively. Note that the term local here indicates that the quantities are defined with respect to the local plane of incidence $(\hat{n}_i, \hat{n})$. Under the Tangent Plane Approximation we assume that the local fields $\mathbf{E^s}$ and $\mathbf{H^s}$ at a point $\mathbf{r}$ on the surface are equal to the fields reflected by an equivalent infinite plane tangent to the point $\mathbf{r}$. This applies separately for each polarization, and translates into:

$$\mathbf{E}^s_\perp = R_\perp \, \mathbf{E}^i_\perp \tag{4.12a}$$

$$\mathbf{H}^s_\parallel = R_\parallel \, \mathbf{H}^i_\parallel \tag{4.12b}$$

where $R_\perp$ and $R_\parallel$ are the Fresnel Reflection coefficients for the two polarizations. The Fresnel coefficients depend on the incident angles and the dielectric properties of the scattering surface [Ulaby et al. (1982)]. The remaining polarized field can be found as:

$$\mathbf{E}^s_\parallel = \eta_s \hat{n}_r \times \mathbf{H}^s_\parallel = -\eta_s R_\parallel \mathbf{H}^i_\parallel \times \hat{n}_i \tag{4.13a}$$

$$\mathbf{H}^s_\perp = \frac{1}{\eta_s} \hat{n}_r \times \mathbf{E}^s_\perp = -\frac{1}{\eta_s} \hat{n}_i \times R_\perp \mathbf{E}^i_\perp \tag{4.13b}$$

where $\hat{n}_r$ is the unit vector in the reflected direction (see figure 4.3). To this point, we

can write the tangential fields inside the integral by putting together all the previous equations, as follows:

$$\hat{n} \times \mathbf{E}^s = \hat{n} \times \left(\mathbf{E}^s_\perp + \mathbf{E}^s_\parallel \right) = \tag{4.14}$$
$$= \hat{n} \times \left[R_\perp \mathbf{E}^i_\perp - \eta_S R_\parallel \mathbf{H}^i_\parallel \times \hat{n}_i \right] = \hat{n} \times R_\perp \mathbf{E}^i_\perp - \eta_S R_\parallel \mathbf{H}^i_\parallel (\hat{n} \cdot \hat{n}_i)$$

Here, we have used the property of scalar products: $\mathbf{a} \times \mathbf{b} \times \mathbf{c} = \mathbf{b} (\mathbf{a} \cdot \mathbf{c}) - \mathbf{c} (\mathbf{a} \cdot \mathbf{b})$, and the fact that $\mathbf{H}^i_\parallel$ and $\hat{n}$ are orthogonal to each other, so their scalar product is zero. Similarly, we find the tangential magnetic field as:

$$\hat{n} \times \mathbf{H}^s = \hat{n} \times \left(\mathbf{H}^s_\parallel + \mathbf{H}^s_\perp \right) = \tag{4.15}$$
$$= \hat{n} \times \left[R_\parallel \mathbf{H}^i_\parallel - \frac{1}{\eta_S} \hat{n}_i \times R_\perp \mathbf{E}^i_\perp \right] = \hat{n} \times R_\parallel \mathbf{H}^i_\parallel + \frac{1}{\eta_S} R_\perp \mathbf{E}^i_\perp (\hat{n} \cdot \hat{n}_i)$$

The fields in (4.14) and (4.15) can be substituted into the vector term $\mathbf{p}$ in (4.7) to finally obtain the scattered field $\mathbf{E}^s$ from equation (4.6). We regroup some terms and bring outside of the integral those that do not depend on the integration variable, to finally write $\mathbf{E}^s$ as follows:

$$\mathbf{E}^s = -E_0 \frac{jk_0}{(4\pi)^2 R_1 R_2} e^{-jk_0(R_1+R_2)} \iint_S \mathbf{p} \, e^{j\mathbf{q}\cdot\mathbf{r}} \, dS \tag{4.16}$$

where the tangential fields in the vector term $\mathbf{p}$ are given by (4.14) and (4.15). Equation (4.16) constitutes the starting point for the development of the Facet Approach that will be illustrated in paragraph 4.4. In (4.16), the term $\mathbf{q} = \mathbf{q}(\mathbf{r}) = k_0 [\hat{n}_s(\mathbf{r}) - \hat{n}_i(\mathbf{r})]$ is known as the scattering vector. Once the scattered field is known, we can calculate several quantities, like the scattered power, or the bistatic Normalized Radar Cross Section (NRCS), defined as:

$$\sigma_0^{pq} = \frac{4\pi R_2^2 \left\langle \left| \mathbf{E}^s_{pq} \right|^2 \right\rangle}{A \left| \mathbf{E}^i_{pq} \right|^2} \tag{4.17}$$

where A is the total surface area from which the field is scattered, and the subscripts p and q refer to the polarization of the incident and scattered field. Note that (4.17) gives us the means to compute both the co-polarized (when $p = q$) and the cross-polarized (when $p \neq q$) NRCS.

4.3.2 The Geometrical Optics Approximation

The KA provides an explicit form for the vector term $\mathbf{p}$ in (4.7), but it still leaves the integral as a complicated function of the surface S and its local normal vectors and reflection coefficients. The most common and easy approximation is known as the Geometric Optics (GO) or Stationary-Phase Approximation (SPA) [Bass and Fuks (1979), Ulaby et al. (1982)]. The GO represents a high-frequency limit of the KA, and indeed it coincides with KA in the limiting case that the EM wavelength vanishes, and the surface becomes infinite so that no edge effects exist [Valenzuela (1978)]. This approximation considers that the scattering occurs only in the direction of specular reflection, and allows to take the term $\mathbf{p}$ outside of the integral (4.16) leaving the exponential term as the only term in the integral. The total scattered field is the result of the superposition of fields generated by a large number of perfectly reflecting facets (mirrors) on the surface, oriented exactly in the direction of the receiver. The reflection from each specular point is as coherent as the incoming signal, but the total scattered field from different specular points is incoherent, as the phase of the received signal fluctuates randomly [Soulat (2003)]. The phase of the scattered signal will depend on the geometry, the number and location of the mirrors and the way they change in time. Such a incoherent scattering holds for large standard deviation of the sea surface height (rough surfaces). More precisely, the condition required for the applicability of the GO is the following [Bass and Fuks (1979)]:

$$(q_z \sigma_z)^2 \gg 1 \tag{4.18}$$

where q_z is the z-component of the scattering vector q, and σ_z is the standard deviation of the sea surface heights. The parameter $(q_z \sigma_z)^2$ is known as the Rayleigh parameter. It is important to remark that the general condition for the KA, requiring a radius of curvature large enough with respect to the wavelength, can be satisfied even for large standard deviation of the sea surface height, namely for the GO applicability condition. More specifically, if we assume that the height of the surface is a normally distributed zero mean random process with variance σ_z^2, then the average radius of curvature appeari g

in the KA applicability criterion in equation (4.1) can be written as [Ulaby et al. (1982)]:

$$r_c = l^2/2.76\sigma_z \tag{4.19}$$

Which means that relatively large standard deviations σ_z (compared to the wavelength) can be accepted, as long as the surface correlation length l remains large enough to preserve an acceptable radius of curvature r_c. Equation (4.16) shows that the scattered field is given by a rapidly fluctuating integral over the rough surface. However, the overall contribution to the scattering is given by specular points only, implying that wherever there is power scattered towards the receiver, the local normal to the surface must coincide with the scattering vector $\mathbf{q}$. Mathematically, this means imposing that the derivative of the phase of the exponential is equal to zero (phase stationarity):

$$\frac{\partial Q}{\partial x} = \frac{\partial Q}{\partial y} = 0 \tag{4.20}$$

where $Q = k_0 \left(\hat{n}_s - \hat{n}_i \right) \cdot \mathbf{r} = \mathbf{q} \cdot \mathbf{r}$. This in turn translates into:

$$\frac{\partial Q}{\partial x} = q_x + q_z \frac{\partial z(x,y)}{\partial x} = 0 \rightarrow \frac{\partial z\left(x,y\right)}{\partial x} = -\frac{q_x}{q_z} \tag{4.21}$$

$$\frac{\partial Q}{\partial y} = q_y + q_z \frac{\partial z(x,y)}{\partial y} = 0 \rightarrow \frac{\partial z\left(x,y\right)}{\partial y} = -\frac{q_y}{q_z} \tag{4.22}$$

Since $\hat{n} \times \mathbf{E}^s$ and $\hat{n} \times \mathbf{H}^s$ are function of the surface derivatives, which are now known, they do not depend on the integration variable anymore and the term $\mathbf{p}$ can be brought outside of the integral (4.16), to finally obtain:

$$\mathbf{E}^s = K\mathbf{p} \iint_S e^{j\mathbf{q}\cdot\mathbf{r}} dS \tag{4.23}$$

where we have defined $K = -jk_0 E_0 \Big/ \left[(4\pi)^2 R_1 R_2 \right] e^{-jk_0(R_1+R_2)}$. Eq.(4.23) represents the scattered field under the GO approximation, in a vector formulation. To this point, the usual way to proceed is to calculate the NRCS given by eq. (4.17), which implies an averaging of the scattered power. The calculation of the average scattered power is

carried out in [Ulaby et al. (1982)], and it reduces to the calculation of:

$$\left\langle |I_1|^2 \right\rangle = \iint_S \left\langle \exp\left[jk_0 \left(\hat{n}_s - \hat{n}_i \right) \left(\mathbf{r} - \mathbf{r}' \right) \right] \right\rangle dS dS' \tag{4.24}$$

Under the assumptions of Gaussian distribution of the surface heights, isotropy of the surface roughness and of course large Rayleigh parameter $(q_z \sigma_z)^2$, some simplifications can be made within the integral, to lead to:

$$\left\langle |I_1|^2 \right\rangle = \frac{2\pi A_0 q^2}{q_z^4 \sigma_s^2} \exp\left[-\frac{(q_x/q_z)^2 + (q_y/q_z)^2}{2\sigma_s^2} \right] \tag{4.25}$$

where σ_s^2 is the Mean Square Slope (MSS) of the sea surface, and A represents the area of the scattering surface. From this, the NRCS is derived as:

$$\sigma_0{}^{pq} = \frac{\pi (k_0 q \, |U_{pq}|)^2}{q_z{}^4} P\left(-\frac{q_x}{q_z}, -\frac{q_y}{q_z} \right) \tag{4.26}$$

where:

- U_{pq} are polarimetric coefficients, whose expression is [Ulaby et al. (1982)]:

$$U_{hh} = M_1 \left[R_{\parallel} \left(\hat{h}_s \cdot \hat{n}_i \right) \left(\hat{h} \cdot \hat{n}_s \right) + R_{\perp} \left(\hat{v}_s \cdot \hat{n}_i \right) \left(\hat{v} \cdot \hat{n}_s \right) \right] \tag{4.27a}$$

$$U_{vh} = M_1 \left[R_{\parallel} \left(\hat{v}_s \cdot \hat{n}_i \right) \left(\hat{h} \cdot \hat{n}_s \right) - R_{\perp} \left(\hat{h}_s \cdot \hat{n}_i \right) \left(\hat{v} \cdot \hat{n}_s \right) \right] \tag{4.27b}$$

$$U_{hv} = M_1 \left[R_{\parallel} \left(\hat{h}_s \cdot \hat{n}_i \right) \left(\hat{v} \cdot \hat{n}_s \right) - R_{\perp} \left(\hat{v}_s \cdot \hat{n}_i \right) \left(\hat{h} \cdot \hat{n}_s \right) \right] \tag{4.27c}$$

$$U_{vv} = M_1 \left[R_{\parallel} \left(\hat{v}_s \cdot \hat{n}_i \right) \left(\hat{v} \cdot \hat{n}_s \right) + R_{\perp} \left(\hat{h}_s \cdot \hat{n}_i \right) \left(\hat{h} \cdot \hat{n}_s \right) \right] \tag{4.27d}$$

and $M_1 = q \, |q_z| \left/ \left\{ \left[\left(\hat{n}_i \cdot \hat{h}_s \right)^2 + (\hat{n}_i \cdot \hat{v}_s)^2 \right] k_0 q_z \right\} \right.$;

- q_x, q_y and q_z are the x- y- z- components of the scattering vector $\mathbf{q}$, and q is its norm;

- $P\,()$ is the two-dimensional Gaussian PDF of the slopes along x and y coordinates;

Note that the final NRCS contains the PDF of the surface slopes, which, under the assumption of Gaussian-distributed surface heights, is still Gaussian. Equation 4.26 represents the final expression for the NRCS, under GO approximation in its vector form.

The same result can be obtained if a different approach is followed, by calculating the istantaneous scattered power from a single specular point using the GO approximation, and then average the total scattered power as the sum of the contributions from each specular point on the surface. This alternative approach was first derived by [Kodis (1966)], and extended to the bistatic case by [Barrick (1968)], and has been shown to produce the same result for NRCS as that illustrated in eq. (4.26) [Ruffini et al. (1999), Soulat (2003)]. The Geometric Optics approximation is widely used, for its simplicity and ease of implementation, but it suffers some limitations. We will show in chapter 5 that, in the case where the transmitter and receiver lie in the $x - z$ plane, the GO shows no sensitivity to polarization other than through the Fresnel reflection coefficients. Furthermore, the average formulation of GO is a useful tool to quickly model the impact of surface roughness on the scattered field, but its parameterization of surface roughness with a Gaussian PDF effectively reduces complex surface roughness conditions to just two values of the variances of the surface slope to describe the sea surface. The average formulation thus prevents insight to be gained into the instantaneous behavior of the scattering and on how distinct features on the sea surface may contribute to the scattering. Finally, it is worth pointing out once again that the Z-V model makes use of a GO formulation for scalar fields [Bass and Fuks (1979)], whereas the GO formulation presented here, and illustrated in [Ulaby et al. (1982)], is a vector formulation of GO, specific for EM fields. The main difference between the two formulations lies in the fact that the factor multiplied by the PDF of slopes in the equation for the NRCS of the Z-V model (eq. 28 in Zavorotny and Voronovich (2000)) is simply given by the Fresnel reflection coefficients $R_\perp$ and $R_\parallel$, whereas in the vector formulation by [Ulaby et al. (1982)] this factor is given by the polarimetric coefficients U_{pq}, which expression is more complex than the simple reflection coefficients. However, we will show that for the GNSS-R geometry of transmitter and receiver both lying in the $x - z$ plane the vector formulation for GO and the scalar Z-V one are the same. This also implies that the sensitivity to polarization remains merely linked to the Fresnel reflection coefficients.

4.4   The Facet Approach

In this section, we present the EM model used in our GNSS-R Simulator to compute the scattering, and referred to as the Facet Approach (FA). As mentioned in paragraph 4.2, the FA represents a novel implementation of the Kirchhoff Approximation (KA). We will show that it preserves the advantages of KA over the high frequency GO by providing a better representation of the scattering and polarization properties, but reduces the computational cost compared to KA, making it more practical to simulate scattering from larger surfaces. The FA is a new approach to calculate the scattering from large-scale surface roughness components based on solving the Kirchhoff integral in (4.16), for a surface S represented by an ensemble of n planar facets, each of them tilted and oriented by the waves. An example of a 1D surface approximated by planar facets is shown in figure 4.4.
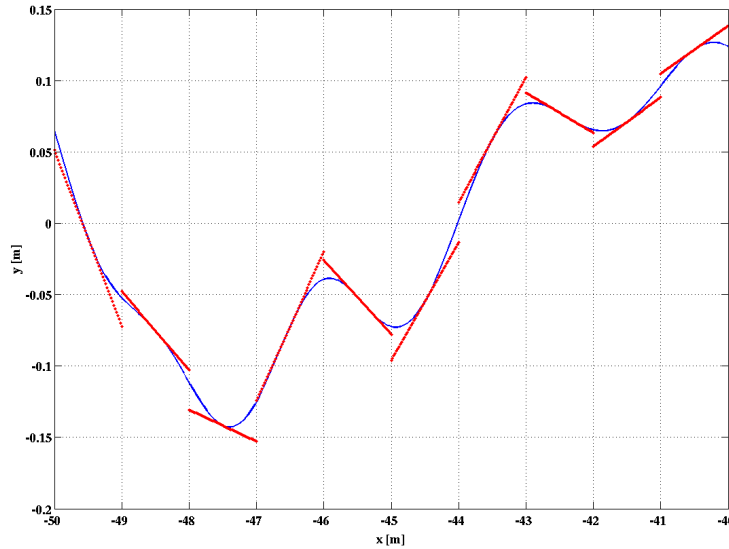
FIGURE 4.4: A portion of a 100 m 1D sea surface, with its associated facets.

In principle, the Far-Zone approximation can be applied both with respect to the entire surface S, and with respect to each facet. For the FA, we apply the Far-Zone approximation with respect to each facet, and this causes some changes in some of the terms in equation (4.16). The terms R_1 and R_2 become the ranges from the transmitter and receiver to the central point of the facet, and are therefore dependent upon the particular

position of the facet considered. The incident and scattering unit vectors $\hat{n}_i$ and $\hat{n}_s$ no longer refer to the specular point on the surface, but to the central point of the facet, causing also the terms $\mathbf{p}$ and $\mathbf{q}$ to be facet-dependent. The integral (4.16) can therefore be split into the sum of integrals over each facet as follows:

$$\mathbf{E}^s = \iint_S K\mathbf{p}e^{j\mathbf{q}\cdot\mathbf{r}}dS = \sum_{m=1}^{n} \mathbf{E}^s_{f_m} = \tag{4.28}$$

$$= \left[K_1 \iint_{f_1} \mathbf{p}_1 e^{j\mathbf{q_1}\cdot\mathbf{r_1}}dS_1 + K_2 \iint_{f_2} \mathbf{p}_2 e^{j\mathbf{q_2}\cdot\mathbf{r_2}}dS_2 + ... + K_n \iint_{f_n} \mathbf{p}_n e^{j\mathbf{q_n}\cdot\mathbf{r_n}}dS_n \right]$$

where $S = f_1 \cup f_2 \cup ... \cup f_n$, and:

- $K_m = -jk_0 E_0 \Big/ \left[(4\pi)^2 R_1^m R_2^m \right] e^{-jk_0\left(R_1^m + R_2^m\right)}$, and R_1^m / R_2^m are the ranges from the transmitter/receiver to the central point of the m-th facet;

- $\mathbf{p}_m = \hat{n}_s^m \times \left[\hat{n}^m \times \mathbf{E}^s - \eta_s \, \hat{n}_s^m \times (\hat{n}^m \times \mathbf{H}^s) \right]$ is the vector term for the m-th facet, and $\hat{n}^m$ is its local normal;

- $\mathbf{q}_m = k_0 \left(\hat{n}_s^m - \hat{n}_i^m \right)$ is the scattering vector relative to the m-th facet.

We assume that each facet has projections of its sides along the x and y direction (L_x and L_y respectively) equal to each other, and that these projections are also the same for all facets. We now focus on the scattered field from a single facet, which can be written in an analytical form. If the facet is sufficiently large compared to the wavelength of the incident radiation, the EM scattering from the facet can be assimilated to that from an infinite plane. This makes the vector term $\mathbf{p}_m$ constant across a facet, and allows it to be taken outside the integral, as follows:

$$\mathbf{E}^{f_m}_s = K_m \mathbf{p}_m \iint_{f_m} e^{j\mathbf{q}_m\cdot\mathbf{r}_m}dS_m \tag{4.29}$$

The vector term $\mathbf{p}_m$ can be evaluated by applying the KA through (4.14) and (4.15). At this point, the rest of the integral simply becomes the integral of an exponential term over a facet, which tilt along x and y can be known. In order to solve the integral, we first need to convert it from dS_m to $dx_m dy_m$. The integration variable is given by

$\mathbf{r}_m = [x_m, y_m, z_m(x_m, y_m)]$, but for a single facet, which is an inclined finite plane, the analytical expression for $z_m(x_m, y_m)$ is well-known, and given by:

$$z_m = \alpha_m x_m + \beta_m y_m \tag{4.30}$$

where α_m and β_m represent the inclinations of the plane along x and y, given by:

$$\alpha_m = \frac{\partial z_m}{\partial x} = -\frac{n_x^m}{n_z^m} \beta_m = \frac{\partial z_m}{\partial y} = -\frac{n_y^m}{n_z^m} \tag{4.31}$$

The quantities n_x^m, n_y^m and n_z^m are the components of the local normal to the m-th facet $\hat{n}^m$. The differential dS_m is linked to $dx_m dy_m$ through the Jacobian as follows:

$$dS_m = \left| \frac{\partial \mathbf{r}_m}{\partial x} \times \frac{\partial \mathbf{r}_m}{\partial y} \right| dx_m dy_m \tag{4.32a}$$

$$\frac{\partial \mathbf{r}_m}{\partial x} = [1 \ \ 0 \ \ \alpha_m] \tag{4.32b}$$

$$\frac{\partial \mathbf{r}_m}{\partial y} = [0 \ \ 1 \ \ \beta_m] \tag{4.32c}$$

so we finally get:

$$\left| \frac{\partial \mathbf{r}_m}{\partial x} \times \frac{\partial \mathbf{r}_m}{\partial y} \right| = \sqrt{1 + \alpha_m^2 + \beta_m^2} \tag{4.33}$$

Using (4.33) in (4.29) we get:

$$\mathbf{E}_s^{fm} = K_m \sqrt{1 + \alpha_m^2 + \beta_m^2} \mathbf{p}_m \int_{-L_x/2}^{L_x/2} \int_{-L_y/2}^{L_y/2} e^{j\mathbf{q}_m \cdot \mathbf{r}_m} dx_m dy_m \tag{4.34}$$

At this point, we can solve the integral of the exponential in a closed-form, as follows:

$$
\begin{aligned}
\mathbf{E}_s^{f_m} \quad &=\mathbf{g}_m \int\limits_{-L_x/2}^{L_x/2} \int\limits_{-L_y/2}^{L_y/2} e^{jq_{x,m}x_m} e^{jq_{y,m}y_m} e^{jq_{z.m}(\alpha_m x_m+\beta_m y_m)} dx_m dy_m \\
&= \mathbf{g}_m \int\limits_{-L_x/2}^{L_x/2} e^{j(q_{x,m}+q_{z.m}\alpha_m)x_m} dx_m \int\limits_{-L_y/2}^{L_y/2} e^{j(q_{y,m}+q_{z.m}\beta_m)y_m} dy_m \\
&= \mathbf{g}_m \left(\left.\frac{e^{j(q_{x,m}+q_{z.m}\alpha_m)x_m}}{j(q_{x,m}+\alpha_m q_{z,m})}\right|_{-L_x/2}^{L_x/2} \left.\frac{e^{j(q_{y,m}+q_{z.m}\beta_m)y_m}}{j(q_{y,m}+\beta_m q_{z,m})}\right|_{-L_y/2}^{L_y/2} \right) \\
&= \mathbf{g}_m \left(\frac{2j\sin\left[(q_{x,m}+q_{z,m}\alpha_m)L_x/2\right]}{j(q_{x,m}+q_{z,m}\alpha_m)} \cdot \frac{2j\sin\left[(q_{y,m}+q_{z,m}\beta_m)L_y/2\right]}{j(q_{y,m}+q_{z,m}\beta_m)} \right)
\end{aligned}
$$

$$(4.35)$$

where $\mathbf{g}_m = K_m \sqrt{1+\alpha_m^2+\beta_m^2}\,\mathbf{p}_m$. We can then multiply and divide each of the terms in brackets for $L_x/2$ and $L_y/2$ respectively, to write them as *sinc* functions. The final result for the scattered field from a single facet will be [Clarizia et al. (2012)]:

$$
\mathbf{E}_s^{f_m} = -\mathbf{g}_m \left(L_x L_y sinc\left[(q_{x,m}+q_{z,m}\alpha_m)L_x/2\right] sinc\left[(q_{y,m}+q_{z,m}\beta_m)L_y/2\right]\right) \qquad (4.36)
$$

where we have defined $sinc(x) = \frac{\sin(x)}{x}$. The total scattered field in (4.28) can be then evaluated by summing coherently (accounting for the phase term) the scattered fields from each facet, given by (4.36). The sinc terms that appear in equation (4.36) clearly indicates that the FA treats the facets as radiating antennas, with a specific non-zero width main lobe, which allows some scattered power in directions away from the specular direction. The width of the sinc lobe decreases with increasing facet size, so that large facets have scattered power concentrated around the specular direction in a narrow lobe. An illustration of the radiating lobes for facets of two different sizes is illustrated in figure 4.5.

The width of the sinc lobe also depends on the overall incidence and scattering geometry at the facet. An example of how such lobe varies for different geometries is illustrated in figure 4.6.

(a)   (b)
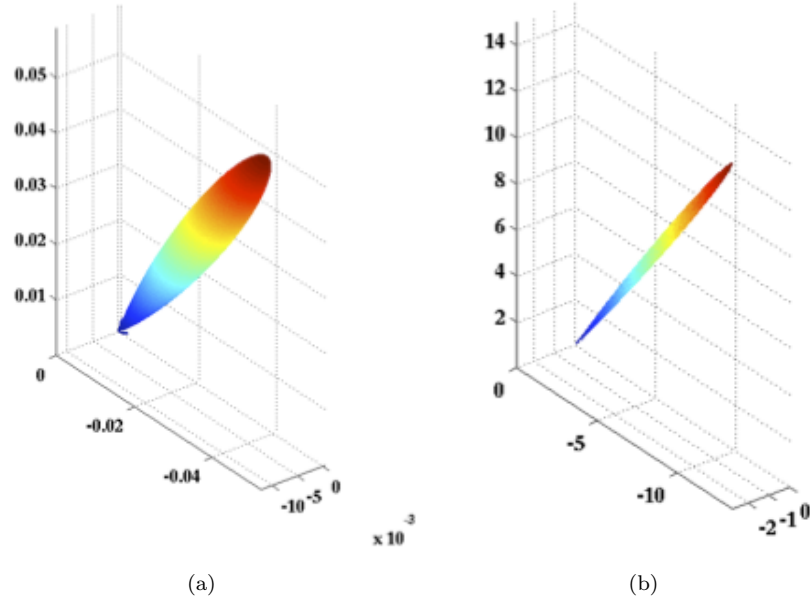
FIGURE 4.5: An example of the 3D radiating lobe for a smaller facet (left) and a larger facet (right). The colors refer to the distance from each point on the surface of the lobe to the origin of the lobe.

(a)

(b)
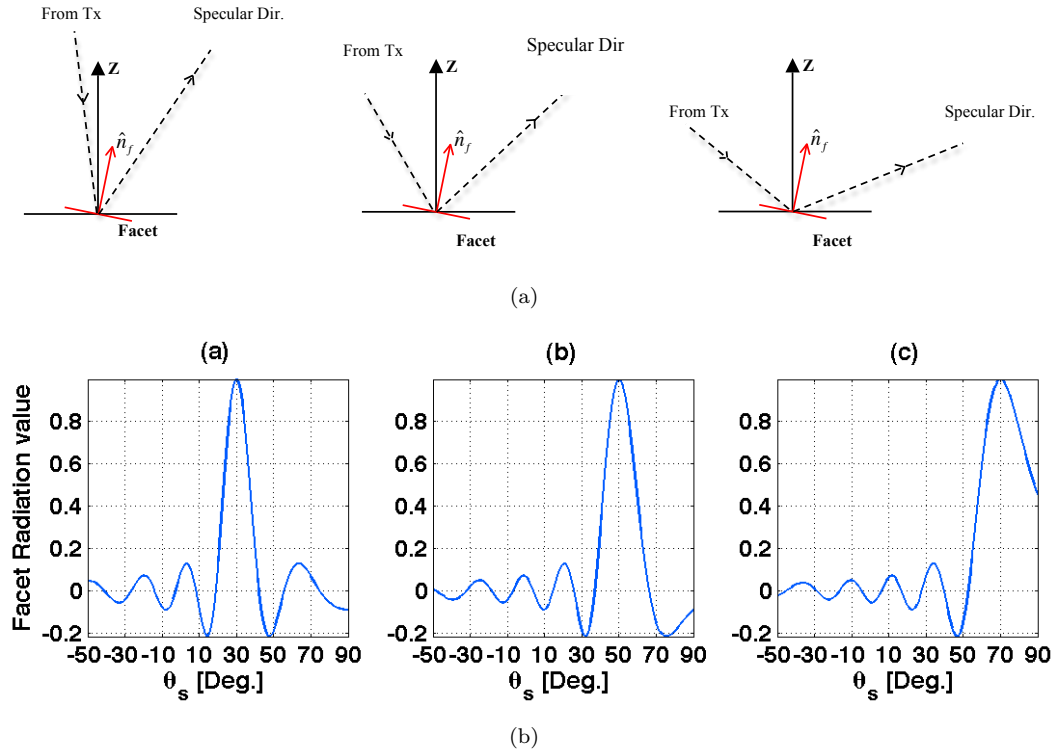
FIGURE 4.6: First row: schematic of geometry for three different cases, where a 1 m facet is tilted with an angle of 10° away from the local normal, and the incidence angle is 10° (a), 30° (b) and 50° (c). Second row: Plot of a 1D sinc function (the first sinc term in equation (4.36)), as a function of the scattering angle, for the three cases.

Figure 4.6 shows in 1D, on the $x-z$ plane, how the width of the sinc increases, particularly the half lobe towards the receiver, when the incidence angle increases too. Here the side of the facet has been kept equal to 1 m. This distortion of the lobe is intrinsically linked to the equation in (4.36), and it is basically caused by the x-, y- and z-component of the **q** vector, which form the arguments of the sinc functions. More specifically, since the scattering vector **q** is built as the difference between two unitary vectors, it is not a unitary vector itself, and therefore its magnitude and components can change significantly, depending on the incidence and scattering angles. A simple example can help illustrate this effect: for a nadir-pointing monostatic case, we would have the unit incidence and scattering vector both aligned with the z-axis, in opposite directions, such that the **q** vector will only have a z-component, and will have a magnitude of 2. If instead the incidence and scattering angles were to be $45°$, the resulting **q** vector would still have a z-component only, but with a magnitude of $\sqrt{2}$. On the other hand, in the extreme case of unit incidence and scattering vectors aligned along x ($\theta_i = \theta_s = 90°$), the **q** vector would have only a x-component, of magnitude 2. This effect has been detected before. Figure 4.7 (a) shows the distorted sinc lobe from [Balanis (1989)], representing the modelled scattering pattern of a finite conducting plate, for an incident plane wave. Figure 4.7 (b) shows a plot of the first sinc term in (4.36), where the incident, scattering angle and local normal have been matched to the example shown in [Balanis (1989)]. The two sinc functions in figures 4.7 (a) and (b) are the same, which also confirms the validity of equation (4.36) of the FA. This distortion of the sinc lobe could be a matter of concern, since the scattered power from a facet does not appear to drop fast enough for directions away from the specular, when the angle between the incident vector and the local normal is high (figure 4.6 (c)). The FA model could therefore produce a higher scattered power that the actual one, from areas within the glistening zone that are far from the SP. In physical terms, one might therefore expect the width of the sinc lobe to depend only on the facet size, and to be centered at the direction of reflection, which depends on the facet inclination. However, we will show in chapter 5 that the scattering results when width of the sinc lobe is fixed are not consistent with results obtained from Geometrical Optics, while those obtained from the FA model without any constraint on the sinc lobe are much more consistent with GO. For this reason, we have used the FA

model mathematically derived, and expressed by equation (4.36), as this is the correct approximation.

(a)

(b)
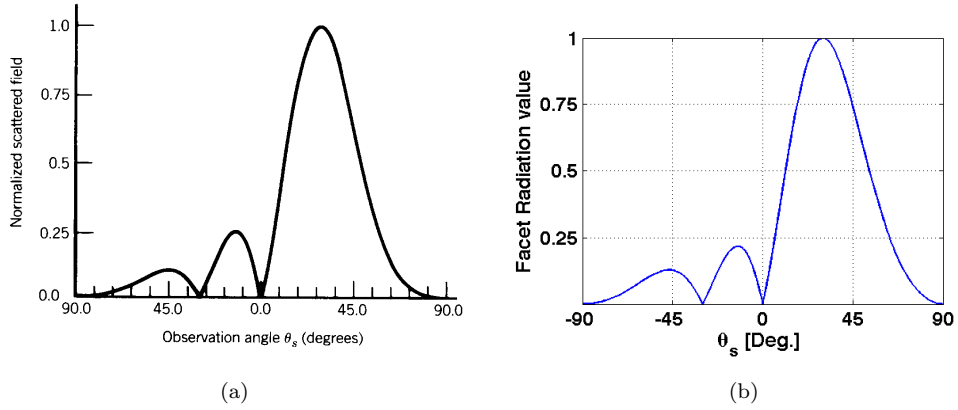
FIGURE 4.7: (a) plot of the scattered field from a finite conducting plate, of side 2λ, where a plane wave hits the plate with an incidence angle of 30° [Balanis (1989)]. (b) 1D plot of first sinc term in (4.36), computed for the same parameters as in (a).

4.5 Choosing the facet size

The size of the facets is a key parameter that affects the applicability of FA. The choice of facet size has to be a trade-off between the need to comply with the KA conditions on roughness, the ability of the facets to adequately approximate the underlying sea surface, and computational expense. Therefore the choice of facet size cannot be entirely arbitrary but must be governed by some specific criteria. The criteria we adopt here to choose the size of the facet stem from considerations first presented in [Bass and Fuks (1979)] to discuss the applicability of the Kirchhoff approximation. These relate to geometrical conditions illustrated in figure 4.8, which constitute the starting point for the formulation of the criterion for KA applicability, formulated in (4.1).

With reference to figure 4.8, it is considered that the reflection of an electromagnetic wave at a point A on the surface can be taken to occur as if from a tangent plane centered at that point, if one can identify a region on the tangent plane Σ_r with linear dimensions which are large relative to the EM wavelength, but which also does not deviate noticeably at the edges of the region from the underlying surface. This region on the tangent plane is what we define as a facet. The argument above translates into
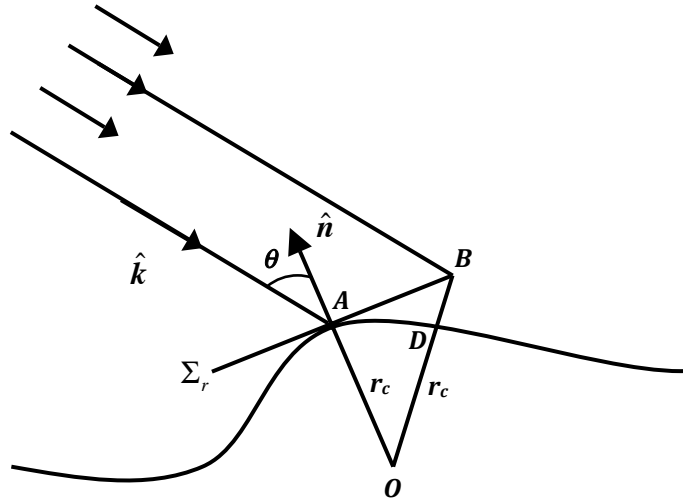
FIGURE 4.8: Illustration of the tangent plane Σ_r and its local coordinate system, with the half-length AB of the facet and the distance from the underlying surface BD.

the two mathematical conditions [Bass and Fuks (1979)]:

$$AB \gg \frac{1}{k_0 \cos(\theta)} \tag{4.37}$$

$$BD \ll \frac{\cos(\theta)}{k_0} \tag{4.38}$$

where AB and BD are the segments shown in figure 4.8. We can easily see that:

$$BD = OB - OD = \sqrt{AB^2 + r_c^2} - r_c \tag{4.39}$$

where r_c is the local radius of curvature of the surface. Thus, we can express both (4.37) and (4.38) in terms of AB as:

$$AB \gg \frac{1}{k_0 \cos(\theta)} \tag{4.40}$$

$$AB \ll \sqrt{\left[\frac{\cos(\theta)}{k_0}\right]^2 + 2\frac{r_c \cos(\theta)}{k_0}} \tag{4.41}$$

In our case, AB represents half the size of our facet, and criteria (4.40) and (4.41) will be used to determine the appropriate facet size [Clarizia et al. (2012)]. It is worth noting that the inequalities (4.40) and (4.41) can be more or less difficult to satisfy, depending on the quantitative interpretation of the much greater than and much smaller than inequality signs. We could choose to interpret those as AB having to be larger (or

smaller) than the term on the right-hand side by a factor of, say, at least 10. In chapter 5, we analyse how the choice such a factor strongly influences and can ultimately limit the applicability of (4.40) and (4.41), and that a stringent condition like the choice of a factor of 10 makes the KA not applicable in most cases. In our simulations, shown in the next chapters, we have therefore relaxed these conditions by considering a factor smaller than 10. It is interesting to note that, if we combine (4.40) and (4.41) we obtain a condition similar to the standard applicability condition (4.1) of the Kirchhoff Approximation, namely:

$$\sqrt[3]{2k_0 r_c} \cos(\theta) \gg \sqrt[3]{1 - \cos^4(\theta)} \tag{4.42}$$

For simplicity, in our simulations we will use the standard Kirchhoff Approximation condition (4.1) to define what constitutes large-scale surface roughness compliant with KA, and the conditions (4.40) and (4.41) to determine the size of the facets.

CHAPTER 5

The Effect of Sea State in Spatial Maps of Scattering

5.1 Introduction

In this chapter, we exploit the FA-based scattering simulator for realistic ocean surfaces, and investigate the results through spatial maps of scattering from these surfaces. First we focus on the methodology to simulate explicit realizations of linear gaussian sea surfaces, with different sea states. We consider sea surfaces composed of wind waves only, obtained from different theoretical wave spectra (Elfouhaily, JONSWAP), and mixed sea surfaces composed of wind waves and a swell. For these surfaces, we calculate the EM scattering of a simple incident spherical wave, using the FA method, outlined in Chapter 4. We validate the FA through comparison of its scattering results with both GO and a numerical implementation of the full KA, for the same sea surface conditions. Next, we focus on how the scattering results change for different underlying sea surfaces in the space domain, leaving those relative to the delay-Doppler domain to be discussed in Chapter 6. The results are first presented in the form of spatial maps of Normalized Radar Cross Sections (NRCS), where the NRCS is calculated individually for each facet

on the sea surface. In order to investigate potential polarization effects, we analyse the ratio between NRCSs of different polarization, and call it the Polarization Ratio (PR). Subsequently, we examine results in the form of NRCS and PR curves, as a function of the scattering angle, calculated from the whole surface, as a coherent summation of the contributions from all the facets. In both cases, we show that the scattered power and polarization ratio are well-correlated with the underlying sea surface from which the scattering originated, and they are sensitive to differences of the sea surface conditions. The last section of the chapter shows how this FA-based simulator, developed for L-Band and in a GNSS-R context, actually works well also for other incident wavelengths, and different scattering geometries (i.e. monostatic), providing a further proof of its flexibility and versatility. Some of the work and results shown here were presented in a recent publication in IEEE Transactions on Geoscience and Remote Sensing, by [Clarizia et al. (2012)].

5.2 Simulations of 3-D Elfouhaily Ocean Wave Fields

The generation of ocean surface maps was carried out using a technique based on filtering a white Gaussian process with a specified wave spectrum. This is a well-established technique, commonly found in literature [Rino et al. (1991), Corsini et al. (1999), Toporkov and Brown (2000), Arnold-Bos et al. (2007a)], which preserves the Gaussian statistics of sea surface elevations and slopes, while allowing to specify particular spectral properties of the wave field. Several theoretical models for wave spectra are available in literature [Pierson and Moskowitz (1964), Hasselmann et al. (1973), Fung and Lee (1982), Apel (1994), Elfouhaily et al. (1997)]. The surfaces here are generated through filtering a 2D realization (a matrix) of white noise with the directional wave slope spectrum developed by [Elfouhaily et al. (1997)]. From now on, we will simply call such spectrum the Elfouhaily spectrum, and will refer to the surfaces generated using this spectrum as Elfouhaily surfaces. A schematic of this approach is shown in figure 5.1.

This produces a wave field entirely defined by the wind speed and the wind direction.
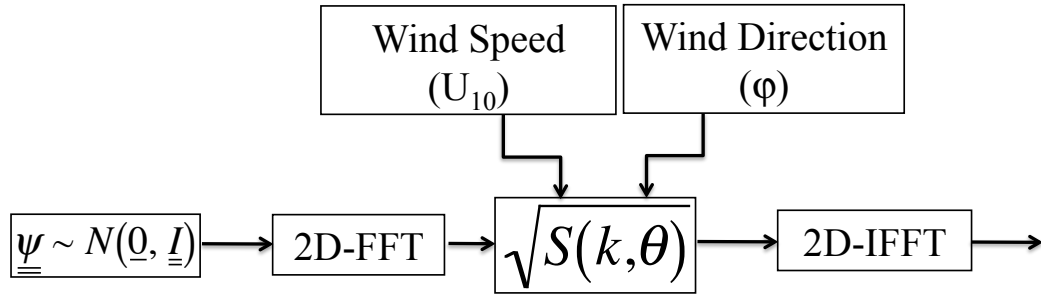
FIGURE 5.1: An illustration of the approach to generate a realization of a sea surface.

In principle, the Elfouhaily spectrum also requires the wave fetch[1] to be specified, however we assume fully developed seas for our simulations, and therefore used a constant value for the inverse wave age, equal to 0.84 [Elfouhaily et al. (1997)]. The surfaces generated through this method have gaussian statistics, and are described as linear, as they can be interpreted as superpositions of 2D sinusoidal components, whose amplitude is proportional to the square root of the wave spectrum at the specified wavenumber [Corsini et al. (1999)]. The distribution of surface heights is Gaussian, and it can be demonstrated that the distribution of slopes is also Gaussian [Ruffini et al. (1999),Soulat (2003)]. It is worth recalling here that our objective is to simulate the scattering from large-scale roughness of the ocean only, using the FA simulator. Here we are not considering the scattering from small-scale features, for which the diffusive EM scattering would need to be calculated using a different scattering model. This means that a wave number cut-off needs to be chosen to identify the surface components that constitute the large-scale roughness. Therefore only the spectral components of the spectrum for wave numbers below that cut-off will contribute to the generation of the sea surface. Several attempts exist in the literature to propose an objective method to choose this cut-off [Garrison et al. (1998)], [Zavorotny and Voronovich (2000)], [Thompson et al. (2005)] but there is no consensus. In our case, we determined the cut-off experimentally by simulating the sea surfaces for a small enough cut-off wavenumber, and by evaluating numerically the radius of curvature of the surface to verify a posteriori if it satisfies the KA criterion, shown in equation (4.1) in chapter 4. All the sea surfaces shown in this and the following chapters are illustrated as maps of sea surface heights, expressed in

---

[1]The wave fetch is the wave generation region, namely the length of water over which wind is blowing in a particular direction, and thus generating waves (fetch is expressed in meters).

meters. Three examples of wind-generated surfaces are shown in Fig. 5.2(a)-(c). Figure 5.2 (a) and (b) show surfaces generated with wind speeds of 5 m/s and 10 m/s, and a 0° wind direction with respect to the x-axis. Figure 5.2 (c) corresponds to a wind speed of 10 m/s, and wind direction of 60°.

(a)

(b)

(c)
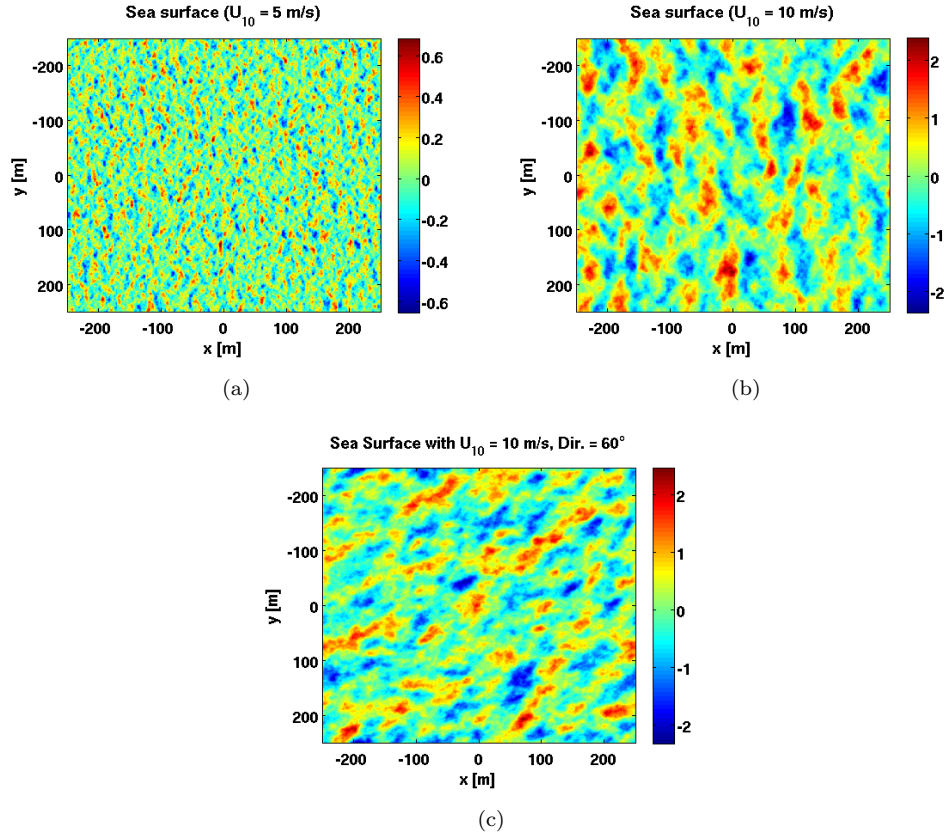
FIGURE 5.2: (a) Sea surface (in meters) generated from the Elfouhaily spectrum, for a patch of 500 m x 500 m, at 0.2 m resolution, for a wind speed of 5 m/s and a wind direction of 0°; (b) Elfouhaily sea surface for a wind speed of 10 m/s and 0° wind direction; (c) Elfouhaily sea surface for a wind speed of 10 m/s and 60° direction.

The surfaces shown in figure 5.2 clearly show the changing roughness with increasing wind speed. In this case, the wave heights increases with increasing wind speed, as does the dominant wavelength, as the peak of the Elfouhaily spectrum shifts towards smaller wavenumbers for increasing wind speeds [Elfouhaily et al. (1997)]. Note that here a larger wind speed does not mean a rougher sea in terms of small scale ripples, but rather higher and longer waves. Although a change in the direction of the waves can clearly be seen by comparing figures 5.2 (b) and 5.2 (c), the Elfouhaily spectrum does not produce a strongly directional sea, where the wavefronts are clearly defined. In the next paragraph, we will show that other spectra (like the JONSWAP wind wave spectrum) are

capable of reproducing seas with a much more pronounced directionality than Elfouhaily. The simulated surfaces in figure 5.2 are large enough to include a sufficient number of dominant ocean wavelengths for both wind speeds considered. In the case of the 10 m/s wind speed, the surface is able to capture on the order of five dominant wavelengths. The need to establish and capture the spectrum up to the wavenumber cut-off would set in principle an upper bound to the size of the resolution cell in space. However, it is possible to increase the resolution in space by zero-padding in the wavenumber domain, which is equivalent to taking a longer spectrum and low-pass filtering it. The cut-off wavenumber used to simulate these surfaces was equal to 2π rad/m, and it corresponds to a cut-off wavelength of 1 m, which is roughly equivalent to five times the incident radar wavelength (0.19 m) in the case of L-band. This is not a very high wave number cut-off, and it does not impose excessive filtering of the original surface. We checked a posteriori that this cutoff produces a surface that satisfies the KA roughness criterion (4.1). As seen in chapter 4, this criterion depends on the incident radar wavenumber, as well as on the incidence angle and the radius of curvature. The radii of curvature along x and y have been calculated through the following equations:

$$r_c^x = \frac{\left[1 + \left(\frac{\partial z}{\partial x}\right)^2\right]^{3/2}}{\left|\frac{\partial^2 z}{\partial^2 x}\right|} \tag{5.1a}$$

$$r_c^y = \frac{\left[1 + \left(\frac{\partial z}{\partial y}\right)^2\right]^{3/2}}{\left|\frac{\partial^2 z}{\partial^2 y}\right|} \tag{5.1b}$$

Figure 5.3 shows a 10 m/s sea surface snapshot, and the corresponding maps of absolute value of radii of curvature, calculated along the x-direction and y-direction. The radii of curvature are on average slightly smaller along the x-direction, because this is the direction in which the waves are travelling, and with the largest surface curvature.

The left-hand term of the KA roughness criterion in equation (4.1) was therefore computed using an incidence angle equal to 20°, a realistic value for GNSS-R geometries, and the median radius of curvature of the surface along x, which is a more robust and preferable choice over the mean. The resulting values is about 8, which is reasonably
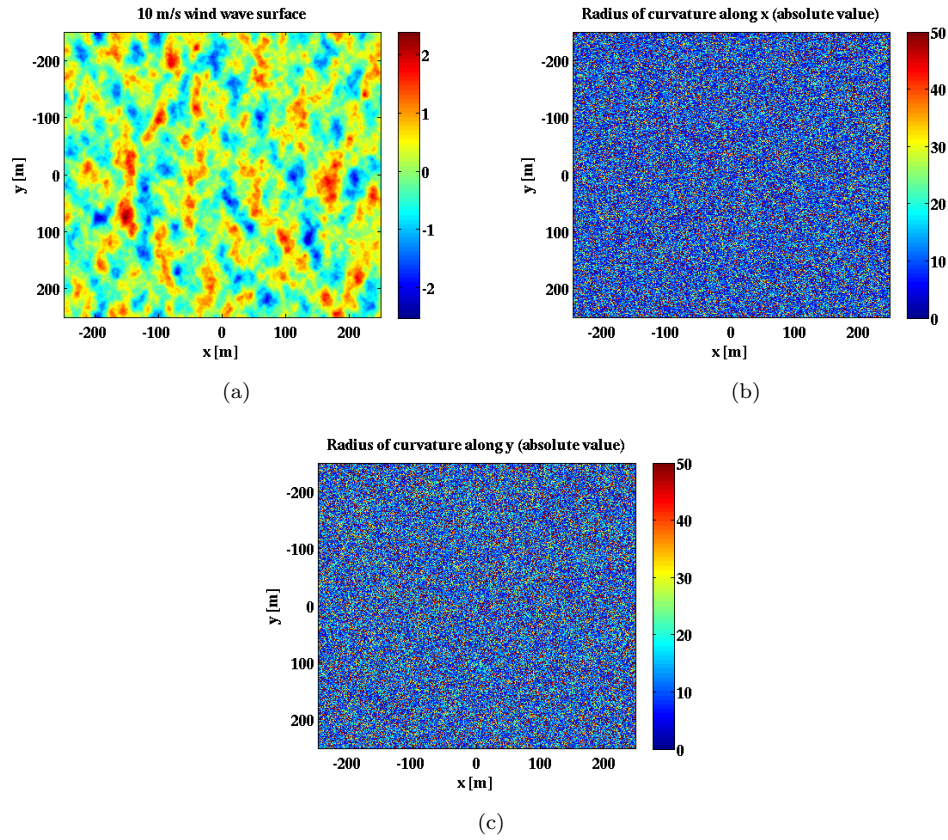
FIGURE 5.3: A 10 m/s sea surface snapshot in meters (a), and the corresponding radii of curvature along x (b) and y (c), in absolute values.

larger than 1. Figure 5.4 shows a pure swell component, modeled as a simple 2-D sinusoidal wave, with amplitude of 1 m and wavelength of 100 m, and traveling parallel to wind direction (a) and in a direction 60° from the wind direction, clockwise from the x-axis (b).
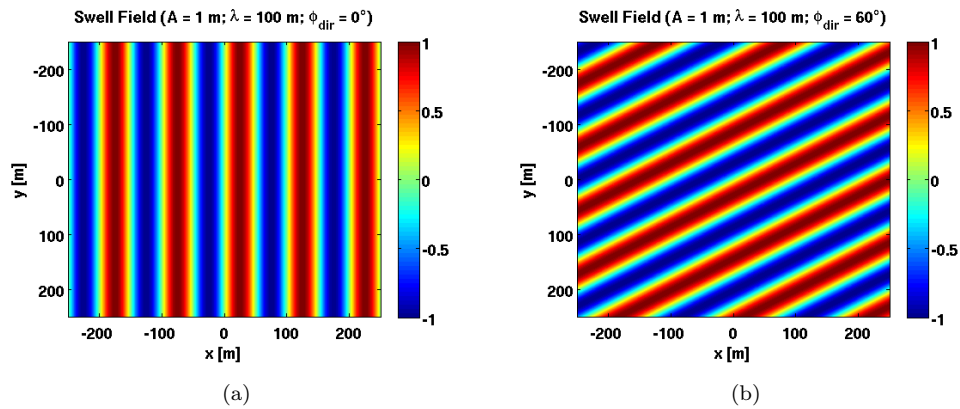
FIGURE 5.4: Swell field (in meters), modelled as a 2D sinusoidal wave with amplitude of 1 m, wavelength of 100 m, and travelling in a direction of 0° (a) and 60° clockwise (b) with respect to the x-axis.

Figure 5.5 (a) and (b) show a sea surface resulting from the superposition of a wind wave surface like that shown in 5.2 (b), with the swell in figure 5.4 (a) and (b) respectively. We notice that the effect of the swell, whose amplitude in this case is not particularly high, appears clearly visible in the final surfaces, as well as its direction. The swell can of course influence more or less the configuration of the final surface, depending on the amplitude and wavelength of the underlying wind waves, as well as those of the swell itself.

(a)   (b)
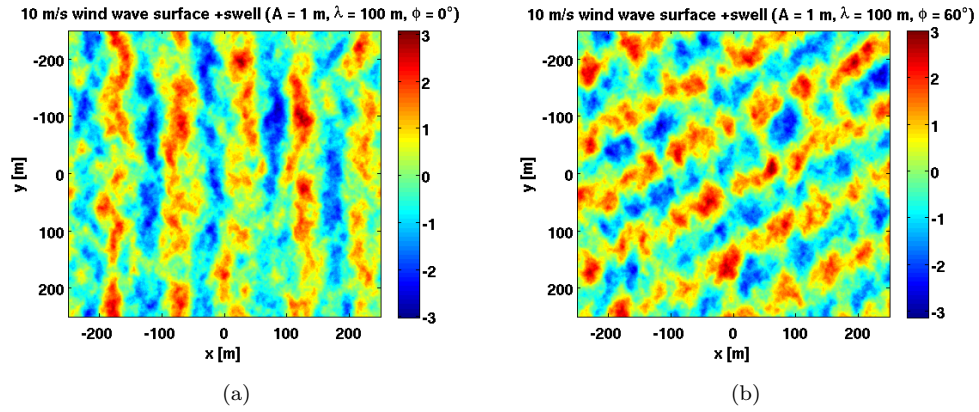
FIGURE 5.5: Composition of the 10 m/s wind wave surface of figure 5.2(b) with the swell shown in 5.4 (a) and 5.4 (b). Heights are expressed in meters.

This last example illustrates how explicit sea surface simulations give the flexibility to consider realistic and more complex sea states, featuring co-existing wind and swell waves, which cannot be represented using a simple PDF of slopes, as in the case of GO. Note that the surfaces in figure 5.5 are still linear, as their spectrum will simply be the one of the original wind wave surface, plus an extra spectral component at the wavenumber of the swell. The surfaces we have presented are characterized by different roughness, and it is at this stage convenient to define a measure of such roughness. We define the roughness for each surface as the sum of the Mean Square Slopes (MSS) along the x- and y-direction of the $x - y$ plane where the sea surface is situated, as follows:

$$RO = MSS_x + MSS_y \qquad (5.2)$$

This represents an important parameter, as it changes the sea surface configuration, and its response to the scattering of GPS signals.

5.3 Simulations of 3-D JONSWAP Ocean Wave Fields

In this section, we explore sea surfaces simulated with a different spectrum from the Elfouhaily one, known as the Joint North Sea Wave project, (JONSWAP) spectrum [Hasselmann et al. (1973)]. This is an empirical spectrum, derived from data collected during the homonymous project, off the western shore of Denmark. It can be considered as a fetch-limited version of a theoretical Pierson-Moskovitz spectrum [Pierson and Moskowitz (1964)], except that the wave spectrum is never fully developed, and may continue to develop through non-linear wave-wave interactions, even for very long distances and time. Therefore in the JONSWAP spectrum, waves continues to grow with distance or time, and the peak in the spectrum is more pronounced. The latter turns out to be particularly important for the simulation of non-linear surfaces, or to have a spectrum that changes in time according to theory of Hasselmann [Hasselmann (1966)]. This spectrum is usually used in shallow water situations (near the coast), while the Elfouhaily spectrum in its fully developed version is more suitable to describe waves in open ocean. Examples of JONSWAP spectra for different fetch values are illustrated in figure 5.6.
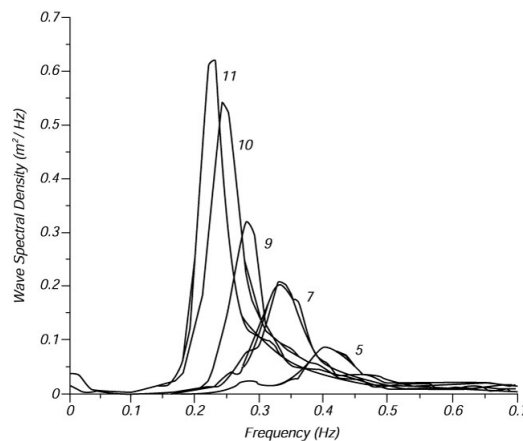
FIGURE 5.6: Illustration of JONSWAP spectra for different fetch values.

Compared to the Elfouhaily one, this spectrum produces seas with a higher directionality. The term directionality here refers to the configuration of the waves and the roughness of the sea surface. A sea with high directionality of the waves will have wavefronts very well defined, and will be very similar to a pure swell. This intuitively implies

that when the waves of a directional sea change direction, this change is clearly visible. When the directionality of the waves is low, then the waves do not show well defined wavefronts, as it happens for the Elfouhaily surfaces, and a change in direction of such waves is less visible (see figures 5.2 (b) and 5.2 (c)). In terms of sea roughness and MSS, a highly directional sea will have a much lower MSS in the direction parallel to the wavefronts, compared to that in the direction orthogonal to the wave fronts, whereas for a poorly directional sea the two MSS values are very similar. Followind the definition of roughness through equation (5.2), a definition of directionality here is also important, as its high impact on the scattering behaviour makes it the other crucial parameter of the sea surface to be taken into account. In order to express numerically the directionality of different seas, we define it as the ratio of the MSS along the x-direction, and the MSS along the y-direction, as follows:

$$\mathrm{DP} = \frac{\mathrm{MSS_x}}{\mathrm{MSS_y}} \tag{5.3}$$

The JONSWAP spectrum offers the possibility to increase or decrease the directionality by simply changing the parameter N, which is the exponent of the cosine defining the spreading function [Hasselmann et al. (1973)]. For simplicity, the parameter N will be used in the following sections, and throughout the entire dissertation to distiguish JONSWAP surfaces with different directionality (N=24 and N=840), and it will be called directional parameter. Two examples of sea surfaces simulated using the JONSWAP spectrum, for two different values of N, are shown in figure 5.7.
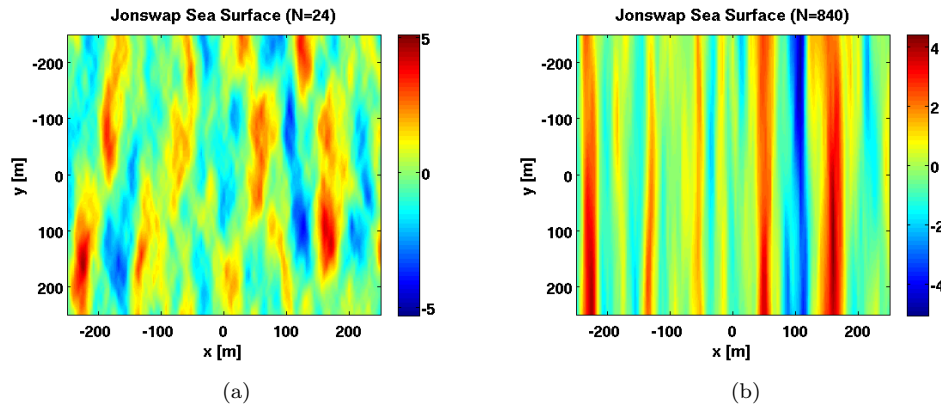
FIGURE 5.7: (a) JONSWAP sea surface (in meters), simulated using a resolution of 1 m, with a spreading function parameter of N=24 (a) and N=840 (b).

It is worth pointing out that even though the procedure to simulate the JONSWAP

surfaces would be the same as that shown in figure 5.1, we have not simulated them, but they have been provided by Dr. Alessandro Toffoli and his team from the Swinburne University of Technology in Melbourne, Australia. The surfaces in figure 5.7 have a peak period of 10 s, which is comparable with the one of the Elfouhaily surfaces at 10 m/s. However, their Significant Wave Height[2] (SWH) is much larger, and therefore the waves are much steeper for the JONSWAP surfaces. At this point, it is worth emphasizing that the roughness parameter RO and the directionality parameter DP, expressed respectively in equations (5.2) and (5.3), along with the travelling direction of the waves ϕ, represent the three fundamental parameters that synthetically describe the waves on the surface, and that affect the most the scattering of GPS signals from the sea surface. In the following sections, differences in the scattering caused by different sea states will be essentially described in terms of scattering sensitivity to these three parameters.

5.4 Configuration of the Scattering Scenario

The scattering geometry has been shown in figure 4.3 in chapter 4, with an emphasis on the transmitter and the receiver lying in the xz plane, and the sea surface on the $x - y$ plane. In our simulations, the transmitter and receiver are in a spaceborne configuration, and their altitudes are about 20000 km and 680 km, respectively. These correspond to the typical altitude of a GPS satellite, and of the Low-Earth-Orbiting UK-DMC satellite [Gleason et al. (2005)]. The position of the transmitter is fixed with a constant range and incidence angle, equal to $20°$, which is a realistic value for a GNSS-R geometry. The receiver range is also fixed while in the results we vary its scattering angle, which ranges from $-10°$ to $50°$ from the global vertical. The specular direction corresponds therefore to a scattering angle $\theta_s^g = 20°$, and the scattering is analysed within an angular cone $60°$ wide, where there is still a quasi-specular scattering regime. The incident wave is an L-band (= 19 cm) spherical wave, as expressed in (4.8) in chapter 4, with unitary amplitude. At this stage, it is convenient to introduce the horizontal and vertical unit

---

[2]The SWH is the average height (crest to trough) of the 1/3 largest waves, and it is usually expressed as 4 times the standard deviation of the heights.

polarization vectors $\hat{h}_i, \hat{v}_i$ for the incident wave, and $\hat{h}_s, \hat{v}_s$ for the scattered wave, defined with respect to the plane of incidence $(\hat{n}_i, \hat{z})$ and the scattering plane $(\hat{n}_s, \hat{z})$, respectively. These are defined in [Ulaby et al. (1982)], and are given by:

$$\hat{h}_i = -\hat{x}\sin(\phi) + \hat{y}\cos(\phi) \tag{5.4a}$$

$$\hat{v}_i = -\left[\hat{x}\cos(\theta^g)\cos(\phi) + \hat{y}\cos(\theta^g)\sin(\phi) + \hat{z}\sin(\theta^g)\right] \tag{5.4b}$$

$$\hat{h}_s = -\hat{x}\sin(\phi_s) + \hat{y}\cos(\phi_s) \tag{5.4c}$$

$$\hat{v}_s = \hat{x}\cos(\theta^g_s)\cos(\phi_s) + \hat{y}\cos(\theta^g_s)\sin(\phi_s) - \hat{z}\sin(\theta^g_s) \tag{5.4d}$$

Given that both the transmitter and the receiver lie in the xz plane, and their azimuth angles ϕ and ϕ_s are zero, the incident and scattered polarization vectors can be simply expressed in our case as:

$$\hat{h}_i = -\hat{y} \tag{5.5a}$$

$$\hat{v}_i = -\hat{x}\cos(\theta^g) - \hat{z}\sin(\theta^g) \tag{5.5b}$$

$$\hat{h}_s = \hat{y} \tag{5.5c}$$

$$\hat{v}_s = \hat{x}\cos(\theta^g_s) - \hat{z}\sin(\theta^g_s) \tag{5.5d}$$

For the results in space domain presented in this chapter, two cases of incident polarization have been considered: The first is horizontal polarization $(\hat{h}_i)$, and the second is vertical polarization $(\hat{v}_i)$. Although it is recognized that real incident GNSS signals are Right Hand Circularly Polarized (RHCP), here the scattering is analysed assuming a linearly polarized incident signal (H or V), for simplicity and comparison with existing scattering models commonly found in literature. Generally speaking, the results for circular polarization could be easily derived from these, since circular polarization is simply a linear combination of the linear polarization components.

5.5 Comparison of the FA with GO and KA

An initial set of simulations was generated to compare the results of the FA with the GO and a numerical implementation of the full KA. The latter was obtained by computing

the KA integral given in (4.16) with a standard numerical integration method, applied to a sea surface realization, generated at very high resolution. Due to computational limits and the necessity of a very high resolution in the sea surface generation, this full KA method has only been applied for small areas of the ocean surface. However, the surface considered is still large enough to include a sufficient number of dominant ocean wavelengths, to ensure that the scattering is statistically representative of all relevant processes on the surface. The dimensions of the new surface realization were 50 m by 50 m, generated with a very high spatial resolution of 2 cm. The calculation was performed for an Elfouhaily surface with wind speed of 4 m/s, and 0° direction. Such a low wind speed ensures that the 50 × 50 m surface can represent about three dominant ocean wavelengths (about 17 m for a 4 m/s Elfouhaily spectrum). From this surface, we have calculated the scattered NRCS expressed in (4.17), where the scattered field has been computed through:

1. The full KA through numerical integration of the Kirchhoff integral (4.16);

2. The FA, through equations (4.28) and (4.36);

3. The GO, using equation (4.26).

For the implementation of the FA, we need to choose the size of the facet based on inequalities (4.40) and (4.41) introduced in chapter 4. In our case, using an incidence angle of 20° and the median radius of curvature along x for an Elfouhaily 4 m/s sea surface, the conditions (4.40) and (4.41) require the facet size to be much greater than 0.06 m and much less than 1.7 m. In our case, we have changed the much larger and much smaller signs of inequalities (4.40) and (4.41) respectively into more manageable larger and smaller signs. Indeed, when the facet side is taken to be larger and smaller than the right-hand side terms of (4.40) and (4.41) by a certain factor α, the range of acceptable facet size becomes very narrow for a surface filtered with a 1 m cutoff wavelength, or in some cases there is no suitable facet size. This effect is shown in Figure 5.8. Here, the upper and lower bounds for the facet side are shown as a function of the cutoff wavelength. The different colors refer to different factors α with which inequalities (4.40) and (4.41) are considered, while different line styles refer to different

wind speeds. In (4.40) and (4.41), the Elfouhaily surfaces have been used to compute median radius of curvature, and the continuous and dashed lines refer respectively to surfaces with a wind speed of 4 m/s and 10 m/s.
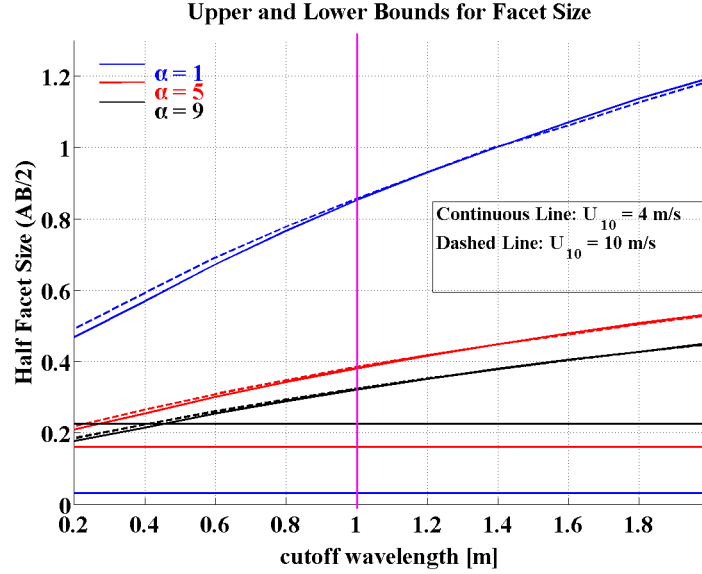
FIGURE 5.8: Upper and lower bounds for the facet size, illustrated as half the size of the facet, as a function of the cutoff wavelength, for low and high wind speed.

In figure 5.8, we can see that if $\alpha = 1$ (blue lines), namely if we take the inequalities with simple larger and smaller signs, then there is a much wider choice of facet sizes, for a variety of cutoff wavelengths. In particular, a cutoff wavelength of 1 m, marked through a magenta vertical line, and used to generate the sea surfaces, allows to use facets as small as about 0.1 m, and as large as more than 1.7 m. For the other cases of $\alpha > 1$, the range of choices of facet size reduces to about [0.4 m - 0.8 m] at the 1 m cutoff wavelength ($\alpha = 5$), until we find for the same cutoff wavelength a very narrow range of suitable facet size when $\alpha = 9$. Therefore, we consider $\alpha = 1$, and we investigate the results for different facet sizes. We present the FA results for three different facet dimensions (0.5, 1, and 1.5 m), that comply with the upper and lower bounds shown in figure 5.8, and we compare these results against the GO and the full KA.

Fig. 5.9(a) shows the horizontal copolarized (HH) NRCS in decibels [Clarizia et al. (2012)], averaged over 50 realizations of the Elfouhaily sea surface, for a wind speed of 4 m/s. The average NRCS is shown for HH polarization only, as results for VV polarization were similar. From fig. 5.9(a), we see that the NRCS calculated using the
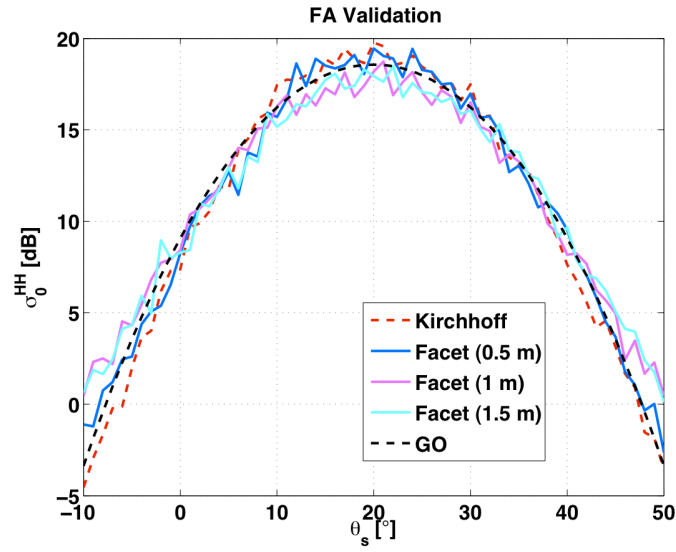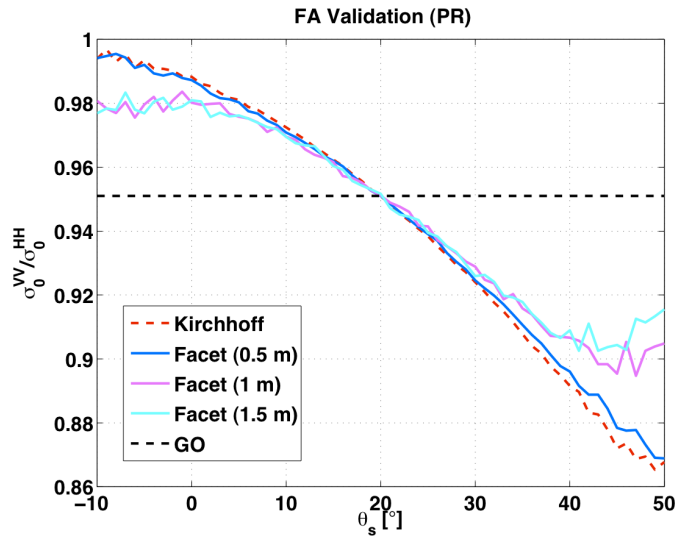
FIGURE 5.9: Horizontal copolarized NRCS (a) and PR (b) plotted against scattering angle for the full KA, the GO, and the FA with three choices of facet size. The results were averaged over 50 sea surface realizations for a wind speed of 4 m/s. The scattering angle value of 20° corresponds to the specular direction.

FA is in good agreement with the full KA for all three facet sizes, and that they all exhibit oscillations that are comparable with the KA curve. The NRCS from the FA are slightly lower than the KA within 20° of the specular direction (for scattering angles between 0° and 40°) and become slightly higher than the KA further away from the specular direction. As expected, the FA computed with the smallest facet size (0.5 m) gives the closest results to the KA. The FA results corresponding to 1.5 m facets, close to the upper limit of the facet size condition, differs most from the KA, by approximately 2 dB around the specular point. The patterns and oscillations in the NRCS also seem to become more different from those of the KA curve when the facet size increases. The FA led to a large reduction in computation times compared with the full KA. For facet size of 0.5 m, the FA computations were faster by a factor of almost 600, while for facet size of 1.5 m, the improvement in computation time was by more than 7000. The computations were done on workstations with dual-core processors, with a CPU of 3 GHz and RAM of ~8 GB. The reduced computation time represents an important benefit of the FA, where larger facets lead to lower computational cost and the ability to handle larger surfaces, while still providing a reasonable level of accuracy compared with the full KA. fig. 5.9(a) also shows the NRCS evaluated with the GO. The variance of the Gaussian slopes (MSS) was computed through integration of the Elfouhaily slope spectrum, up to the same wavenumber cut-off as used for the simulation of the explicit surfaces. The GO results are close to the full KA, which means that GO still provides a good approximation of the scattering, in an easy to implement method. However, it offers only limited means of exploring polarization, and the scattering from complex sea surfaces, because it only relies on a statistical description of such surfaces. In order to investigate polarization effects in spatial scattering, we use the Polarization Ratio (PR), defined as

$$\mathrm{PR} = \frac{\sigma_{VV}^0}{\sigma_{HH}^0} \tag{5.6}$$

Fig. 5.9(b) shows the PR for the full KA, the FA for three different facet sizes, and the GO, again as a function of the scattering angle. In all cases, the PR is lower than 1, evidence that the scattered HH component is always stronger than the scattered VV component. It is interesting to note that the PR computed with the FA shows sensitivity to polarization similar to the full KA, through a decreasing trend with increasing

scattering angles. The PR exhibits the same behavior around the specular direction for the KA and FA for all the facet sizes. Some differences appear between the KA and FA away from the specular direction, with the smallest facet size showing best agreement with KA over the widest range of angles (as expected). We note also the deterioration in the ability of the FA to match the KA at angles more than $10°$ from the specular direction when the facet size increases from 0.5 to 1 m. The PR for the GO shows no variation with respect to the scattering angle and it is simply equal to the ratio of the vertical and horizontal polarization Fresnel reflection coefficients of seawater. This happens when the transmitter and receiver lie in the $x - z$ plane, which allows to simplify the polarization vectors of (5.4), and express them as in (5.5). Given that the incident and scattering vectors $\hat{n}_i$ and $\hat{n}_s$ also lie in the $x - z$ plane, the scalar products $\hat{h}_s \cdot \hat{n}_i$ and $\hat{h} \cdot \hat{n}_s$ become zero in the expressions for the U-terms reported in (4.27), in chapter 4. The U-terms of GO can be therefore written as:

$$U_{hh} = M_1 R_\perp \left(\hat{v}_s \cdot \hat{n}_i \right) \left(\hat{v} \cdot \hat{n}_s \right) \tag{5.7a}$$

$$U_{hv} = 0 \tag{5.7b}$$

$$U_{vh} = 0 \tag{5.7c}$$

$$U_{vv} = M_1 R_\parallel \left(\hat{v}_s \cdot \hat{n}_i \right) \left(\hat{v} \cdot \hat{n}_s \right) \tag{5.7d}$$

and the ratio between U_{vv} and U_{hh} reduces simply to the ratio of the reflection coefficients $R_\parallel$ and $R_\perp$, which are both constant values. This also implies that for GO there are no cross-polarized components. In figure 5.9b, it can be noticed that the single PR for the GO matches the value of the PR for the full KA and the FA in the specular direction, as expected.

5.6   Spatial Maps of Scattering

In this section, we analyse maps of scattering of L-band spherical waves from realistic sea surfaces, where the scattering is computed using FA. The results are presented in the form of Normalized Radar Cross Sections (NRCSs) and Polarization Ratios (PRs),

to investigate both the characteristics of the scattered power and the polarimetric effects. Here we illustrate spatial maps of NRCS and PR, which means that the scattered power is not computed from the whole simulated surface, but rather from each single facet, which represents a pixel of the scattering image. We will show that this type of scattering visualization is very useful to look at how the explicit sea surface features, and particularly the wave crests and troughs, scatter the incident power, and how a map of such scattering is related to the sea surface. However, this type of analysis ignores the phase with which each facet scatters, and consequently the phase interference that is generated, which strongly affects scattering from the whole sea surface. In this section, we first start by looking at how much these spatial maps are influenced by parameters that are not related to sea state, like geometry, and size of the facets. For simplicity, these investigations are only done through Elfouhaily surfaces. Subsequently we fix the geometry and the facet size, and we concentrate on the scattering with respect to different sea state. Scattering results are presented for Elfouhaily wind waves, composite Elfouhaily wind waves and swell, and JONSWAP surfaces, all illustrated in sections 5.2 and 5.3. In this chapter, the analysis is restricted to the scattering from linear/Gaussian surfaces, while the same analysis on non linear sea surfaces will be presented in chapter 8. Figure 5.10 illustrates an example of sea surface and relative scattering. The top left picture is a 10 m/s Elfouhaily sea surface snapshot, and the co-polarized HH component of the NRCS is shown in dB on top right. The bottom left picture illustrates instead the cross-polarized HV component of the NRCS in dB, while the bottom right picture shows the map of PR, in absolute values, as described in equation (5.6). Here, the facet size is chosen to be 1 m x 1 m, and the computations are now for 500 m x 500 m areas of the sea surface. Such a surface does not of course represent a realistic glistening zone from spaceborne, which would be on the order of 10s of km. However, it is easy to handle computationally, and sufficient to represent a meaningful wave field, and to show the effect of the waves on the scattered signals.

Figure 5.10 shows that the FA is a vector formulation, and it is able to provide cross-polarization components (HV and VH), which are usually neither predicted by the scalar Z-V formulation commonly employed for GNSS-R scattering, nor predicted by the Ulaby vector formulation of GO, when the transmitter and receiver are in the plane of incidence
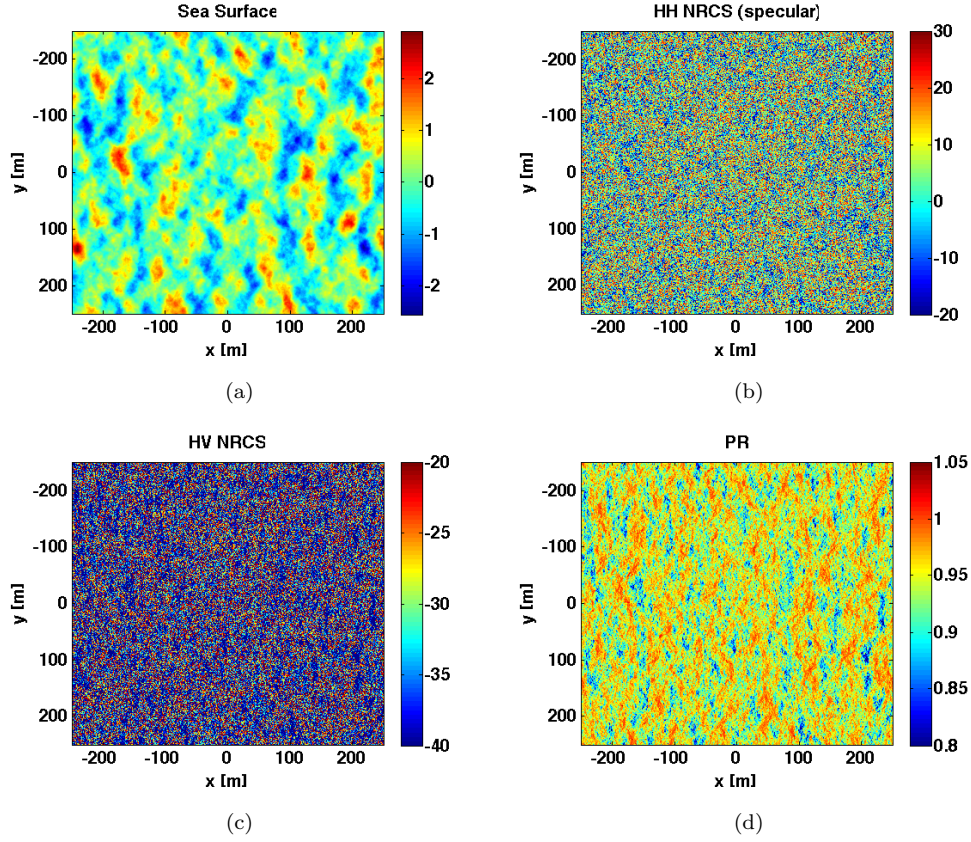
FIGURE 5.10: A snapshot of a 10 m/s wind wave surface in meters (top left), the corresponding copolarized HH NRCS (top right) and cross-polarized HV NRCS, both in dB (bottom left) and a map of PR in absolute values (bottom right). The incidence angle is 20°, and the receiver is in the specular direction. Both the transmitter and the receiver are in a spaceborne configuration.

($U_{vh} = U_{hv} = 0$). The HH component of the RCS displays patterns associated with the configuration of the scattering sea surface; their similarity will be more widely discussed in section 5.6.3. It is interesting to note that even cross-polarized components show patterns related to the underlying sea surface, and a structure similar to the co-polarized NRCS. However, they are much smaller than the co-polarized scattering components, and for this reason we are not going to analyse them in details, but will concentrate on the results from co-polarized NRCSs.

5.6.1 Radar Cross Section for different geometries

In this subsection the variations of spatial maps of NRCS and PR are analysed when the incident angle is fixed, and the scattering angle of the receiver θ_s^g varies. The HH component of NRCS and the PR have been calculated from the 10 m/s, 0° direction

wind wave surface shown in figure 5.10, for a fixed incidence angle $\theta_i^g = 20°$, and three values of the scattering angle $\theta_s^g = 0°, 20°$ and $40°$. The results are shown in figure 5.11. The HH component of NRCS is weaker in the two quasi-specular cases, and different and stronger in the specular configuration, as expected. However, it is interesting to note that the explicit features of the sea surface are more visible in the quasi-specular NRCS maps, rather than the specular one, where the NRCS map is much more uniform. This is linked of the slope distribution, and the optimal facet orientation for the three cases. In the specular configuration the scattered power is stronger and more uniform because it mainly comes from facets with slopes close to zero, and that represents the average slope of the facets across the surface. For the other configurations of $\theta_s^g = 0°$ and $\theta_s^g = 40°$, the ideal slopes for a facet to scatter towards the receiver are respectively $-10°$ and $10°$ respectively. These are not the most frequently occurring slopes, and therefore the overall scattered power is weaker, but these slopes occur mostly along the ascending or descending edges of the waves, hence the scattered NRCS highlights these edges in the two non-specular cases. The NRCS for the non-specular cases resembles quite well the x-slope map of the sea surface, with maxima on the ascending wave edges (positive slopes) in the case of $\theta_s^g = 0°$, and instead on the descending wave edges (negative slopes) for $\theta_s^g = 40°$. No significant variations have been noticed in the PR for the three cases, which suggest that PR is mostly determined by the slopes of the sea surface itself, and it is independent of the geometry.

5.6.2 Radar Cross Section for different facet sizes

A brief investigation is carried out here on the use of different sizes of the facet, when the scattering is computed through FA. Figure 5.12 shows spatial maps of NRCS, where the underlying surface is still that shown in figure 5.10, for three facet sizes of 0.5 m, 1 m, and 2 m.

From figure 5.12, we notice that the scattering is more uniform for the 0.5 m case, while in the case of 2 m the scattering is weaker, but with a small number of very bright points of very high NRCS. This happens because larger facets will have a much narrower lobe, which is less likely to be exactly oriented towards the receiver, causing the scattered
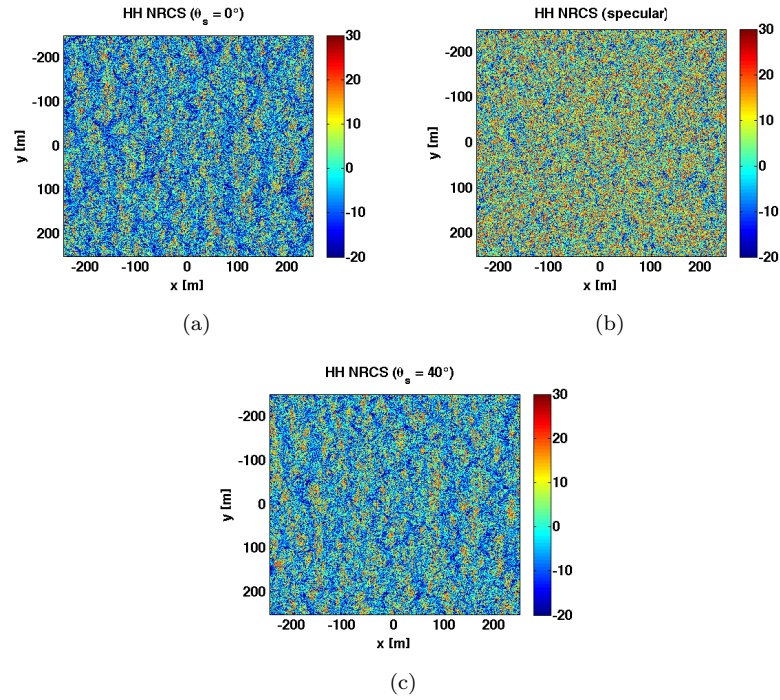
FIGURE 5.11: Spatial maps of NRCS for a fixed incidence angle of 20°, and for three different scattering angles of 0° (top left), 20° (top right) and 40° (bottom middle).
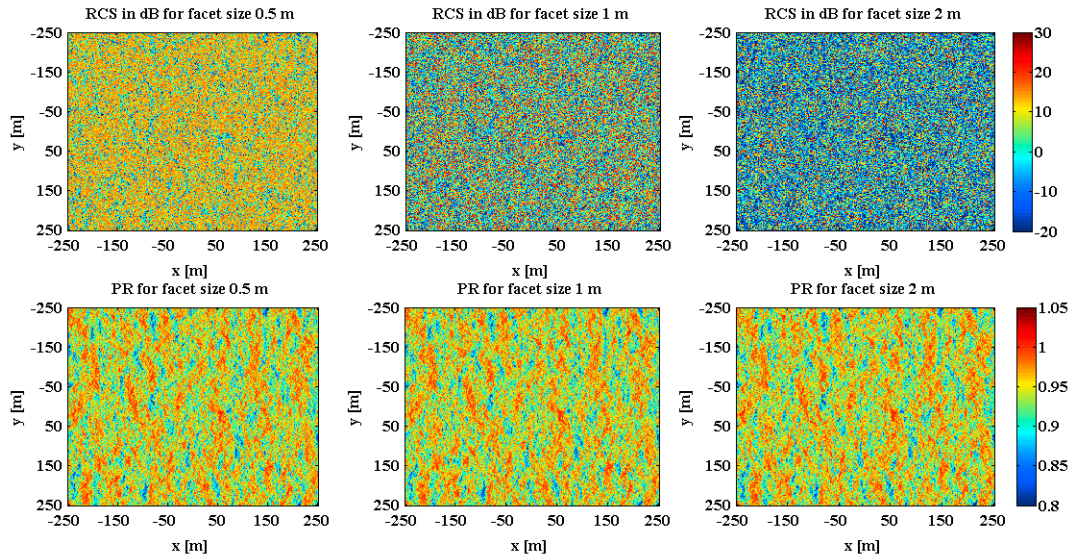
FIGURE 5.12: Spatial maps of NRCS in dB (top row), and PR (bottom row), for a 10 m/s wind wave surface. The scattering here has been calculated using a fixed specular configuration ($\theta_i^g = \theta_s^g = 20°$), and facet sizes of 0.5 m, 1 m and 2 m (from left to right).

power to be lower on average. However, for that small number of points with optimal orientation with respect to the receiver, the power scattered is very strong. While the scattering for the 0.5 m case appears quite uniform, the resolution seems very coarse for 2 m facets, and therefore the explicit features of the underlying scattering suface are less visible. From this analysis, and from the FA validation analysis, it can be concluded that a choice of a 1 m facet is the best one, in that it represents a trade-off between computational costs and ability to properly reproduce the explicit features of the sea surface, through spatial maps of scattering. Once again, no significant differences can be detected from the maps of PR. In the next section, we will fix the geometry to specular, and the facet size to 1 m, and will use it consistently for all the surfaces. It is worth mentioning that the 1 m facet size, which has been basically derived from Elfouhaily surfaces, remains suitable for JONSWAP surfaces too, although for these surfaces more stringent conditions are obtained for the upper and lower bound of the facet size, and 1 m represents roughly the maximum allowed dimension of the facet for such surfaces.

5.6.3   Radar Cross Section for different Wind and Wave Conditions

In this paragraph we focus on NRCS variations with respect to different sea surfaces of different roughness. Figure 5.13 shows the Elfouhaily sea surfaces along the first column, obtained from top to bottom for a wind speed of 5 m/s and 10 m/s, and a 0° wind direction, and finally for a 10 m/s, 0° wind wave field with a superimposed swell, travelling in a different direction (60°) with respect to that of the wind waves. The corresponding HH component of NRCS calculated through the FA is shown in the second column.

It is worth mentioning once again that these images do not represent the power scattered from the sea surface, as sensed by a receiver, since they do not account for the phase of the scattered field from each facet. The phase plays a major role when combining the contributions from all facets (as shown later). Nevertheless, these maps are useful to examine the spatial distribution of the scattered power and to what extent it is influenced by the explicit waves. In figure 5.13, we notice that the NRCS is larger in the low-wind case and decreases for higher wind speed cases, consistently with our
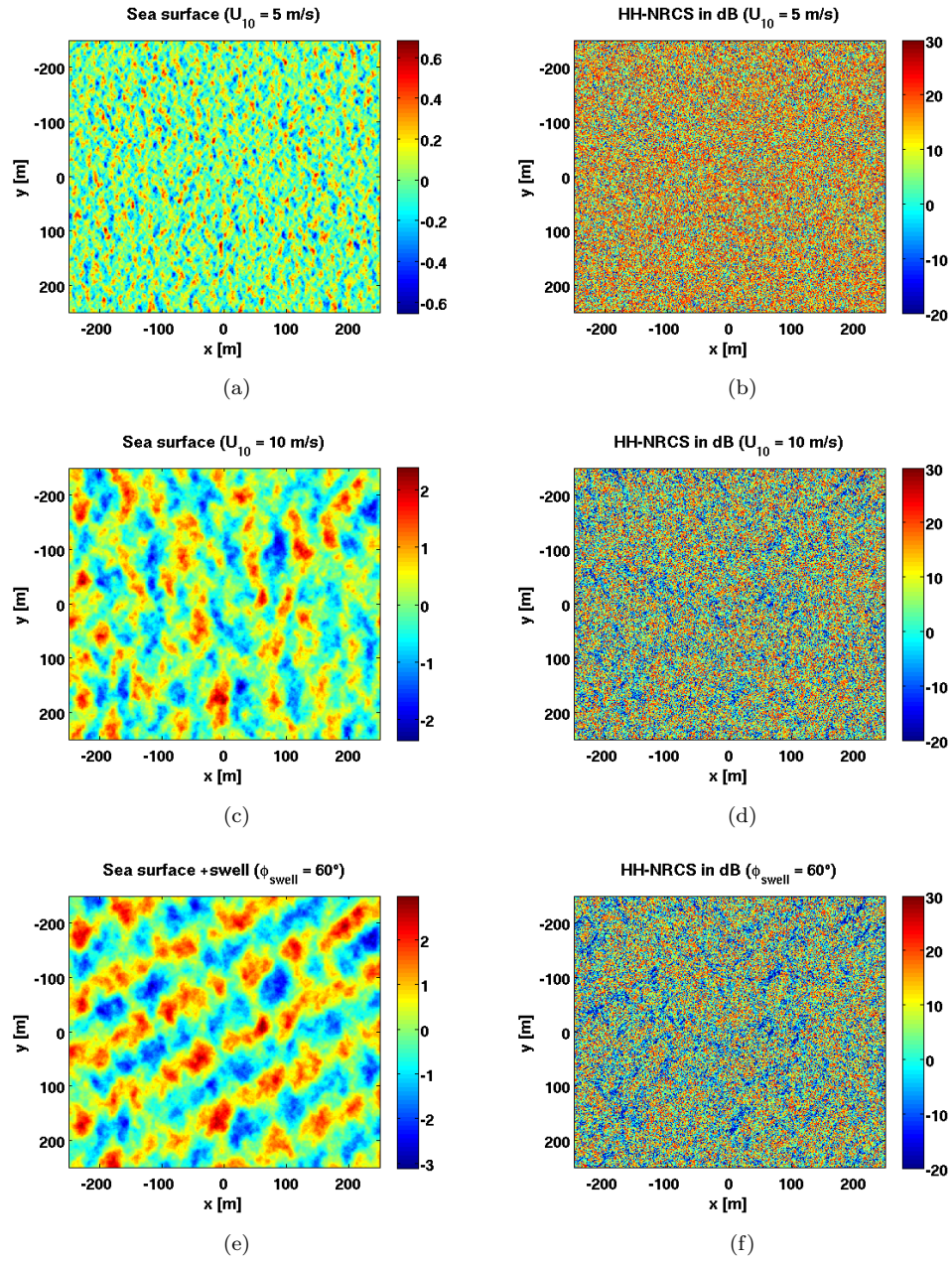
FIGURE 5.13: Elfouhaily sea surfaces in meters (left column) and corresponding HH-NRCS, in dB (right column).

expectations of decreased scattering in the specular direction for rougher seas. All the NRCSs in Fig. 5.13 exhibit some wave patterns that are related to the corresponding wave field, particularly in the high-wind-speed and high-wind-speed-plus- swell case. In particular, diagonal wave patterns aligned with the swell wave crests can be seen at the bottom right of figure 5.13, suggesting an influence of this particular swell train on the distribution of the scattered power over the sea surface. Figure 5.14 shows JONSWAP surfaces on the left column, and the HH-NRCS on the right column.
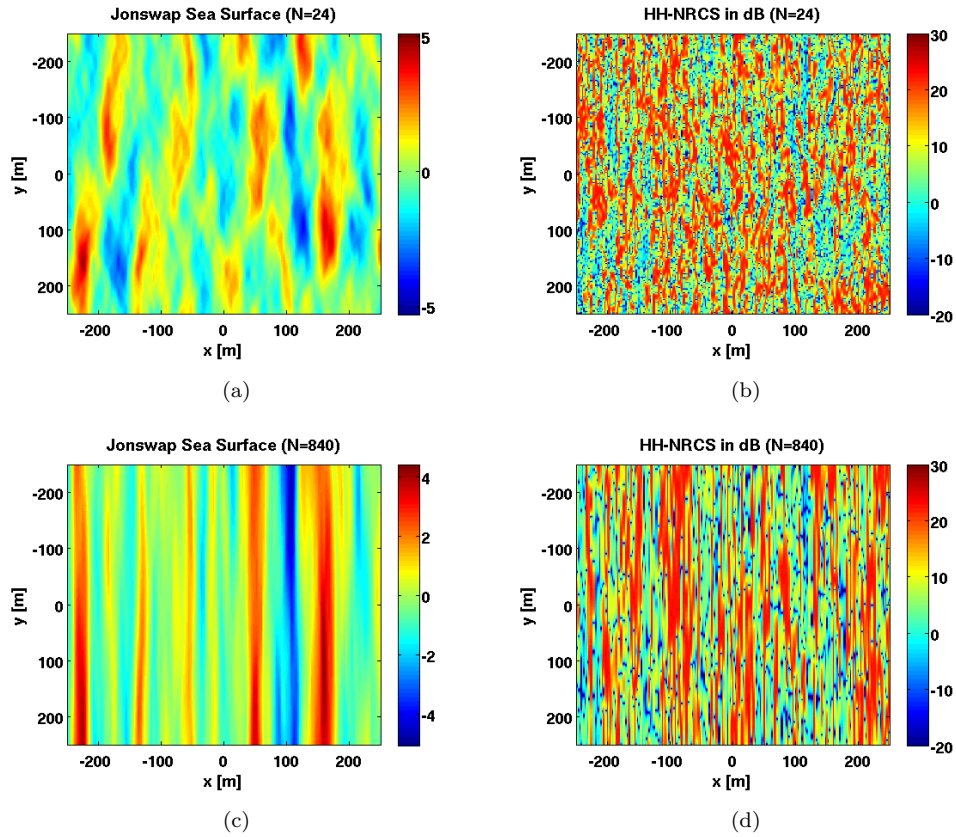
FIGURE 5.14: JONSWAP sea surfaces (in meters), for N=24 (top left) and N=840 (bottom left), and corresponding HH-NRCS, in dB (right column).

In this case the similarity between the underlying surface and the scattering map is even stronger than the Elfouhaily surfaces, as some of the wavefronts on the sea surface form analogous structures in the NRCS. This is due to both the higher directionality and the higher steepness of JONSWAP surfaces, for which the slope and consequently the scattering modulation is stronger, and the wavefronts appear more visible in the scattering map. In figure 5.14, we also notice an overall stronger NRCS for JONSWAP surfaces compared to the Elfouhaily case shown in figure 5.13. This is again due to the

high directionality of the waves, causing y-slopes very close to 0, which is the average optimal y-inclination of the facets to scatter power towards the receiver, in a narrow area around the SP.

5.6.4   Polarization Ratio for different Wind and Wave Conditions

We now analyse the behaviour of PR for different sea states. Figure 5.15 and 5.16 show maps of PR in absolute values on their right column, respectively for Elfouhaily and JONSWAP surfaces. These maps are deliberately illustrated together with maps of the x-slopes (on the left column of figure 5.15 and 5.16), to show how strongly the two are related. We recall here that negative x-slopes correspond to facets oriented towards the receiver (descending edges of the waves), while positive slopes characterize facets oriented towards the transmitter (ascending edges of the waves).

In figure 5.15 and 5.16, the features seen in the x-slope maps are the same as in the corresponding PR map. The PR in figure 5.15 exhibiting crests-and-troughs patterns closely matching those of the waves, and the presence and directionality of the swell is easily detected as an oblique pattern across the surface aligned with the line of the swell wave fronts. The similarity between PR and x-slopes is even stronger for JONSWAP surfaces. We notice that the PR is generally less than 1, which suggests that the HH component is overall stronger than the VV component, in accordance with a higher HH Fresnel scattering coefficient for seawater, compared to the VV one. Furthermore, the minima and maxima of the PR coincide with negative minima and positive maxima of the slopes respectively. This means that HH and VV components are very similar when the scattering occurs from zero-slope flat facets, and become increasingly different from each other when the inclination of the facets increases. The minima of PR are the most interesting ones, as they correspond to slopes oriented towards the receiver, and also because their values are significantly different from 1. The maxima of PR are only slightly higher than 1, and since they occur for facets oriented towards the transmitter, it is reasonable to assume that both the HH and the VV components scattered towards the receiver are quite weak. It is however interesting to point out that an amount of scattering from these facets is still present, and this is probably due to the secondary
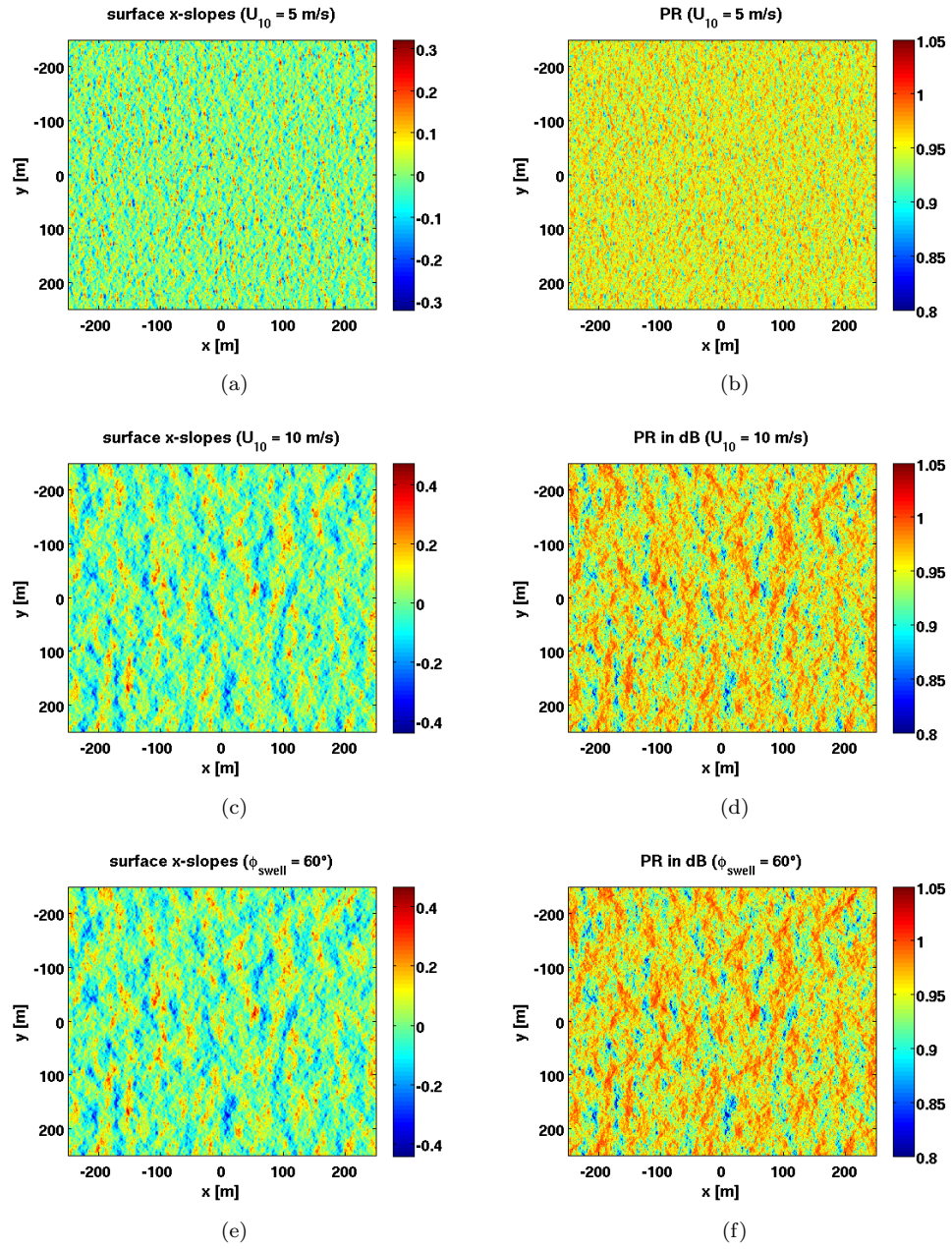
FIGURE 5.15: Elfouhaily (with and without swell) sea surface x-slopes (left column) and corresponding PR (right column).
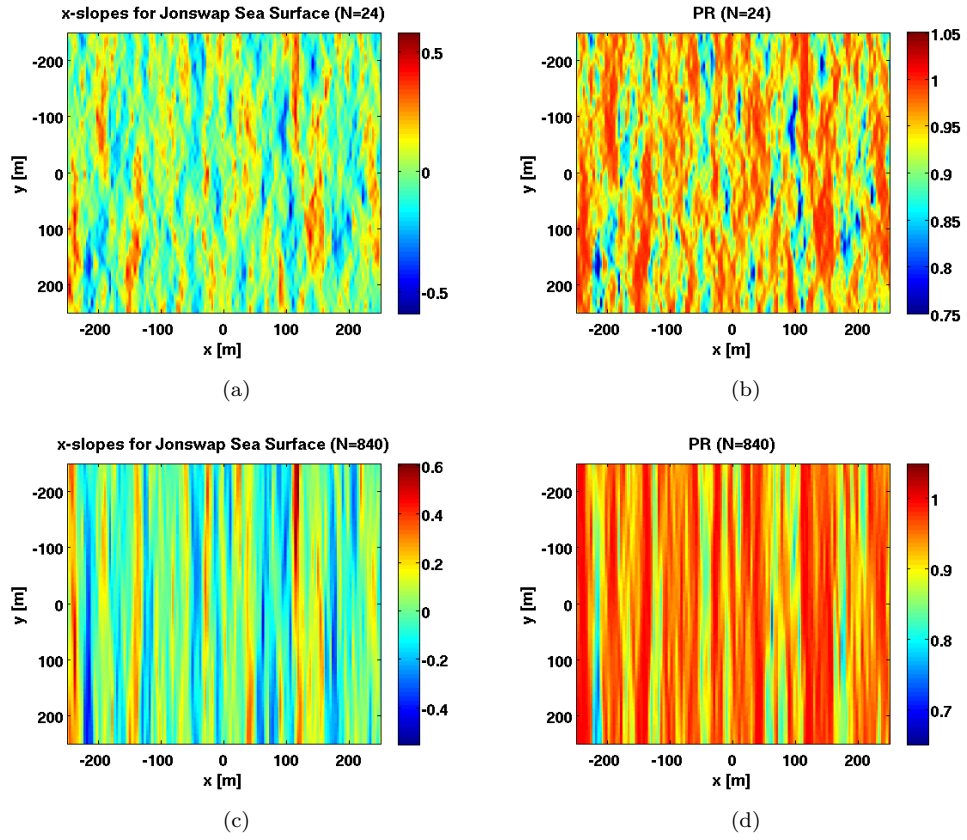
FIGURE 5.16: JONSWAP Sea Surface x-slopes (left column) and corresponding PR (right column).

lobes of the sinc function, which determine some scattered power even for directions very far from the specular. Figure 5.17 shows a scatter plot of the PR versus slopes along x, for different types of linear surfaces. This plots illustrates graphically the correlation between PR and the x-slopes, seen in figures 5.15 and 5.16. It highlights a characteristic banana shape, with a saturation effect of the PR for increasing slopes. The reason for this effect is unknown, but this corresponds to facets that are not oriented towards the receiver. In figure 5.17, we notice a much larger spreading of the PR values for a fixed slope in the Elfouhaily case, compared to the JONSWAP case where the dependence between PR and x-slopes is almost one-to-one, and the scatter plot collapses into a well-defined line. The reason for that lies once again in the strong directionality of one compared to the other, and the fact that the scattering and the PR have a dual dependence on both the x-slopes and the y-slopes. In the Elfouhaily case, such a dual dependence is much heavier, as the slopes vary in both directions, causing much more

variability in the PR values. For The JONSWAP cases, the dependence upon the y-slopes almost disappears, and therefore a PR value can be directly mapped into a x-slope value.
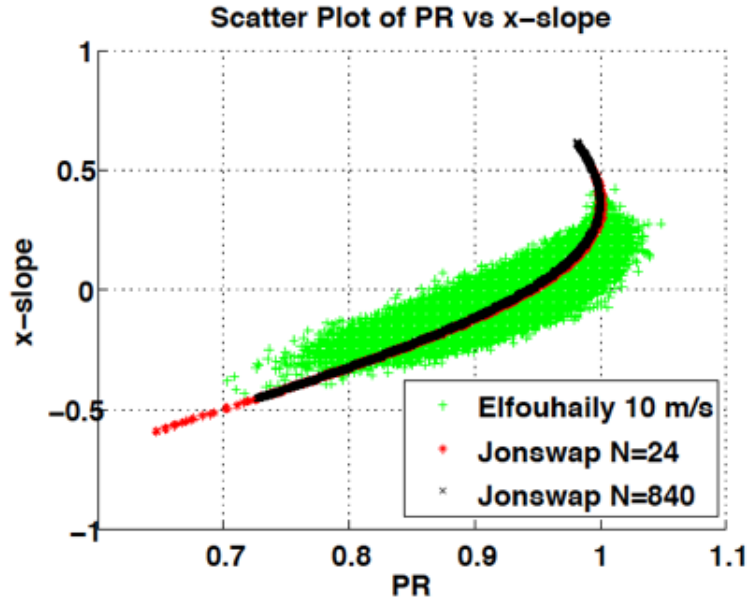
FIGURE 5.17: Scatter Plot of PR versus surface slopes along x (the Banana plot).

5.7 Plots of NRCS and PR for varying scattering angle

In the previous sections, the contribution from each facet has been analyzed separately, in the form of spatial maps of scattering. In reality the scattered power from the sea surface arrives at the receiver as the sum of the contributions from all the facets on the surface. This means that the total electric field is the coherent sum over all facets of the complex electric fields from each of them, which causes a constructive/destructive interference of the phase terms from each facet, producing a final scattered power which is lower than the sum of the scattered powers from each facet. Summing the contribution from all the facets of the sea surface will produce a single value of the scattered power from that surface, and here the scattered power is analysed for a fixed incidence angle, and for varying scattering angles, producing curves of NRCS and PR. This represents a standard way to analyse results from a scattering model, and its general sensitivity to parameters, both for monostatic [Johnson et al. (1998), Soriano et al.

(2001), Voronovich and Zavorotny (2001)] and for bistatic geometrical configurations [Elfouhaily et al. (2001), Khenchaf (2001), Arnold-Bos et al. (2007a), Arnold-Bos et al. (2007b)]. Moreover, this type of analysis is useful to predict how the scattering behaves when one moves across the glistening zones, from the central areas of quasi-specular scattering, towards the edges, where the scattering is non-specular and the scattering angles are increasingly different. In this section, we focus on the analysis of the sensitivity of the FA model to varying sea states, by means of plots of NRCS and PR for different sea surfaces. Table 5.1 summarizes roughness and directionality parameters of the surfaces that will be analysed in this paragraph. Table 5.1 highlights that an increase in the wind

	Elf. 5 m/s	Elf. 10 m/s	JON. N=24	JON. N=840	Comp 10 m/s Swell 50 m	Comp. 10 m/s Swell 100 m	Comp 10 m/s Swell 250 m
MSS_x	0.0048	0.0091	0.0193	0.0202	0.0413	0.0174	0.0104
MSS_y	0.0023	0.0052	0.0008	0.00002	0.0053	0.0053	0.0052
RO	0.0071	0.0143	0.0201	0.0202	0.0466	0.0227	0.0156
DP	2.09	1.75	26.71	1195.00	7.79	3.28	2.00

TABLE 5.1: Roughness (MSS_x, MSS_y, RO) and directionality (DP) of Elfouhaily wind wave surfaces (Elf.), composite Elfouhaily surfaces with a swell (Comp.), and JON-SWAP surfaces (JON.) that are here the object of our analysis.

speed (from 5 to 10 m/s) increases the total roughness, as both MSS_x and MSS_y become larger. When a swell travelling along the x-direction is superimposed, this causes an increase of the MSS along x only, while the MSS along y remains roughly the same. A decrease of the swell wavelength (from 250 m to 50 m) produces overall steeper slopes along x, and therefore a even higher MSS_x. As far as directionality is concerned, all the Elfouhaily surfaces, with and without a swell, have comparable DP, which is much lower than those characterizing the JONSWAP surfaces. Before presenting plots of NRCS and PR for different sea surfaces, and recalling the discussion about the variable width of the sinc lobe presented in chapter 4, we want to first show the comparison between NRCS plots for the standard FA, the altered FA where the width of the sinc lobe is fixed, and finally of GO, for the same set of parameters. Figure 5.18 shows the NRCS computed using the FA (blue), by summing coherently the contribution from each facet,

the NRCS calculated from the classical GO (black), and finally the NRCS calculated using FA, but assuming the width of the sinc lobe to be constant and simply centered around the direction of reflection (red). Here the width of the lobe has been chosen as the one we would have from a flat facet, with a nadir incidence and scattering, as this would be equivalent to the radiation lobe of a planar patch antenna [Balanis (1982)]. Figure 5.18 clearly shows that the original FA is in much closer agreement with GO, as compared to the FA where the size of the lobe has been altered based on physical considerations.
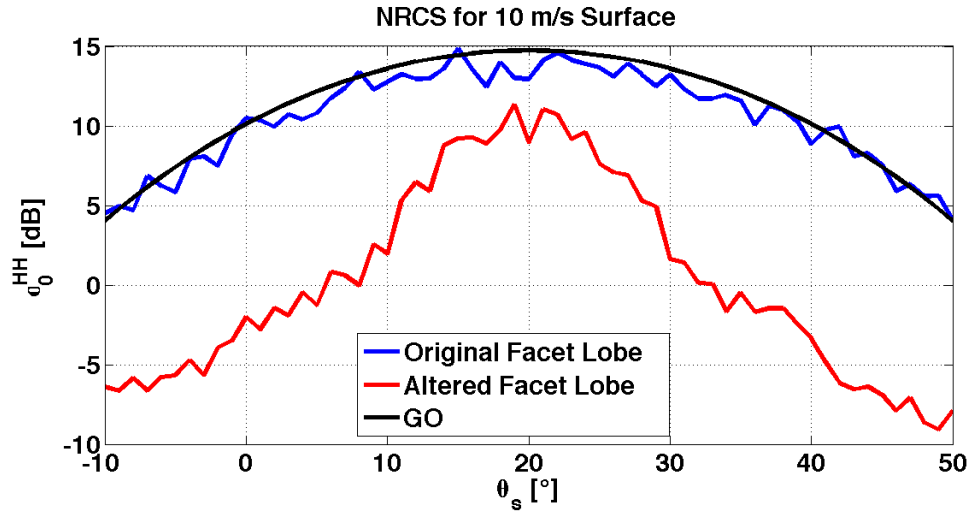
FIGURE 5.18: NRCS curves for FA, GO, and FA with a sinc lobe of fixed width for each facet. The FA-based NRCSs has been calculated from an explicit sea surface realization, and have been averaged over 50 realizations.

5.7.1 Scattering results for different sea surface roughness

A plot of the average HH NRCS (a) and of the PR (b) is shown in Fig. 5.19 for the surfaces described in table 5.1, with and without swell. Results for JONSWAP surfaces will be shown separately in the next subsection, since we have only one surface realization for them, and could not produce an average version of NRCS and PR. For these plots the receiver range is kept constant, while the scattering angle varies over a range of angles up to 30° on either side of the specular direction. The transmitter incidence angle is still 20°, as it can be seen from the maximum NRCS value at the specular direction. The NRCS and PR curves were averaged over 50 realizations of the sea surface in order to reduce the variability due to the individual waves in single realizations, and look at the

mean trend. The NRCS curves are listed in the legend for increasing roughness (from the blue to the cyan curve), and clear changes of these curves can be noticed across these curves. The blue NRCS, which corresponds to the lowest roughness (Elfouhaily surface with $U_{10} = 5$ m/s) has the highest peak for the specular configuration of transmitter and receiver (at $\theta_s = 20°$), but the fastest power dropoff as one moves away from the specular configuration. As the roughness increases, the NRCS curve becomes lower in the middle, and higher at her branches, until collapsing into an almost flat line, where the scattered power is roughly the same for all the transmitter-receiver configurations. This is consistent with the fact that for increasing roughness the scattered power at the SP decreases, and more power is instead scattered from areas away from the SP. However, it is worth pointing out that apart from the purely wind wave cases, where both $MSS_x and MSS_y$ increase, the increase in total roughness for the wind waves plus swell cases is due to an increase in the roughness along the x-direction only. This would suggest that the sensitivity of the NRCS curves seen in figure 5.19 (a) is mostly influenced by the roughness along x. As for the NRCS, we computed the PR averaged over the same 50 realizations, for the same range of scattering angles and wind speeds, shown in figure 5.19 (b). The PR exhibits the usual decreasing trend with increasing scattering angles, but changes in the PR curves for different roughness are confined to either low or high scattering angles. For high scattering angles in particular, it can be noticed that PR decreases for increasing roughness. These changes are interesting, mostly because they happen in a non-specular configuration, like the edges of the glistening zones, therefore suggesting that these are the areas where polarization has a major impact. However, these are also areas where the scattered signal is much weaker, and generally speaking where the validity of the facet approach itself starts to break down, because they are far from the specular direction.

5.7.2 Scattering results for different directionality and directions

In this section, we present results for Elfouhaily surfaces, when the waves travel in different directions, as well as for JONSWAP surfaces. Figure 5.20 shows NRCS (a)
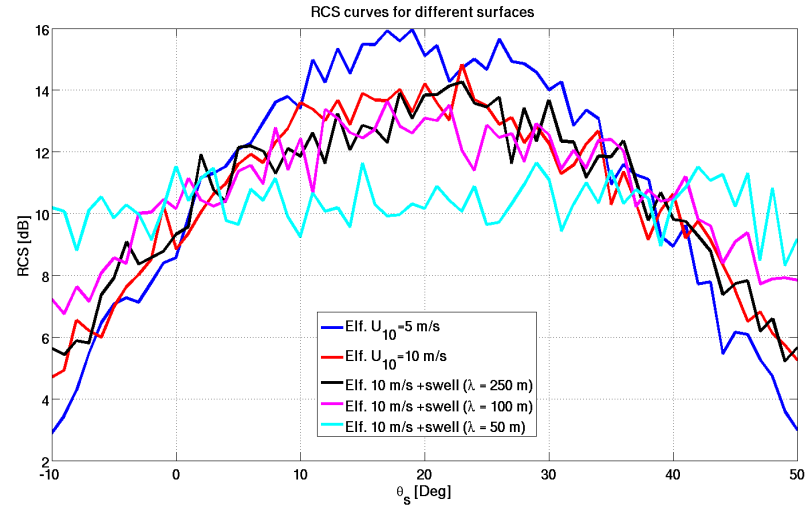
(a)
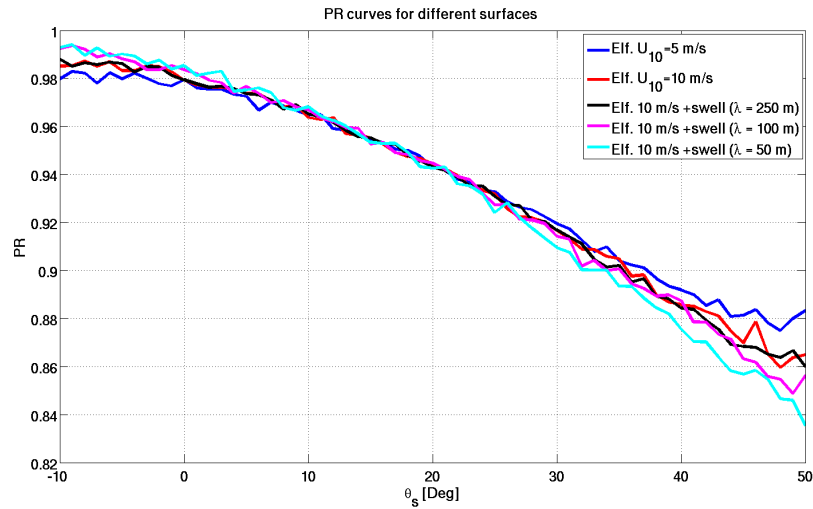
(b)

FIGURE 5.19: (a) Average HH-NRCS in dB, plotted against scattering angle. The specular direction corresponds to the scattering angle value of 20°. Results are shown for different sea surfaces of different roughness, all based on the Elfouhaily spectrum. The results were averaged over 50 realizations of the sea surface.(b) average PR versus scattering angle, for the same sea surfaces.

and PR (b), for different types of Elfouhaily-based surfaces, when the waves travel in a direction of 0° (continuous lines) and of 90° (dashed line).
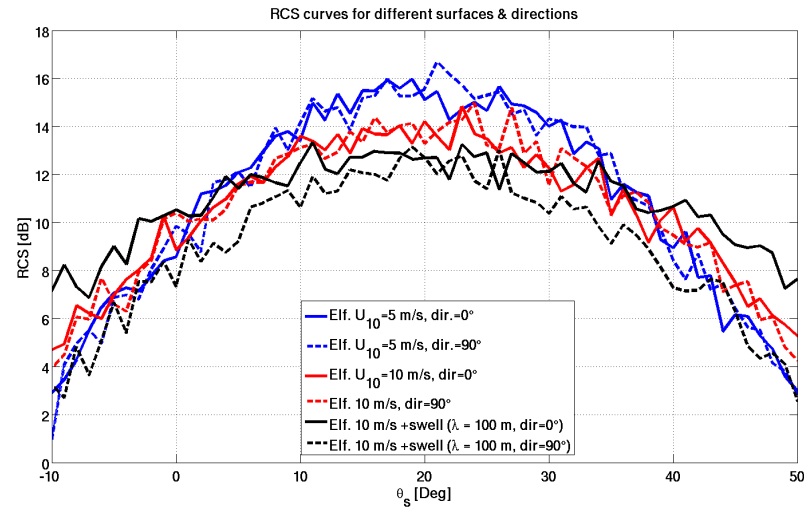
(a)
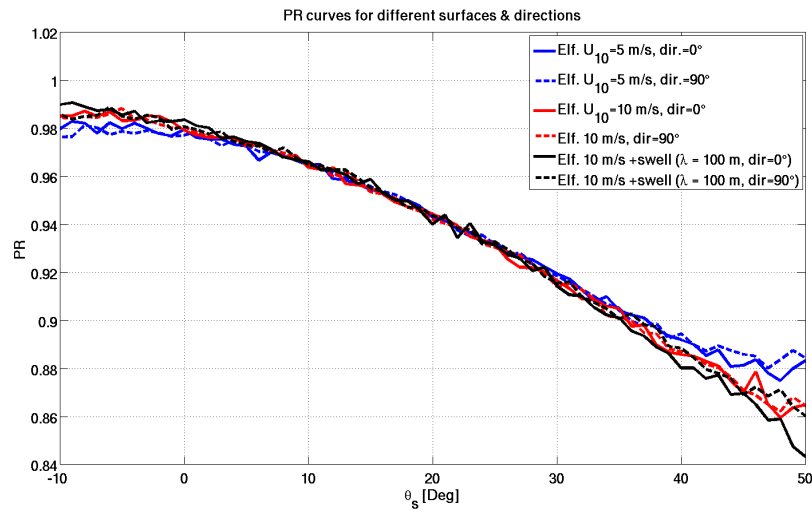
(b)

FIGURE 5.20: (a) Average HH NRCS in dB against scattering angle, for different Elfouhaily-based sea surfaces and different directions. The results were averaged over 50 realizations of the sea surface.(b) average PR versus scattering angle, for the same sea surfaces.

In this case, the total roughness of the sea surface does not seem to enhance the detectability of a changing direction of the waves. This happens mainly when both the MSS_x and the MSS_y increase or decrease in the same way (wind speed of 5 m/s and 10 m/s, shown in blue and red), such that the directionality of the sea surface (the DP parameter) remains constant. However, as the waves become more directional (wind

speed of 10 m/s plus a swell, shown in black), then a change in direction becomes more and more visible in the NRCS. Interestingly, the NRCS around the specular scattering angle remains roughly constant when the direction is changed. In some ways this is not unexpected, because when the scattering angle remains reasonably close to the specular one, the ideal x- and y-inclinations of the facets to scatter power towards the receiver remain close to zero too, and the overall number of facets with these characteristics does not change when the surface is rotated. As we move away from the specular configuration, the rapidity with which the power drops off depends mainly on the MSS along the x-direction. When the surface is rotated by 90°, the MSS_x and the MSS_y are exchanged, and the lowest one is now along the x-direction, causing a more rapid power dropoff. Figure 5.20 also shows in (b) PR curves as a function of the scattering angle, but again no significant changes are detected in polarization. We now move on to the results for JONSWAP surfaces, which are characterized by a much stronger directionality compared to the Elfouhaily ones, as shown by their DP parameter in table 5.1. Figure 5.21 shows NRCS curves (a) and PR curves (b) for JONSWAP surfaces for different directionality (N=24 and N=840), and for different travelling directions of the waves ($\phi = 0°$ and $\phi = 90°$). It is worth mentioning that the surfaces from which the NRCS and PR are obtained are ~ 1 km², therefore bigger than the Elfouhaily ones (0.25 km²).

The NRCS patterns for a 0° wave direction (black and blue lines) show little variation with respect to the scattering angles, recalling the NRCS seen in figure 5.19 (a) for the swell with a very short wavelength (50 m) on top of wind waves. This confirms that such a flat NRCS is reached when a very high roughness along x is achieved, which happens for example when the waves are very steep along the x-direction (either high amplitude, or short wavelength). The fact that the central values of NRCS for N=840 (black line), characterized by higher roughness, are consistently larger than those for N=24 (blue line), which has lower roughness, is a bit surprising, as it is not consistent with the trend in roughness shown in figure 5.19. However, we recall that these plots correspond to a single realization, from which a general trend is difficult to establish. Furthermore, these surfaces are very different from the Elfouhaily ones, particularly in terms of directionality. The changes we mainly want to highlight in figure 5.21 (a) concern the direction. For such directional surfaces, the NRCS configuration changes

(a)

(b)
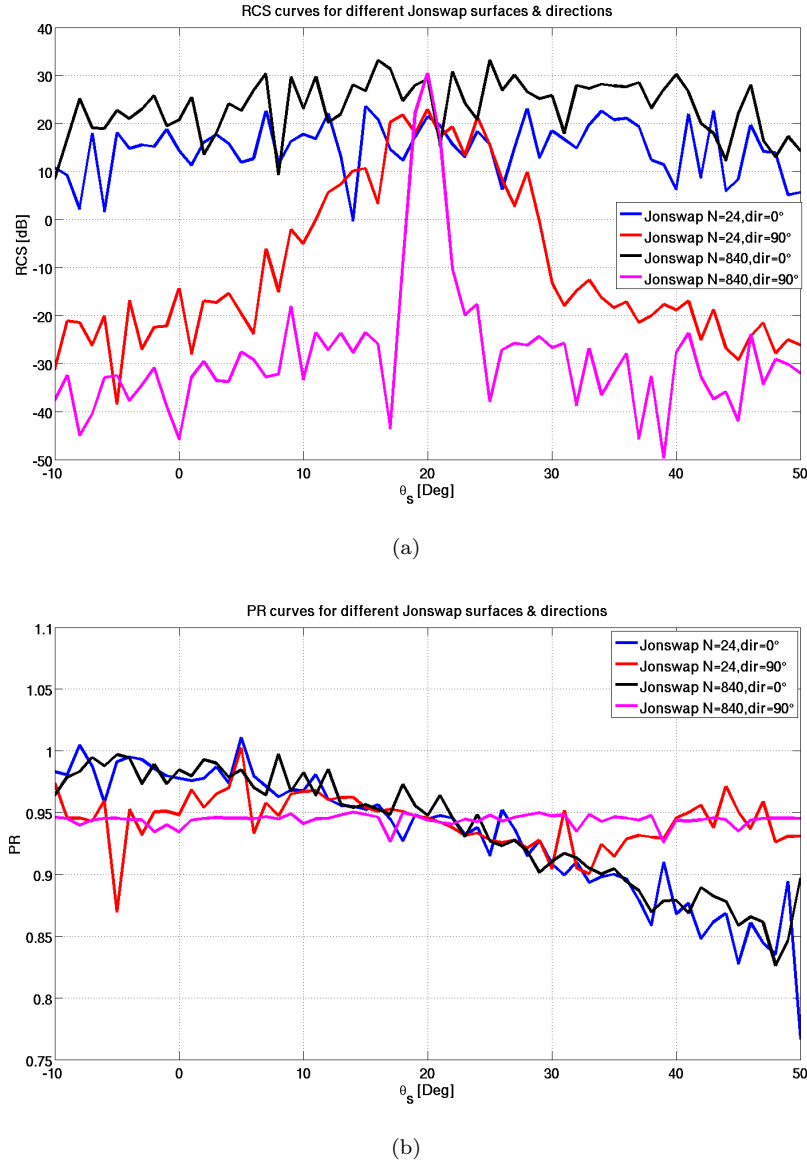
FIGURE 5.21: (a) Average HH NRCS in dB against scattering angle, for different JONSWAP sea surfaces with different directionality and directions. The results were averaged over 50 realizations of the sea surface. (b), average PR versus scattering angle, for the same sea surfaces.

radically from a defined trend for 0° wave direction, to a peaky function for 90° wave direction, and the peak becomes narrower for increasing directionality. This is expected, as a strongly directional swell-like sea surface travelling in a direction of 90° will have a $MSS_x \simeq 0$. A high amount of power is therefore scattered towards the receiver in the specular configuration, but such scattering will very rapidly decrease as soon as the receiver is moved away from the specular configuration. Notably, the NRCS for N=840 and 90° wave direction (magenta line) is lower than the NRCS for N=24, and 90° wave

direction (red line), as opposed to what happens for the 0° wave direction case. As far as PR is concerned (5.21 b), it is interesting to note that for a wave direction of 90° the PR becomes constant, and simply equal to the ratio of the Fresnel reflection coefficients, similarly to what happens for GO in figure 5.9 (b).

5.8   FA Results for different radar geometry and wavelength

In this last section of the chapter, we want to explore the results of the FA simulator, for different, monostatic radar geometries, and different incident radar wavelengths. The results from the FA scattering are compared with results available in literature, where the scattering is calculated with different (either large-scale or full-scale) EM models. The comparison we are going to illustrate highlights the versatility of the FA simulator, and the possibility to use it even for geometries (i.e. monostatic radars) and microwave frequency bands (i.e. Ku band, C band etc.) different from GNSS-R. Figure 5.22 shows the backscattering NRCS curves calculated using the FA, versus NRCSs illustrated in [Voronovich and Zavorotny (2001)], computed using GO, and the Two-Scale model (TSM) [Bass and Fuks (1979)]. The HH polarized backscattering results in [Voronovich and Zavorotny (2001)] are calculated for a monostatic radar, and an incident Ku band ($\lambda = 0.0214$ m) plane wave, where the scattering occurs from an Elfouhaily sea surface of 15 m/s wind speed. The results are produced using three different cutoff wavenumbers ($k_d = k_0/3, k_0/10, k_0/40$), which can be found in several papers ([Brown (1979), Plant (1986), Donelan and Pierson (1987), Thompson (1988), Jackson et al. (1992)]), and chosen so that the differences in the results for different cutoff wavenumbers can be investigated. The NRCS curves in [Voronovich and Zavorotny (2001)], and here illustrated again in figure 5.22 (a), have been compared to NRCS calculated using the FA, from a 500 m x 500 m Elfouhaily surface, generated using a resolution of 0.1 m, a wind speed of 15 m/s, and the three cutoff wavenumbers used in [Voronovich and Zavorotny (2001)]. The facet size has been chosen here equal to 0.1 m, and compliant with criteria (4.40) and (4.41), where the wavelength is now in Ku band, and the radius of curvature is that for a 15 m/s Elfouhaily wind wave surface. The NRCS calculated

using the FA and averaged over 20 realizations are shown in figure 5.22 (b). Here the number of realizations is the minimum one that allows to produce NRCS curves smooth enough, making their general trend clearly visible, and does not imply high computational and timing costs. Figure 5.22 (b) also shows NRCS reproduced using the GO, and the MSS calculated as integration of the Elfouhaily slope spectrum, up to the three cutoff wavenumbers used in this study. It is worth pointing out that our GO curves do not exactly match those illustrated in [Voronovich and Zavorotny (2001)], and shown in 5.22 (a). This is probably due to a difference in the calculation of the MSS, and at the moment we do not know the reason for such discrepancy, however the difference between the two remains quite small, and it is not important here. Figure 5.22 (b) shows that the FA is similar to GO at relatively small angles, and it predicts a larger amount of scattered power, compared to the TSM. However, its drop in power for increasing angles is much slower than GO, resulting in a good amount of power being scattered even at relatively large angles, similarly to full-scale models like the TSM.

Figure 5.23 (a) and (b) show instead how FA compares to GO and Physical Optics (PO) results illustrated in [Johnson et al. (1998)]. The geometry in [Johnson et al. (1998)] is still monostatic, but the scattering surface is assumed to be a Perfect Electric Conductor (PEC). The incident wave is once again within the Ku Band (f=14 GHz, $\lambda = 0.0214$ m), but its a tapered Gaussian beam, and the surface size is $64\lambda \times 64\lambda$. The sea surface has been generated using a Pierson-Moskovitz spectrum [Pierson and Moskowitz (1964)], with a wind speed of 4 m/s, and a resolution is about 2 mm [Johnson et al. (1998)]. The results have been analysed considering two different lower cutoff wavenumbers for the sea surface generation ($k_{dl} = 0.282$ rad/m, 4.58 rad/m), and a single upper cutoff wavenumber, equal to half the incident wavenumber ($k_u = k_0/2$). The resulting NRCS curves for GO and PO from [Johnson et al. (1998)] are shown in figure 5.23 (a). The polarization of the NRCS illustrated can be either HH or VV, because the results are the same when the scattering occurs from a PEC. Figure 5.23 (b) shows the NRCS curves, averaged over 10 realizations, calculated for FA, where we have tried to match all the parameters to those in [Johnson et al. (1998)]. The only exceptions are the incidence wave, which we have left as a simple spherical wave, and the sea surface spectrum, where we have still used the Elfouhaily one. Furthermore, the number of realizations was set

(a)

(b)
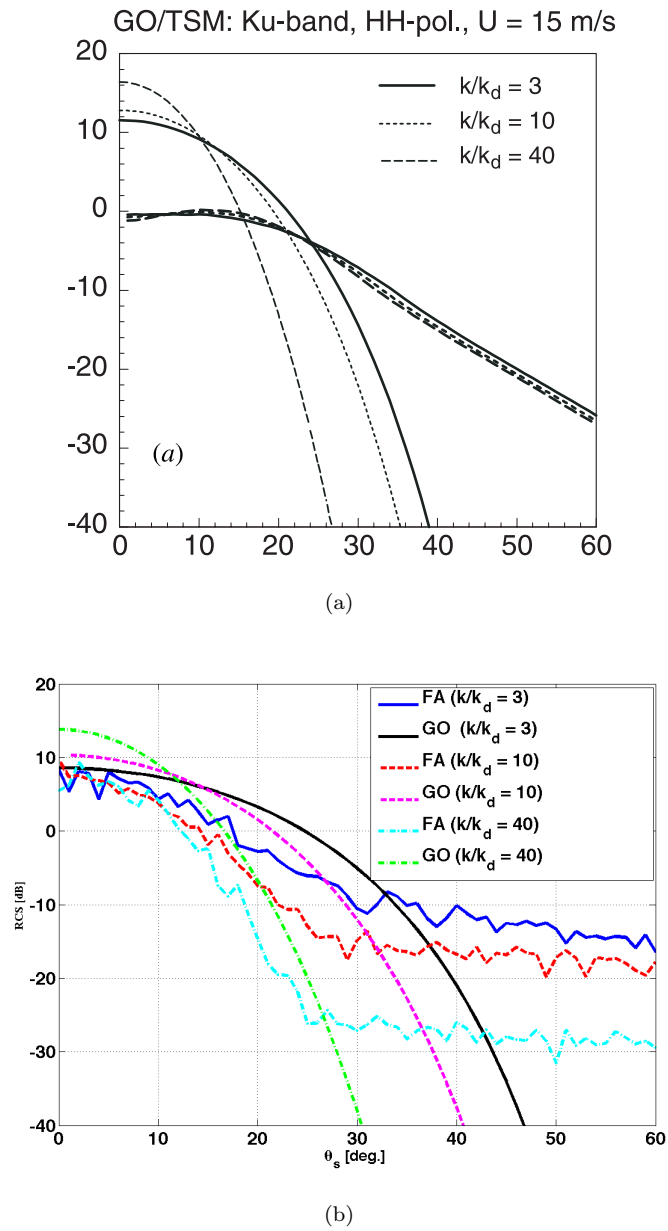
FIGURE 5.22: (a) GO- and TSM-NRCS from [Voronovich and Zavorotny (2001)] for HH polarization versus angle, for three different cutoff wavenumbers. (b) NRCS results from FA and GO, where the MSS used to calculate the GO curves are derived from integration of the Elfouhaily slope spectrum, up to the cutoff wavenumber relative to the curve.

to 64 in Johnsons simulations, while in our case we have once again kept it low enough to reduce computational costs, and to smooth out the NRCS curves in a sufficient way to be able to look at their general trend. The size of the facet has been chosen equal to 0.1 m, as in the previous case, because the incidence wave is still in Ku band. Figure 5.23 (b) also shows the NRCS curves calculated for GO, and we notice once again a slight discrepancy with those shown in figure 5.23 (a). The discrepancy here is likely to be linked to the different types of spectra (Pierson-Moskovitz vs Elfouhaily) used to generate the sea surface, and to calculate the MSS. From figures 5.23 (a) and (b) we notice that the FA curves exhibit an overall reasonable agreement with PO curves, and they are closer to PO behaviour than GO, as expected. The FA curves drop more slowly compared to GO, but also to PO, and they are lower than GO for angles close to nadir. Finally, we note that FA is more sensitive to different lower cutoff wavenumbers, compared to the other two scattering models.

5.9 Conclusions and Summary

In this chapter, we have presented a method to simulate sea surfaces from a given (Elfouhaily) wind wave surface spectrum, and we have illustrated Elfouhaily surfaces with and without a superimposed swell, and JONSWAP surfaces with different directionalities. The scattering from such surfaces was computed in the spatial domain through the FA, illustrated in chapter 4. The FA scattering results have been validated against the full Kirchhoff integral and the GO. The FA method has shown a comparable accuracy with respect to the full Kirchhoff integral, and much lower computational costs. A comparison with GO shows instead that FA is more sensitive to polarization, and allows to produce both instantaneous results from single sea surface snapshots, and average results from a number of realizations. We have shown that the FA proves a versatile tool to investigate the relation between the forward scattering and the ocean wave field, here through 2D maps of the scattered power fields, and 1D plots of scattered power for different scattering angles. Results computed in this chapter are all in the space domain, and they show on the whole that the scattering simulator works well, and delivers results consistent with the structure of the sea surface and its waves, and with

(a)

(b)
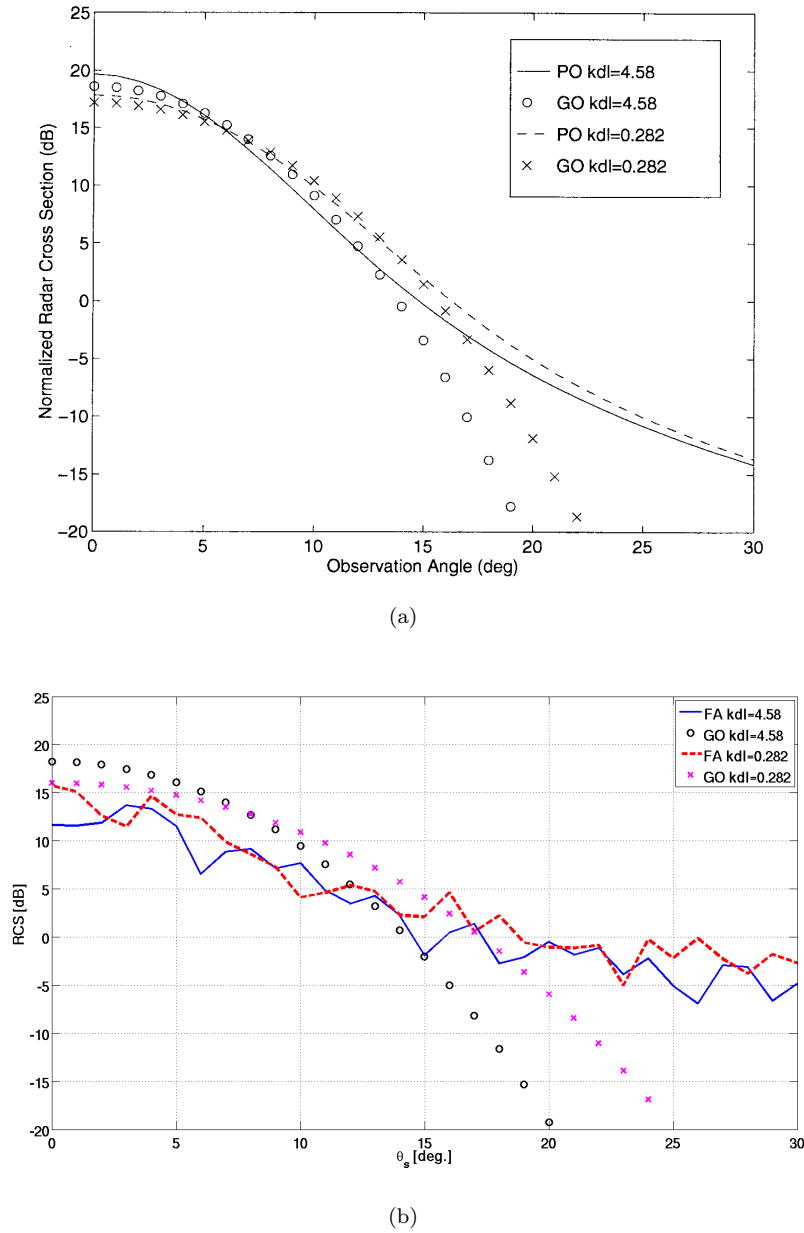
FIGURE 5.23: (a) GO- and PO-NRCS from [Johnson et al. (1998)] for HH polarization versus angle, for two different lower cutoff wavenumbers, and a single upper cutoff wavenumber. (b) NRCS results from FA and GO, where the MSS used to calculate the GO curves are derived from integration of the Elfouhaily slope spectrum [Elfouhaily et al. (1997)], where the integration range is given by the cutoff wavenumbers specified.

changing sea state parameters of the sea surface. They also show that such simulator is very flexible and versatile, as it can be successfully used to describe a variety of radar scattering processes. Different radar configurations (monostatic, bistatic), and different incident wavelengths can be adopted, as long as the facet size is carefully recalculated based on the new parameters. The instantaneous maps of NRCS and PR show clear correspondence between the distribution of the scattering and the underlying wave field. Spatial maps of the PR also exhibit patterns strikingly similar to the underlying wave field, and in particular to the map of slopes. The similarity between NRCS/PR maps and the underlying surface is even more pronounced when the surfaces are characterized by steeper waves, and higher directionality (JONSWAP surfaces). 1D Plots of NRCS for Elfouhaily-based surfaces show a trend dependent upon the roughness of the wave field. As the surfaces become more and more directional (JONSWAP surfaces), the NRCS starts to be affected not only by the roughness (sum of MSS), but also by the directionality of the waves (ratio of MSS). In particular, a change in the direction of the waves becomes more and more detectable in the NRCS plots as the directionality of the surface increases. The average PR curves show an overall little sensitivity to changing sea state in general, except in some cases, for scattering directions far away from the specular direction, where the validity of the FA and of the KA in general is questionable.

CHAPTER 6

The effect of Sea State on Delay-Doppler Maps

6.1 Introduction

In this chapter, we investigate the results of the FA-simulator in the delay-Doppler domain, which is the domain where GNSS reflections are actually mapped. We analyse delay-Doppler Maps (DDMs), generated using different Delay-Doppler (DD) resolutions, and how they respond to various sea state parameters. Our main aim here is to produce a baseline characterization of the influence of different sea states on DDMs, in a linear surface regime. After a brief illustration of the impact of the WAF on DDMs, we present the sea-state analysis on DDMs where the WAF is not applied. The main reason for this is the difficulty to retrieve sea state parameters from instantaneous DDMs when the WAF is applied. Moreover, this represents a convenient choice, in line with our aim, as it allows to isolate the effects related to the sea conditions on the scattering in DD domain, and remove any extra effect in the DDM (i.e. noise, ambiguity function), related to the signal itself, or the processing. The sea-state sensitivity analysis is first carried out on DDMs generated at a coarser DD resolution, but representing the scattering from the

133

entire glistening zone. After that, we examine high resolution DDMs, that is subsets of a DDM, representing the scattering from only small subareas of the glistening zone, located in different position in space, but mapped in delay-Doppler domain at much finer resolution than that adopted so far. We will highlight how an improved delay-Doppler resolution in the DDM can lead to much better capability to extract properties of the sea surface from DDMs, and potentially become a tool for a 1D or 2D imaging of the sea surface.

6.2 Delay-Doppler Maps for Realistic Glistening Zones

In this section, we present DDMs, simulated for large, realistic Glistening Zones (GZ). The sea surface is now a large area of 100 km by 100 km, which is comparable to the size of a typical glistening zone in a spaceborne GNSS-R configuration. The sea surface has been generated using a resolution of 0.2 m, a cutoff wavelength of 1 m, and a wind speed of 10 m/s. An explicit simulation of such a large surface with the given resolution would inevitably impose some computational and memory limitations. Therefore, we have used the assumption of spatial stationarity of the sea surface, meaning that the statistical properties of the surface heights (and slopes) are invariant in space. This allows to simulate a large sea surface by replicating a single, much smaller sea surface patch. Such a technique provides a sea surface sufficiently close to reality, provided that a sufficient number of cycles of the dominant ocean wavelength is included in the small surface patch, in order to make them statistically representative of the random process we are simulating. The DDMs calculated and illustrated in this section refer therefore to roughly 100 km x 100 km glistening zones, generated by replicating smaller sea surface square patches, usually 0.5 km up to 1 km of side. The dominant ocean wavelengths for the sea surface considered for this analysis are not larger than 110 m. The scattering has been calculated using facets of 1 m by 1 m, and the complex scattered fields from each facet have been coherently accumulated in DD domain, taking into account the phase with which each facet scatters. Following the same mathematical steps as for the Z-V model illustrated in [Clarizia et al. (2009b)] and in chapter 3, the Woodward Ambiguity Function of pseudorandom GPS sequences has been applied to each DD pixel

of scattered field to simulate the effect of the real GPS-R receiver matched filter. The squared absolute value for each DD cell has then been computed to finally produce the DDM. Before looking at the details of the results, it is worth explaining how the GPS-R receiver is actually implemented in our simulator, and specifying what type of geometry is assumed for the simulations.

6.2.1 DDM Generation

A rigorous way to implement the GPS-R receiver would be to first produce the total scattered signal as the sum of the signals scattered from all the facets on the glistening zone. The signal scattered from a single facet can be in turn expressed as the incident GPS signal, attenuated and shifted in delay and Doppler frequency, where the attenuation is given by the complex scattered electric field from each facet, and the delay and Doppler shifts are different across the facets. At this point, a numerical 2D (delay-Doppler) cross-correlation with a virtual replica of the transmitted signal should be performed in order to obtain the scattered signal as a function of the delay and Doppler frequency. This is not difficult to implement numerically, and it can be made much faster if the 2D cross-correlation in time domain is instead performed in the frequency domain, since a 2D correlation would become the product between the FFT of the scattered signal and the replica. However, there exists another more efficient way to do this, which was originally described in [Gleason (2006)] and was used to produce the Z-V based DDMs shown in chapter 3. This exploits the approximation of the WAF of pseudo-random C/A codes through a triangular function multiplied by a sinc function, as shown in equation (3.7) of chapter 3. Therefore, once the delay and Doppler range and resolution have been chosen, one can simply map the power scattered from each facet in the delay-Doppler domain, and subsequently apply the WAF to this ideal DDM. The first step is to coherently accumulate in each DD cell the complex scattering contributions from the facets whose associated delay and Doppler frequency corresponds to that cell. The DDM obtained from this operation is an ideal DDM, namely it is the DDM one would obtain had the WAF been a simple delta function. After this, one needs to apply the WAF, so that the value at a given delay-Doppler cell becomes the sum of the value at

that cell, plus those in the adjacent cells, weighted by the product of the triangular and sinc function value in that cell. This DD-mapping plus WAF method produces a final DDM very similar to the one obtained from the full 2D cross-correlation, with negligible differences between the two. This mainly relies on the fact that the C/A code WAF can be approximated through a closed-form function, and this approximation has been demonstrated to be accurate enough [Zavorotny and Voronovich (2000)]. Notably, this method is much faster than the 2D cross-correlation. In the DD-mapping plus WAF technique, we associate a single WAF value for each DD cell, and therefore we implicitly assume that the DD cell is not too large, or the DD resolution is not too coarse. Indeed, a DDM with a coarser resolution can have values of the WAF changing significantly within the single DD cell, up to the point that the association of a single WAF value for a given cell can no longer be considered acceptable. In that case, it would be more suitable to produce a DDM with a resolution fine enough to allow for the assumption of single WAF value within a DD cell, and then degrade the resolution by coherently merging neighbouring DD cells.

6.2.2 Geometrical Configuration

In order to make it easier to analyse the DDM sensitivity to sea state, we keep the transmitter-receiver geometry as simple as possible, and unchanged for all simulations. The transmitter and receiver are located in the $x-z$ plane. Their altitudes are still those typical of a spaceborne GNSS-R configuration, assuming the receiver to be at the same altitude of the UK-DMC satellite (~ 680 km). The transmitter and receiver velocity are also those of a GPS (~ 3.6 km/s) and UK-DMC satellite (~ 7.8 km/s), but the velocity vectors have no y-component. This produces iso-Doppler lines parallel to the y-axis, on the $x-y$ plane. The described geometrical configuration is shown in figure 6.1.

6.2.3 FA-DDM vs Z-V DDM

Figure 6.2(a) shows an example of a noise-free single-look DDM of scattered power simulated using the FA, from a single sea surface realization. The DDM is computed using the DD-mapping plus WAF method, for a Doppler and delay resolution of 50 Hz
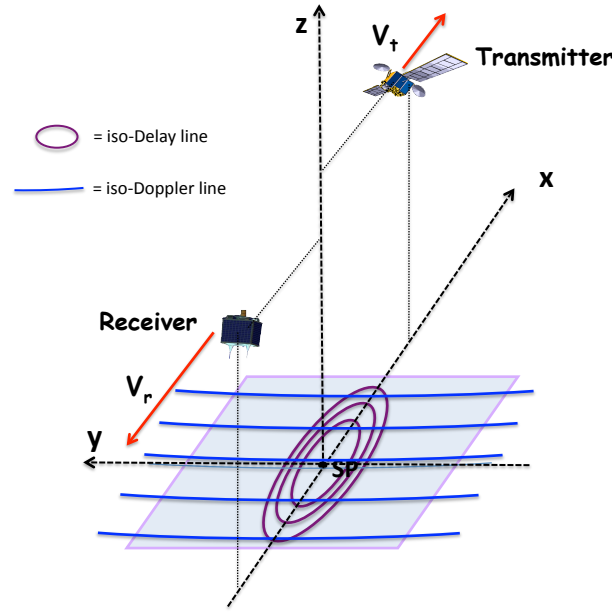
FIGURE 6.1: An illustration of the approach to generate a realization of a sea surface.

and 0.1 chip respectively. A DDM of the scattered power computed from the Z-V model is shown in Fig. 6.2(b) for the same sea state [from Clarizia et al. (2012)]. The two components of the MSS needed to compute the Z-V DDM were obtained by integration of an [Elfouhaily et al. (1997)] surface wave spectrum for a 10 m/s wind speed, up to the cutoff wavelength of 1 m. These are the same wind speed and cutoff wavelength used to generate the explicit sea surface realization for the FA DDM. Although both the FA and the Z-V DDM correspond to the same sea state conditions, they are of course not exact equivalents, since the Z-V DDM corresponds to a statistical average of the scattered power over an infinite number of looks, whereas the FA-DDM represents the distribution of power from a single deterministic sea surface realization. Accordingly, while the FA DDM exhibits the same overall horseshoe shape as Z-V, it also presents a more patchy structure than Z-V.

Figure 6.2(a) still shows the typical overall power distribution of a DDM, mostly along the horseshoe shape, with a peak of the scattered at or around the SP, and a power drop-off along the branches of the horseshoe shape. However, there are some considerable differences with respect to the classical (Z-V) DDM of figure 6.2(b). First, the overall amplitudes of the two maps are not the same, which is still reasonable, given that the
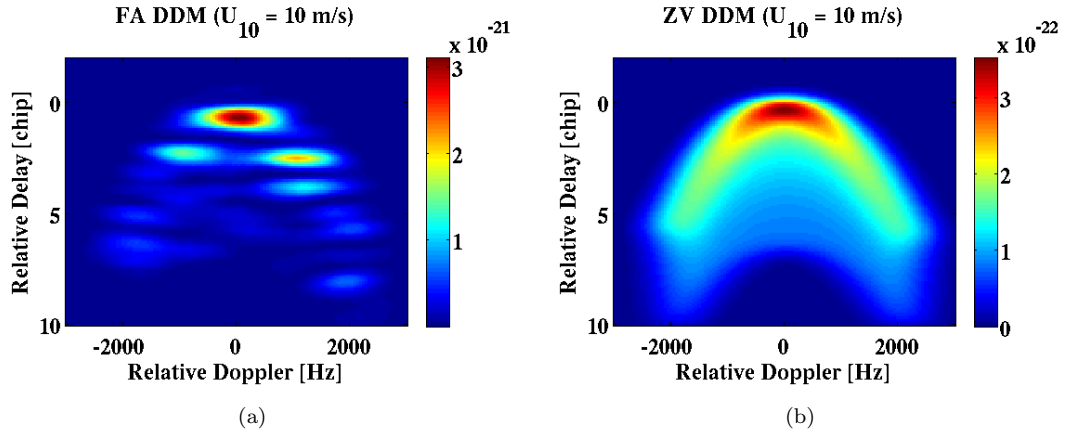
FIGURE 6.2: DDM computed using FA and 1 m^2 facets, and (b) DDM computed using the Z-V model, both for Elfouhaily ocean wave spectrum and $U_{10} = 10$ m/s.

FA DDM is an instantaneous map with fluctuating values, while the Z-V DDM is the result of an average formulation. Second, the power structure between the two DDMs is different, as the FA-DDM exhibits a patchy structure, while that in the Z-V model is more continuous and uniform. We have found that the patches in the FA-DDM occur in different positions in the DD domain for different instantaneous sea surface realizations (see figure 6.3 (b) in the next paragraph), and for different sea states. This would at a first instance suggest an influence on the scattering of the particular features of the sea surface realization. However, we will show in the next section that such effect is purely due to the random phase that characterizes each DD cell, and in particular to the WAF applied to the complex-valued DDM.

6.3 The Effect of WAF on simulated DDMs

In this section, we investigate more closely the effect of WAF on the DDMs, and how heavy its impact is on the final structure of DDM. We show in particular that the WAF is mainly responsible for the patchy structure of the DDM, shown in figure 6.2, and its effect heavily compromises the capability to retrieve sea state parameters from DDMs obtained from instantaneous sea surface realizations. First, it is useful to decompose the DDM, to show clearly the effect of the WAF. Figure 6.3 shows the magnitude (a) and phase (b) of the DDM originally obtained through a simple delay-Doppler mapping of the scattered power. This DDM already contains in each DD cell a constructive/destructive

phase interference effect, due to the coherent summation of the scattering from all the facets within each cell. Figures 6.3 (c) and (d) show respectively the magnitude and phase of the final DDM, where the WAF has been applied to the original complex-valued map illustrated in 6.3 (a)-(b). This highlights that the net effect of the WAF is to generate patches across the DDMs, through a coherent combination of the values of neighbouring cells. Although they tend to occur in different locations of the DD space, we notice that these patches have an horizontal, quasi-periodic structure. This is due to the phase structure shown in figure 6.3 (b), which fluctuates but is characterized by bands of approximately constant mean value along the delays. This is expected, as the phase term is given by the scattering path length, which fluctuates through the surface height variations around a mean value that is the same for a given delay (the path length for a flat surface is the same along iso-delay lines). Furthermore, the patches in the DDMs in figure 6.2 (a) and 6.3 (b) are about 1 chip wide in delay, and 1 KHz wide in Doppler, thus reflecting the width of the WAF along the delay and Doppler. Figure 6.3 highlights another very important effect: some of the strong patchy returns appearing in the final DDM in figure 6.3 (c) do not actually correspond to regions where there is high scattered power in the original DDM in figure 6.3 (a), or viceversa.

This might seem somewhat surprising, but it is not, if the effect of the phase is taken into account. The return in a given DD cell in 6.3 (c) is created as the weighted combination of the complex values from that cell and the adjacent cells, with the weights given by the WAF. This does not correspond to only combining the absolute values of the adjacent cells as seen in figure 6.3 (a), but the absolute values multiplied by a phasor, whose exponent is essentially shown in 6.3 (b). When the contribution of the cells are combined together, this causes some constructive/destructive interference, which is determined by the phase of the cells combined, and ultimately lead to a final DDM which can be equally similar or different from the original one. This leads to the conclusion that the patches we see in the DDM are generated by the WAF, and their value and locations across the DD domain are simply the result of interference between the random phases of DD cells, and do not carry any relevant information about the sea state. Conversely, these patches tend to obscure the effect of different sea surface conditions in the DDM, making an analysis of DDM sensitivity to sea state based on individual realizations
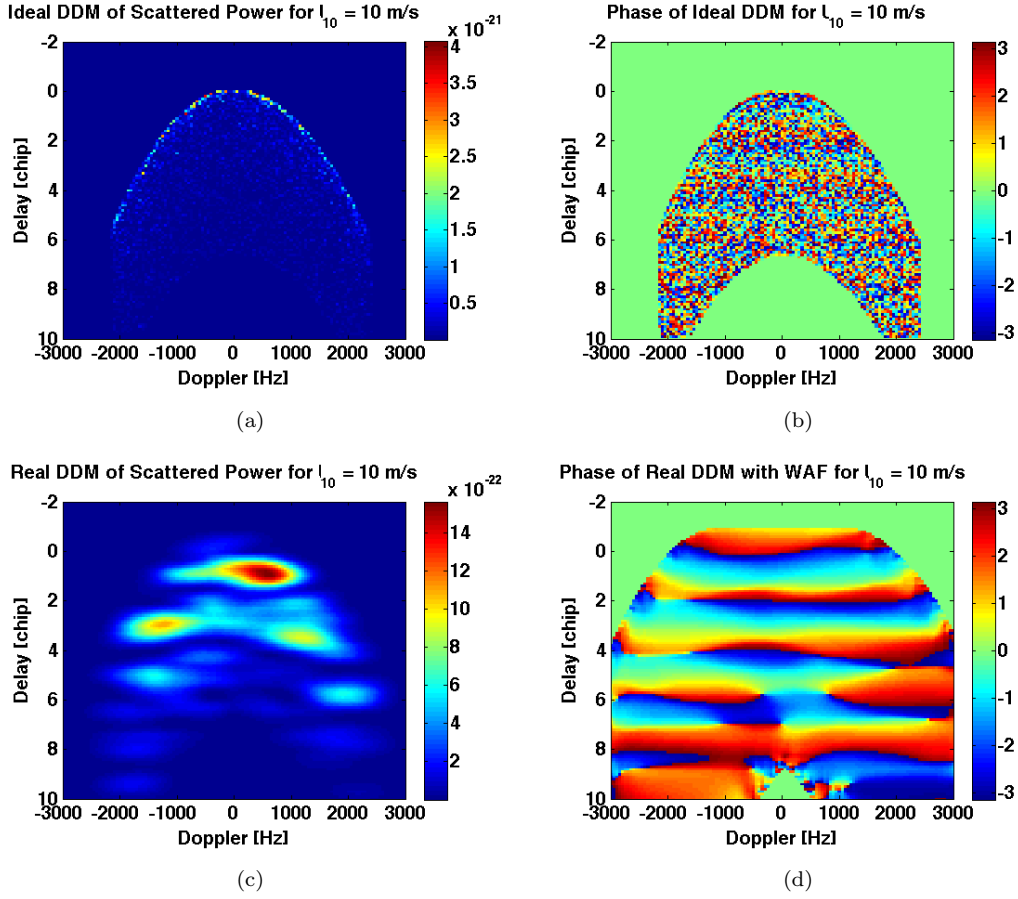
FIGURE 6.3: (a) Scattered power from original DDM (w/o WAF); (b) Phase map of original DDM (w/o WAF); (c) scattered power from real DDM (WAF applied); (d) phase map of real DDM (WAF applied). The delay and Doppler frequency values are expressed relative to those at the SP.

quite challenging. For this reason, we have decided to present the results of the sea state sensitivity analysis applied to the original DDMs, obtained prior to the application of WAF. These DDMs can be considered ideal, because they would be obtained if an ideal delta-function WAF is considered. In this sense, the analysis we illustrate in the next sections can be considered as a general baseline investigation and characterization of the influence of different sea states on the scattering purely mapped in a delay-Doppler domain, with no additional (signal-related or processing-related) effects included, that would alter or degrade the DDM.

6.4 FA-DDM Sensitivity to Sea Surface Conditions

In this paragraph, we present an analysis of noise-free WAF-free DDMs, for different sea surfaces. Following the approach adopted in chapter 5, we first analyse DDM variability with respect to varying roughness on the surface, and then we focus on the effect of different directionality and direction of the waves. For a clearer reading and interpretation of the results, the DDMs, from which several functions and values are also derived, are here presented and analysed as maps of scattered signal (or magnitude), rather then maps of scattered power.

6.4.1 Sensitivity to sea surface roughness

Here we investigate the variability of DDMs with respect to different roughness conditions. The surfaces we consider for this analysis are the same as those shown in chapter 5, that is wave surfaces simulated using the Elfouhaily wind wave spectrum [Elfouhaily et al. (1997)], with and without a swell component of different wavelengths, and the JONSWAP [Hasselmann et al. (1973)] surface spectrum. We recall that both roughness and directionality parameters for these surfaces have been illustrated in table 5.1 in chapter 5. Figure 6.4 shows the DDM of signal scattered from each of these surfaces.

Figure 6.4 highlights some progressive changes of the Elfouhaily-based DDMs. The low-roughness low-wind speed case at the top left of figure 6.4 shows a DDM with a stronger signal around the SP, and a considerable amount of scattering along the horseshoe shape, as well as for those DD cells in the vicinity of the horseshoe shape. As the roughness increases (higher wind speed, presence of a swell), the amount of scattered signal decreases, until reaching very low levels (mixed sea surface with a swell of 50 m/s). The characteristics of DDMs change radically when we move from Elfouhaily surfaces to JONSWAP surfaces. For JONSWAP cases, the DDMs are on the whole characterized by a much stronger scattered signal along the horseshoe shape, and at the specular point. The high scattered signal along the horseshoe shape is expected to be caused by the very low y-slopes that characterizes these surfaces. The DD cells along the horseshoe shape of the DDM correspond to points in space where a very small y-slope
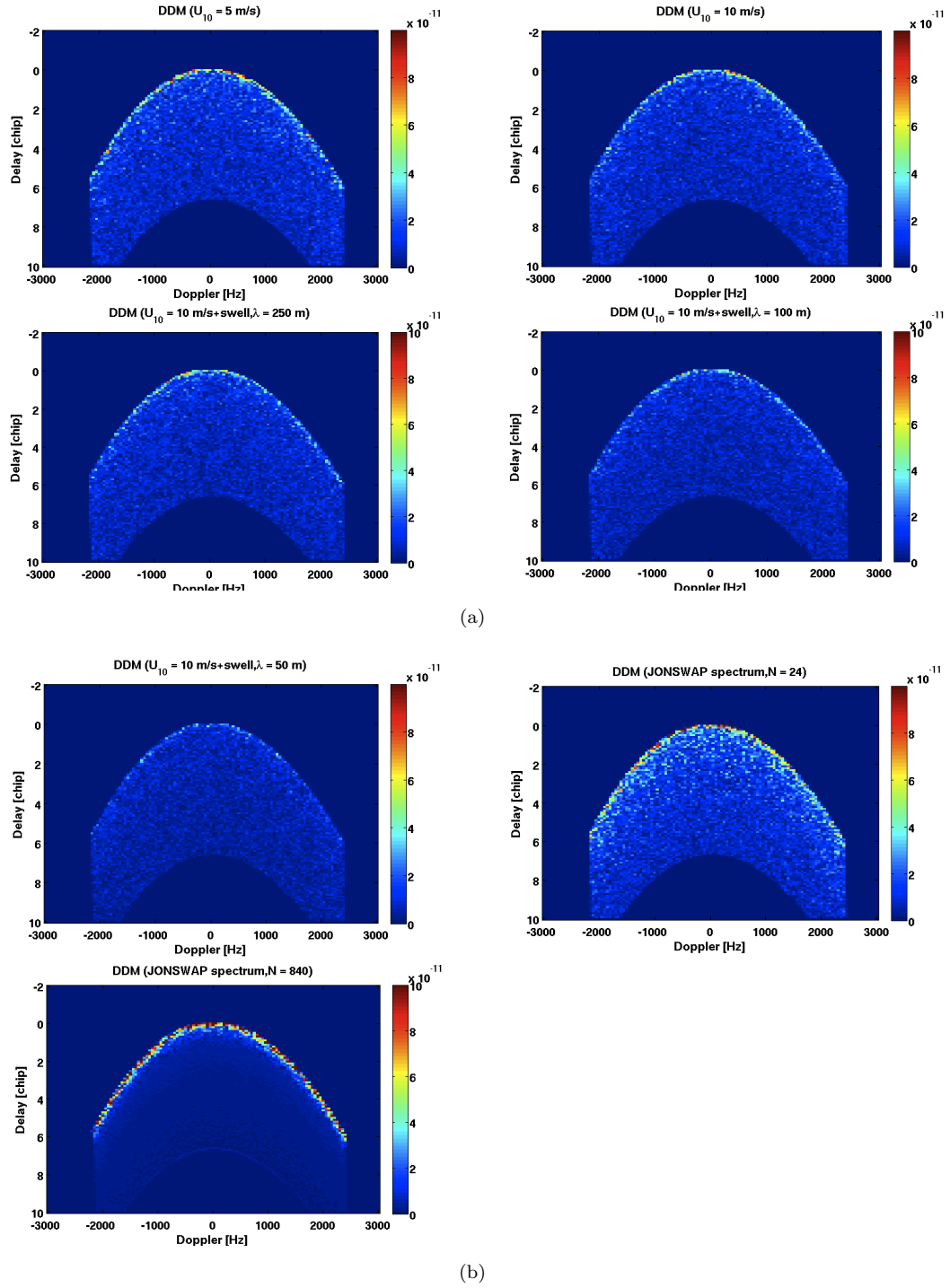
FIGURE 6.4: DDMs of scattered signals, for Elfouhaily wind wave surfaces at different wind speeds (5 m/s and 10 m/s), composite surfaces of 10 m/s wind speed with a swell component of varying wavelength (250 m, 100 m and 50 m), and JONSWAP surfaces with different directionality (N=24 and N=840). All the waves travel here in a 0° direction.

(approaching zero) is required to scatter the incident signal towards the receiver, and this condition is met in this case. This would be also confirmed by the fact that the highest scattered signal along the horseshoe shape is found for the case of N=840 (bottom left of figure 6.4), characterized by the lowest y-slopes among all the surfaces. Another interesting aspect is linked to the scattering in the vicinity or inside the horseshoe shape for JONSWAP surfaces. Notably, the scattering is quite high for these two DD locations for the case of N=24, even higher than the Elfouhaily cases, while the scattered signals disappears completely for DD locations other than the horseshoe shape, when the sea is very directional, and becomes almost a pure swell (N=840). Given that the JONSWAP surfaces have MSS along x comparable to some of the Elfouhaily surfaces, these effects must be once again a consequence of the very low MSS along y. However, the JONSWAP DDM of N=24 exhibits an the overall stronger scattering behaviour in the vicinity of the horseshoe shape, compared to all the other cases. The reason behind such scattering pattern is not completely understood. In order to analyse in deeper details the variability of these DDMs along the delay and Doppler axis separately, we also investigate delay waveforms at 0 Hz Doppler, and integrated delay and Doppler waveforms. The delay waveforms at 0 Hz Doppler, already mentioned in chapter 2, represent the central DDM column, and they describe the scattered signal as a function of the delay only, at zero Doppler. The analysis of these delay waveforms remains useful, particularly because they have been used as a tool to investigate the GPS scattering variations with respect to different surface roughness in a number of studies [Garrison et al. (1998),Zavorotny and Voronovich (2000), Garrison et al. (2002), Cardellach et al. (2003), Komjathy et al. (2004), Gleason et al. (2005), Thompson et al. (2005)], before recognizing more recently that the full DDM delivers much more information [Germain et al. (2004)]. The integrated delay and Doppler waveforms are obtained respectively through integration of the DDMs shown in figure 6.4 along the delay (summation of all the rows) and along the Doppler (summation of all the columns). From a spatial point of view, the integrated delay waveform for a given delay expresses the integrated power scattered from an annulus on the GZ corresponding to that delay. The integrated Doppler waveforms express instead for each Doppler value the signal scattered from the whole Doppler bin. Given that the Doppler bins are in our case parallel to the y-axis,

moving across the Doppler bins corresponds essentially to a change in the scattering angle. In this sense, they are related to the NRCS curves shown in chapter 5, and they exhibit a similar behaviour to that of the NRCS for varying sea state. However, the fundamental difference with the NRCS curves is that the scattering here refers to a much wider surface (the glistening zone), whereas the NRCS were computed from a single sea surface patch. Figures 6.5 to 6.7 illustrate respectively the delay waveforms at zero Doppler, the integrated delay waveforms and the integrated Doppler waveforms for varying sea surface roughness, calculated from the DDMs shown in figure 6.4.
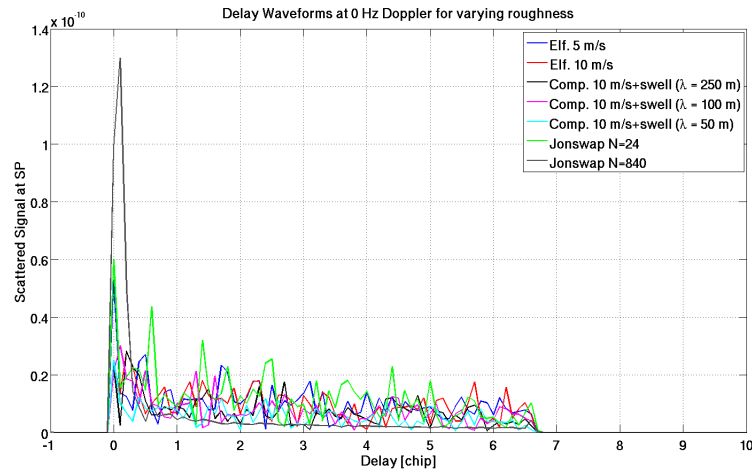
FIGURE 6.5: Delay waveforms at zero Hz Doppler, for different types of surfaces, characterized by different roughness.
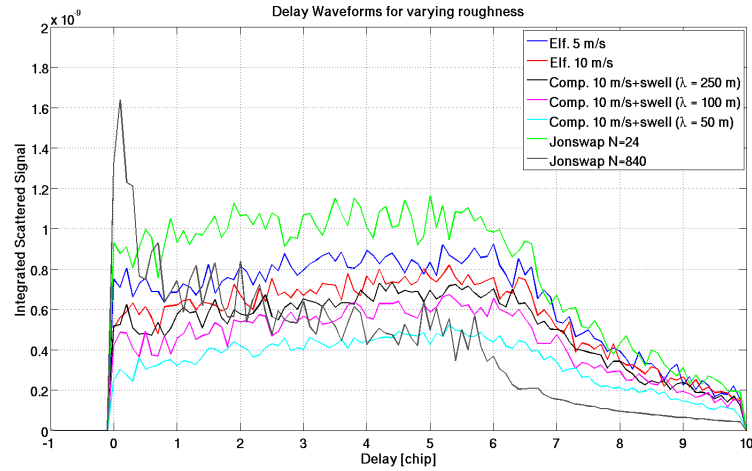
FIGURE 6.6: Delay waveforms integrated incoherently (through summation of the amplitudes) along the Doppler axis, for different types of surfaces, characterized by different roughness.

Delay waveforms in figure 6.5 are not clearly distinguishable from each other, except for
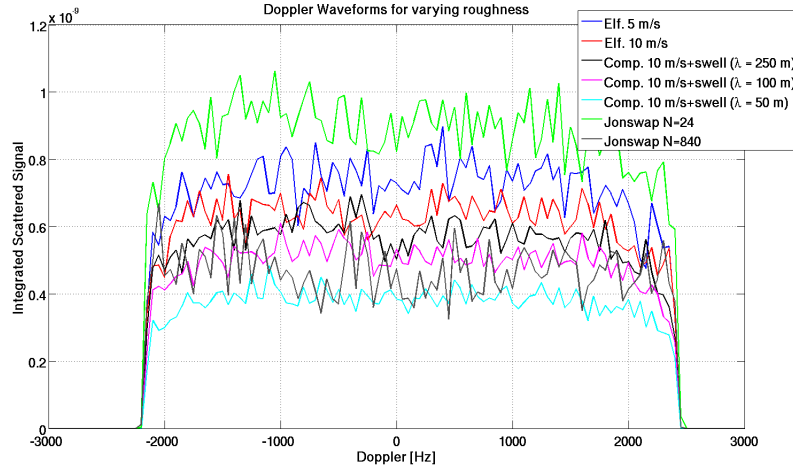
FIGURE 6.7: Doppler waveforms integrated incoherently (through summation of the amplitudes) along the Delay axis, for different types of surfaces, characterized by different roughness.

the very peaky case of JONSWAP $N=840$, where the trailing edge of the waveform is also considerably smoother than the other waveforms, expressing a very high scattered signal at the SP and a rapid signal drop-off away from the SP. More interesting results are indeed given by the integrated delay waveforms in figure 6.6, where a decreasing general trend of the waveforms can be noticed for Elfouhaily surfaces with increasing roughness. This trend is consistent with what has been shown for NRCS curves in figure 5.19 of chapter 5, too. The fact that the waveforms for JONSWAP surfaces do not follow such trend in roughness is probably due to their y-slopes and directionality being extremely different from the Elfouhaily surfaces. The waveform for JONSWAP $N=840$ is characterized by a sharper and more pronounced peak compared to all the other cases, and a more rapid decay for increasing delays, confirming a strong specular return, and very low power outside the horseshoe shape. As for the corresponding DDM, the reason why the integrated delay waveform for JONSWAP case of $N=24$ is the highest among all seems unclear. The integrated Doppler waveforms in figure 6.7 also show a progressive decrease of values, and even a decrease in the variability of the oscillations with increasing roughness of Elfouhaily surfaces, thus being fully consistent with NRCS plots of chapter 5. Once again, the waveform for the JONSWAP case of $N=24$ is the highest one, while the lowest one in this case is given by the mixed sea surface case with a swell of small wavelength (50 m). The result shown in figures 6.5-6.7 suggest therefore that the general scattering trend of surfaces based on the Elfouhaily spectrum,

already shown through NRCS in chapter 5, is maintained also in DD domain, while
the JONSWAP surfaces seem to belong to a different category, that does not follow
the behaviour outlined for the Elfouhaily surfaces. A final attempt to summarize the
results of DDMs of scattered signal with respect to varying roughness of the underlying
scattering surface is shown in figure 6.8. The median and MAD have been preferred
over the mean and standard deviations, because they are statistically more robust with
respect to outliers that we have found in the DDMs.
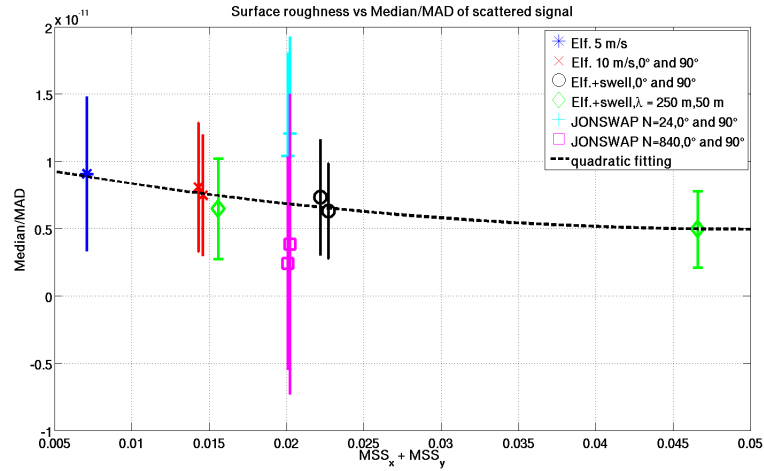
FIGURE 6.8: Median DDM values as symbols, and Median Absolute Deviations (MAD)
as errorbars, versus the total roughness of the values across DDMs of the scattering
from different types of surfaces. A quadratic fitting to the median values is also shown.

Figure 6.8 highlights a decreasing trend of the DDM median with increasing roughness,
for surfaces generated from the Elfouhaily spectrum, consistently with the trends shown
by delay and Doppler waveforms. In this case, it is also interesting to notice that the
variability of the scattered signal across the whole DDM, expressed through the Median
Absolute Deviation (MAD) also seems to decrease with increasing roughness. Such a
decreasing variability was also suggested by the Doppler waveforms shown in figure 6.7.
As expected, the median and MAD for the DDMs from JONSWAP surfaces do not
follow the same trend, and are distant from the quadratic function that fits well the rest
of the data in figure 6.8. This suggests once again that the directionality of the surfaces
(which was not too different among the Elfouhaily surfaces, but instead much higher for
the JONSWAP ones) affects the general dependence of the DDM values with respect to
the roughness of the underlying surfaces. It might be thought for example that there is
not only one, but multiple quadratic functions, parametererized with respect to different

surface directionalities, that describe reasonably well the dependence of the DDM values with respect to the roughness of the sea surface. At this stage, this remains however only an hypothesis, as a much larger number of surfaces and simulations would be needed to either prove or disprove it. Figure 6.8 has been generated through calculations of the median and MAD of the values across the simulated DDM. Recent studies in literature [Marchan-Hernandez et al. (2010)] try to relate similar parameters, like the volume of normalized DDMs from real data, to the roughness of the surface (MSS, SWH), and it is therefore useful to compare these results to what we obtained from FA-simulated DDMs. Figure 6.9 shows on the left the volume of normalized noise-free and WAF-free DDMs, simulated using FA, as a function of the total MSS of our simulated sea surfaces, while the volume of normalized DDMs from real data from [Marchan-Hernandez et al. (2010)] is shown on the right. The values of the DDM volumes inevitably do not match, as the DDMs used in [Marchan-Hernandez et al. (2010)] were much smaller (only 16 x 16 points), computed at a coarser resolution, and only those DDM values exceeding the estimated noise floor were considered for the calculation of the DDM volume. Moreover, the MSSs detected from real measurements in [Marchan-Hernandez et al. (2010)] are larger than those of the surfaces we simulated. Nevertheless, a similar quadratic-like increasing trend can be identified in both cases.
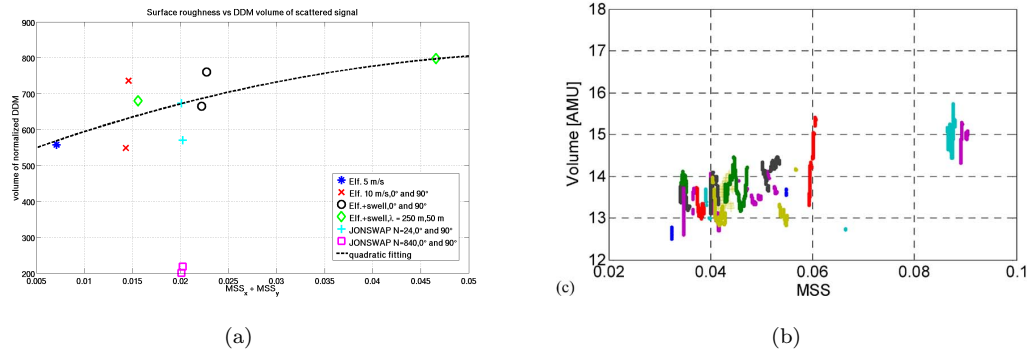
FIGURE 6.9: (left) Volume of Normalized DDMs as a function of total roughness, for the scattering from different simulated sea surfaces. (right) normalized DDM volume calculated from real measurements in [Marchan-Hernandez et al. (2010)].

6.4.2 Sensitivity to sea surface directionality and direction

A DDM analysis analogous to that shown for roughness in 6.4.1 is carried out here for different directionalities, and directions of the waves on the sea surface. Figure 6.10 shows DDMs for different types of sea surfaces, two of which are based on the Elfouhaily sea surface spectrum (Elfouhaily surface of wind speed 10 m/s, and composite surface of 10 m/s wind speed with a superimposed swell), and the other two are based on JONSWAP sea surface spectrum ($N=24$ and $N=840$). For each of these surfaces the DDMs are shown for two different travelling direction of the waves (or swell): those on the left are for waves travelling along the x-axis ($0°$) and those on the right are for waves travelling along the y-axis ($90°$).

For the Elfouhaily-based DDMs on the first and second row from the top of figure 6.10, a change in the wave direction from $0°$ to $90°$ is suggested from the left to the right by a mild decrease of the overall scattered power for points along the horseshoe shape, away from the SP. This was an expected effect, as a change in direction translates into an inversion of the MSS along the $x-$ and $y-$direction, and a more rapid power dropoff is produced along the DDM horseshoe shape when the MSS along x becomes lower. Intuitively, this effect becomes stronger as the difference between the two MSS becomes stronger too, namely as the sea surface becomes more and more directional. It is therefore not surprising that this effect is more visible for the JONSWAP case of $N=24$ (third row from the top of figure 6.10), until reaching its highest strength for the JONSWAP case $N=840$. This last case produces a resulting DDM with a very different signal distribution for the two directions. For the $0°$ direction of the waves, the signal is concentrated all along the horseshoe shape, and it remains considerably strong even for points far away from the SP, while for $90°$ direction of the waves the signal drops off very quickly away from the SP, and along the horseshoe shape, and a large amount of scattered signal accumulates instead in a narrow Doppler band around the 0 Hz Doppler value. This visual DDM analysis already suggests therefore that a change in direction is much more detectable when the directionality of the surface is high, as it was already highlighted for NRCS in chapter 5. As in 6.4.1, we have analysed delay and Doppler

(a)

(b)
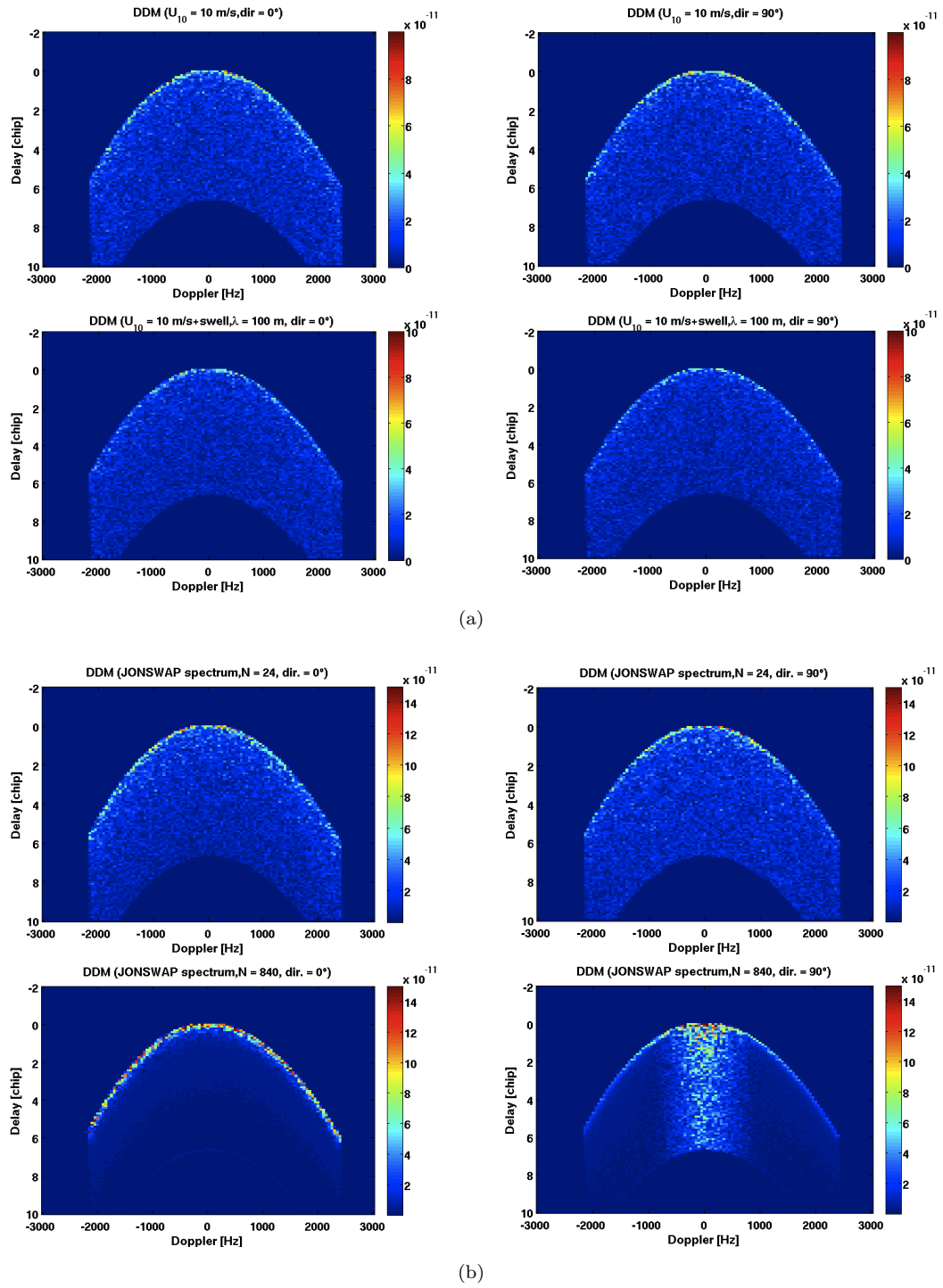
FIGURE 6.10: DDMs of scattered signals, for 10 m/s Elfouhaily wind wave surfaces and different wave direction (first row), composite surfaces of 10 m/s wind speed with a swell component of wavelength 100 m and different swell direction (second row) and JONSWAP surfaces with different directionality (N=24 and N=840) and different wave directions (third and fourth row). The colorscales for Elfouhaily and JONSWAP surfaces are different due to the strong differences in the DDM values.

waveforms for the DDMs shown in figure 6.10. These waveforms are illustrated in figures 6.11-6.13.
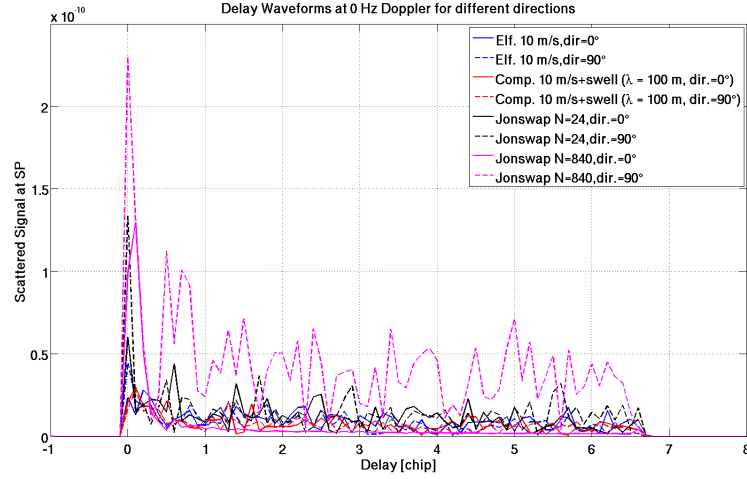
FIGURE 6.11: Delay waveforms at zero Hz Doppler, for different types of surfaces, with different wave directionality and direction.
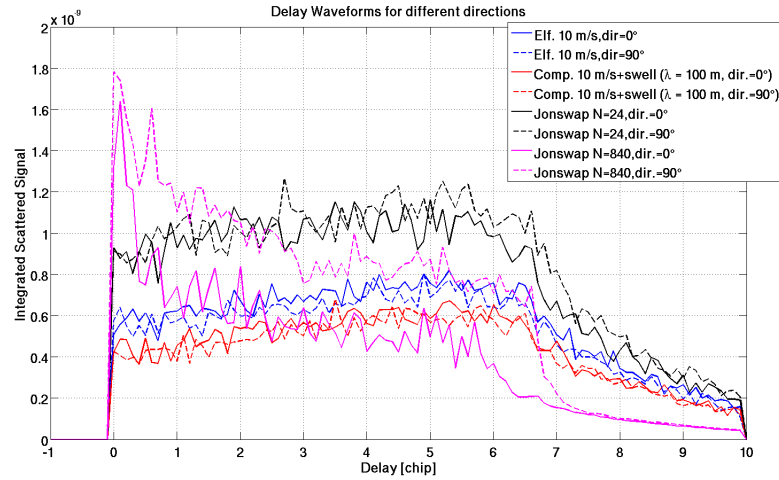
FIGURE 6.12: Delay waveforms integrated incoherently (through summation of the amplitudes) along the Doppler axis, for different types of surfaces, with different wave directionality and direction.

The delay waveforms at 0 Hz Doppler in figure 6.11 are again difficult to distinguish from one another due to their high variability, except for the JONSWAP case of N=840, where the 0° wave direction waveform is characterized by a smooth and well-defined trailing edge, while that for 90° wave direction case exhibits the highest variability among all the trailing edges. The integrated delay waveforms in figure 6.12 for the two wave directions are progressively more and more different from each other as the directionality of the waves increases (from pure Elfouhaily wind wave surfaces, to Elfouhaily surfaces with a
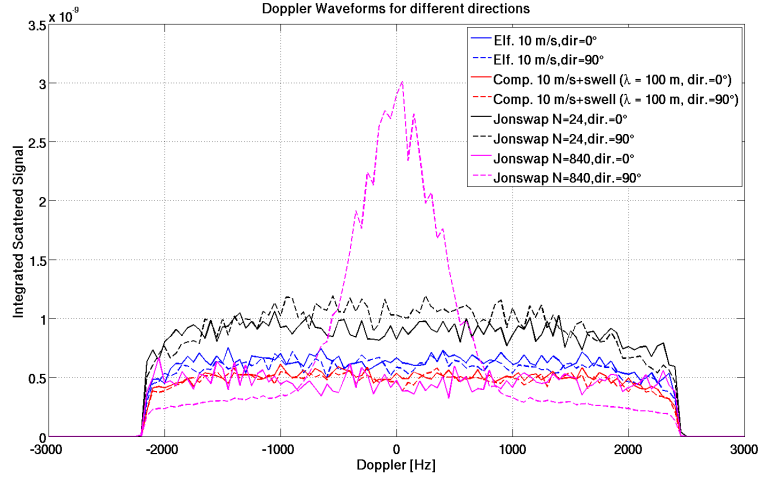
FIGURE 6.13: Doppler waveforms integrated incoherently (through summation of the amplitudes) along the Delay axis, for different types of surfaces, with different wave directionality and direction.

swell component, to JONSWAP surfaces with lower directionality), until they become clearly distinguishable when the directionality is very high. A similar type of trend is shown for the Doppler waveforms in figure 6.13, where the direction becomes clearly detectable for the JONSWAP case of N=840. In this case, an attempt has been made to quantify these changes, and to clearly identify the direction of the waves, through the introduction of a Doppler bandwidth. This has been defined as the Doppler range where a certain percentage of the total scattered signal (the integral of the Doppler waveform) is contained. We have chosen this percentage to be here equal to 80%, simply to include a good amount of the total signal. Table 6.1 shows the Doppler bandwidth calculated for each waveform. The Doppler bandwidth acts as a good indicator of different wave directions, and of course its performance improves for increasing directionality of the waves.

We conclude our analysis with figure 6.15, which shows the DDM Median-MAD variability with respect to different directionality, and direction of the waves. The directionality, defined in chapter 5 as the ratio of the MSS along x and y, is here expressed in logarithmic scale. This is a very handy representation, since an MSS ratio farther from the zero value refers to increasing directionality of the waves, and a positive or negative value of this ratio represents respectively a 0° and 90° wave travelling direction.

In figure 6.14, it is rather difficult to establish a general trend for the median values of

Type of Surface	B_{eff} [Hz]
Elf. 10 m/s, $\phi_{wind} = 0°$	3500
Elf. 10 m/s, $\phi_{wind} = 90°$	3500
Elf. 10 m/s + swell, $\phi_{wind} = \phi_{swell} = 0°$	3500
Elf. 10 m/s + swell, $\phi_{wind} = 0°, \phi_{swell} = 90°$	3400
JON. N=24, $\phi_{wave} = 0°$	3500
JON. N=24, $\phi_{wave} = 90°$	3300
JON. N=840, $\phi_{wave} = 0°$	3600
JON. N=840, $\phi_{wave} = 90°$	2000

TABLE 6.1: Doppler bandwidth (B_{eff}) for different types of surfaces, and different wave directions.
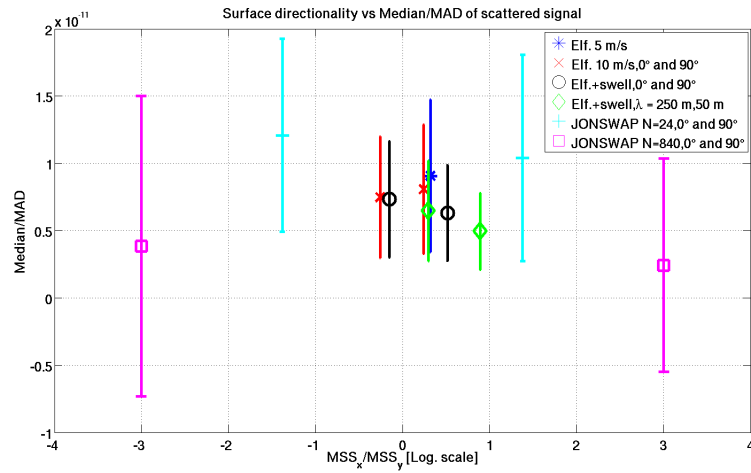
FIGURE 6.14: Median and Median Absolute Deviations (MAD) of the values of DDMs versus the directionality of the surfaces, for different types of surfaces, and different wave directions.

DDMs, and once again the locations of the symbols (median) and errorbars (MAD) of the JONSWAP cases are very different from the Elfouhaily cases. No relevant differences can be noticed with respect to different wave directions. One thing that can be observed is instead an overall increasing variability of the scattered signal across the DDM for increasing sea surface directionality. If we look at the DDMs again for JONSWAP highly directional surfaces in figure 6.10, we notice that the range of scattered values is indeed larger compared to the Elfouhaily cases. The DDMs for the JONSWAP cases are characterized by very bright DD cells, where a high amount of signal is scattered, and also DD cells of very low values, or where almost no signal is scattered.

6.5   FA DDMs at High Resolution

In section 6.4, we have shown and analysed noise-free instantaneous FA-based DDMs from the entire Glistening Zone, using the typical resolution of UK-DMC maps. We have illustrated and discussed the sensitivity of these DDMs to different sea conditions, particularly with respect to different roughness, and wave directionality and direction. The results obtained are indeed interesting and encouraging, particularly so if one considers that the delay-Doppler resolution used in the previous paragraph is quite coarse, as the contributions from large areas of the glistening zone are accumulated all in the same DD cell. Intuitively Such a coarse DD resolution still rules out any possibility to detect in DD domain instantaneous sea surface characteristics, such as dominant wavelength, direction of the waves, or presence of swell, that we have shown instead in spatial maps of scattering in chapter 5. In this paragraph we present therefore a type of analysis that to some extent enables to identify in a DD domain those instantaneous features of the sea surface that are visible in space domain. This analysis takes into consideration subsets of WAF-free delay-Doppler maps, generated at very high resolution, for different sea surfaces. This analysis would ultimately correspond to a pure transformation of the spatial maps of scattering into the DD space. An approach like this has little practical applicability at present, due to the very high resolution required, and the assumptions of no ambiguity among DD cells in the DDM (a delta-WAF). However, it allows us to explore the signature of the explicit features of individual sea surface realizations in

the DDM, highlighting the potential of GNSS-R as a tool for 1D or 2D imaging of the ocean surface. This potential can be indeed translated into a real capability for the near future, if a higher DD resolution can be achieved, and the WAF can be narrowed down. In what follows, we discuss how to choose a high enough DD resolution, based on the spatial sampling requirements, and we will show examples of DDM subsets at high resolution, and for different wind and wave conditions.

6.5.1 Choice of DD resolution

The Delay-Doppler resolution is established by the features on the sea surface that we wish to preserve when going from the space domain to the DD domain. First of all, a suitable sampling step along x and y, that we call dx and dy, should be determined such that the sea surface is adequately sampled. The sampling step is of course derived from the Nyquist criterion, but it should also be chosen based on what features on the sea surface we are interested in. As an example, if we are only interested in the dominant wavelength, then it is sufficient to sample at a rate twice as large as the wavenumber of the peak of the Elfouhaily spectrum, used to generate the sea surface. On the other hand, if we want to adequately sample all the waves on the sea surface, then the sample rate should be chosen based on the spectrum of the surface itself, and be at least twice the cutoff wavenumber of the spectrum. We also know that in practice the factor two of the Nyquist criterion should be increased, in order to obtain a good sampling. Once the sampling steps dx and dy have been chosen, then it is not difficult to numerically calculate the delay sampling step $d\tau$ and the Doppler sampling step df associated with those spatial sampling steps. For this calculation, it is convenient to consider the area of the GZ around the specular point. This is the area where iso-delay lines separated by a given delay are spatially more distant, and where a delay step $d\tau$ corresponds to the maximum spatial distance. Therefore, assuming a spatial stationarity of the waves across the GZ, a $d\tau$ appropriately chosen in the area at and around the SP guarantees an adequate spatial sampling of the waves across the entire GZ. As regards the Doppler resolution, the iso-Doppler lines also experience a distorsion, but for the size of the GZ considered in this study they can be assumed to a good approximation equally spaced,

and parallel to each other. For this calculation, as for all simulations presented in this dissertation, we have kept the geometry of the satellites unchanged, and for simplicity we have set the y-component of the velocity vector of the satellites to be zero, such that the iso-Doppler lines are parallel to the y-axis. We begin the calculation of the optimal DD resolution $d\tau$ and df by first establishing the spatial steps dx and dy with which we want to sample the sea surface. We therefore consider the specular point $SP = [0, 0, z_{sp}]$, and another point $P = [dx, dy, z_p]$ separated from the SP by the sampling steps dx and dy. The z-coordinates of SP and P are two heights of the sea surface, and they are therefore random variables, written as follows:

$$z_{SP} \sim N\left(0, \sigma_h\right) \tag{6.1a}$$

$$z_P \sim N\left(0, \sigma_h\right) \tag{6.1b}$$

Then, the delay sampling step $d\tau$ is simply the difference in delays of these two points, and it can be written as follows:

$$d\tau = \frac{1}{c}\left[\sqrt{\left(x_{tx} - dx\right)^2 + \left(y_{tx} - dy\right)^2 + \left(z_{tx} - z_p\right)^2} + \right. \tag{6.2a}$$

$$+ \sqrt{\left(x_{rx} - dx\right)^2 + \left(y_{rx} - dy\right)^2 + \left(z_{rx} - z_p\right)^2} - \tag{6.2b}$$

$$\left. - \sqrt{x_{tx}^2 + y_{tx}^2 + \left(z_{tx} - z_{sp}\right)^2} - \sqrt{x_{rx}^2 + y_{rx}^2 + \left(z_{rx} - z_{sp}\right)^2} \right. \tag{6.2c}$$

Analogously, the Doppler sampling steps df is the difference in Doppler frequency, and can be written as follows:

$$df = \frac{1}{\lambda}\left[\frac{xv_{tx}\left(x_{tx} - dx\right) + yv_{tx}\left(y_{tx} - dy\right) + zv_{tx}\left(z_{tx} - z_p\right)}{\sqrt{\left(x_{tx} - dx\right)^2 + \left(y_{tx} - dy\right)^2 + \left(z_{tx} - z_p\right)^2}} + \right. \tag{6.3a}$$

$$+ \frac{xv_{rx}\left(x_{rx} - dx\right) + yv_{rx}\left(y_{rx} - dy\right) + zv_{rx}\left(z_{rx} - z_p\right)}{\sqrt{\left(x_{rx} - dx\right)^2 + \left(y_{rx} - dy\right)^2 + \left(z_{rx} - z_p\right)^2}} - \tag{6.3b}$$

$$\left. - \frac{xv_{tx}x_{tx} + yv_{tx}t_{tx} + zv_{tx}\left(z_{tx} - z_{sp}\right)}{\sqrt{x_{tx}^2 + y_{tx}^2 + \left(z_{tx} - z_{sp}\right)^2}} - \frac{xv_{rx}x_{rx} + yv_{rx}y_{rx} + zv_{rx}\left(z_{rx} - z_{sp}\right)}{\sqrt{x_{rx}^2 + y_{rx}^2 + \left(z_{rx} - z_{sp}\right)^2}} \right] \tag{6.3c}$$

where c and λ are respectively the speed of light and the incident GPS wavelength, and the transmitter and receiver have position coordinates $TX = [x_{tx}, y_{tx}, z_{tx}]$, $RX = [x_{rx}, y_{rx}, z_{rx}]$ and velocity coordinates $V_{TX} = [xv_{tx}, yv_{tx}, zv_{tx}]$, $V_{RX} = [xv_{rx}, yv_{rx}, zv_{rx}]$. The general expressions in (6.2) and (6.3) are simplified if we account for the fact that $yv_{tx} = yv_{rx} = 0$. In the examples that follow, our baseline surface will generally by an Elfouhaily sea surface, generated using 10 m/s wind speed. For simplicity, we are interested in capturing the dominant wavelength in DD domain, which for n Elfouhaily surface with a 10 m/s wind speed is about 111 m (the x-wavenumber of the spectrum peak is at 0.0565 rad/m). If we assume that the waves travel along the x-direction, then the more stringent sampling requirement is along x, too. In order to sample this wavelength adequately, we should therefore require a spatial step of dx=10 m, roughly ten times smaller than the dominant wavelength on the surface. Given that we are also investigating seas with changing directions of the waves, we choose dy to be equal to 10 m too. As said, z_{sp} and z_p are random gaussian variables, and the simplest choice would be to use their zero mean in equation (6.2). However, this would produce a $d\tau$ very small, on the order of $4 * 10^{-7}$ chips. Given that the surface fluctuates randomly, causing random fluctuations of $d\tau$ too, we have decided to simulate a large number of occurences of the gaussian variables z_{sp} and z_p, using the standard deviation of a typical Elfouhaily 10 m/s sea surface ($\sigma_h = 0.65$ m), and calculate $d\tau$ for each occurence of z_{sp} and z_p, using dx=10 m and dy=10 m. We have then selected the $10th$ percentile of the ensemble of $d\tau$ obtained from the simulations as the high-resolution delay step, and this is equal to about 0.0005 chips. The choice of such a small percentile might suggest that the final delay step is still too coarse to capture the delay variability at a high-resolution. However, it represents a good trade-off between the need for a high resolution and an attempt to maintain such resolution reasonably realistic. In addition to this, the choice of $d\tau = 0.0005$ chips was supported by empirical tests, which showed an adequate degree of resolution in the DDMs, compared to other values for $d\tau$ like the median or higher percentiles. The Doppler step df was instead simply calculated in the same way, for the same values of dx and dy, using (6.3), although df was not very sensitive to variations of the heights of P and SP. Its value has been chosen equal to 0.5 Hz. This analysis has also highlighted that both $d\tau$ and df are in this case not

strongly affected by dy, the former because the y-coordinates of both transmitter and receiver are zero, and the delay equations in (6.2) are completely dominated by their x- and z-coordinates, and the latter because in this particular case the iso-Doppler lines are more or less parallel to the y-axis, and their configuration is such that they sample the space only along x. It is also worth mentioning that we should in theory change the delay and Doppler resolution when the underlying sea conditions change (for example, a smaller delay/Doppler resolution would be needed for a surface generated at wind speed lower than 10 m/s). However, we have empirically checked that the delay and Doppler resolution chosen remain suitable for all the sea states of the surfaces we use here for the high-resolution analysis, and for simplicity we have therefore decided to use fixed delay and Doppler resolutions for all the high-resolution DDMs. The results we are going to present in this and the next sections will show zoomed portions of DDMs, processed at high resolution (0.0005 chips, and 0.5 Hz), and without accounting for the effect of the WAF. The choice of the high-resolution delay and Doppler step makes the DD cells about 100 times smaller than those of the UK-DMC real DDMs, as well as of the FA-based DDMs simulated so far. Intuitively, the generation of a whole DDM for the entire GZ, at such a high resolution, would imply huge timing and memory costs. Therefore, we have processed at high resolution only three DDM subsets, at three given locations in DD: the first is the area at and around the specular point, where the signal strengh is the highest; the second is along one of the branches on the horseshoe shape, where the signal is still reasonably strong, and the third one is inside the horseshoe shape, where the signal strength is quite low, but the configurations of the delay and Doppler lines is favourable. These three DDM subsets represents our three test cases for the high-resolution analysis. The three DDM subsets analysed at high resolution, and shown in figure 6.15 (a), correspond to specific areas of the GZ in space domain, and these are illustrated in figure 6.15 (b). Note that the last test case, represented by the DDM subset inside the horseshoe shape, corresponds to two different surface subareas in space, highlighted in purple in 6.15 (b). This shows that for that location in DD domain there is a spatial ambiguity, due to the fact that there is a double intersection between iso-Delay and iso-Doppler line. The scattered signal for DD locations inside the DDM horseshoe shape is the results of the merging of signals scattered from two distinctive

surface patches in space.
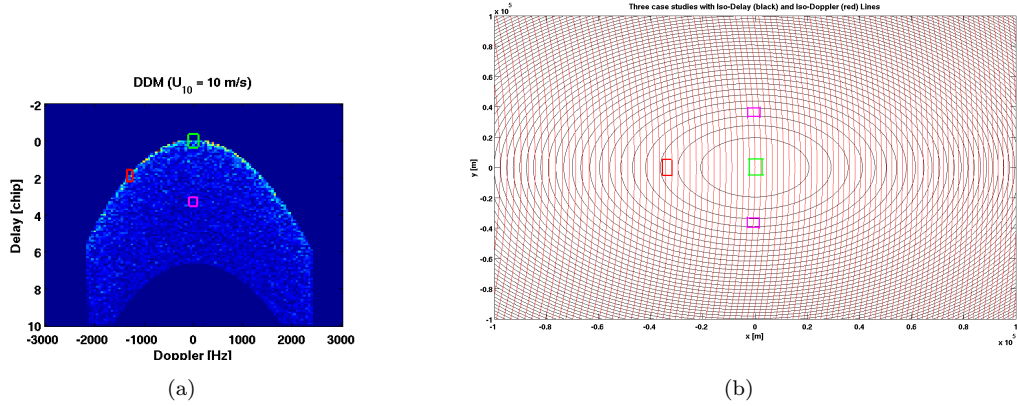
FIGURE 6.15: (a) DDM subsets chosen for high-resolution analysis. (b) 100 km x 100 km Glistening Zone (GZ), with superimposed iso-delay (black, delay step of 1 chip), and iso-Doppler (red, Doppler step of 100 Hz) lines, and the three space locations corresponding to the three DDM subsets (highlighted with the same colour as the corresponding DDM subset).

6.5.2   High-res DDM around the specular point

In this section, we present the results for different sea conditions, and for the first case around the SP, shown in green in figure 6.15. The surfaces we consider here are patches of about 1300 m $\times$ 1300 m, generated with a resolution of 1 m, centered at the specular point. The corresponding DDM subsets are generated for a delay-Doppler range of [-0.025 0.025] chips, and [-35 35] Hz, with delay and Doppler resolutions of 0.0005 chips and 0.5 Hz. Strictly speaking, the entire range of delays and Doppler chosen for the DDM subsets would not only correspond to the sea surface area considered, but to a larger area. However, most of the signal in the DDM subset still comes from the surface considered. Additionally, we can assume that the receiving antenna has a small footprint, and it is only capturing the power coming from the surface chosen for this analysis. A picture of the area considered, along with iso-delay and iso-Doppler lines for the delay-Doppler range chosen is shown in figure 6.16.

As for the full DDM illustrated in paragraph 6.4, here DDM subsets are analysed for Elfouhaily surfaces, with and without a swell component, and for JONSWAP surfaces of different directionality. Figure 6.17 shows Elfouhaily wind wave surfaces on the left column, generated from top to bottom with a 5 m/s wind speed and 0° wind direction,
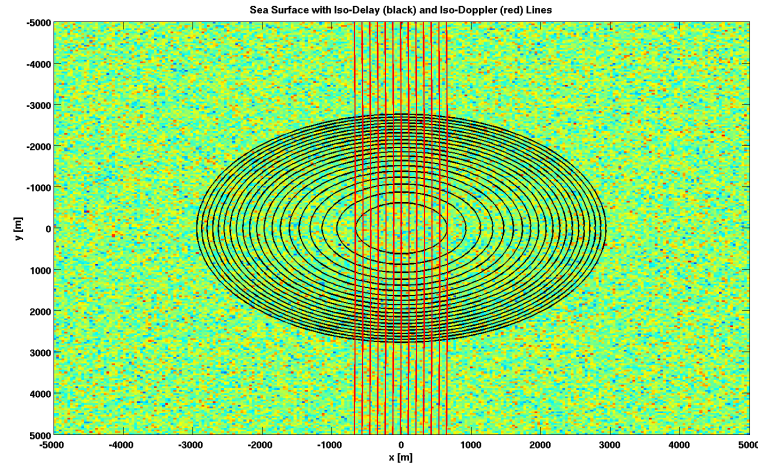
FIGURE 6.16: Illustration of the first test case, given by the area around the SP at the intersection between iso-delay (black) and iso-Doppler (red) lines. For illustration purposes, the iso-delay and iso-Doppler range mapped here are respectively [-0.02, 0.02] chips and [-30, 30] Hz, with a delay step of 0.001 chip and a Doppler step of 5 Hz.

and a 10 m/s wind speed with 0° and 90° wind direction. The corresponding high-resolution DDM are shown on the right column of figure 6.17. The first two rows show results for different wind speeds (5 m/s and 10 m/s) and a 0° wave direction, while the last row shows results for 10 m/s wind speed and 90° wave direction. Even if we are very close to the SP, a horseshoe shape is already visible in the DDMs as a mild curvature.
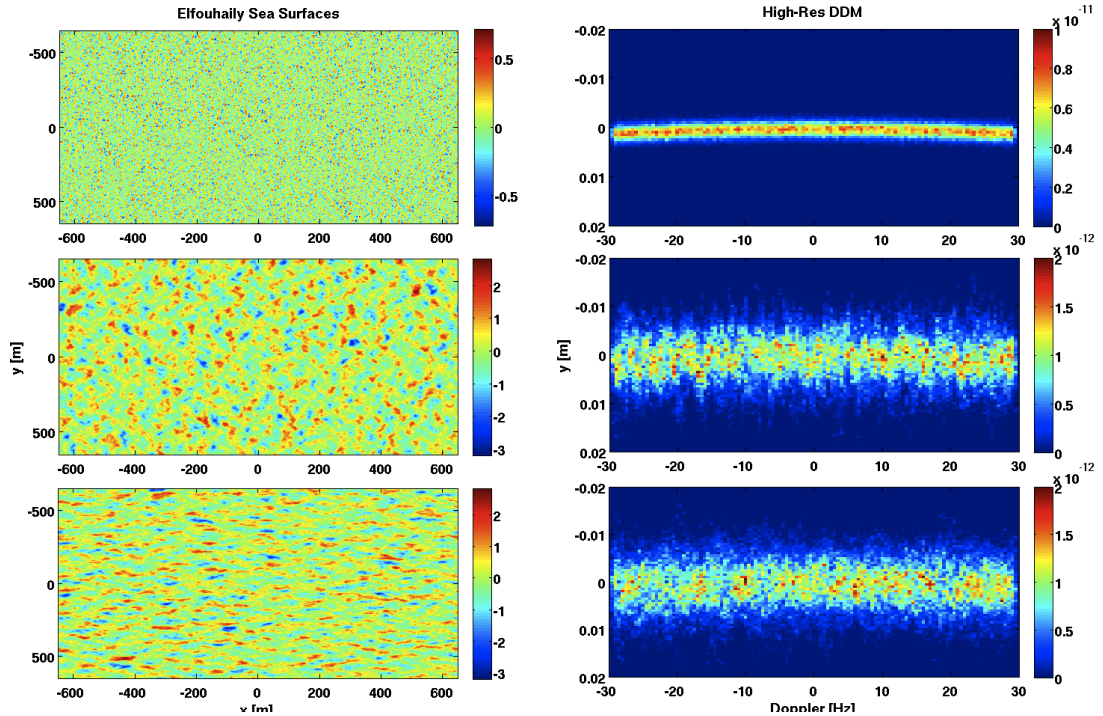
FIGURE 6.17: Left column: sea surfaces in meters, for different wind speeds and wave directions. Right column: corresponding high-res DDM of scattered amplitude.

Figure 6.17 highlights that the range of delays spanned by the signal in the DDM is narrower for lower wind speed, and broader for larger wind speed, consistent with the broader waveforms seen in the corresponding surfaces. The total scattered signal at zero Hz Doppler frequency in the DDMs in figure 6.17 is confined within an estimated delay range of 0.0035 chips for the 5 m/s wind speed case, and 0.016 chips for the 10 m/s wind speed case. These delay ranges can be directly linked to the standard deviation of heights σ_h of the underlying sea surfaces. A specular point whose height oscillates within two to three σ_h for a given surface will produce a scattered signal within the same delay range as those of the DDMs in figure 6.17. No other relevant information (i.e. no dominant wavelength, etc.) can be extracted from these DDMs, but this is mainly due to the type of surfaces (Elfouhaily), which are neither very directional, nor exhibiting a clear dominant wavelength. More interesting results are obtained when a swell of reasonably high amplitude ($A = 2$ m) is superimposed on Elfouhaily wind waves. Figure 6.18 shows two sea surfaces on the left, consisting of a 10 m/s, 0° wave direction Elfouhaily sea, with a superimposed swell, travelling in a direction of 0° (top) and 90° (bottom). The corresponding DDM subsets are shown on the right column.
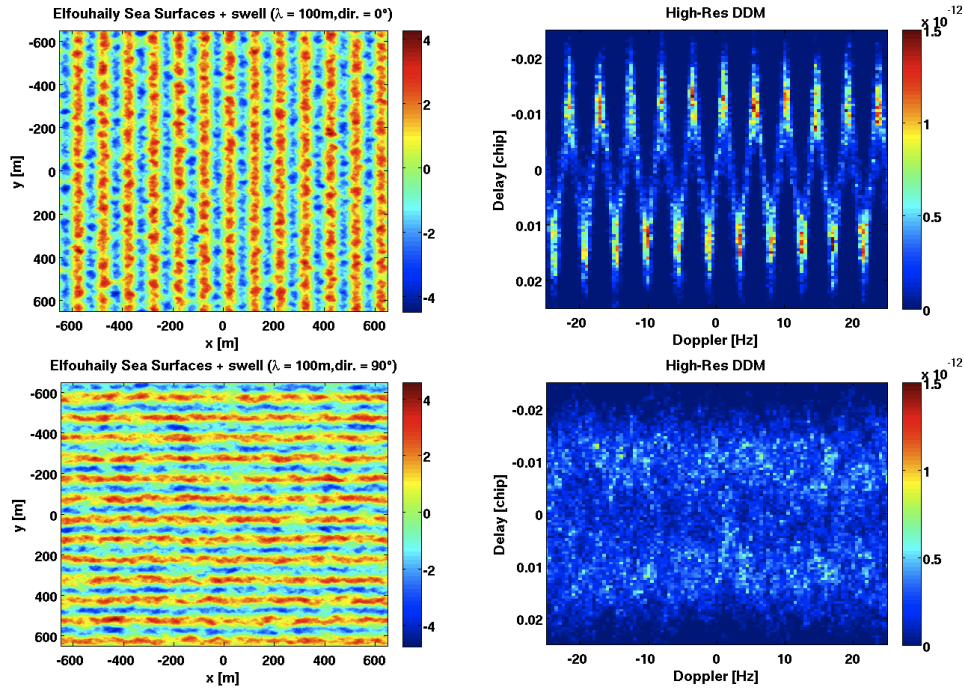
FIGURE 6.18: Left column: sea surfaces in meters, for wind sea plus swell of different directions (0° and 90°). Right column: corresponding high-res DDM.

In figure 6.18, when the swell travels along the 0° direction, with its wavefronts parallel

to the iso-Doppler lines, both the amplitude and the wavelength of the swell are clearly visible in the DDM, respectively along the delays and the Doppler frequencies. The range of the fluctuations along the delay axis, and their frequency along the Doppler axis, could easily be converted into the amplitude and frequency of the ocean swell. The peak-to-peak delay estimation of the swell height at zero Doppler is on the order of 0.04 chips, which corresponds to a peak-to-peak surface height range at the specular point of 6.4 m. In addition to this, the wavelength of the swell from the DDM is estimated to be roughly 4.5 Hz, which translates into the effective 100 m wavelength of the swell (recalling from paragraph 6.5.1 that 5 Hz is about 110 m). Notably, when the direction of the swell is changed, the overall range of heights of the sea surface can still be recovered (through estimation of the delay range in the DDM), but any information about the swell wavelength, and generally speaking about the presence of a predominant wave component is lost. This effect is however expected, as the Doppler and delay sampling of the sea surface for this location of the DDM correspond respectively to a sampling along the x-axis, and a sampling of the wave amplitudes. When the waves and particularly the swell travels along the x-axis, or generally speaking along the direction of the iso-Doppler lines, then the wavelength of the predominant component is fully captured by the sampling along x, whereas if the sampling direction is different from the wave propagation then clearly the wavelength is no longer detectable. In some ways, this happens because the DDM subset at the SP represent a 1D sampling only (along x, or along the iso-Doppler lines) of a 2D wave surface, and the circular symmetry of the delays at the SP does not allow to detect the wavelength of the waves, when they travel obliquely to the x-axis. It is however worth noting that in figure 6.18 a characteristic signal distribution in the DDM within two bands at higher and lower delays still remain, even when the direction of the swell has changed. This signal distribution in the DDM can still suggest the presence of crests and troughs of a predominant wave component, which produce a stronger scattering due to their slopes close to zero, at higher or lower delays due to their heights. The total scattered amplitude within these bands of the DDM is expectedly lower for the 90° wave direction case, compared to the 0° direction case, because when the waves travel in a direction of 90° then a single Doppler bin will not represent the scattering from an entire crest or trough, but rather from alternate

sections of crests and troughs. Figure 6.19 shows the same plots as for figure 6.18, but now with a changing wavelength of the swell. This change still be visible in the high-res DDM, along the Doppler, when the swell fronts are parallel to the iso-Doppler lines, as in the cases shown in figure 6.19. Once again the wavelengths along the Doppler have been estimated from the DDMs in figure 6.19. Their values are respectively 2.25 Hz, 4.5 Hz and 11.3 Hz, corresponding to the actual spatial wavelengths of the swell components on the left of figure 6.22 (50 m, 100 m and 250 m from top to bottom).
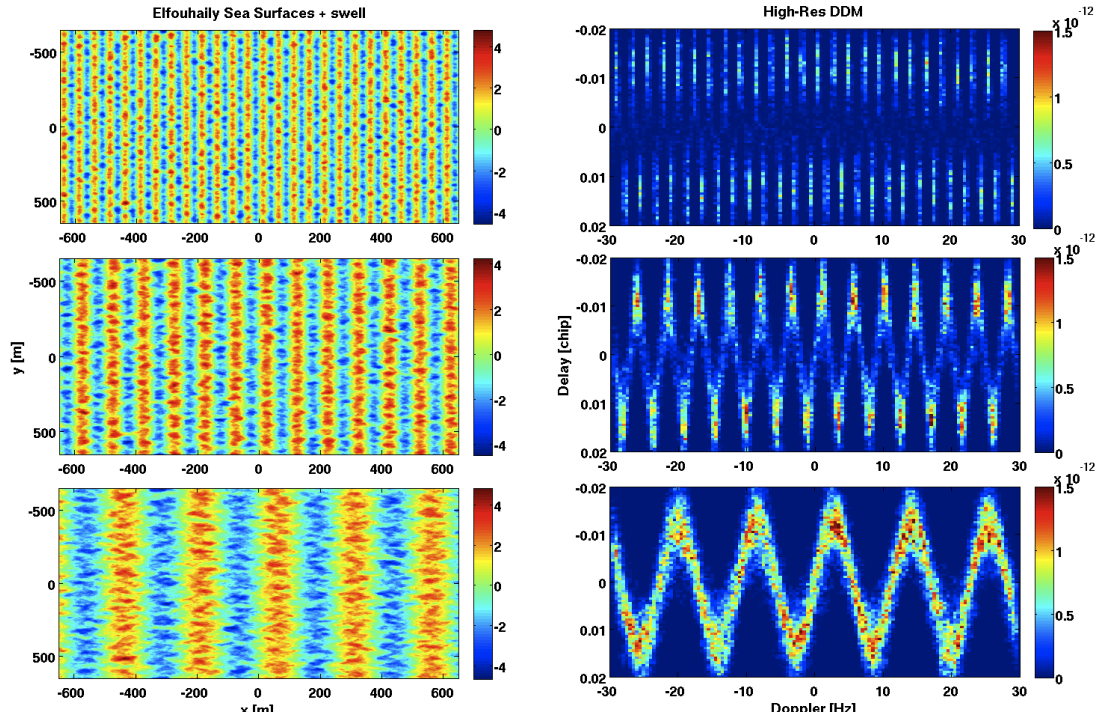
FIGURE 6.19: Left column: sea surfaces in meters, for wind sea plus swell of different wavelength (50 m, 100 m and 250 m) Right column: corresponding high-res DDM.

Finally, figure 6.20 shows the results of high-resolution DDMs for the JONSWAP sea surfaces with different directionality and direction. The left column of figure 6.20 represents this time an integration of the original JONSWAP surface along the y-direction (parallel to the iso-Doppler lines), whereas the right column shows the corresponding high-resolution DDMs. Figure 6.20 highlights how a progressively increasing directionality of the surface increases the similarity between the overall shape of the DDM and that of the integrated sea surface along y. In this sense, the high-resolution DDM becomes a 1D imaging of the sea surface, when the directionality is sufficiently high, and when the wavefronts travel parallel to the iso-Doppler lines. It can also be noticed that for highly directional surfaces a change in the direction of the waves is still detectable

from the high-res DDM at the SP, since the configuration of the DDM changes when the direction of the waves is changed, and horizontal patterns similar to wavefronts become visible in the DDM (on the bottom row of figure 6.20).
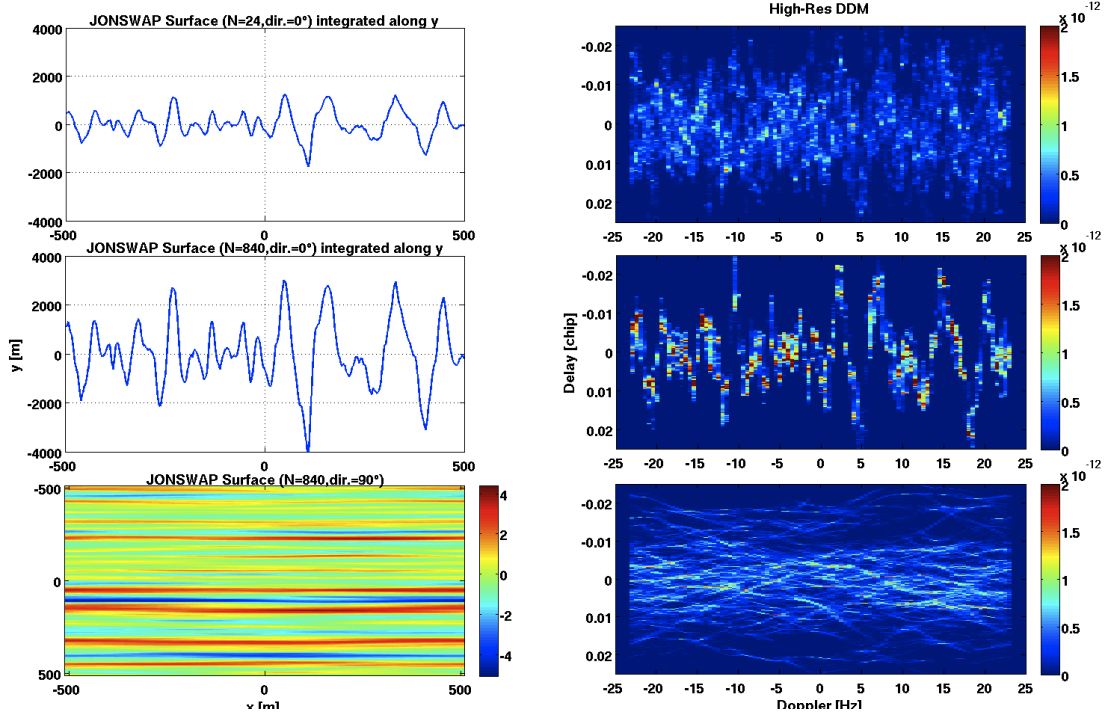
FIGURE 6.20: Left column: sea surfaces in meters, simulated from JONSWAP spectra, with different directionalities and directions (N=24 and $\phi = 0°$ at the top, and N=840 and $\phi = 0°$ in the middle, and N=840 and $\phi = 90°$ at the bottom). The first two surfaces from top are integrated along the y-direction, to emphasize their similarity with the DDM. Right column: corresponding high-res DDM.

6.5.3 High-Res DDM away from the Specular Point

We now analyse DDMs at high resolutions for the second case, namely the area of the GZ away from the SP, but still along the horseshoe shape. This area, along with overlaid iso-delay and iso-Doppler lines, corresponding to the delay-Doppler range chosen, is shown in figure 6.21 (a). The results we obtain for this case are very similar to those obtained at the SP, illustrated in 6.5.2. Apart from an overall lower scattered signal, and a slightly improved delay resolution, due to the iso-delay lines becoming closer to each other away from the SP, the high-resolution DDMs are simply those at the SP, but with an overall oblique trend, since we are now along one of the branches of the horseshoe shape. For this reason, we present only one example of sea surface and corresponding DDM. A 10 m/s, 0° wind direction Elfouhaily wind sea is assumed, with a superimposed swell

of amplitude 2 m, wavelength of 100 m, and with a $0°$ travelling direction, illustrated in figure 6.21 (a). The corresponding high-res DDM is shown in figure 6.21 (b), with the same delay and Doppler resolution as for those used in the previous DDMs. Once again, the structure of the sampling is such that the iso-Doppler lines sample along the x-direction, and the iso-delay lines sample the heights of the sea surface points. The overall results and conclusions are consequently not different from those drawn in the previous paragraph.
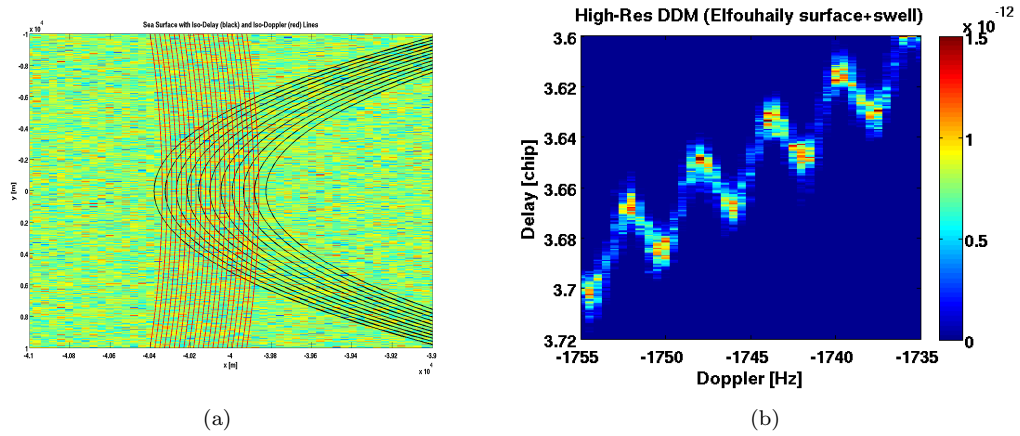
FIGURE 6.21: (a) Area away from the SP, with overlapped iso-delay (black) and iso-Doppler (red) lines. (b) Corresponding High-res DDM.

The DDM in 6.21 (b) is characterized by an overall lower scattered signal compared to those at the SP, shown in paragraph 6.5.2. However, the amplitude of the sea registers again in the DDM as clear oscillations along the delay. If the swell travels parallel to the iso-Doppler lines, as in this case, then its wavelength is related to the distance between the peaks in the DDM. Interestingly, the fronts of the swell field, directed towards the transmitter, appear attenuated in the DDM. This is expected as the area under analysis is far away from the SP (~ 40 km), and the incidence and scattering angles are not in specular configuration. Even in this case the information related to the swell wavelength is lost if the swell travels in a different direction with respect to the propagation direction of the iso-Doppler lines.

6.5.4 High-Res DDM at zero Doppler frequency and nonzero delays

We conclude this High-Res analysis of FA-DDM for linear surfaces by looking at the scattering results for an area mapped in a DD location around the zero Doppler, and delays larger than zero. In terms of DDM subset, this corresponds to the signal between the branches of the horseshoe shape. From a spatial point of view, this corresponds to the double intersection between the iso-delay (black) and iso-Doppler (red) lines, highlighted in figure 6.22.
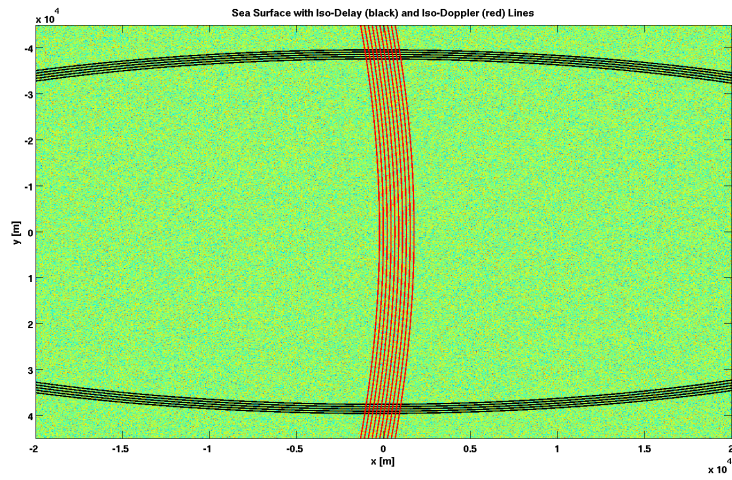
FIGURE 6.22: An example of sea surface with overlapped iso-delay (black) and iso-Doppler (red) lines for the high-res DDM at zero Doppler and non-zero delays.

This area is characterized by a weak scattered signal, mainly because it is quite small, and away from the specular direction. It is also affected by the well known left-/right ambiguity with respect to the x-axis, characterized by the double intersection between iso-delay and iso-Doppler lines, for which the power contributions from two different spatial regions are mapped in the same DD interval. However, in this location the DD mapping is quite favourable, as the iso-delay and iso-Doppler lines are almost orthogonal to each other. The DD mapping produces results similar to the spatial maps, because the delay and Doppler dimensions no longer sample just along the x-direction, but along both the x- and the y-direction. Intuitively, this suggests a likely improvement in the sensitivity of DDM to detect wave direction. The analysis has been carried out here for surfaces with either a clear dominant component (wind waves with a swell) or surfaces with directional waves (JONSWAP), because these are the surfaces where the wave

patterns are clearly defined, and that have a clear influence on the high-resolution DDM. An example of high-resolution DDMs for mixed surfaces (illustrated in figure 6.18) of wind waves, and a swell travelling in two different directions (0° and 90°), are shown on the top row of figure 6.23. The bottom row shows instead an interesting alternative view of the DDM itself, that is its 2D-FFT. In this case, we have selected a central portion of the DDM subsets (to exclude the edges), and we treat the selected portions as 2D spatial scattering maps, to look at their spectral properties. This is rigorously not true, as these DDMs do not represent a spatial map of scattering. However, the configuration of the iso-delay and iso-Doppler lines in this case is such that they resemble a surface sampling along the x- and y-direction. Thus it is reasonable and very useful to look at their spectra to identify specific components or characteristics.
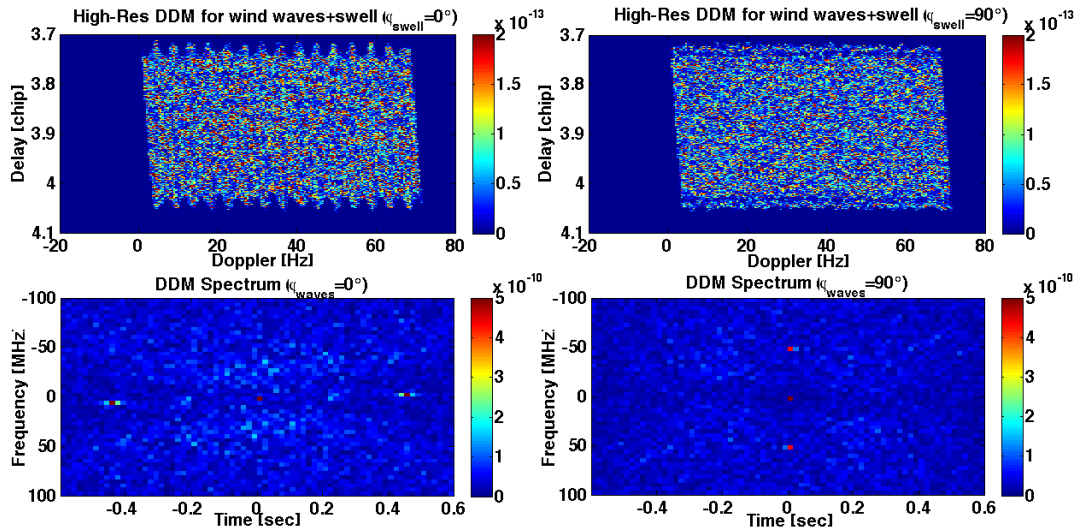
FIGURE 6.23: Top Row: High-resolution DDM for mixed sea surface of wind waves, and a swell of amplitude 2m, wavelength of 100 m, and travelling in a direction of 0° (left) and 90° (right). Bottom row: 2D-FFT of the DDMs above.

It is worth recalling here that these DDMs have been obtained by merging (coherently) two DDMs obtained from two different sea surface realizations, simulated using the same set of parameters. This has been done to reproduce the spatial ambiguity in the DDM, and to investigate whether any relevant conclusion can be still drawn from the results, even when the ambiguity is in place. In figure 6.23, a strong spectral component can be clearly identified, indicating the presence of a swell, with a high enough amplitude, superimposed on wind waves. The spectral components are in particular located along the spectral time axis roughly at 0.44 sec, which corresponds to a 2.27 Hz Doppler

wavelength. This in turn corresponds to a spatial wavelength of ~ 50 m, which is half of the actual spatial wavelength of the swell. This factor of $1/2$ is probably linked to the periodicity of the scattering, which is about half a wavelength of the swell, because the crests and the troughs, both having ~ 0 slopes, will scatter the incident signal in approximately the same manner. Therefore, if we multiply the scattering spatial periodicity by a factor of 2, we ultimately retrieve the wavelength of the predominant swell component on the sea surface. A change in the direction of the swell makes its spectral component still quite visible, now along the spectral frequency axis. The estimation of the wavelength is in this case slightly more complicated, as the delay axis in the DDM does not immediately correspond to a spatial axis, but it is influenced by both a shift in space, and a height variation of the sea surface. In this case, the components are located at a frequency of ~ 50 MHz, corresponding to a delay in chips of 0.02. This delay, multiplied by a factor of 2, is for a flat surface comparable to a spatial wavelength of 100 m, that is the wavelength of the swell. In figure 6.23, a slight rotation effect can be also noticed in the spectra, which is believed to be a consequence of the iso-delay and iso-Doppler lines not being perfectly orthogonal to each other. Figure 6.24 shows another example of high-resolution DDMs and their spectra, for other two cases of mixed wind waves and swell travelling in a $0°$ direction, and with different wavelengths of the swell (illustrated in figure 6.19).
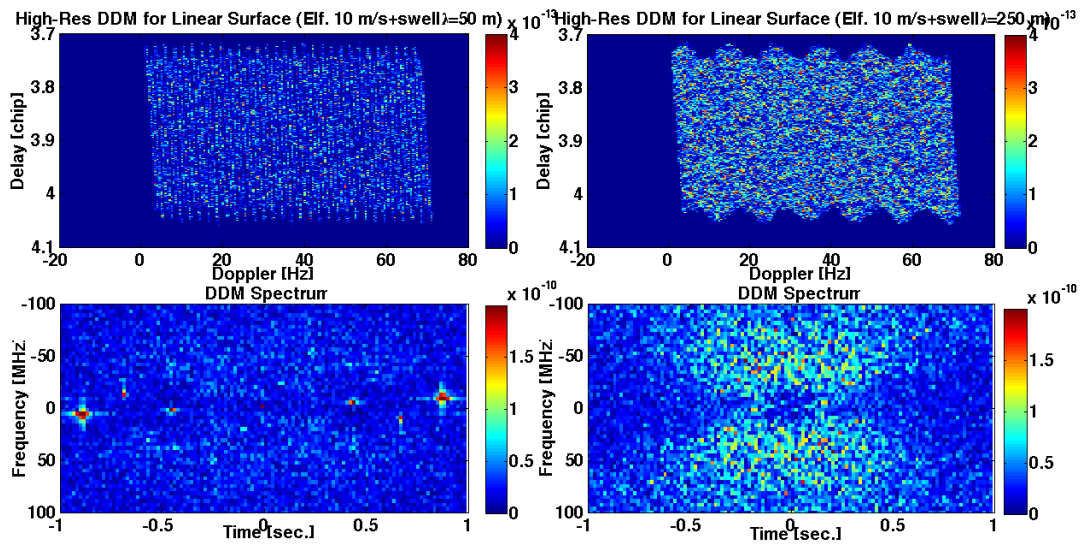
FIGURE 6.24: Top Row: High-resolution DDM for mixed sea surface of wind waves, and a swell of amplitude 2m, travelling direction of 0, and a wavelength of 50 m (left) and 250 m (right). Bottom row: 2D-FFT of the DDMs above.

In figure 6.24, the smallest wavelength of the swell can be estimated from the DDM spectrum (bottom left), as the strongest spectral peak is located at about 0.88 sec, which corresponds to a 1.13 Hz Doppler wavelength. This Doppler wavelength, multiplied by a factor of two, corresponds to a spatial wavelength of 50 m. The swell with the large wavelength of 250 m, (shown on the right of figure 6.24), does not appear to be detectable from the DDM spectrum, as the spectral peaks cannot be identified. In some ways this could be surprising, since a swell with a larger wavelength, travelling along the x-axis, is sampled even better along the Doppler. However, this surface has got a much lower directionality compared to the other smaller swell wavelengths, which means that even the spatial scattering map for this case is much more random, and does not clearly show wavefronts of the underlying surface, The difficulty to retrieve the properties of the sea surface from the scattering map in space makes is even harder to retrieve them from the DDMs. It is also important to clarify that the results in figure 6.23 and figure 6.24 are obtained assuming that the swell components on the two different sea surface locations contributing to the DDM are in phase (a crest is summed to a crest, and a trough is summed to a trough). Obviously this represents one of the two optimal configurations, the other being when a crest is summed to a trough and viceversa, because the power scattered from the crests and troughs of the two spatial locations will add constructively. When the actual configuration of the two sea surfaces is different from one of these, then the detectability of the swell component starts to decreases, until it can no longer be identified in the DDM spectrum when the two swell components are out of phase. We conclude this analysis by presenting examples from JONSWAP surfaces, with a high directionality (N=840), and with waves travelling in a 0° and 90° direction. The high-res DDMs together with the corresponding spectra are shown in figure 6.25. The JONSWAP surfaces used to produce these maps are slightly smaller than the Elfouhaily ones (1021 m x 1021 m), and therefore their DDMs span a shorter range of delays and Doppler frequencies.

As for the previous DDMs, here we illustrate high-resolution DDMs, and their spectra, respectively on the top and bottom row of figure 6.25. In figure 6.25, we notice an overall strong scattering for the 90° direction, as a results of the x-slopes of the waves being very close to zero, which is the optimal slope value along x, to scatter power at the
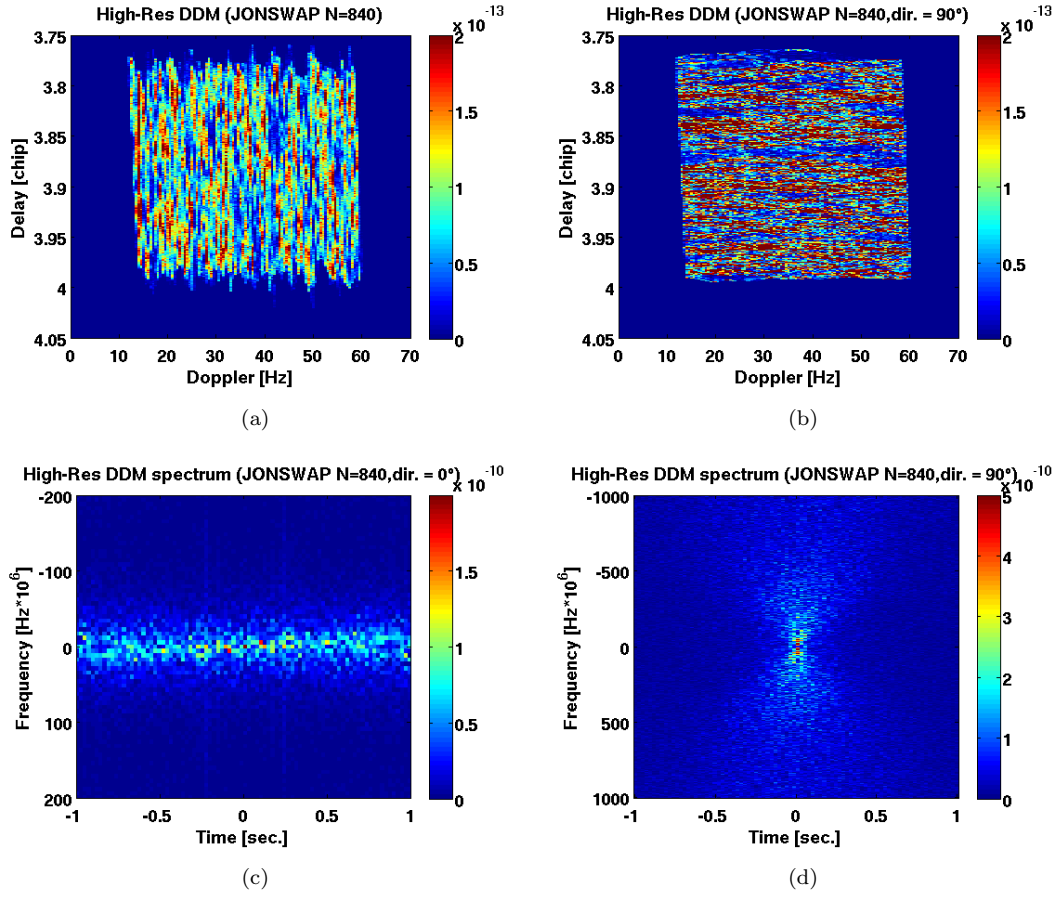
FIGURE 6.25: Top Row: High-resolution DDM for mixed sea surface of wind waves, and a swell of amplitude 2m, travelling direction of 0°, and a wavelength of 50 m (left) and 250 m (right). Bottom row: 2D-FFT of the DDMs above.

receiver from this spatial location. Moreover, we can clearly see patterns in the DDMs resembling the wavefronts, and oriented in a very different way for the two directions. The DDM spectra do not convey information about a dominant wave component, but it certainly identify two clear wave travelling directions of 0° and 90° for the two cases. The difficulty in identifying clear wave components is however mostly due to the spatial ambiguity that here affects the high-res DDMs. An interesting result is obtained when such ambiguity is removed. Figure 6.26 shows the NRCS map from the sea surface patch considered, and the corresponding high-resolution DDMs, and highlights similar features and patterns between the two, when the spatial ambiguity is removed. In such a circumstance the high-resolution DDMs could be considered as a good estimate of the 2D reflectivity (NRCS) map the underlying sea surface.
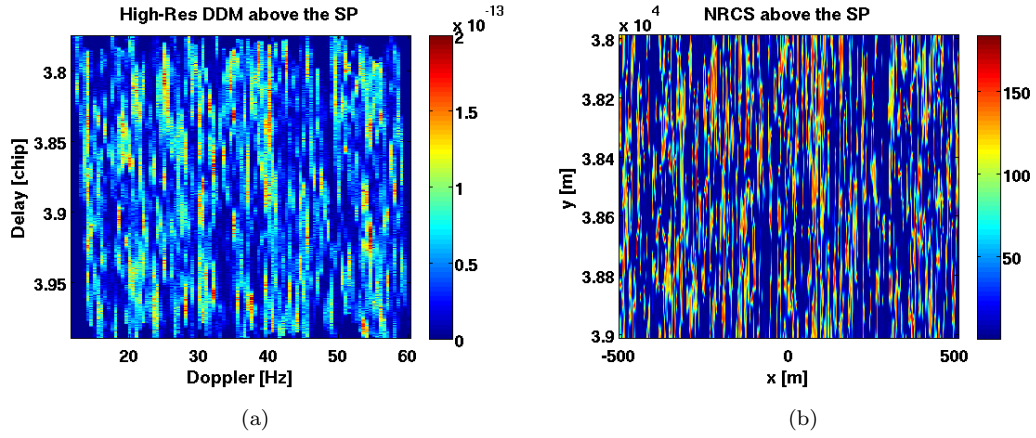
FIGURE 6.26: Top Row: (left) NRCS maps of the surface patch above the SP, in absolute values. (Right) High-resolution DDM obtained only from the scattering for the surface patch above the SP (no spatial ambiguity).

6.6 Conclusions and Summary

In this chapter we have analysed the results of the FA simulator in DD domain. This analysis has been presented in a backward way, starting from the illustration of a simulated DDM with the WAF, using the resolution of UK-DMC DDMs, and highlighting in particular the patchiness in the DDM brought about by the WAF. We then presented results from DDMs without the WAF, and DDMs where both the WAF has been removed and the DD resolution has been increased. We have also shown how this gradually improves the final results, leading to the detection of a signature of the sea state in the DDM, or even to the perspective to obtain a 1D or 2D imaging of the sea surface in high-resolution WAF-free DDMs. As far as the sea surface roughness is concerned, the analysis conducted on WAF-free DDMs, computed using the resolution of UK-DMC DDMs, as well as on delay and Doppler waveforms, has highlighted that both the overall scattered signal from the whole DDM, and the variability of this signal across the DDM decrease quadratically for rougher seas, particularly when the roughness increases along the transmitter-receiver direction projected onto the sea surface plane (the x-direction). If the maps are normalized, then an increasing quadratic trend is obtained with increasing roughness, and this is found to be consistent with previous studies from real measurements [Marchan-Hernandez et al. (2010)]. However, this trend can be identified only for surfaces with a comparable directionality of the waves. It might be possible

that different trends (curves) describing the dependence of the scattered signal upon the surface roughness can be defined, and parameterized with respect to the surface directionality. Such hypothesis should however be confirmed through further investigations into the scattering from a large number of surfaces with different roughness and directionality. A clear conclusion is that the wave directionality is an important parameter, that affects the DDM dependence on sea surface roughness. The directionality of the waves influences also the detectability of the wave directions in DDMs. A changing direction of the waves for highly directional surfaces that are similar to a pure swell is very well detected in the DDM, since the signal distribution changes completely across the DDM. A Doppler bandwidth has been defined and used as an indicator of wave direction, and its performance improves for increasing directionality of the waves. After this analysis, conducted on the whole DDM, we have analysed DDM subsets computed at high resolution, and we have shown that this would allow not only to retrieve general surface properties, but to actually detect in the DDM some of the explicit features simulated in the original sea surfaces. The high-resolution analysis has been conducted for three different cases, corresponding to three different spatial locations and DDM subsets. The high-resolution DDMs computed in the vicinity of the specular point allow to retrieve the overall range of heights of the sea surface, along the delay. The wavelength of a swell superimposed on wind waves can also be detected, as long as the swell has a sufficient amplitude and represents the dominant component of the sea surface, and it is travelling in a favourable direction, parallel to the iso-Doppler lines. Generally speaking, this type of DDM could ultimately produce a 1D imaging of the ocean surface, if the iso-Doppler lines are aligned with the wavefronts, and if the wavefronts themselves are clearly distinguishable (the wave directionality is high enough). The analysis conducted on DDM subsets along one of the branches of the horseshoe shape produces results very similar to those for DDMs at the specular point, in terms of retrievable surface parameters. The DDMs at zero Doppler and delays larger than zero can potentially constitute a 2D imaging of the ocean surface, if the spatial ambiguity is removed. This happens because this particular location in the DD domain corresponds to iso-delay and iso-Doppler lines almost orthogonal to each other, resembling a $x - y$ sampling of the surface. When the spatial ambiguity is not eliminated, some properties of the sea surface can still be

retrieved in certain conditions, particularly is the waves from the two surfaces patches are reasonably in phase with each other. When this condition is verified, it is possible to retrieve some sea surface parameters (i.e. the wavelength and direction of a swell, or of the dominant wave component in general) directly through the DDM spectrum, without the need for a DDM conversion into a map of scattering in the space domain. A swell superimposed on wind waves produces a peak in the DDM spectrum, and its wavelength and direction can be identified from the position of the peak. Other properties of the surface like wave direction are visible in the DDM for sea surfaces with either a dominant component, or with a strong directionality of the waves. Although very interesting, this type of study still offers results and perspectives that are not achievable with the current available technologies. However, several aspects of GNSS-R offer room for improvement of DD resolution in the immediate future, and scope for high-resolution investigations. These include the current and future availability of a number of navigation signals (i.e.Galileo, Compass/Beidou etc.), as well as improved codes, bandwidth, modulation and processing schemes of forthcoming GNSS systems. In addition to this, there are ongoing studies among the scientific GNSS-R community focused on the application of deconvolution techniques to remove the effect of the ambiguity function [Valencia et al. (2011a)], on the use of established signal processing techniques (superresolution techniques) to increase the resolution to GNSS-Reflectometry [Clarizia et al. (2009a)], and finally on the appealing perspective to exploit GNSS-Reflectometry for bistatic SAR in a non-distant future [Cherniakov (2008)].

CHAPTER 7

Polarization Effects in DD Domain

7.1 Introduction

In this chapter, we analyse the effect of polarization in the delay-Doppler domain. The importance of polarization for GNSS scattering, recognized for the first time in [Zuffada et al. (2004)], is also discussed in a more recent study by [Thompson et al. (2005)], where polarization has been explored using a refined GO model based on a vector formulation. The results of both these studies are presented as delay waveforms from scattered LHCP and RHCP signals, and they show a scattered RHCP component larger than predicted, especially for low incidence and scattering angles. In [Zuffada et al. (2004)], an attempt is made to link the individual LHCP and RHCP delay waveforms to different wind speeds and directions, through scattering simulations. In contrast, the study conducted by [Thompson et al. (2005)] was based on data from an airborne campaign, where both RHCP and LHCP scattered signals were collected off a Puerto Rico site. In that study, the RHCP component was found to be systematically higher than the predictions made with the refined GO model, particularly at low incidence and scattering angles.

Both the analyses remain to-date the first attempts to investigate polarization in delay domain from GNSS-R signal, for wind and wave retrievals. One of their major outcome is that the RHCP scattering component is not negligible, and can actually contain important sea surface-related information. However, they do not investigate the ratio between the differently polarized components, and they do not contain a comprehensive characterization of the changes of polarization in delay-Doppler domain, with respect to different properties of the sea surface. In the present chapter, we try to address such characterization, through an investigation of DDMs of polarization ratio for different types of surfaces, and we show how some of the DDM properties can be effectively linked to sea surface characteristics. The results presented here show which effects of sea surface properties on polarization are visible and detectable in DDMs, computed at the delay-Doppler resolution used for UK-DMC maps. High-resolution DDMs of the polarization ratio have also been investigated, but the results obtained are similar to those seen in the full DDMs, and therefore they are not shown here.

7.2   Delay Doppler Maps of Polarization Ratio

In this section we investigate how polarization varies for different characteristics and parameters of sea surfaces. This is done through investigations of delay-Doppler maps of polarization ratio, which we will call from now on PR-DDM. PR-DDMs are generated and analysed for different types of sea surfaces, namely linear non directional (Elfouhaily) surfaces, with or without a superimposed swell, linear surfaces with a more pronounced directionality (JONSWAP), and weakly non linear surfaces in the next chapter. In the previous chapters, PR has always been presented as the ratio of vertical to horizontal received components, when the transmitted signal is always co-polarized with the received signal (VV/HH). Such a straightforward approach was adopted because we were mainly examining PR in space, and were assuming a simple incident monochromatic wave. For delay-Doppler analysis, we need to fully take into account the Right-Hand Circular Polarization (RHCP) of the GPS transmitted signal, and therefore look at ratio of differently polarized received components, when the transmitter signal is RHCP. The

PR we consider here can be therefore defined as follows:

$$PR = \frac{E_{RV}}{E_{RH}} \tag{6.3a}$$

where the subscripts R indicates RHCP, and the subscripts H and V indicate horizontal and vertical polarization respectively.

7.2.1 PR-DDM for Linear Surfaces

Examples of PR-DDMs, without and with WAF are shown in figures 7.1 and 7.2, respectively for an Elfouhaily 10 m/s wind sea, with a superimposed swell, and for a highly directional JONSWAP sea surface. The swell and the JONSWAP sea waves are travelling along x , in a 0° direction (left columns) and along y, in a 90° direction (right columns). The PR-DDMs are obtained by applying the WAF separately to the single polarised DDMs, and then by taking their ratio. This procedure is consistent to a PR derivation that would be done by a real receiver.
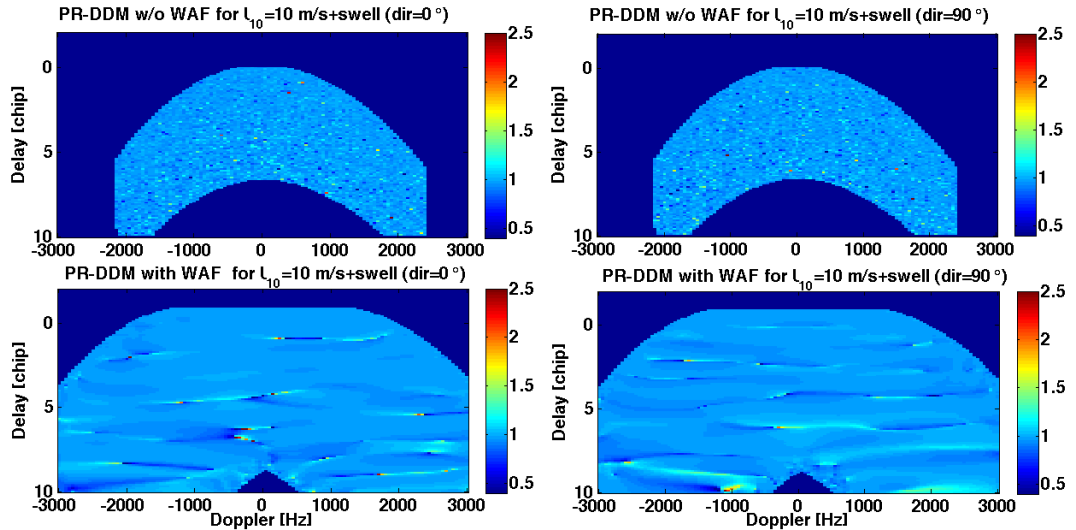
FIGURE 7.1: Top row: PR-DDMs without WAF, for Elfouhaily sea surface generated at 10 m/s wind speed, and with a superimposed swell ($A = 2m, \lambda = 100m$), travelling in a direction of 0° (left) and 90° (right). Bottom row: PR-DDMs with WAF, for the same sea surfaces.

In figures 7.1 and 7.2, the PR-DDMs with WAF are affected by the patchiness caused by the random phase, as expected. As in chapter 5, our polarization analysis is therefore focused on DDMs without the WAF. The PR-DDMs for swell travelling in different
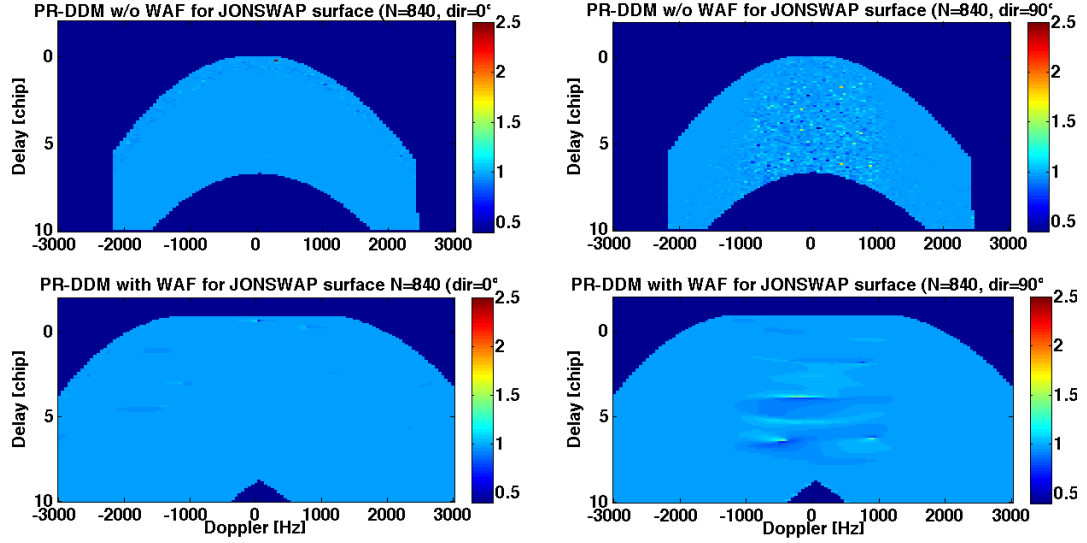
FIGURE 7.2: Top row: PR-DDMs without WAF, for JONSWAP sea surface generated with a directional parameter of N=840, and with waves travelling in a direction of $0°$ (left) and $90°$ (right). Bottom row: PR-DDMs with WAF, for the same sea surfaces.

directions appear very similar to each other, while the structure of the PR-DDMs for the JONSWAP surface changes considerably when the direction of the waves is changed. This behaviour has already been shown in chapter 6, for DDMs of scattered signal. Figures 7.1 and 7.2 also suggest that a change in the direction of the waves is more or less visible in the DDM depending on the directionality of the sea surface. Thus, wave directionality influences not only the scattered signal, but also the polarization. As for chapter 5, an investigation has been carried out into how polarization properties are related to the sea surface roughness and directionality. The results are presented in figure 7.3 (a) and (b). They show a plot of the median as symbols, and median absolute deviation (MAD) as errorbars, of the PR across the DDM, versus the wave roughness (a) and the wave directionality in logarithmic scale (b), for different types of linear surfaces.

Figure 7.3 highlights that the median of PR-DDM remains constant in all cases, and approximately equal to the ratio between the Fresnel reflection coefficients for seawater (~ 0.97). From figure 7.3 (a), no significant relationship can be detected between the sum of mean square slopes along x and y, and the PR, suggesting that polarization is not influenced by the overall roughness of the sea surface. An effect on polarization can be instead associated to wave directionality and direction. In figure 7.3 (b), the MAD decreases for increasing directionality of the waves. This suggests that the sea depolarizes

(a)

(b)
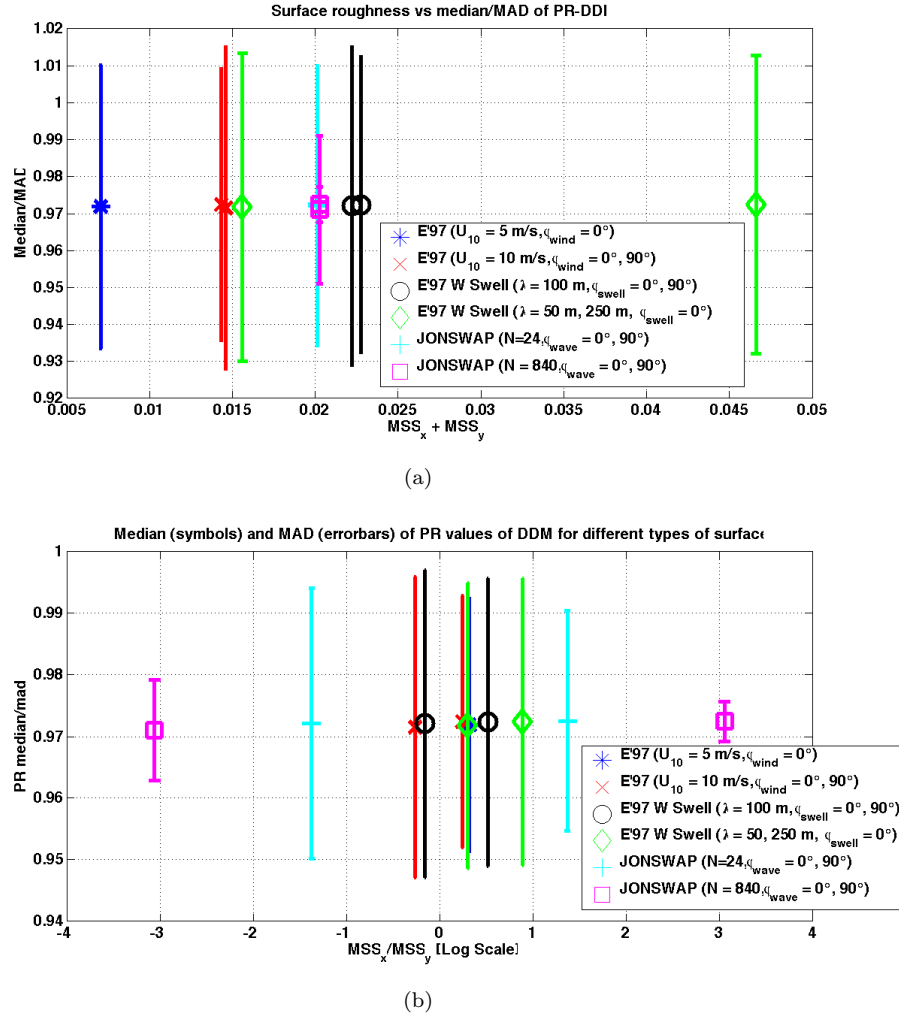
FIGURE 7.3: (a) Plot of median (symbols) and MAD (errorbars) of the PR values of the DDMs versus sea surface roughness, expressed as the sum of Mean Square Slopes (MSS) along x and y, for different types of sea surfaces (E97 refers to Elfouhaily surfaces). (b) Plot of median (symbols) and MAD (errorbars) of the PR values of the DDMs versus sea surface directionality, expressed as ratio of mean square slopes along x and y, and illustrated in logarithmic scale.

more when its waves are less directional (Elfouhaily), while the depolarization of the scattered signal is weaker for highly directional seas (JONSWAP). Recalling that a flat surface, with zero x- and y-slope, would simply equal to the ratio of the Fresnel reflection coefficients), the higher variability of both the x- and the y-slopes of weakly directional surfaces like the Elfouhaily ones might be responsible for a higher variability of PR. Conversely, JONSWAP surfaces are characterized by a even stronger variability of the x-slopes (their waves are steeper along x), but a very low variability of the y-slopes, that are close to zero. The net effect of this is that the depolarization for these surfaces is weaker. In conclusion, the MAD of values across DDMs represent good indicators of

the type of sea from which the scattering occurs, as they are able to convey information about the directionality of the underlying sea surface. Our interest is also in detecting wave direction. This is hard to identify in weakly directional seas as in figure 7.1, and easier to detect in DDMs for highly directional seas in figure 7.2, where the PR distribution changes completely across the DD domain for different wave directions. In figure 7.2 we can notice that the PR-DDM variability is symmetric around the ratio of reflection coefficients of seawater. Thus, the Doppler waveforms for the DDMs in figure 7.2, obtained through an integration along delays, would neither highlight any significant difference between the two cases, nor capture the stronger variability of DDM values at zero Doppler and non-zero delays in figure 7.2 (b). For this reason, a good way to capture the localized DDM variability in the case of PR is through the definition of different Doppler waveforms, obtained by computing the MAD (rather than the sum) of values within a single Doppler bin. These MAD-Doppler waveforms will represent the overall variability of values for each Doppler bin, and they are illustrated in figure 7.4, for different types of sea surfaces.
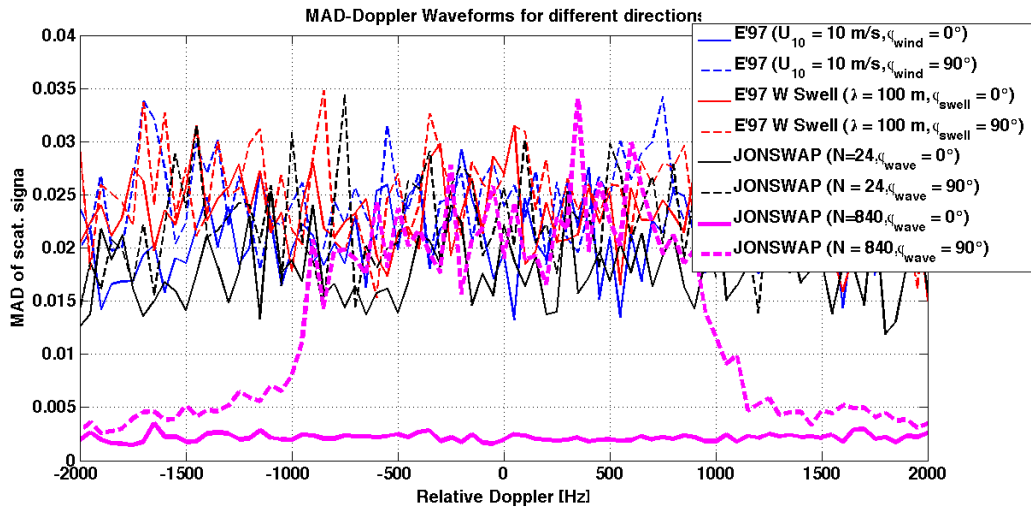
FIGURE 7.4: MAD-Doppler waveforms, for different types of sea surfaces (E97 refers to Elfouhaily surfaces).

In figure 7.4, two Doppler waveforms in particular, represented through magenta lines, correspond to the highly directional JONSWAP surfaces, with waves travelling in a $0°$ (continuous line) and $90°$ (dashed line) direction. The strong differences seen in this two Doppler waveforms reflect those seen in the DDMs in figure 7.2. An easy way to characterize these waveforms is once through the effective bandwidth, where the

percentage chosen to capture the variability is still 80%. Calculations of the effective bandwidths for MAD-Doppler waveforms are illustrated in table 7.1, for pairs of surfaces characterized by the same parameters, but different wave directions.

Type of Surface	MAD	B_{eff} [Hz]
Elf. 10 m/s, $\phi_{wind} = 0°$	0.0231	2500
Elf. 10 m/s, $\phi_{wind} = 90°$	0.0243	2500
Elf. 10 m/s + swell, $\phi_{wind} = \phi_{swell} = 0°$	0.0240	2600
Elf. 10 m/s + swell, $\phi_{wind} = 0°, \phi_{swell} = 90°$	0.0256	2600
JON. $N=24$, $\phi_{wave} = 0°$	0.0211	2500
JON. $N=24$, $\phi_{wave} = 90°$	0.0221	2500
JON. $N=840$, $\phi_{wave} = 0°$	0.0027	2600
JON. $N=840$, $\phi_{wave} = 90°$	0.0138	1800

TABLE 7.1: Doppler bandwidth (B_{eff}) of MAD-Doppler waveforms for the analysed sea surfaces.

Even for PR, the difference in bandwidth between waves travelling in different directions is stronger for JONSWAP surfaces, while no difference is detected for Elfouhaily surfaces. B_{eff} for PR appears to be slightly less sensitive to changes in direction compared to that defined for DDMs of scattered signal. Nevertheless, it still manages to capture the difference in bandwidth between the two highly directional cases, which was clearly visible in the waveforms in figure 7.4. One last way to investigate PR variability and its link with sea state is through the PDF of PR values across the DDM. These PDFs are illustrated in figure 7.5, still for several types of surfaces. Even in this case, we can clearly see the effect of high wave directionality, that contributes to change the shape of the PDF, making it narrower and peakier, and reflecting the decrease in MAD for highly directional surfaces. The median of the PDFs remains roughly the same for all surfaces.
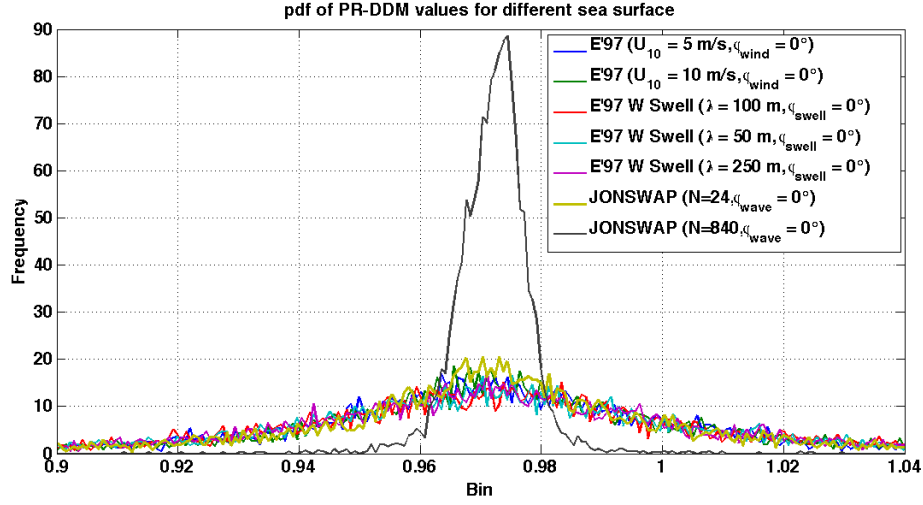
FIGURE 7.5: PDF of PR values across DDMs, for different types of surfaces.

7.3 Conclusions

In this chapter, we have shown how polarization ratio in delay-Doppler domain is affected by different properties of the sea surface. We have shown that polarization is not affected by the total roughness of the sea surface, but it is influenced by the wave directionality and direction. We have illustrated in particular that the sea depolarizes more the incident signal, when the directionality of its waves is low, such that their wavefronts are more random, and poorly defined. While the directionality of the underlying waves can be estimated using the MAD of the PR values across the DDM, the wave direction can be detected using the MAD of values within each Doppler bin in the DDM. This produces Doppler waveforms of MAD values, and from them a Doppler bandwidth can be used as an indicator of wave direction. As in the case of DDMs of scattered signal, shown in chapter 6, this Doppler bandwidth performs well when the waves are sufficiently directional. Finally, we have shown an alternative way to look at the effect of wave directionality in DDMs, through the PDF of PR values across DDMs. In particular, the shape of these PDFs becomes narrower and peakier for highly directional seas. Even though these results are still based on the assumption of an ideal delta WAF, and do not take into account any noise in the DDM, they demonstrate that polarization effects exist in delay-Doppler maps, and they have an impact on DDMs even at relatively coarse delay-Doppler resolution. The sea state effect on polarization is not very strong,

and the results are based on simulations only, because there are no real polarimetric GNSS-R data available. Despite that, the analysis presented in this chapter confirm that polarimetric effects in DDM can be already reproduced from large-scale scattering models, and can integrate or convey additional information on waves, and potentially on nonlinear properties of the sea surface (as it will be illustrated in chapter 8). This study, together with previous polarimetric analyses illustrated in [Zuffada et al. (2004)] and [Thompson et al. (2005)] should contribute to turn the attention of the GNSS-R community towards polarization as a crucial parameter to look at for future GNSS-R missions.

CHAPTER 8

GNSS-R Scattering and DDMs from non-linear Sea Surfaces

8.1 Introduction

Nonlinearities of the sea surface waves are relevant to GNSS-R, as they alter the Gaussianity of the distribution of sea surface heights and slopes on the surface. The importance of nonlinearities of the sea surface has been recently shown by [Cardellach and Rius (2008)], where a retrieval of the full PDF of slopes was performed from GNSS-R measurements. In that paper, the retrieved slope PDF was found to be approximately gaussian, but with a clear skewness, which was related to the local wind, and in particular to the up and down asymmetries in the surface wave slopes, along the direction of the wind. In this chapter, we investigate the scattering from non-linear non-Gaussian sea surfaces, and compare the results with respect to linear surfaces. Following the approach pursued so far, we first analyse the impact that instantaneous weakly non linear surfaces have on the spatial scattering maps, and then we illustrate the effect of nonlinearities on the final DDMs. Simulations of non linear sea surfaces are presented in section 8.2, and compared with the linear one from which they originated. We then

proceed by showing results in space domain, through spatial maps of NRCS and PR, for the linear and non linear case (section 8.3). After that, we focus on the manifestation of nonlinearities in the DD domain, and we present DDMs of scattered signal for non linear sea surfaces. The DD-investigation is carried out using entire DDMs computed at a coarser (UK-DMC like) DD resolution (section 8.4). Finally, section 8.5 is devoted to the effect of nonlinearities on DDMs of polarization ratio (PR-DDM).

8.2 Linear and Non Linear Sea Surfaces

So far we have worked with linear surfaces, which from a mathematical point of view are a linear superposition of sinusoidal waves, with amplitudes and frequencies described by the sea surface wave spectrum. In this case, according to the central limit theorem, the surface elevations are Normal (Gaussian) distributed. When a surface becomes non linear, the interactions between the different wave components start to play a major role in the determination of the surface elevations and slopes. In this study, we only use surfaces that are Weakly Non-Linear (WNL), thus we neither consider extreme waves, nor strongly nonlinear interactions. As defined in [Longuet-Higgins (1963)], a surface can be considered WNL when the ordinary representation as the sum of independent random components is valid to a first approximation, but quadratic and higher- order interactions between the components cannot be entirely neglected. Some simple examples of realistic non-linear effects are shown in figure 8.1.

Figure 8.1(b) shows a modification of the simple sinusoid in figure 8.1(a), to have higher, peakier crests, and shallower, flatter troughs, an effect that is often observed in the ocean. Figure 8.1(b) shows another non-linear effect, that causes an asymmetry between the ascending and descending wavefronts of a sinusoid. From a statistical point of view, both the heights and slopes of non linear surfaces exhibit deviations from the gaussian distribution, producing skewness and kurtosis (third- and fourth-order moment respectively) in their statistical distributions. The former describes the asymmetry of the wave profile, and the latter provides an indication of the peakedness of the distribution, as well as the occurrence of extreme events, since it also measures heavy tails. With
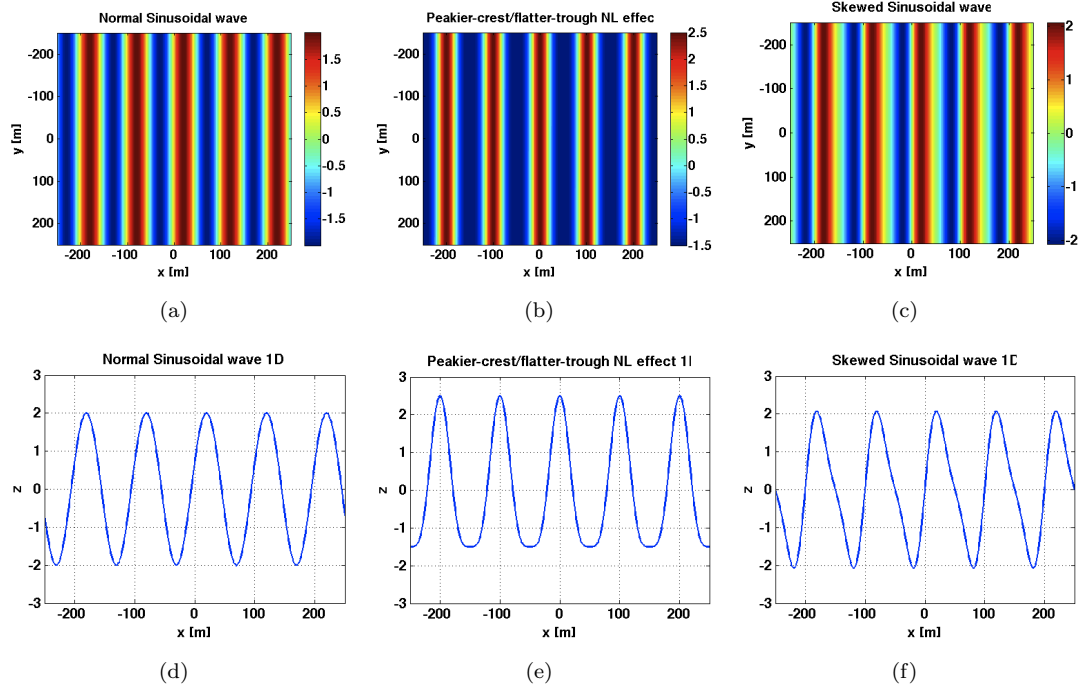
FIGURE 8.1: (a) plain 2D sinusoidal wave (top) and 1D profile (bottom), both expressed in meters; (b) WNL sinusoidal wave (top) and 1D profile (bottom) with higher peakier crests and lower flatter troughs; (c) WNL skewed sinusoidal wave (top) and 1D profile (bottom).

reference to figures 8.1 (b) and (c), the first shows a loss of symmetry in the height distribution (height skewness), while the second shows a loss of symmetry in the slope distribution (slope skewness).

8.2.1 Non-linear Surface Generation

The simulated WNL surfaces presented in this chapter have been provided by Dr. Alessandro Toffoli, from the Swinburne University of Technology, in Melbourne, Australia. They are derived from two equations, expressing the kinematic and dynamic boundary conditions of the potential Euler equations at the sea surface [Zakharov (1968)], and containing the time evolving surface elevation, and the vertical velocity and potential of the water flow [for details see Toffoli et al. (2010), and references therein]. These equations are simulated numerically using the so-called Higher Order Spectral Method, or HOSM [West et al. (1987)]. In the simulations illustrated in [Toffoli et al. (2010)], a third-order expansion is used, such that a four-wave interaction is included.

The simulations normally start from a linear sea surface, which evolves in time, gradually assuming non-linear characteristics. The datafile that has been provided contains the initial linear sea surface, at $t = 0$, and a sequence of 10 WNL sea surfaces, captured with a time step of about 6 peak periods (T_p). The linear surfaces used in this chapter, from which the WNL ones are then derived, are simulated using the JONSWAP spectrum. The JONSWAP spectrum is the one normally chosen because it is effectively a fetch-limited version of the Pierson-Moskovitz spectrum [Pierson and Moskowitz (1964)], hence the wave spectrum is never fully developed, and may continue to develop due to non-linear wave-wave interactions for a very long time. The surfaces have been generated with a steepness parameter $ka = 0.12$, large enough to allow for the development of the nonlinearities, a peak period $T_p = 10s$, a $SWH = 6m$ and a directional parameter of $N = 840$. The choice of a high directional parameter is linked to the fact that the statistical distributions of strongly directional sea surfaces exhibit the strongest deviation from the gaussian case, and the highest skewness and kurtosis. This is not just a coincidence, as it has been demonstrated that strong deviations from gaussian and second-order statistics occur for narrow-banded near-unidirectional wave spectra, where most of the energy is confined within a narrow range of frequencies and directions [Onorato et al. (2001)]. Similarly to chapter 5, the surfaces are made of 512 x 512 samples, generated with spatial steps of $\delta x = \delta y = 2.5$ m. A cubic interpolation has been applied to the surfaces to reduce the spatial steps down to 1 m, to be able to apply the FA with 1-m facets.

8.2.2   Statistical properties of the new surfaces

A closer look at the original linear surface, and the sequence of WNL surfaces has highlighted that the directionality of the linear surface is the strongest one (smallest MSS_{cross} / MSS_{up}), and that it decreases progressively through the temporal sequence of WNL surfaces. This is an unfortunate aspect, as it makes the detection of differences between linear and WNL surfaces harder, due to the fact that such differences will be a combination of the effects of nonlinearities and of different directionalities between the

surfaces. Because of that, we have selected two WNL surfaces to compare to the non-linear case, that have almost identical directionality, but they are reasonably different from each other in terms of skewness and kurtosis. The top row of figure 8.2 shows from left to right the initial linear surface at $t = 0$, and the two WNL surfaces, originated from the linear one, at time instants of $8T_p$ and $9T_p$ respectively. The middle and bottom row of figure 8.2 show respectively maps of x- and y-slopes for the corresponding surfaces.
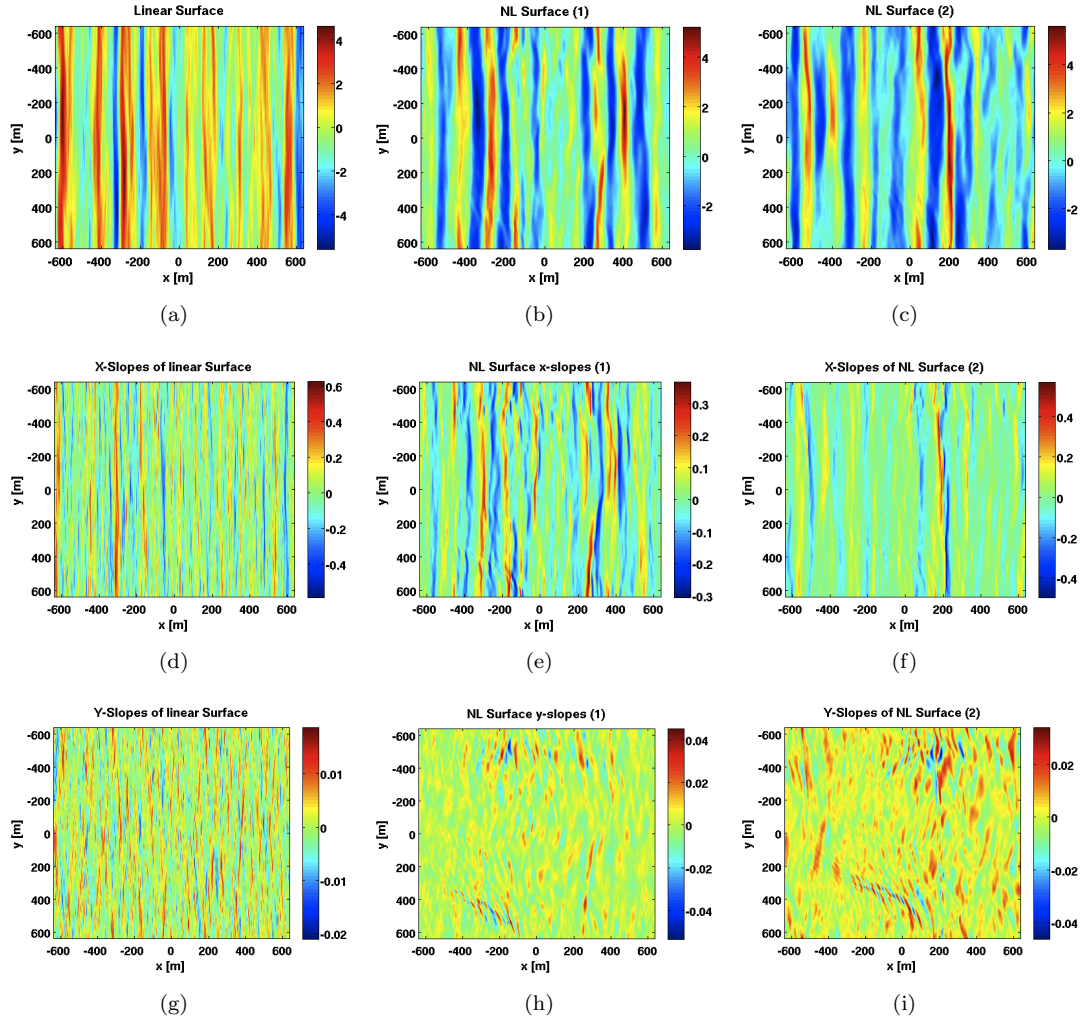
FIGURE 8.2: Linear and WNL surfaces (top row, left to right) in meters, along with a map of their x-slopes (middle row) and y-slopes (bottom row).

First, we can clearly notice from the minimum and maximum values of the sea surface elevations that the WNL surfaces have higher crests and lower troughs. As expected, maps of the x-slopes, which are the dominant ones, share similar patterns with the surface elevation maps, while maps of the y-slopes are less related to the elevation maps, but they still exhibit some interesting features, that seem to undergo a distorsion. Figure

8.3 shows respectively the histogram of heights (top row), of x-slopes (middle row) and of y-slopes (bottom row) of the linear and non-linear surfaces in figure 8.2. The most relevant statistical parameters of the three surfaces are instead illustrated in table 8.1.
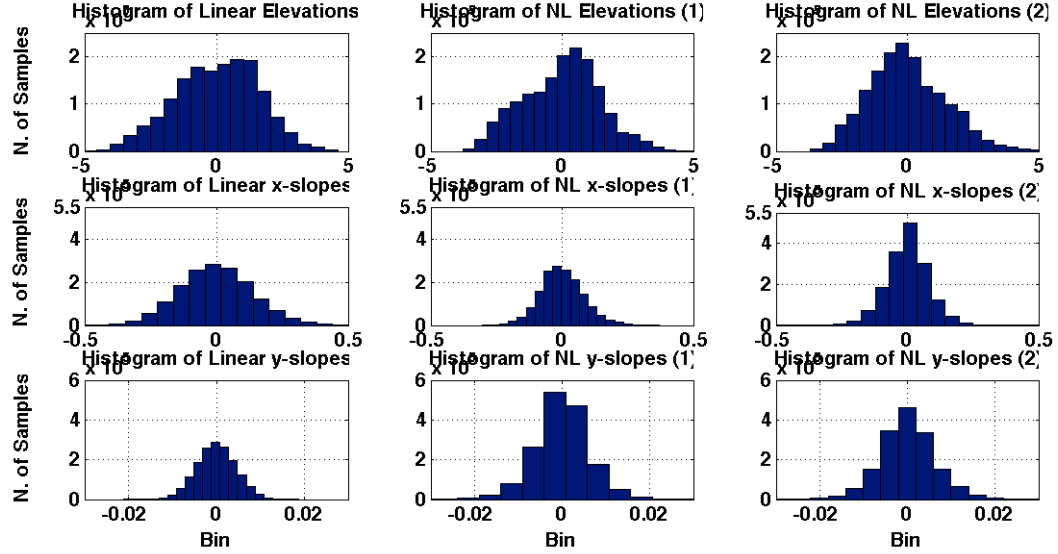
FIGURE 8.3: Histograms of surface elevations, x-slopes and y-slopes (top to bottom) for the original linear surface (left column) and for the two WNL surfaces (middle and right column).

From figure 8.3, we can notice that the height distributions of all the surfaces appear quite asymmetric and irregular, compared to the slope distributions. The linear surface itself exhibits a PDF of elevations that is different from the expected gaussian one. Indeed, being the surface a single realization of the linear process, it is possible that the statistical distributions of elevations for single realizations deviate considerably from the expected distribution, especially for surfaces with a high directional parameter. Even though sea surfaces are commonly classified as either linear or non-linear based on the height distribution, what really affects the scattering is the distribution of slopes, and in particular of the x-slopes, which represents the orientation of the facets along the transmitter-receiver line. Looking at the slope distribution for the three cases in figure 8.3, and their statistical parameters in table 8.1, we notice a positive skewness of the x-slopes for the first WNL surface (central column), as the distribution is skewed towards the left. This means that a larger number of facets face towards the receiver (positive x-coordinate), compared to those facing towards the transmitter (negative x-coordinate). The second WNL surface is instead characterized by a slightly negative skewness of the

	Lin. Surface	NL Surface 1	NL Surface 2
Height Mean	0.0036	2.5732e-4	-5.3465e-4
Height Std	1.5920	1.4632	1.4635
Height Skewness	-0.1881	-0.0049	0.4149
Height Kurtosis	2.7100	2.6877	3.1243
x-Slope Mean	-1.2215e-4	-2.9634e-5	2.4415e-5
x-slope Std	0.1384	0.0824	0.0832
x-slope Skewness	0.1501	0.2872	-0.1016
x-slope Kurtosis	3.0984	3.4392	5.4306
Y-Slope Mean	5.7707e-9	-1.7014e-7	-9.2889e-7
Y-Slope Std	0.0045	0.0064	0.0065
Y-Slope Skewness	0.0025	-0.0878	-0.1733
Y-Slope Kurtosis	3.0057	5.5901	5.0415

TABLE 8.1: Statistical parameters of elevations, x-slopes and y-slopes for the three surfaces.

x-slopes, indicating that more facets are oriented towards the transmitter. Notably, a surface with skewed slopes eliminates the ambiguity of wave direction, by conveying information about the versus of propagation. Unfortunately, the skewness for the linear case is not that of a typical linear surface (0), confirming that this particular realisation is not very representative of a true linear surface. For this reason, in our analysis we look at the statistical properties for the three cases, and try do identify the effect of these properties on the scattering. The second WNL surface (right column) is also characterized by a very peaky x-slope distribution, which reflects in the high kurtosis shown in table 8.1.

8.3   Scattering from linear and non linear sea surfaces in spatial domain

In this section, we investigate the scattering in the spatial domain, and differences between the linear and the WNL cases. Similarly to chapter 4, we present here an analysis of 2D spatial maps of NRCS and PR, and investigate their relationship with the underlying sea surfaces.

8.3.1   Spatial maps for single realization

Figure 8.4 show maps of NRCS and PR for the linear surface, and the WNL sea surfaces with different directionalities, shown in figure 8.2. For the NRCS maps, we look at the received horizontal polarization from a RHCP transmitted signal, while for PR we consider the ratio between the received V- and the received H-polarization.

In figure 8.4, the maps of NRCS (left column) and PR (right column) follow quite closely the x-slope maps of the surfaces, shown in the middle row of figure 8.2. For the non-linear case, they exhibit the same patterns as those of the x-slope maps, as well as those characteristic features that are illustrated in the y-slope maps. The NRCS amplitudes are linked to the x-slope values, and the higher values for the WNL surfaces are due to the lower standard deviation of x-slopes characterising these surfaces. The PR amplitudes are also influenced by the x-slopes, and we can see that the maxima of PR remain more or less the same, due to the saturation effect of the PR for high positive slopes. The minimum values of PR is instead obtained for the linear surface, which is the surface containing the lowest negative slopes among all the surfaces. Given that the characteristics of NRCS and PR maps seem to be mostly linked to the slope distribution, a better way to look at differences induced by nonlinearities is through histograms of PR, in figure 8.5, which represent the PR statistical distribution. Histograms of NRCS have also been checked, but they are not shown here, as we could not identify any significant changes in them, linked to sea surface skewness and kurtosis.
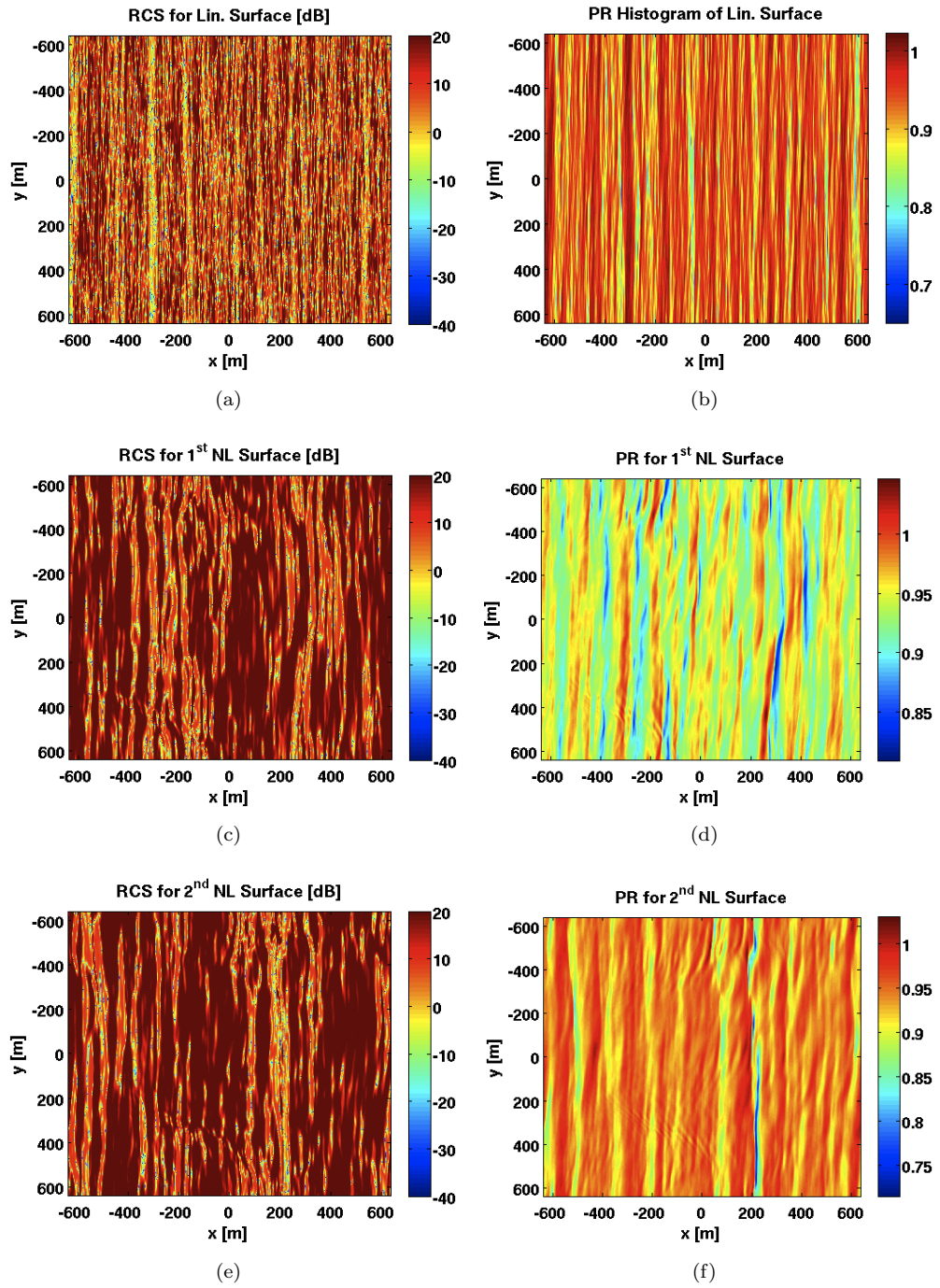
FIGURE 8.4: Left column: maps of H-polarized RCS for linear surface, and the two WNL surfaces (top to bottom). Right column: maps of PR for the same surfaces (V-polarized component/H-polarized component).
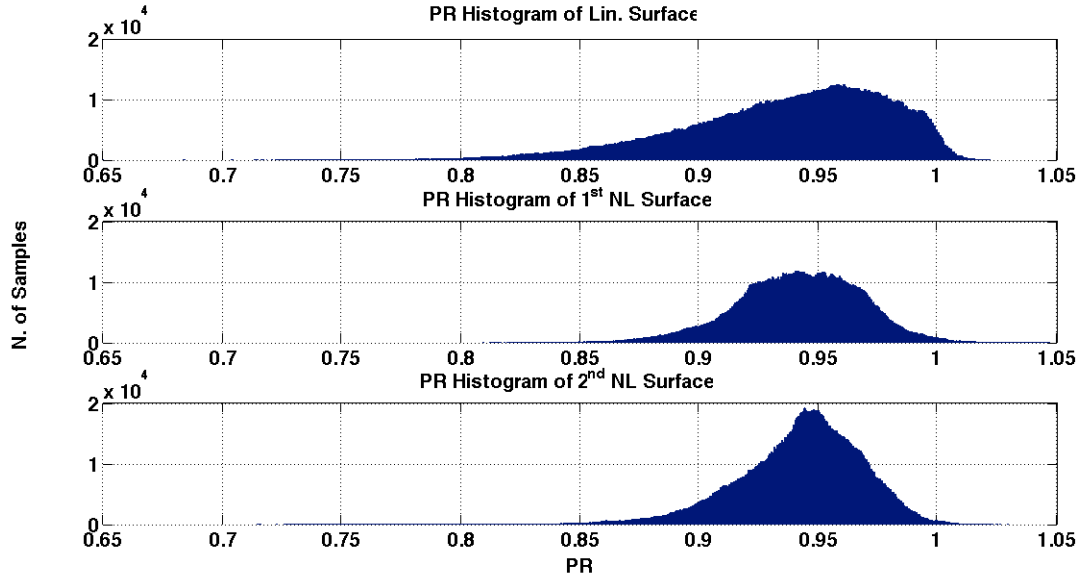
FIGURE 8.5: Histograms of PR for linear surface (top) and for the two WNL surfaces (middle and bottom).

Figure 8.5 shows interesting changes in the PR distributions, which seem to be related to the nonlinearities of the sea surface. The PR histogram for the linear surface shows an increase of the PR up to the value of ~ 0.95, and a saturation just beyond 1. The PR distribution is here in line with the scatter plots of PR vs x-slopes seen in chapter 5 (the so-called banana plots in Fig. 5.17). The PR distribution for the first WNL surface shows a clear tendency for more PR values between 0.9 and 0.95. It is therefore consistent with the x-slope distribution for that surface, since the shift in the PR distribution with respect to the linear case reflects the shift in the distribution of the x-slopes towards negative values (Fig. 8.3), and the negative skewness of x-slopes (table 8.1). For the second WNL surface, whose PR distribution is shown at the bottom of figure 8.5, the peakedness in the PR distribution is matched by the increased kurtosis of the x-slopes seen in table 8.1. An analysis of spatial NRCS and PR curves has also been conducted in the same way as those illustrated in chapter 5. The results are however not shown, as we could not identify any significant effects on the plots that could be related to sea surface nonlinearities.

8.4   Delay-Doppler Maps for realistic Glistening Zones

In this section, we look at DDMs simulated for a realistic glistening zone, and computed using a coarse (UK-DMC) DD resolution, for surfaces shown in figure 8.3 and for both a 0° and 90° wave travelling direction. The DDMs are analysed once again without including the effect of WAF, and they are shown in figure 8.6.
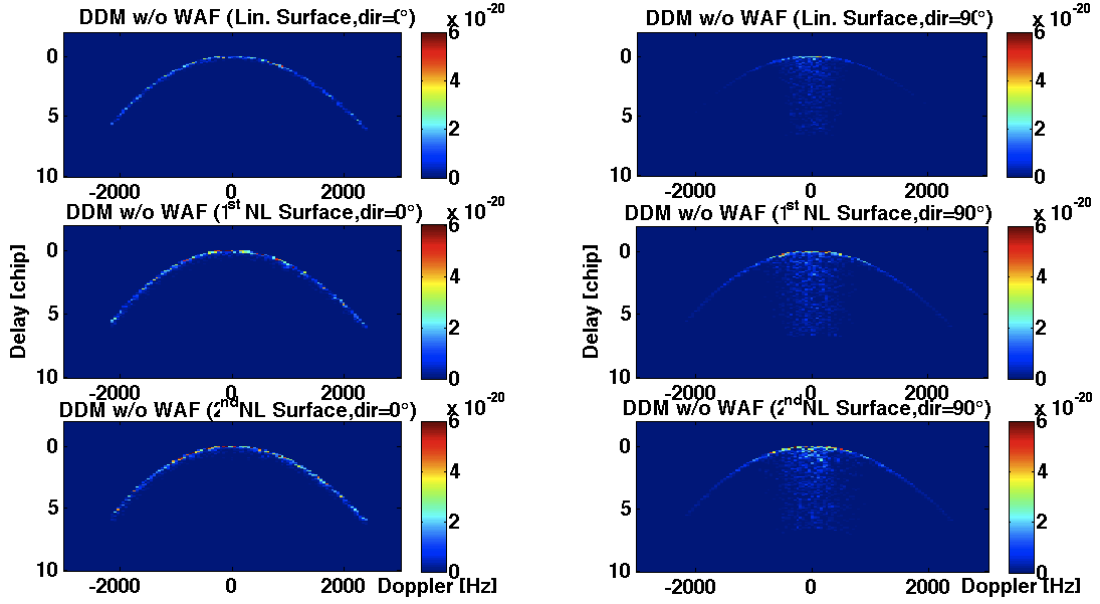
FIGURE 8.6: Full DDMs without WAF, for the linear surface and the two WNL cases (top to bottom), and for a wave travelling direction of 0° (left) and of 90° (right).

Figures 8.7 and 8.8 show the delay waveforms (top) and the Doppler waveforms (bottom), obtained through the usual incoherent integration along the Doppler and delay of the DDMs in figure 8.6, for a travelling direction of the waves of 0° and 90° respectively.

There are no major effects visible in both the DDMs and the waveforms, that can be related to nonlinearities. The overall lower values for the linear case compared to the WNL ones, that characterize both the DDM and the waveforms, are primarily the result of the differences in the roughness among the surfaces. While the two WNL cases produce DDMs and waveforms with no significant differences for the 0° wave direction case, some mild differences can be detected for the 90° wave direction case. The DDM obtained for the second WNL surface, and for a 90° wave travelling direction, shown at the bottom right of figure 8.6, exhibits some bright points right below the SP. These points are not present for the first WNL surface, whose DDM is shown in the middle of the right
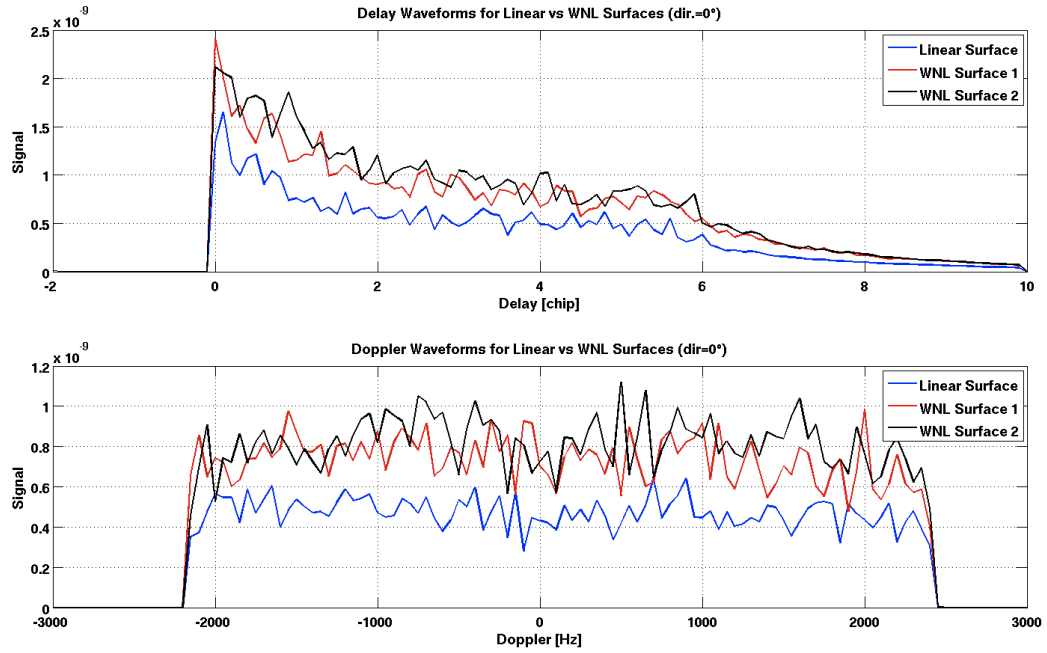
FIGURE 8.7: Delay waveforms (top) and Doppler waveforms (bottom), for the linear surface and the two WNL surfaces, for waves travelling in a direction of 0°.
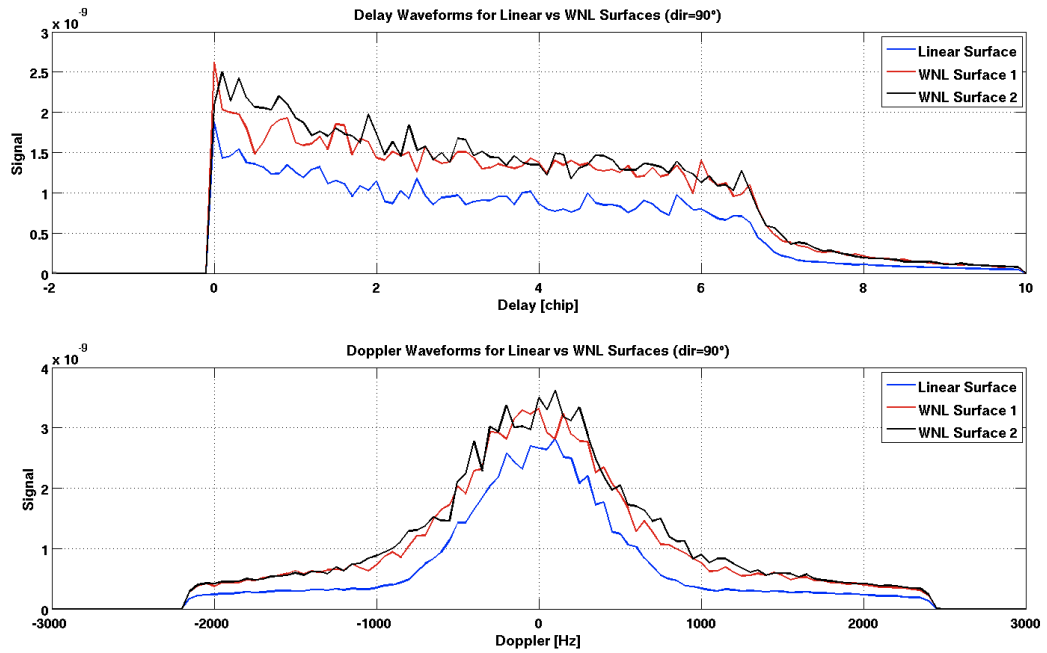
FIGURE 8.8: Delay waveforms (top) and Doppler waveforms (bottom), for the linear surface and the two WNL surfaces, for waves travelling in a direction of 90°.

column in figure 8.6. Similarly, the delay and Doppler waveform of the second WNL surface, illustrated in black in figure 8.8, exhibit overall slightly larger values around the peak, compared to the other WNL case in red. This might be partly linked to the higher kurtosis of the x-slopes for the second WNL surface, which in this case translates into a kurtosis of the y-slopes of the facets because the surface is rotated by 90° (to have a wave travelling direction of 90°). The kurtosis causes a larger number of facets to have a y-slope very close to zero, which in turn strenghtens the scattered power distribution for those points in the DDM immediately below the SP. This remains an hypothesis at this stage, and would need to be confirmed by further tests and analyses, conducted on multiple realizations. A different way to look at the effect on nonlinearities upon the scattering is through the PDF of DDM values. These PDFs are shown in figures 8.9 and 8.10, for the three surface under analysis, respectively for a travelling direction of the waves of 0° and 90°.
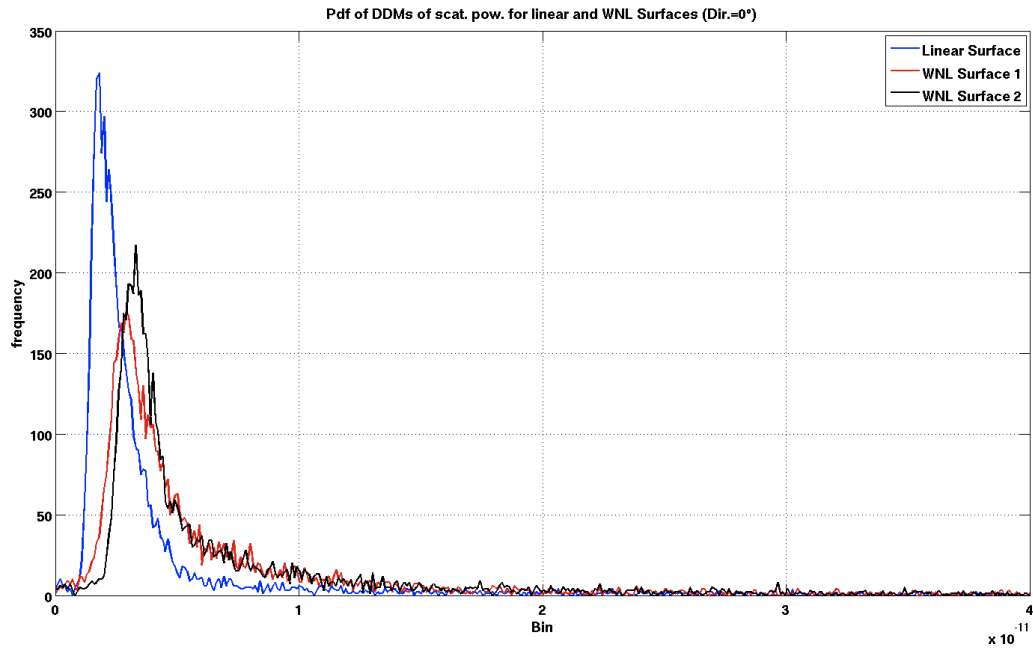
FIGURE 8.9: Pdf of DDM values, for the linear surface (blue) and the two WNL surfaces (red and black), for waves travelling in a direction of 0°.

Beside the difference between the linear case and the WNL ones, due to the different roughness and directionality between the two surfaces, we also notice in figure 8.9 a difference in the distribution between the two WNL cases. The two WNL surfaces are characterized by very similar roughness and directionality, and the differences in
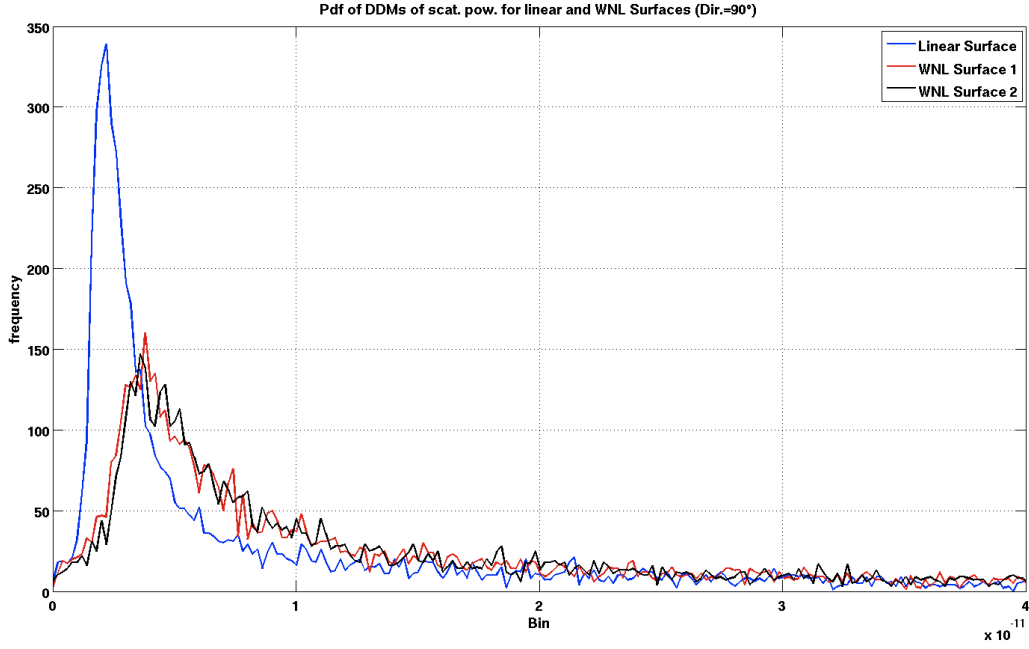
FIGURE 8.10: Pdf of DDM values, for the linear surface (blue) and the two WNL surfaces (red and black), for waves travelling in a direction of 90°.

their PDFs are probably linked to higher-order moments like skewness and kurtosis. However, it is also worth pointing out that the distributions shown in figures 8.9 and 8.10 mostly highlight the very low contributions coming from the facets that are not oriented in a favourable way, while the high contributions coming from the facets that are oriented towards the receiver are in the tail of the distribution. A way to characterize these differences in the distributions of scattered power, and link them to skewness and kurtosis of the slopes remains therefore challenging. In the following paragraph, we will see that a relationship between scattering and slope nonlinearities is potentially much easier to identify if the PR is used instead of the scattered power.

8.5 Non Linear Surfaces and Polarization

Nonlinearities on the sea surface are characterized more easily through PR rather than scattered signal. This is due to the fact that PR shows a much more well-defined dependence upon the dominant slopes, as illustrated by the banana plots in figure 5.17. As a consequence of this, the PDF of the PR values across the DDM is similar to a gaussian, and it is possible to associate a skewness or kurtosis of the PR distribution

directly to a skewness and kurtosis of the underlying slopes. Figure 8.11 shows coarse resolution PR-DDMs without WAF, for the linear sea surface (top row) and the two WNL surfaces (middle and bottom row), and for a 0° wave travelling direction (left column), and a 90° wave travelling direction (right column).
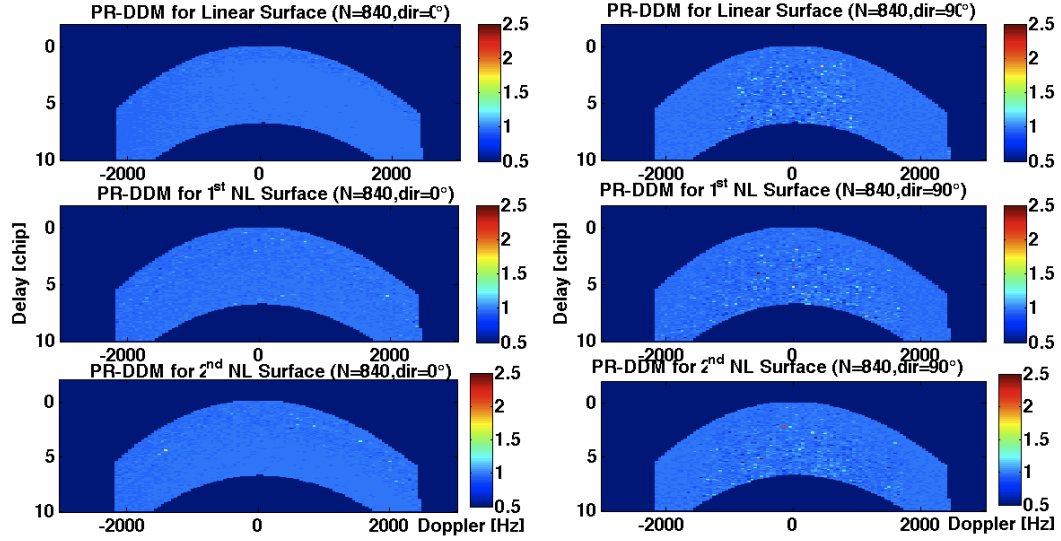
FIGURE 8.11: Left column: PR-DDMs without WAF, for JONSWAP Linear surface (top), and WNL surfaces (middle and bottom), with waves travelling in a 0° direction. Right Column: PR-DDMs without WAF, for the same surfaces, but with waves travelling in a 90° direction.

Apart from the differences in the DDMs linked to different directionality and direction of the waves, discussed in chapter 6, not much can be said about non-linear waves from figure 8.11. An analysis of the statistical distribution of the PR-DDM values in figure 8.11 reveals however some interesting characteristics. Figures 8.12 (a) shows the PDFs of PR values for the three surfaces under analysis, for a 0° travelling direction of the waves. For comparison, the PDF of the x-slopes is also shown in figure 8.12 (b).

In figure 8.12 (a), we can notice a more pronounced asymmetry for the PR distribution of the first WNL surface (red), compared to the other two cases. The PDF highlights a larger number of facets with PR values lower than the average (~ 0.97), which would be consistent with the positive x-slope skewness (larger number of negative slopes) that characterizes this surface, as shown in red in figure 8.12 (b). It is worth noting that here the PDF for the linear case (blue) does not show the asymmetry that characterized the spatial PR distribution, illustrated in figure 8.5, and attributed to the PR saturation for values beyond 1. This is however not too surprising, as the PR distribution illustrated

PDF of PR values of DDM

(a)

PDF of x-slopes

(b)
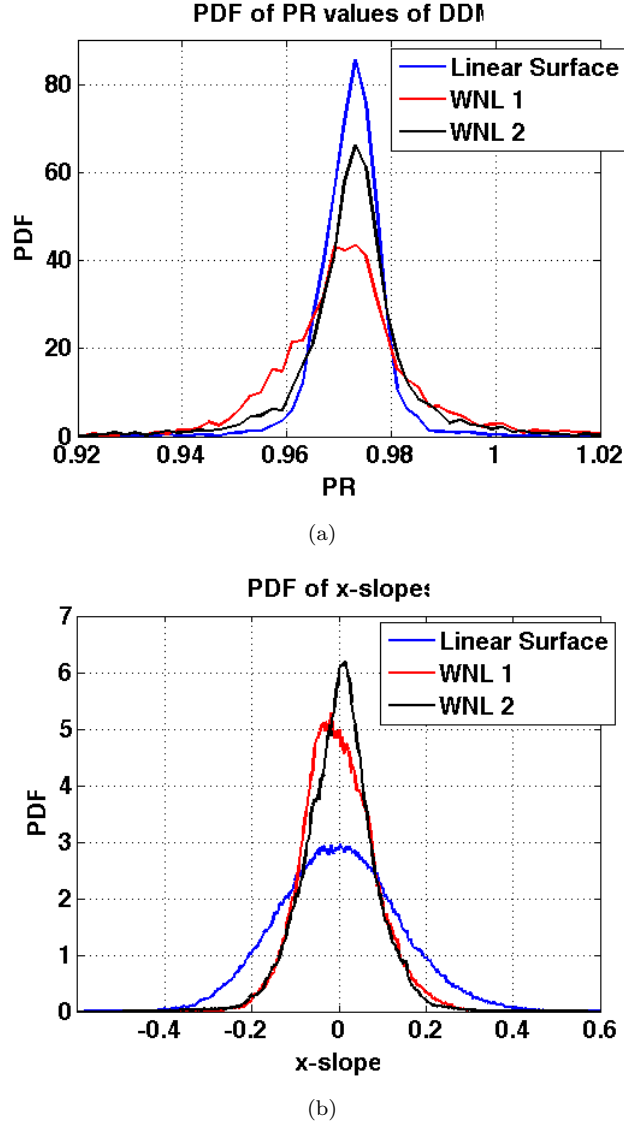
FIGURE 8.12: (a) Pdf of PR values across the DDMs for the linear surface (blue) and the two WNL surfaces (red and black), for a 0° wave travelling direction. (b) Pdf of x-slopes for the three cases.

in 8.12 refers to a distribution in delay-Doppler domain, and relative to a much larger glistening zone of hundreds of kilometers (while that of figure 8.5 was only for a small patch, of side 0.5 km, and centered at the SP). The kurtosis is harder to detect, because the higher directionality of the linear surface is dominant and produces a very peaky PDF for the linear case. However, the width of the peak for the second WNL surface (black), is smaller compared to the other two cases, and this would match the high kurtosis of the x-slopes for this case (shown in black in figure 8.12 (b)). Finally, we show in figure 8.13 the PR distribution for a 90° wave travelling direction, along with the PDF of y-slope for the three surfaces.

(a)

(b)
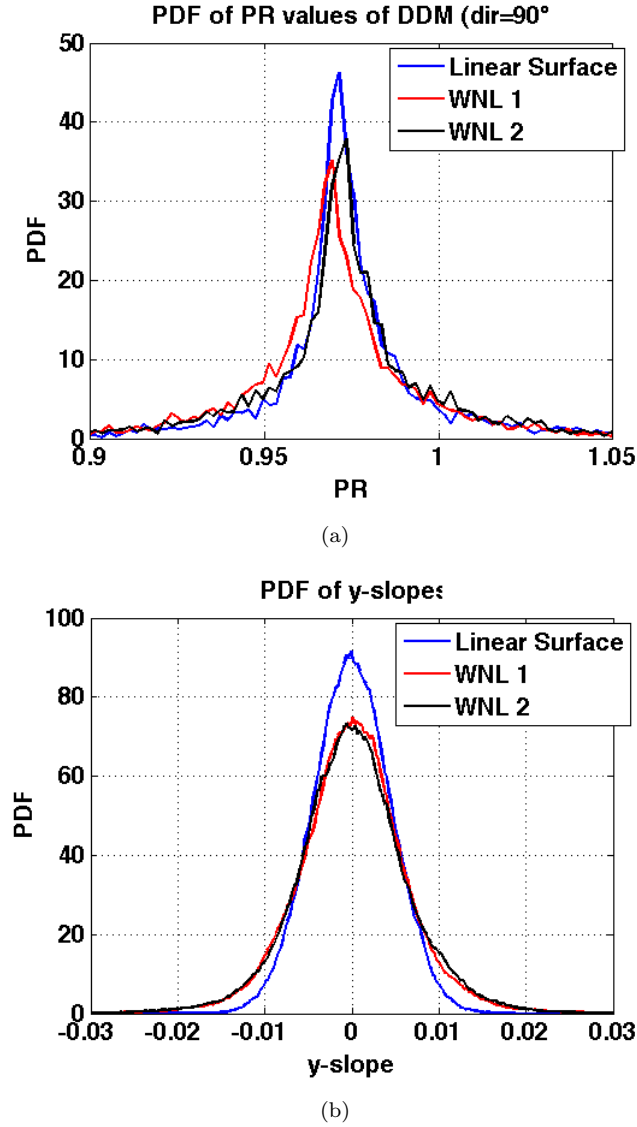
FIGURE 8.13: (a) Pdf of PR values across the DDMs for the linear surface (blue) and the two WNL surfaces (red and black), for a 90° wave travelling direction. (b) Pdf of y-slopes for the three cases.

Figure 8.13 shows a shift in the peak of the PR distribution of the first WNL surface (shown in red), compared to the other two cases. We could not find an obvious explanation for such a shift, as in this case the waves are travelling orthogonal to the incidence plane, and there is no major skewness of the y-slopes in this case. However, it might be possible that the scattering is still influenced by the skewness of the x-slopes. It is worth mentioning that even in this case an analysis of DDM subsets (of both scattered power and PR) computed for high DD resolution has been carried out, to investigate the effect of non-linear waves. The analysis did not highlight any significant effect in high-resolution DDMs, that could be clearly and unequivocably attributed to non-linear

waves. This is probably due to the fact that the DDM subsets only offer a high-resolution picture of what happens in selected areas of the glistening zone. In this sense, non-linear effects are identified better in the DD domain if the scattering picture the entire glistening zone is available, even at a coarser resolution. For brevity and simplicity, the results of the high resolution analysis are therefore not shown.

8.6   Conclusions

In this chapter, we have considered the GNSS-R scattering for non linear sea surfaces. The degree of nonlinearity can be expressed as skewness and the kurtosis of the statistical distribution of the slopes along x and y. The effects of non-linear waves have been investigated with the FA model both in the space domain and in the DD domain, through respectively an analysis of RCS and PR, and the analysis of DDMs. The results in space domain have revealed the influence of the skewness and kurtosis of the slope distribution on the PDF of PR. Regarding the single look coarse resolution DDMs, the effect of nonlinear waves are hard to detect. Some mild effects have been detected in the DDMs, that could partly be linked to the kurtosis of the slope distribution, but they are often mixed up with the random phase of each DD cell, and with instantaneous features linked to the particular realization. A promising approach for detecting non-linear effects in the DDMs is to look at the PDF of PR values of coarse-resolution DDMs. We have found a shift in the PR distribution towards lower values for the first WNL surface, that is consistent with the positive skewness of the x-slope distribution of the surface. Furthermore, the peakier PR distribution for the second WNL surface also matches the higher kurtosis of the x-slope distribution of that surface. These represents exciting results, that could open up new perspectives into the possibility of exploiting polarization to detect non-linear waves on the surface of the ocean, and strenghtening even further the importance of polarization for future GNSS-R missions. However, these conclusions need far more analysis to be confirmed. In particular, the effects of nonlinear waves on polarization need to be tested on a large number of sea surface realizations. This should include both truly linear surfaces, and non-linear surfaces with a high enough skewness and kurtosis of the slope distribution, to make these effects visible. Unfortunately, we

did not have these surfaces to perform a deeper analysis, and we leave it as a future work that needs to be done.

CHAPTER 9

Conclusions and Perspectives

9.1 Summary and Conclusions

The main aim of this dissertation was to assess the way the ocean waves influence
the GPS signal scattering, providing a comprehensive characterization of the response
of GPS reflected signals to different wind and wave conditions. This was first done
through the use of real data, and then through simulations of the scattering of GPS
signals from realistic ocean surfaces. Initially a retrieval of ocean roughness parame-
ters from four UK-DMC GNSS-R datasets has been performed through a least-square
fitting of data delay-Doppler maps to theoretical ones, generated using the existing
Zavorotny-Voronovich model. The retrievals have been compared and validated against
measurements from co-located NDBC buoys, and theoretical calculations, and a reason-
able agreement was observed, even though the four case studies corresponded to quite
atypical seas [Clarizia et al. (2009b)]. Subsequently, a GPS scattering simulator has
been developed using explicit 3D ocean surface representations, and an innovative facet-
based scattering model, called the Facet Approach (FA). The simulator has produced
interesting and promising results in terms of scattering sensitivity to different complex
linear (Gaussian) surfaces, and to weak nonlinearities of sea surface, and it has shown

some effects on polarization linked to the sea surface characteristics. Results in spatial domain have been presented as 2D maps of NRCS and PR. These exhibit clear features related to the explicit waves of the underlying sea surface [Clarizia et al. (2012)]. When moving from the spatial to the delay-Doppler domain, an extensive analysis of WAF-free DDMs of both scattered GPS power and polarization ratio, computed at a coarse DD resolution, has been carried out for a variety of different ocean surfaces, both linear and non-linear. This analysis has in particular highlighted the importance of:

1. Wave directionality, as it is a parameter that influences the DDM dependence on sea surface roughness, the ability to discriminate different wave directions, and the depolarization of the scattered signal;

2. Polarization, as it can convey information on wave direction and directionality, and potentially be used to identify nonlinearities on the sea surface

An investigation into DDM subsets, computed at a high DD resolution, and corresponding to different locations across the glistening zone, has also been presented. It has been shown that under certain conditions (i.e. wavefronts travelling parallel to the iso-Doppler lines, or wavefronts that are reasonably in phase when the spatial ambiguity affects the DDM subset) these maps could provide useful information about wave parameters like the range of surface heights, the wavelength of the dominant wave component (i.e. a swell), or the direction of the waves, through the DDM spectrum. In particular, these DDM subsets can potentially become a 1D or 2D map of sea surface reflectivity, the latter when the spatial ambiguity is removed. The research and results presented in this PhD dissertation represent novel contributions to the field of GPR-Reflectometry. The analysis of satellite GPS-R data represents the first one that makes use of the whole DDM and of data collected onboard a satellite. This complements previous analyses of satellite delay waveforms [Gleason et al. (2005)] and of DDMs from aircraft campaigns [Germain et al. (2004)]. The results obtained offer convincing evidence for using GNSS-R to retrieve wind and wave data using a small passive instrument that could easily be fitted on more satellites [Clarizia et al. (2009b)]. The GPS polarimetric scattering simulator developed for this PhD is the first simulator conceived for GPS-R purposes,

that makes use of explicit sea surface realizations, and of an innovative polarimetric large-scale scattering model (FA). Although similar formulations exist in literature [Balanis (1989)], the equations for the FA scattering model, as well as the criteria for the choice of the facet size, have been derived independently in this dissertation. The results from the simulator have highlighted the importance of wave directionality, a parameter whose importance has never been stressed before in GNSS-R, and has confirmed the importance and potentials of polarization, which had already been recognized by [Zuffada et al. (2004)] and [Thompson et al. (2005)], using scattering models different from FA. In particular, we have carried this even forward by identifying two wave parameters (wave directionality and wave direction) that mostly affect polarization ratio. Finally, we have presented some promising results on the effect of nonlinearities on DDMs, and in particular on polarization ratio. These results need further analyses and tests to be confirmed. If this happens, then this would constitute a further demonstration of the effect of non-linear waves in GPS-Reflectometry, shown for the first time in [Cardellach and Rius (2008)], and would stress even further the importance of polarization as a potential source of information for sea surface nonlinearities.

9.2 Future Work

Several aspects of the analysis conducted in this dissertation require some extra study and investigation for the future.

- The results on the retrievals of sea surface roughness certainly offer some scope for future GNSS-R missions for wind and wave monitoring, but the limited number of datasets (four UK-DMC GPS-R data) available at that time does not make it conclusive. A necessary step forward would be therefore to analyse all of the UK-DMC collections of GPS reflections. This would allow to consolidate the results from the four datasets used so far, by extending the conclusions to a much larger ensemble of data collection, corresponding to heterogeneous wind and wave conditions. This task is being currently carried out in the context of the WaveSentry

project (http://groupspaces.com/WaveSentry/), and the results will be available later in 2012.

- As regards the GPS scattering simulator, one important way forward is to extend the scattering model, by including the scattering contributions from small scale roughness components. The FA model itself is a large-scale scattering model, and although this is generally thought to be the dominant scattering mode [Zavorotny and Voronovich (2000)], there are suspitions that a Bragg-type scattering due to small scale roughness can in particular affect the areas at the edge of the GZ. This could contribute to fill gaps between the theoretical DDMs and the measured DDMs, where a much slower power drop-off has been observed compared to simulated DDMs, indicating more scattered power away from the SP than that predicted by the Z-V model. One interesting approach could be to assume slightly rough facets, and calculate the scattering by combining a deterministic large-scale contribution, where the inclination is known for each facet, with a statistical small-scale contribution of the small ripples on each facet. Similar approaches are already present in the literature [Arnold-Bos et al. (2007a), Arnold-Bos et al. (2007a), Franceschetti et al. (1998), Zhang et al. (2011)], but none of them has been so far applied in a GNSS-R context.

- This dissertation has also undoubtedly proved that both sea surface nonlinearities and polarization are two aspects well worth considering and exploring in greater details for the future. A more extensive study on a larger number of different nonlinear surfaces should be addressed in the future to consolitate and characterize better the effect of such nonlinearities. The study on polarization presented here should be completed with an analysis of PR changes with respect to different geometries, and above all different incidence/scattering angles. This would allow not only to confirm the changing polarization behaviour observed in [Zuffada et al. (2004)] and [Thompson et al. (2005)] for different scattering angles, but also to establish what geometrical configuration enhances best the polarimetric effects in GPS signal scattering. Furthermore, the effects on polarization, here investigated through simulations only, should be explored with some real data collected at

spaceborne, which are at present not available since only a single polarization has been captured from the UK-DMC satellite.

- Some of the assumptions that we have used for DDM simulations could be also thought as improvements needed for future GNSS-R missions. The study conducted here characterized the DDM response to different sea surfaces, without considering the effects of signal processing (WAF) and noise, and assuming in some cases that a DDM can be computed at a high DD resolution. Therefore, an increase in the DDM resolution, and a reduction of both the effect of WAF and of the noise floor can be identified as important aspects where the effort should be concentrated in the future, to improve the DDM capability to convey information about sea surface waves. As far as noise in the DDMs is concerned, the GNSS-R experiment onboard the UK-DMC was designed as a simple proof-of concept, and even though it met and far exceeded the goal, the electronics of the instrument was not optimized, and the reflections were affected by a relatively high thermal noise in the receiver, as well as several limitations and problems in the receiver hardware. Great improvements have already been brought in the receiver hardware capability (by P. Jales, PhD student at SSTL), and future GNSS-R missions (like the forthcoming SSTL TechDemoSat) are expected to deliver near-real time DDMs with an improved quality of the signal reflection, and with a much lower noise floor. The WAF is also expected to be much narrower in the future, thanks to the forthcoming availability of new navigation signals, such as those from Galileo or Beidou/Compass (the chinese navigation satellite system), characterized by a much wider bandwidth, and an improved matched filter. Recent studies have also been conducted on applying established signal processing techniques that increase the resolution to GNSS-Reflectometry, with a particular focus on the MUSIC algorithm [Bouchereau et al. (2001)]. This is a statistical technique that exploits the presence of thermal noise of the observations, and the orthogonality of the signal and noise subspace, to derive a delay profile at higher resolution than that dictated by the GPS correlation function [Bouchereau et al. (2001), Clarizia et al. (2009a)]. The only requirement for the application of this technique is a high enough sampling rate of the received signal. The super-resolution algorithm has been tested

so far through simulations, showing a promising increase in delay resolution [Clarizia et al. (2009a)]. Studies and experiments are currently being conducted to prove the applicability of this technique to the full DDM, taking into account the Doppler shift, and producing a 2D high-resolution delay-Doppler profile. It is also worth pointing out that an increase in the resolution could potentially lead to the use of GNSS-R for surface wave imaging, and produce high-resolution DDMs like those shown in this dissertation. More work is needed in the near future in all this fields to ultimately produce improved DDMs, and increase the capability to extract information about the sea surface from them.

- Finally, an interesting future application, brought about by the appealing and exciting perspective of surface wave imaging through GNSS-R shown in this research, could be the use of GNSS signals of opportunity for bistatic SAR. The concept of Bistatic SAR using navigation signals is not new [Cherniakov (2008)], but the unsuitability of the GPS signals never made it really worthwhile. The current and future availability of new navigation signals, multiple reflections, innovative signal processing and improved receivers has the potentials to increase radically the capability of such a technique, making it in my opinion well worth being attempted in a not too distant future.

9.3 Recommendations for Future GNSS-R Missions

The results of this study have contributed to identify some key recommendations for the GNSS-R missions still to come. These can be summarized as follows:

1. As far as GNSS-R acquisitions are concerned, calibration of the GNSS-R data, and the availability of a large validation datasets are fundamental. The GPS scattering simulator has shown that some of the DDM sensitivity to sea surface characteristics is related to the amplitudes of the scattered signal in the DDM. This is therefore an information that needs to be preserved and exploited when the sea surface roughness is retrieved from DDMs. For validation, the locations of the UK-DMC GPS-R acquisitions were chosen only based on locations of NDBC

buoys. A large potentially much more extended collocation dataset could be built for the future, including in situ instruments like buoys, as well as satellites able to provide roughness information (i.e. altimeters, scatterometers, SAR). In view of this, the timing and locations of the captured reflections for future GNSS missions should be carefully chosen in order to maximize the available collocation dataset for validation.

2. The sensitivity of polarization with respect to different sea surfaces, with different complexity, constitute one of the most important findings of this PhD research, and justifies the need for two receiving antennas for future GNSS-R missions, able to capture both LHCP and RHCP scattered signals. This will polarization effects (both linear and circular) should be investigated in real data, hopefully confirming the effects of sea surface properties on polarization detected in the simulations.

On the basis of the work presented in this PhD dissertation, and the recommendations listed above, the conclusion can be reached that the future of GNSS-R as a technique for observing the ocean looks promising, and the support for this technique from the scientific community should be strong and sustained. Over the next few years, with the launch of new positioning systems and new GNSS-R receivers or constellations of receivers, rapid progress in developing these techniques further is to be expected.

Appendix I

Analysis of GNSS-R delay-Doppler maps from the UK-DMC satellite over the ocean

M. P. Clarizia,[1,2] C. P. Gommenginger,[1] S. T. Gleason,[1] M. A. Srokosz,[1] C. Galdi,[2] and M. Di Bisceglie[2]

[1] A study of the retrieval of sea surface roughness using Global Navigation Satellite System-Reflectometry (GNSS-R) from satellite is presented. Delay-Doppler Maps (DDMs) from the SSTL UK-DMC satellite are analyzed to retrieve directional Mean Square Slopes (MSSs). Results are compared to theoretically-derived MSSs and in situ measurements from co-located buoys of the National Data Buoy Center (NDBC), showing good agreement in most cases. Here, the whole DDM, a more complete source of information, is exploited for the first time using satellite GNSS-R data. These are potentially able to provide high spatial and temporal sampling, and therefore offer an improved way to observe wind and waves by means of a very modest instrument. **Citation:** Clarizia, M. P., C. P. Gommenginger, S. T. Gleason, M. A. Srokosz, C. Galdi, and M. Di Bisceglie (2009), Analysis of GNSS-R delay-Doppler maps from the UK-DMC satellite over the ocean, *Geophys. Res. Lett.*, *36*, L02608, doi:10.1029/2008GL036292.

1. Introduction

[2] It has been widely demonstrated that signals emitted from Global Navigation Satellite System (GNSS) constellations (GPS, GLONASS, and Galileo) can be used not only for positioning, but also for remote sensing. In particular, GNSS signals scattered by the surface of the ocean carry information about the sea surface, and can be exploited to investigate its geophysical properties. This technique, first proposed by *Martin-Neira* [1993], and now known as GNSS-Reflectometry (GNSS-R), represents an innovative approach to ocean remote sensing. *Ruffini et al.* [2003] pointed out that GNSS-R for oceanography primarily aims at investigating three important geophysical parameters, namely directional Mean Square Slope (MSS), Significant Wave Height (SWH) and Mean Sea Level (MSL). Consequently, GNSS-R has both scatterometric (sea roughness, wind speed and direction) and altimetric (SWH and MSL) applications. Excellent temporal sampling, global coverage, and long-term GNSS mission lifetimes are among the factors of GNSS signals which make this technique very attractive, and particularly suitable for observing the ocean surface, which is highly variable in space and time. Our analysis focuses on the investigation of sea surface roughness using satellite-measured GPS-Reflected signals from the Surrey Satellite Technology Ltd UK-DMC mission, which are the only satellite GNSS-R data available to-date.

From these data, we have retrieved MSS in two orthogonal directions and the principal wave slope direction, using a 2D representation of the scattered GPS signal power as a function of the time delay and the Doppler frequency, the so-called Delay-Doppler Map (DDM). To-date, researchers have analyzed 1D delay waveforms from data collected during airborne campaigns [e.g., *Garrison et al.*, 1998; *Cardellach et al.*, 2003] or from the UK-DMC satellite [*Gleason et al.*, 2005], to derive total mean square slope or sea surface wind speeds. The advantages of using 2D DDMs were highlighted by *Germain et al.* [2004], who inferred directional MSS using DDMs from data collected during an airborne campaign. In our case, we benefit from the twofold advantage of using DDMs and satellite data, which in principle are globally distributed and constantly available and accessible, without the need to fly ad-hoc campaigns. The GNSS-R technique is based upon a bistatic configuration of the transmitter and receiver, and the scattering problem involves L-Band (1.2–1.5 GHz) GPS signals transmitted from satellites at altitudes of about 20000 km, which are scattered off the ocean and received onboard the low-orbit sun-synchronous UK-DMC satellite, at an altitude of about 680 km. The main contribution to the scattered signal power at the receiver comes from the Specular Point (SP) on the surface, and an area around it called the Glistening Zone (GZ), which widens with increasing sea surface roughness. The scattering of GNSS signals can be described using Geometric Optics (GO), according to which it depends mainly on the Probability Density Function (PDF) of the large scale surface slopes. If we assume the statistics of the waves are Gaussian, a reasonable assumption, the PDF is entirely characterized by three variables: two MSSs along the major and minor axes of the 2D Gaussian PDF, and an angle which defines the rotation of the principal axis with respect to true north, and therefore identifies the principal scattering direction, to within a 180° ambiguity. We retrieved these geophysical parameters by comparing UK-DMC DDMs with theoretical DDMs from a GO model. Details of the DDM processing are given in section 2. Section 3 explains the retrieval of the directional MSSs and the principal and secondary surface slope directions. In section 4, results are compared with theoretical MSS estimates as well as with collocated in situ data from buoys of the National Data Buoy Center (NDBC). Finally, section 5 states the conclusions.

2. UK-DMC Data Processing

[3] The data were collected onboard UK-DMC, equipped with a GPS receiver, a solid state data recorder and a Left–Hand Circularly Polarized (LHCP) medium gain antenna

---

[1]National Oceanography Centre Southampton, Southampton, UK.
[2]Università degli Studi del Sannio, Benevento, Italy.

Table 1. Available UK-DMC GPS-R Data Collections, Together With Collocated in Situ Measurements by NDBC Buoys[a]

Label	Date/Time	Region	NDBC Buoy Id	Buoy WS (m/s)	Buoy WD (deg)	Buoy MWD (deg)	Buoy SWH (m)	SCR (km)
R12	16/11/04 07:54	NW Pacific	46006	8.3	253	N/A	2.80	[38−56]
R20	21/03/05 07:29	NW Pacific	46002	3.6	297	N/A	4.30	[32−58]
R21	02/05/05 09:16	Hawaii	51001	4.5	23	N/A	1.98	[1−44]
R29	29/10/05 14:40	Virginia	44014	9.4	326	341	1.68	[70−79]

[a]WS is wind speed, WD is wind direction, MWD is mean wave direction, and SCR is space collocation range, given by the distance of the buoy from the closest to farthest SP within the 12-second time interval. The buoy directions are measured clockwise with respect to true north.

(peak gain of 11.8 dBiC) pointing downward, and covering a large footprint (3 dB beam of about 1000 km × 200 km). The Daaxa GPS software receiver we used to process the data on-ground, illustrated by *Gleason* [2006], performs a down conversion of the signal to base band, and samples it at a rate of 5.714 MHz. Subsequently, the signal is coherently correlated with a locally generated C/A code replica to produce a single "look", and multiple looks are then incoherently summed to produce the final delay-Doppler map. DDMs are computed using a delay step of 0.18 C/A code chip (1 chip $\sim 1 \ \mu$s), and a Doppler bin of 100 Hz. The choice of the Doppler bin represents a trade-off between the need to reduce noise and the need to maintain a good resolution and hence preserve features in the map. We coherently integrated 1 ms of data, following *Gleason* [2006], where the maximum correlation power is obtained for a coherent integration time close to 1 ms. This result is linked to the length of the C/A code (which is about 1 ms), as well as to the changing scattering geometry due to the satellite motion, which limits the coherence of the received signal. The incoherent accumulation time was chosen equal to 1 second and 12 seconds respectively. The choice of the 1-second accumulation time is consistent with the averaging used in satellite nadir altimetry. Moreover, it represents a convenient choice, as it allows us to estimate the variability of the parameters within a 12-second time interval. The choice of the 12-second accumulation time helps increase the signal-to noise ratio in the DDM. This gives a smoother DDM, which is easier to fit, but provides no insight into the variability of the retrieved parameters. It is worth noting that during the accumulation time the signal experiences a shift both along the Doppler and (above all) along the delay axes, which must be accounted for when the single looks or the single maps are accumulated. During a 1 second accumulation time, the shift along the delay axis has been estimated for each millisecond, and used to align the consecutive looks before accumulating them. This shift is nearly linear over 1 second (the second derivative of the code delay can be neglected), whereas the shift along the Doppler direction is negligible. For the 12 second accumulation time, the shift along the Doppler direction also starts to play a role, and single 1-second DDMs are aligned using the 2D cross-correlation between them. Here, the analysis was carried out on four data sets only, as they were the only data available at the time. These data were collected at different times, for different Pseudo Random Noise (PRN) codes (which identify the GPS satellites) and different sea conditions. All were collocated with in situ measurements of wind and waves by NDBC buoys to within 1 hour and 100 km [*Gommenginger et al.*, 2002]. Table 1 shows the co-located buoy data for wind speed, wind direction, and Significant Wave Height (SWH), for each data collection. An examination of the buoy wind/wave histories (not shown) indi-

cates that the four situations are atypical seas. The wind/wave history for dataset R12 indicates a moderate but highly variable wind speed with a lot of swell, whereas R20 corresponds to a decaying sea with rapidly decaying wind speed (from 12 m/s to 4 m/s in 12 hours). For R21, the buoy history shows overall steady wind conditions of around 5 m/s wind speed, with some swell, while R29 corresponds to conditions of growing sea.

3. Simulated Delay-Doppler Maps

[4] Once DDMs from satellite data have been generated, we estimate the parameters of interest by comparing them with simulated DDMs. The GO model used was developed by *Zavorotny and Voronovich* [2000] and describes the scattering of GNSS signals from the sea surface. The average GPS scattered power, as a function of delay and Doppler frequency, is:

$$\langle P_S(\tau,f) \rangle \propto \iint \frac{G_R(r)}{R_T^2(r)R_R^2(r)} \frac{q^4(r)}{q_z^4(r)} P\left(\frac{-q_\perp(r)}{q_z(r)}\right) \cdot \chi^2[\tau - \tau_k(r), f - f_k(r)]dr \qquad (1)$$

where r represents the spatial coordinate on the scattering surface, $G_R(r)$ is the receiver antenna gain, $R_T(r)$ and $R_R(r)$ are the ranges between the scattering point and the transmitter and receiver respectively, $\chi[\tau - \tau_k(r), f - f_k(r)]$ is the Woodward Ambiguity Function (WAF) of pseudorandom GPS sequences, function of the delay and Doppler coordinates $\tau_k(r)$ and $f_k(r)$, $q(r) = [q_x(r), q_y(r), q_z(r)]$ is the scattering vector, and finally $P(-q_x(r)/q_z(r), -q_y(r)/q_z(r))$ is the sea surface slope PDF, assumed to be a two-dimensional zero-mean Gaussian distribution. The PDF is characterized by two MSSs along the major and minor axes of the PDF ellipse, and by a rotation angle Φ of the major axis of the PDF (which we take as the principal scattering direction) with respect to true north. However, we emphasize that a 180° ambiguity characterizes the rotation angle due to the symmetry of the PDF. The DDM simulation requires the calculation of the SP, as well as some geometrical conversions, for which the satellite positions and velocities are needed. We have used the actual positions and velocities of GPS satellites and UK-DMC to generate DDMs and fit them to the 1-second measured DDMs. For the fitting to 12-second averaged DDMs, we averaged positions and velocities over a 12-second interval to generate the simulated DDM. An example of a 1-second DDM from UK-DMC data (top), and a modelled DDM (bottom) is shown in Figure 1. This shows similarities in the overall horseshoe shape of the two maps, but the real DDM exhibits some additional horizontal striping patterns, not present in the simulated map. Such patterns could be either linked to some residual speckle
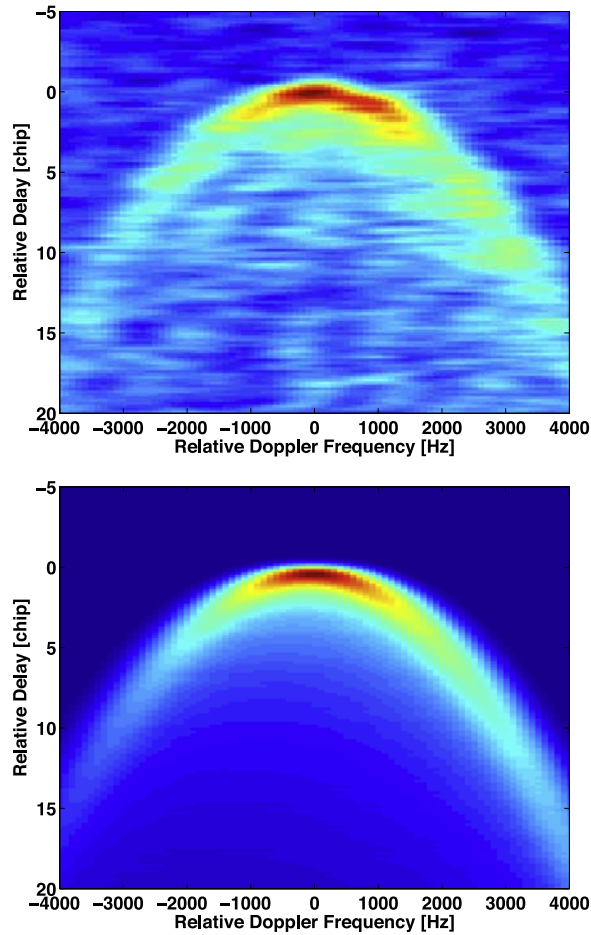
Figure 1. (top) Measured DDM obtained from the first second of UK-DMC R21 data and (bottom) simulated DDM using the Zavorotny-Voronovich model. Both delays and Doppler frequencies are expressed relative to those at the SP.

noise, or other types of scattering (i.e., Bragg scattering), not taken into account by the theoretical model. We have performed a least-square fit between measured and simulated DDM, to find the optimal PDF parameters, for the four data sets. However, we were not able to exploit the magnitude information in the DDMs, and only used the shape for the retrievals, due to the significant difference in the power values. This difference is primarily due to the lack of a calibration of the incident GPS signal, as well as unrecorded effects within the receiver (amplifiers, automatic gain control), affecting the amplitude of the received signals. We defined a scale parameter a and offset parameter b as further variables to be optimized, such that the new simulated DDM becomes $P_S'(\tau, f) = aP_S(\tau, f) + b$. A joint estimation of five variables (MSS_1, MSS_2, Φ, a, b) was performed to minimize the residual error between UK-DMC and modelled DDM, with a standard non linear least-square minimization routine using MATLAB.

4. Results and Discussion

[5] Figure 2a shows the median of 12 retrieved total MSS from 12 1-second DDMs. The variability is represented with the Median Absolute Value (MAD), defined as the median

of the absolute residuals from the median of the data. The choice of more robust statistics to represent the results was dictated by the presence of outliers in the retrievals, possibly caused by convergence of the fitting algorithm to local minima in some cases. The total MSS is simply calculated here as the sum of the two MSSs along the major and minor axes of the PDF ellipse. Figure 2a also shows the single retrieved total MSS from the 12-second average DDM. All results are plotted versus the buoy wind speed for each data collection. Unlike *Germain et al.* [2004], we could not compare our results with altimeter-derived MSSs, as no suitable altimeter data was available within acceptable
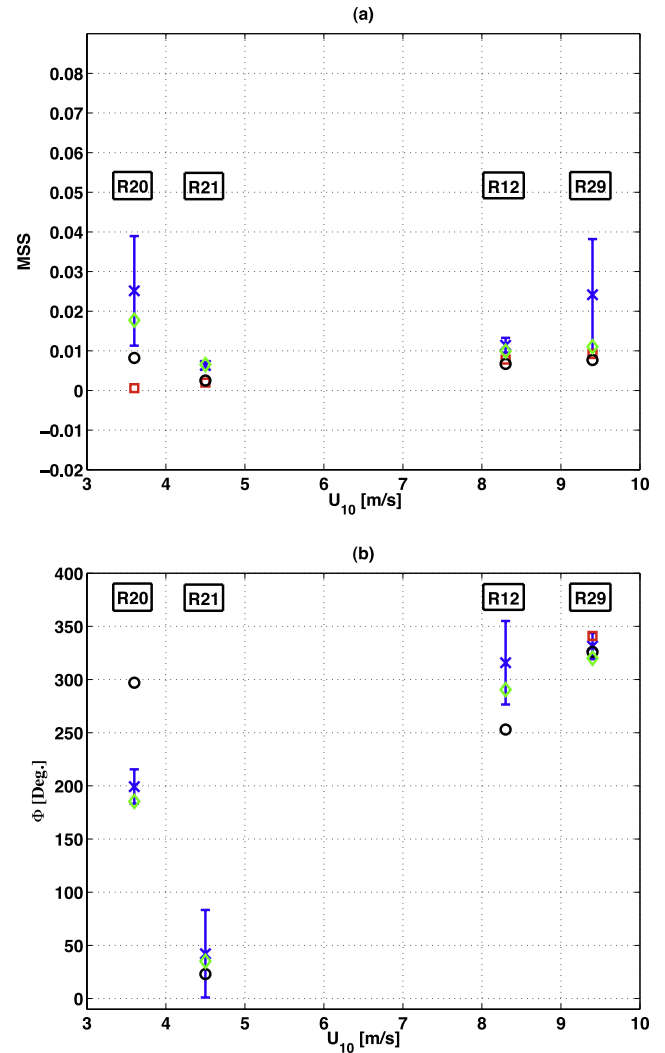
Figure 2. (a) Median of the total retrieved MSSs from 1-second DDMs over 12 seconds (crosses) with MAD (as error bars) and MSSs estimated from 12-second averaged DDM (diamonds), versus buoy wind speed. Total MSSs from the truncated theoretical Elfouhaily wind wave spectrum (squares) and buoy-derived total MSSs (circles) are also illustrated for comparison. (b) Median of the retrieved principal slope directions from 1-second DDMs (crosses) with MAD (error bars) and slope directions estimated from 12-second averaged DDM (diamonds), versus buoy wind speed. Buoy wind directions (circles) and MWD (square) are given for comparison.

space/time separation limits. From Figure 2a, we notice the good agreement and lower variability for the case of R21 (steady conditions with some swell) and R12 (swell, high wind speed variability), compared to the cases of R20 (decaying sea) and R29 (growing sea), where the median MSSs are higher than the buoy measurements. This could be explained for R29 by the stronger wind speed, generating higher short waves, not sensed by the buoys, which would raise the MSS retrieved from the GPS-R signals. The wind/wave conditions for R20 are more subtle, in that the wind speed was quite high (12 m/s) before the acquisition time, and rapidly dropped to 4 m/s at the time the data were collected, possibly leaving behind a wind wave component and therefore a higher MSS, not related to the instantaneous wind speed. In Figure 2a, our estimated MSSs are compared with MSSs calculated by integrating the buoy measured wave spectrum, which covers a range of wavelengths down to 9.75 m only, and by integrating the theoretical *Elfouhaily et al.* [1997] wind wave spectrum, down to a specific wavelength cutoff, which was again set to 9.75 m. The Elfouhaily spectrum is theoretically derived under the assumption of well-developed wind seas, whereas the buoy spectrum is obtained from real measurements.

[6] Figure 2a highlights that our retrieved MSSs show the same behaviour as the buoy-measured MSSs, and are always higher than them, which is consistent with the sensitivity of the GPS wavelength (19 cm) to shorter waves. For MSSs retrieved from single second DDMs, we get good results for the cases of R21 and R12, as the MAD is quite small, and both the buoy and the theoretical Elfouhaily-truncated MSSs are in good agreement with our estimates. Very good results are obtained for MSSs retrieved from averaged 12-s DDMs, as they appear to be quite close to both the values measured by the buoys and the MSSs obtained from the theoretical spectrum, except at R20 (rapidly decaying sea). The retrieved principal surface slope direction results are plotted in Figure 2b versus buoy wind speed. The Mean Wave Direction (MWD) was available only for R29, when wind and wave directions were aligned. As illustrated in Figure 2b, the overall behaviour of the retrieved directions follows that of the buoy wind directions. We find good agreement between our 12-second median principal direction from 12 1-second DDMs and the buoy measurements for R21 and R29. However, we recall that a 180° ambiguity affects our direction retrieval. As compared to MSS, this time we have a complementary behaviour, as we find a higher variability in the retrieved direction for the cases of R21 and R12, and a lower variability for the cases of R20 and R29. Indeed, the PDFs for R20 and R29 are more anisotropic (i.e., the ratio between the retrieved secondary and principal MSS is smaller on average compared to the other two cases), and thus they exhibit a predominant slope direction which is retrieved with less ambiguity. Our retrieved slope directions from averaged 12-s DDMs are also in very good agreement with the buoy measurements, and we notice that the worst match is obtained for R20, as in the case of the MSS.

5. Conclusions

[7] We have analyzed GPS-Reflected DDMs from space-borne altitudes from four UK-DMC data acquisitions and extracted the directional MSS and principal wave slope direction by least-square fitting a theoretical DDM. Our retrieved values are generally consistent with the buoy measurements. The retrieved median MSSs and direction from 1-second DDMs are consistent with both theoretical values and in situ measurements for the four cases. In particular, we obtained good agreement for the median MSS for steady wind and wave conditions with some swell (R21) and for swell with high wind speed variability (R12), and for the median slope direction for R21 and for growing sea conditions (R29). The retrieved MSSs from averaged 12-s DDM are close to the buoy measurements for both MSSs and slope directions, except for the case of decaying sea, with rapidly decaying wind speed (R20). Our analysis of satellite DDMs complements previous analyses of satellite delay waveforms and DDMs from aircraft campaigns. Notably, the exploitation of DDMs allows us to retrieve not only roughness, but also surface slope direction. The results obtained therefore offer convincing evidence for using GNSS-R to retrieve wind and wave data using a small passive instrument that could easily be fitted on more satellites. Our study also highlights marked differences between measured and simulated DDMs which could be linked to either the instrumentation and processing, or geophysical processes not accounted for in the GO-based model. In the latter case, a way forward could be to simulate the whole end-to end scattering problem for an explicit ocean surface, accounting for all the relevant scattering mechanisms. Also, with more UK-DMC data now available, further comparisons between simulated and measured DDMs could be performed for other sea conditions, which would help us understand better what ocean properties affect the GPS-R signals. Collocated data from Altimeters, Scatterometers or Synthetic Aperture Radars may also provide additional information on wind and wave conditions to extend the ground truth for the UK-DMC datasets. Finally, the 180° ambiguity in our direction retrievals could be eliminated, perhaps using the Doppler information, in order to identify how the principal surface slopes are oriented.

References

Cardellach, E., G. Ruffini, D. Pino, A. Rius, A. Komjathy, and J. Garrison (2003), Mediterranean Balloon Experiment: Ocean wind speed sensing from the stratosphere using GPS reflections, *Remote Sens. Environ.*, *88*, 351–362.

Elfouhaily, T., B. Chapron, K. Katsaros, and D. Vandemark (1997), A unified directional spectrum for long and short wind-driven waves, *J. Geophys. Res.*, *102*, 15,781–15,796.

Garrison, J. L., S. J. Katzberg, and M. I. Hill (1998), Effect of sea roughness on bistatically scattered range coded signals from the Global Positioning System, *Geophys. Res. Lett.*, *25*, 2257–2260.

Germain, O., G. Ruffini, F. Soulat, M. Caparrini, B. Chapron, and P. Silvestrin (2004), The Eddy Experiment: GNSS-R speculometry for directional sea-roughness retrieval from low altitude aircraft, *Geophys. Res. Lett.*, *31*, L12306, doi:10.1029/2004GL019994.

Gleason, S. T. (2006), Remote sensing of ocean, ice and land surfaces using bistatically scattered GNSS signals from low Earth orbit, Ph.D. thesis, Univ. of Surrey, Surrey, U.K.

Gleason, S. T., S. Hodgart, S. Yiping, C. P. Gommenginger, S. Mackin, M. Adjrad, and M. Unwin (2005), Detection and processing of bistatically

reflected GPS signals from low Earth orbit for the purpose of ocean remote sensing, *IEEE Trans. Geosci. Remote Sens.*, 43, 1229–1241.

Gommenginger, C. P., M. A. Srokosz, P. G. Challenor, and P. D. Cotton (2002), Development and validation of altimeter wind speed algorithms using an extended collocated buoy/TOPEX data set, *IEEE Trans. Geosci. Remote Sens.*, 40, 251–260.

Martin-Neira, M. (1993), A Passive Reflectometry and Interferometry System (PARIS): Application to ocean altimetry, *ESA J.*, 17, 331–355.

Ruffini, G., O. Germain, F. Soulat, M. Taani, and M. Caparrini (2003), GNSS-R: Operational applications, paper presented at Workshop on Oceanography with GNSS-R Reflections, Barcelona, Spain.

Zavorotny, V. U., and A. G. Voronovich (2000), Scattering of GPS signals from the ocean with wind remote sensing application, *IEEE Trans. Geosci. Remote Sens.*, 38, 951–964.

————————————

M. P. Clarizia, S. T. Gleason, C. P. Gommenginger, and M. A. Srokosz, National Oceanography Centre Southampton, European Way, Southampton SO14 3ZH, UK. (marari@noc.soton.ac.uk)

M. Di Bisceglie and C. Galdi, Università degli Studi del Sannio, Piazza Roma 21, I-82100 Benevento, Italy.

Appendix II

Simulation of L-Band Bistatic Returns From the Ocean Surface: A Facet Approach With Application to Ocean GNSS Reflectometry

Maria Paola Clarizia, *Student Member, IEEE*, Christine Gommenginger, Maurizio Di Bisceglie, *Member, IEEE*, Carmela Galdi, *Member, IEEE*, and Meric A. Srokosz

Abstract—We present the implementation of a facet-based simulator to investigate the forward scattering of L-band signals from realistic sea surfaces and its application to spaceborne ocean Global Navigation Satellite System (GNSS) Reflectometry. This approach provides a new flexible tool to assess the influence of the ocean surface roughness on scattered GNSS signals. The motivation stems from the study by Clarizia *et al.*, which revealed significant differences between delay–Doppler maps (DDMs) obtained from UK-DMC satellite data and DDMs simulated with the Zavorotny–Voronovich (Z-V) model. Here, the scattered power and polarization ratio (PR) are computed for explicit 3-D ocean wave fields, using a novel implementation of the Kirchhoff approximation (KA), which we call the Facet Approach (FA). We find that the FA is consistent with the full KA and the Geometrical Optics (GO) used in the Z-V model, while being less computationally expensive than the KA and able to represent polarization effects not captured by the GO. Instantaneous maps of the bistatic normalized radar cross section computed with the FA show clear patterns associated with the underlying waves. The wave field is particularly visible in the PR, indicating that the scattering is generally dominated by the HH component, particularly from ocean wave troughs. Polarization effects show, for the first time, a strong correlation to the explicit sea surface from which the scattering originated. DDMs of the scattered power computed with the FA reveal patchy patterns and power distributions that differ from those obtained with Z-V and show closer similarities with observed DDMs from UK-DMC.

Index Terms—Facet approach (FA), Global Navigation Satellite System Reflectometry (GNSS-R), Kirchhoff approximation (KA), ocean waves, polarization, scattering.

I. INTRODUCTION

I T IS NOW WELL recognized that navigation signals reflected off the sea surface can be used to investigate properties of the ocean surface. This technique, known as Global Navigation Satellite System Reflectometry (GNSS-R), has been extensively studied in recent years to demonstrate that the re-flected signals contain useful information about the sea surface roughness, linked to ocean surface wind and waves [1]–[9], as well as the sea surface height [10]–[12]. The scatterometric applications of GNSS-R are quite well established, with recent studies showing the possibility of retrieving the directional mean square slopes (DMSSs) from reflected GPS signals collected both from airborne [5] and Low-Earth-Orbiting satellite [6] platforms. In both cases, the DMSSs were extracted from the delay–Doppler map (DDM), a 2-D representation of the scattered signal power in the delay and Doppler domains. The inversion methodology relied on the least square fitting of the observed DDM with a simulated DDM based on the well-known theoretical model by Zavorotny and Voronovich [1] (hereafter referred to as the Z-V model). The Z-V model provides an analytical expression of the average scattered power for GNSS signals in a bistatic forward scattering configuration under the Geometrical Optics (GO) scattering limit. The average scattered power depends on the roughness of the ocean surface through the 2-D probability density function (PDF) of the slopes of the large-scale surface roughness. In the case of linear ocean waves, the PDF is Gaussian and entirely characterized by the DMSS in two orthogonal directions. Clarizia *et al.* [6] applied the Z-V model to fit DDMs from the UK-DMC satellite. The study showed good general agreement between the spaceborne DDMs and the theoretical model, and the retrieved DMSS compared favorably against *in situ* measurements from buoys. Yet, the study also highlighted substantial differences in the structure and power distribution of the measured DDM compared with those simulated with the Z-V model, particularly away from the specular reflection point, where patchy patterns seen in the data were missing in the simulated DDMs. These differences may be due to several factors. Residual speckle noise due to the limited incoherent averaging time in the satellite observations could be partly responsible for the patchiness seen in the measured DDMs, which would not be present in the simulated Z-V DDMs for which the temporal averaging is effectively infinite. Other elements affecting the measured DDMs could be thermal noise in the receiver or limitations or problems in the receiver hardware. Conversely, it is also conceivable that the differences may originate from limitations of the modeling or from the simplified way of describing complex sea surfaces through a Gaussian PDF of the sea surface heights and slopes. In this paper, we chose to investigate the observed discrepancies through the use of

explicit 3-D representations of the sea surface and by adopting the more general theoretical framework of the Physical Optics (PO) scattering approximation [also known as the Kirchhoff approximation (KA)] in order to simulate the forward scattering of L-band signals from the sea surface. The aim is not to propose a new model to fit spaceborne GNSS-R data from large glistening zones (GZs) but rather to develop a flexible tool to investigate the interactions and mechanisms on the sea surface that affect the GNSS signal scattering and determine how to produce simulated DDMs that are closer to the observations. Explicit representations of the sea surface allow us to consider a much wider range of sea surface conditions, including complex combinations of wind waves and swell traveling in different directions. In this paper, we consider only ocean waves with linear Gaussian statistics, but the approach will allow future investigations of the impact of nonlinear ocean wave phenomena on GNSS-R ocean reflections. Hence, this approach offers new investigative capabilities, where we may consider how and to what extent different wind and wave conditions affect the GNSS scattering, and what further information may be extracted about nonlinear waves, whose influence on the skewness of PDFs has already been suggested based on real GNSS-R reflections [7]. In this paper, we simulate the scattering through a novel facet-based implementation of the KA applied to explicit sea surfaces. We will call this method the Facet Approach (FA). We will show that the FA retains the advantages of the full KA for the representation of the scattering properties (compared with the high-frequency GO approximation used in Z-V) but considerably simplifies the calculation of the KA by applying it to facets approximating the sea surface. As a result, the scattered field can be calculated directly for the large-scale roughness components present in a sea surface realization, thus depending on the actual features of the simulated sea surface rather than on a simple statistical description of the wave field. Simulating the scattering from individual sea surface snapshots also provides the flexibility of examining both the instantaneous scattered power from a given snapshot and the average scattered power obtained for an ensemble of successive snapshots. Another important difference of our approach is the use of a vector formulation to model the scattered field, as opposed to scalar formulation used in the Z-V model. This allows us to investigate polarization effects, the importance of which was previously recognized in [13] and the representation of which in large-scale scattering models was attempted recently by Thompson *et al.* [8] using a refined GO model based on a vector formulation. In the future, this facet-based approach will offer the possibility of combining the scattering from specific large-scale roughness features with the contribution from small-scale roughness components, by removing the assumption of flat facets and assuming the existence of ripples within a facet. This would give a two-scale representation of the GNSS-R scattering similar to the classical Two-Scale Model (TSM) [14], which would help to determine the relative contributions of different ocean scales to GNSS-R signals. Hereafter, we present details of the implementation of the facet-based bistatic scattering simulator. These include the simulation of 3-D explicit sea surfaces, the approximation of the sea surface by suitably sized facets given the KA roughness criteria, the calculation of the

polarimetric instantaneous scattering of L-band monochromatic signals in a GNSS-R bistatic scattering configuration, and the comparison of the FA with the full KA and the Z-V model. The results in this study are presented primarily in the form of bistatic radar cross sections (RCSs), but an example of a DDM computed using the FA is also shown and compared with the DDM generated using the Z-V model. The influence of sea state and geometry on the DDMs is left to be examined in greater detail in a later publication. The analysis of the polarimetric RCS reveals interesting dependence between the scattered power and the structure of the wave field, particularly with regards to the polarization ratio (PR). Such polarimetric effects represent a significant result confirming the findings of Thompson *et al.* [8] that polarization effects consistent with observations can be obtained from improved modeling of the large-scale scattering, without the need to introduce small-scale (diffuse) scattering as it is done in many EM models. This paper is organized as follows. Section II introduces the large-scale microwave scattering problem, including consideration of the range of validity of the KA and the GO, and presents our FA. Section III reviews the criteria to be applied to determine the correct size of the facet in order to best approximate the sea surface while obeying the KA conditions of validity. Simulations and results are shown in Section IV, which is divided into the following sections: 1) simulations of sea surfaces with realistic waves in three cases of wind speeds with/without added swell (Section IV-A); 2) description of the configuration and scattering geometry and the characteristics of the transmitted signal (Section IV-B); 3) validation of the new FA against the KA and GO (Section IV-C); 4) results for the RCS for the three wind and wave simulations presented in Section IV-A; 5) polarization results for the three wind and wave simulations presented in Section IV-A; and 6) delay–Doppler mapping of the scattered power obtained with the FA and the Z-V model for a large GZ in a GNSS-R spaceborne scenario and for a single sea state (Section IV-F). Finally, Section V presents the conclusion from this study and outlines improvements and developments of the simulator to be completed in the future.

II. SIMULATING THE ELECTROMAGNETIC SCATTERING

In this section, we briefly review the main aspects of the KA and its high frequency limit, which is GO. Subsequently, we introduce the FA, which will be used for the evaluation of the scattering from the large-scale surface roughness.

A. The Kirchhoff Approximation

The KA [14]–[17], also known as Tangent Plane Approximation or PO, represents the scattering in a quasi-specular regime, and it is generally applicable when the local radius of curvature of the surface is much larger than the incident wavelength, namely [16]

$$\sqrt[3]{k_0 r_c} \cos(\theta) \gg 1 \qquad (1)$$

where k_0 is the wave number of the incident radiation, r_c is the radius of curvature of the surface, and θ is the incidence

angle. The KA is an approximation of the exact solution of the Stratton–Chu equations [18] for the electric ($\mathbf{E^s}$) and magnetic ($\mathbf{H^s}$) fields scattered from a surface S. One formulation of the Stratton–Chu equation for the electric field is the following [17]:

$$\mathbf{E}^s = \frac{-jk_0}{4\pi R_2} e^{-jk_0 R_2} \iint\limits_S \mathbf{p} e^{j\,\mathbf{q}\cdot\mathbf{r}}\, dS \tag{2}$$

with the vector $\mathbf{p}$ given by

$$\mathbf{p} = \hat{n}_s \times [\hat{n} \times \mathbf{E}^s - \eta_s\,\hat{n}_s \times (\hat{n} \times \mathbf{H}^s)] \tag{3}$$

and the other quantities defined as follows.

1) $\mathbf{q} = \mathbf{q}(\mathbf{r}) = k_0[\hat{n}_s(\mathbf{r}) - \hat{n}_i(\mathbf{r})]$ is the scattering vector, where $\hat{n}_s$ is the incident unit vector pointing from the transmitter to the scattering point $\mathbf{r}$ and $\hat{n}_s$ is the scattered unit vector pointing from the scattering point to the receiver.
2) $\hat{n} = \hat{n}(\mathbf{r})$ is the local normal to the surface at the reflection point.
3) η_s is the intrinsic impedance of the medium in which the electric field is scattered.
4) $\mathbf{E^s} = \mathbf{E^s}(\mathbf{r})$ and $\mathbf{H^s} = \mathbf{H^s}(\mathbf{r})$ are the scattered electric and magnetic fields on the interface S.
5) R_2 is the distance from the reflection point on the surface to the receiver.

The geometry of the surface-scattering problem is shown in Fig. 1. We now assume that the incident wave on the surface S is a spherical wave expressed as

$$\mathbf{E}^i = \frac{e^{-jk_0 R_1}}{4\pi R_1} \hat{a}\, E_0\, e^{-jk_0\,\hat{n}_i \cdot \mathbf{r}} \tag{4}$$

where $\mathbf{E_0}$ is the amplitude of the incident signal, R_1 is the transmitter range, and $\hat{a}$ is the incident unit polarization vector. The KA allows us to write the local fields $\mathbf{E^s}$ and $\mathbf{H^s}$ at a point on the surface S as the fields that would be produced by an infinite tangent plane at that point. This is applied separately for each polarization and translates into

$$\begin{aligned} \mathbf{E}_\perp^s &= R_\perp\, \mathbf{E}_\perp^i \\ \mathbf{H}_\parallel^s &= R_\parallel\, \mathbf{H}_\parallel^i \end{aligned} \tag{5}$$

where $\mathbf{H}_\parallel^i = \hat{n}_i \times \mathbf{E}_\parallel^i$. The terms $R_\perp$ and $R_\parallel$ are the Fresnel reflection coefficients for the two polarizations [17], and the subscripts $\perp$ and $\parallel$ denote the horizontally and vertically polarized components of the field, respectively, with respect to the local plane of incidence $(\hat{n}_i, \hat{n})$. The remaining polarized fields can be found as

$$\begin{aligned} \mathbf{E}_\parallel^s &= \eta_s \hat{n}_r \times \mathbf{H}_\parallel^s \\ \mathbf{H}_\perp^s &= \frac{1}{\eta_s} \hat{n}_r \times \mathbf{E}_\perp^s \end{aligned} \tag{6}$$

where $\hat{n}_r$ is the unit vector in the reflected direction (see Fig. 1). The fields $\mathbf{E}^s$ and $\mathbf{H}^s$ on the surface S can therefore be replaced by the sum of their vertically and horizontally polarized components, whose expressions are given in (5) and
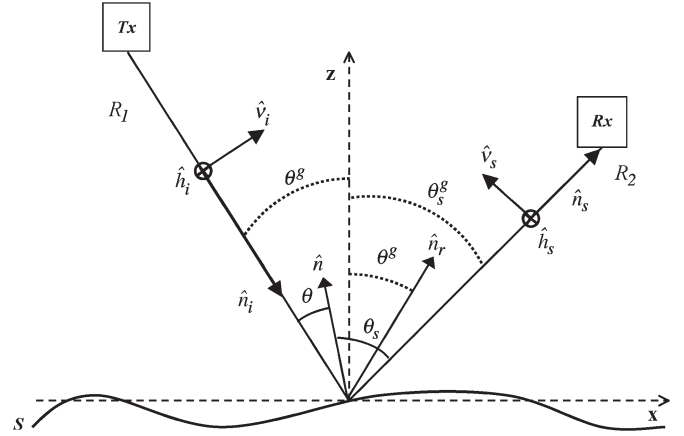
Fig. 1. Geometry of the surface scattering problem. The circled crosses indicate that the horizontal polarization vectors $\hat{h}_i$ and $\hat{h}_s$ are perpendicular to the plane of incidence x–z and directed into the page. Note that the global angles θ^g and θ_s^g are the incident and scattering angles relative to the global normal to the mean sea level (z-axis), whereas θ and θ_s are the local angles relative to the local normal $\hat{n}$ on S.

(6) and substituted into the vector term in (3) to obtain the scattered field $\mathbf{E}^s$ in (2). Finally, the bistatic normalized radar cross section (NRCS) can be defined as

$$\sigma_{pq}^0 = \frac{4\pi R_2^2\,\left|\mathbf{E}_{pq}^s\right|^2}{A\,\left|\mathbf{E}_{pq}^i\right|^2} \tag{7}$$

where A is the surface area and the subscripts p and q refer to the polarization of the incident and scattered field. Note that (7) gives us the means to compute both the copolarized (when $p = q$) and the cross-polarized (when $p \neq q$) NRCSs.

B. The Geometrical Optics Approximation

The KA provides an explicit form for the vector (3), but it still leaves the integral as a complicated function of the surface S and its local normal vectors and reflection coefficients. The most common and easy approximation is known as the GO or Stationary-Phase Approximation [1], [17]. This approximation considers that the scattering occurs only in the direction of specular reflection and removes the dependence of the vector $\mathbf{p}$ in the integral (2), leaving the exponential term as the only term in the integral. The total scattered field is the result of the superposition of the fields generated by a large number of specular points (mirrors) on the surface, reflecting the power in the direction of the receiver. The scattered power is evaluated as an ensemble average and, using some additional assumptions including Gaussian statistics for the sea surface elevations and slopes, can be evaluated in a closed form. This finally leads to the GO expression of the bistatic NRCS, given by [17]

$$\sigma_{pq}^0 = \frac{\pi\,(k_0 q |U_{pq}|)^2}{q_z^4} P\left(-\frac{q_x}{q_z}, -\frac{q_y}{q_z}\right) \tag{8}$$

where U_{pq} are polarimetric coefficients (see [17, eq. (12.23)–(12.26)] for details); q_x, q_y, and q_z are x-, y-, and z-components of the scattering vector $\mathbf{q}$ and q is its norm; and $P(\cdot, \cdot)$ is 2-D Gaussian PDF of the slopes along the x and y coordinates.

The GO approximation is widely used, for its simplicity and ease of implementation, but it suffers some limitations. We will show in Section IV-C that, in the case where the transmitter and receiver lie in the x–z plane, as shown in Fig. 1, the GO shows no sensitivity to polarization other than through the Fresnel reflection coefficients. Furthermore, the average formulation of GO is a useful tool to quickly model the impact of surface roughness on the scattered field, but its parameterization of surface roughness with a Gaussian PDF effectively reduces complex surface roughness conditions to just two values of the variances of the surface slope to describe the sea surface. The average formulation thus prevents insight to be gained into the instantaneous behavior of the scattering and on how distinct features on the sea surface may affect the scattering.

C. The Facet Approach

Here, we illustrate our facet-based approach to calculate the scattering from large-scale surface roughness components based on solving the Kirchhoff integral (2) without the need for strong assumptions as in the case of GO. Equation (2) can indeed be simplified if we approximate the surface S by an ensemble of n planar facets, each of them tilted and oriented by the underlying long waves, and we solve the integral for each facet. We assume that all facets have equal projections of their sides along the x and y directions, namely, L_x and L_y, respectively. Each facet has a uniquely defined local normal. If the facet is sufficiently larger than the wavelength of the incident radiation, the EM fields are constant across the facet. The integral in (2) can be written as the sum of integrals over each facet as follows:

$$E^s = \sum_{k=1}^{n} E^{s,k} = -\frac{jk_0}{4\pi R_2} e^{-jk_0 R_2} \sum_{k=1}^{n} \iint_{S_k} \mathbf{p}^k \, e^{j\mathbf{q}\cdot\mathbf{r}} dS \quad (9)$$

where $\mathbf{p}^k$ is the vector $\mathbf{p}$ for the kth facet. The advantage of this approach lies in the fact that the integral for a single facet can easily be solved in a closed form. Indeed, with the vector $\mathbf{p}^k$ being constant over the facet, it can be taken out of the integral and can be evaluated by applying the KA through (3)–(6). At this point, the rest of the integral simply becomes the integral of an exponential term over a facet, whose tilt along x and y can be known. The final expression for the scattered field from the kth facet is

$$\mathbf{E}^{s,k} = -jk_0 \, \mathbf{p}^k \frac{e^{-jk_0 R_2}}{4\pi R_2} \sqrt{1 + \alpha_k^2 + \beta_k^2} \, e^{-j\mathbf{q}\cdot\mathbf{r}^k}$$
$$\cdot L_x L_y \, \text{sinc}\left[(q_x + q_z\alpha_k)L_x/2\right]$$
$$\cdot \text{sinc}\left[(q_y + q_z\beta_k)L_y/2\right] \quad (10)$$

where $\mathbf{r}^k$ is the coordinate of the central point of the kth facet, L_x and L_y are the side projections of the facet along x and y, respectively, and α_k and β_k are the derivatives of the surface along x and y at the central point of the kth facet. Here, the function $\text{sinc}(x)$ is defined as $\sin(x)/x$. The total scattered field in (9) can be then evaluated by coherently summing the scattered fields from each facet given in (10). The sinc terms
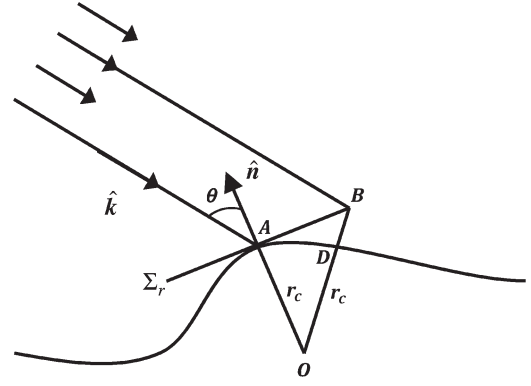
Fig. 2. Illustration of the tangent plane Σ_r and its local coordinate system, with the half-length AB of the facet and the distance from the underlying surface BD.

that appear in (10) clearly indicate that the FA treats the facets as radiating antennas, with a specific nonzero width main lobe, which allows some scattered power in directions away from the specular direction. The width of the sinc lobe decreases with increasing facet size, so that large facets have scattered power concentrated around the specular direction in a narrow lobe. Thus, the method seems to offer a more complete description of the scattering than GO, as it solves the KA for ensembles of finite-size facets approximating the sea surface. Furthermore, the FA displays more sensitivity to polarization with respect to formulations like the Z-V model commonly used to describe GNSS-R scattering. However, it is clear that the size of the facets is a key parameter that will determine the applicability of this new method. The choice of facet size will be a tradeoff between the need to comply with the KA conditions on roughness, the ability of the facets to adequately approximate the underlying sea surface, and computational expense. We discuss in the next section how the choice of facet size is not entirely arbitrary but governed by some specific important criteria.

III. Choosing the Facet Size

The criteria we adopt here for choosing the size of the facet stem from considerations first presented in [16] to discuss the applicability of the KA. These relate to the geometrical conditions shown in Fig. 2, which constitute the starting point for the formulation of the standard roughness criterion given in (1).

With reference to Fig. 2, it is considered that the reflection of an electromagnetic wave at a point A on the surface can be taken to occur as if from a tangent plane centered at that point, if one can identify a region on the tangent plane Σ_r with linear dimensions which are large relative to the EM wavelength, but which also does not deviate noticeably at the edges of the region from the underlying surface. This region on the tangent plane is what we define as a facet. The aforementioned argument translates into the two mathematical conditions [16]

$$AB \gg \frac{1}{k_0 \cos(\theta)} \quad (11)$$

$$BD \ll \frac{\cos(\theta)}{k_0} \quad (12)$$

where AB and BD are the segments shown in Fig. 2. We can easily see that

$$BD = OB - OD = \sqrt{AB^2 + r_c^2} - r_c \qquad (13)$$

where r_c is the local radius of curvature of the surface. Thus, we can express both (11) and (12) in terms of AB as

$$AB \gg \frac{1}{k_0 \cos(\theta)} \qquad (14)$$

$$AB \ll \sqrt{\left[\frac{\cos(\theta)}{k_0}\right]^2 + 2\frac{r_c \cos(\theta)}{k_0}}. \qquad (15)$$

In our case, AB represents half the facet size, and criteria (14) and (15) will be used to determine the appropriate facet size. It is worth noting that the inequalities (14) and (15) can be more or less difficult to satisfy, depending on the quantitative interpretation of the much greater than and much smaller than inequality signs. We could choose to interpret those as AB having to be larger (or smaller) than the term on the right-hand side by a factor of, for example, at least 10. While inequality (14) is easily satisfied with a factor of 10, inequality (15) with such a factor becomes a very stringent condition. This would either imply the use of very small facets or reduce the applicability of KA to only the calmest sea-state conditions. In our simulations, we will relax the condition for inequality (15) by considering a factor smaller than 10, which allows the use of larger facets ($\sim$1 m) to approximate the sea surface. It is interesting to note that if we combine (14) and (15) in a manner similar to what is done in [16], we obtain a condition similar to the standard applicability condition (1) of the KA, namely

$$\sqrt[3]{2k_0 r_c}\cos(\theta) \gg \sqrt[3]{1 - \cos^4(\theta)}. \qquad (16)$$

For simplicity, in our simulations, we will use the standard KA condition (1) to define what constitutes large-scale surface roughness compliant with KA and the conditions (14) and (15) to determine the size of the facets.

IV. NUMERICAL SIMULATIONS AND RESULTS

This section is organized in six sections where we investigate the most important features and limitations of the simulator implemented so far to represent the scattering of GNSS-R signals from ocean surfaces. First, we briefly present how we generate 3-D surfaces with realistic wave fields and show examples for three different wind speed and swell conditions. Next, we introduce some key concepts about the geometrical configuration of the scattering scenario and the characteristics of the signals, and we analyze the results of the FA, comparing it with both the GO and a numerical implementation of the full KA. Then, we examine the instantaneous and average NRCS and PR for the three different sea surface simulations to investigate how sea surface conditions affect the scattered signals. Finally, we present an example of the DDM of scattered power computed using FA for a specific sea state, and we compare it with a DDM obtained using the Z-V model for the same sea state.

A. Simulations of the 3-D Realistic Ocean Wave Fields

The generation of ocean surface maps was carried out using a well-established technique based on filtering a white Gaussian process with a specified theoretical wave spectrum. This approach preserves the Gaussian statistics of the sea surface elevations and slopes while allowing us to specify particular spectral properties of the wave field. It is worth recalling here that our objective is to simulate the large-scale roughness of the ocean only, since we are not considering the scattering from small-scale features at this stage (for which the diffusive EM scattering needs to be calculated using a different approximation). This means that a wave number cutoff needs to be chosen to identify the components that constitute the large-scale roughness. Only the spectral components of the spectrum for wave numbers below that wave number cutoff will contribute to the generation of the sea surface. Several attempts exist in the literature to propose an objective method to choose this cutoff [1], [2], [8] but there is no consensus. In our case, we determined the cutoff experimentally by simulating the sea surfaces for a given cutoff and by evaluating numerically the radii of curvature of the surface to verify *a posteriori* that they satisfy the KA criterion defined by (1).

The ocean wave spectrum used to filter the white Gaussian process was the theoretical directional wave spectrum model by Elfouhaily *et al.* [19]. This model produces a wave field entirely defined by the wind speed and the wind direction. Two examples of wind-generated surfaces are shown in Fig. 3(a) and (b) corresponding to wind speeds of 5 and 10 m/s, respectively. In all cases, the wind direction is $0°$ with respect to the x-axis.

The simulated surfaces are generated with a resolution of 20 cm and are 500 by 500 m, large enough to include a sufficient number of dominant ocean wavelengths for both wind speeds. In the case of the 10-m/s wind speed, the surface is able to capture on the order of five dominant wavelengths. The cutoff wavelength used to simulate these surfaces was equal to 1 m, equivalent to five times the incident radar wavelength in the case of L-band. This is not a very high wave number cutoff, and it does not impose excessive filtering of the original surface. We checked *a posteriori* that this cutoff produces a surface that satisfies the KA criterion, where (1) was computed using the global incidence angle θ^g (see Fig. 1) and the median radius of curvature of the surface in the direction of the wind (x-axis). Note that the median radius of curvature of the surface in the direction of the wind will be smaller than in other directions due to the geometry of the wave field (see Fig. 3).

In Fig. 3(c), we show the 10-m/s wind wave field from Fig. 3(b) with an added swell, modeled as a simple 2-D sinusoidal wave with amplitude of 1 m and wavelength of 100 m and traveling in a direction $60°$ from the wind direction (clockwise from the x-axis). This last example illustrates how these explicit sea surface simulations give the flexibility to consider realistic and more complex sea states, featuring coexisting wind and swell waves traveling in different directions, which cannot be represented using a simple PDF of slopes.
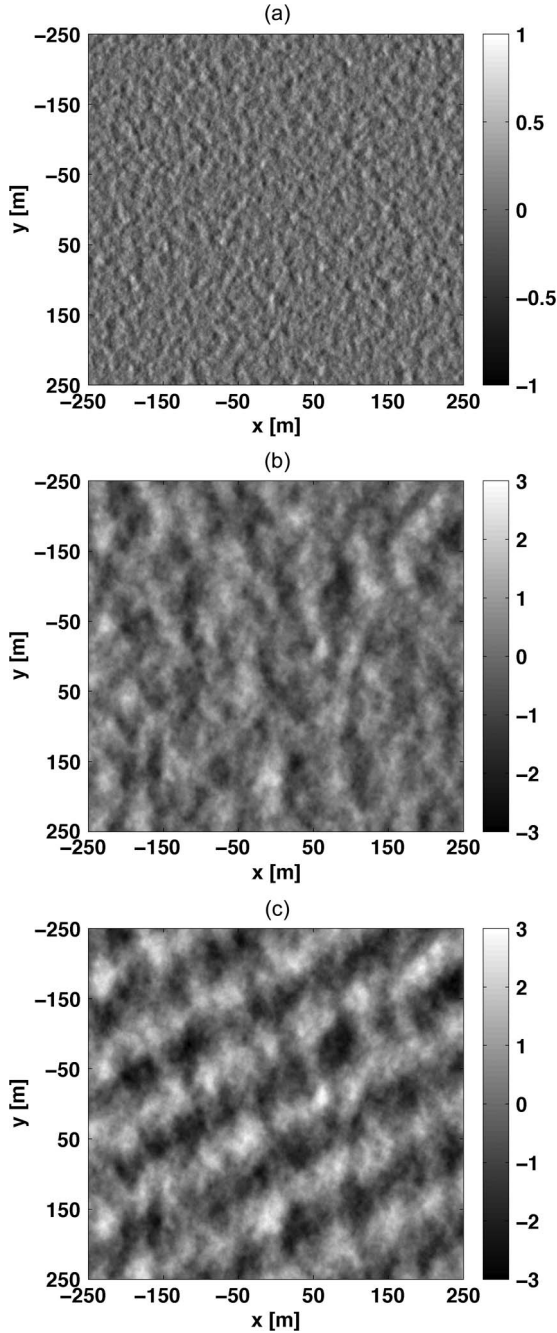
Fig. 3. Three-dimensional ocean wave field over 0.5 km × 0.5 km generated with a 20-cm resolution and a cutoff wavelength of 5 $\lambda_{\text{L-band}}$ ($\sim$1 m). The three subplots correspond to the following: (a) Wind waves for wind speed of 5 m/s, (b) wind waves for wind speed of 10 m/s, and (c) wind waves for wind speed of 10 m/s plus added swell with amplitude of 1 m, wavelength of 100 m, and direction of 60° clockwise with respect to the x-axis. The wind direction is along the x-axis in all cases. Units in grayscale are meters.

B. Configuration of the Scattering Scenario

As shown in Fig. 1, the transmitter and the receiver lie in the $x-z$ plane. In our simulations, the transmitter and receiver are in a spaceborne configuration and their ranges are 20 000 and 680 km, respectively. These correspond to the typical altitude of transmitting satellites in navigation system constellations like GPS and the Low-Earth-Orbiting altitude of the UK-DMC satellite [4], [6]. The position of the transmitter is fixed with a constant range R_1 and incidence angle $\theta^g = 20°$. The receiver

range R_2 is also fixed while its scattering angle is variable and indicated by θ_s^g in Fig. 1, which ranges from $-10°$ to $50°$ from the global vertical. The specular direction corresponds to a scattering angle θ_s^g equal to $20°$. The incident wave is an L-band ($= 19$ cm) spherical wave, as expressed in (4), with unitary amplitude. At this stage, it is convenient to introduce the horizontal and vertical unit polarization vectors $\hat{h}_i$, $\hat{v}_i$ for the incident wave and $\hat{h}_s$, $\hat{v}_s$ for the scattered wave, defined with respect to the plane of incidence $(\hat{n}_i, \hat{z})$ and the scattering plane $(\hat{n}_s, \hat{z})$, respectively. Given that both the transmitter and the receiver lie in the $x-z$ plane, the incident and scattered polarization vectors can be simply expressed as

$$
\begin{aligned}
\hat{h}_i &= \hat{y} \\
\hat{v}_i &= -\hat{x}\cos(\theta^g) - \hat{z}\sin(\theta^g) \\
\hat{h}_s &= \hat{y} \\
\hat{v}_s &= \hat{x}\cos(\theta_s^g) - \hat{z}\sin(\theta_s^g).
\end{aligned}
\tag{17}
$$

Two cases of incident polarization have been considered: The first is horizontal polarization $(\hat{h}_i)$, and the second is vertical polarization $(\hat{v}_i)$. Although it is recognized that real GNSS signals are right hand circularly polarized, the scattering model is expressed here in terms of its linear polarization components, in the hope to gain more insight into physical processes at the ocean surface. The results for circular polarization are easily derived from these, since circular polarization is simply of a linear combination of the linear polarization components.

C. Validation of the FA

An initial set of simulations was generated to compare the results of the FA with the GO and a numerical implementation of the full KA. The latter was obtained by computing the KA integral given in (2) with a standard numerical integration method, applied to a new realization of the sea surface generated at much higher resolution than for the FA. Due to computational limits, this full KA method can only be applied for relatively small areas of the ocean surface. However, the surface must be large enough to include a sufficient number of dominant ocean wavelengths to ensure that the scattering is statistically representative of all relevant processes on the surface. The dimensions of the new surface realization were 50 m by 50 m, generated with a very high spatial resolution of 2 cm. This calculation was performed for a wind speed of 4 m/s aligned along the x-direction. This low wind speed ensures that the 50×50 m surface can represent about three dominant ocean wavelengths (about 17 m for a 4-m/s Elfouhaily spectrum). Similarly, we calculated the scattered RCS for the GO for the same wind speed conditions using (8).

For the implementation of the FA, we need to choose the size of the facet based on inequalities (14) and (15) introduced in Section III. As discussed previously, the size of the facet is a tradeoff between the need to properly represent the underlying sea surface (for which large number of small facets is best) and the need to obey the KA roughness conditions (for which fewer larger facets is more suitable). In our case, using the same angle and radius of curvature as in the Kirchhoff criterion, the conditions (14) and (15) require the facet size to be greater than
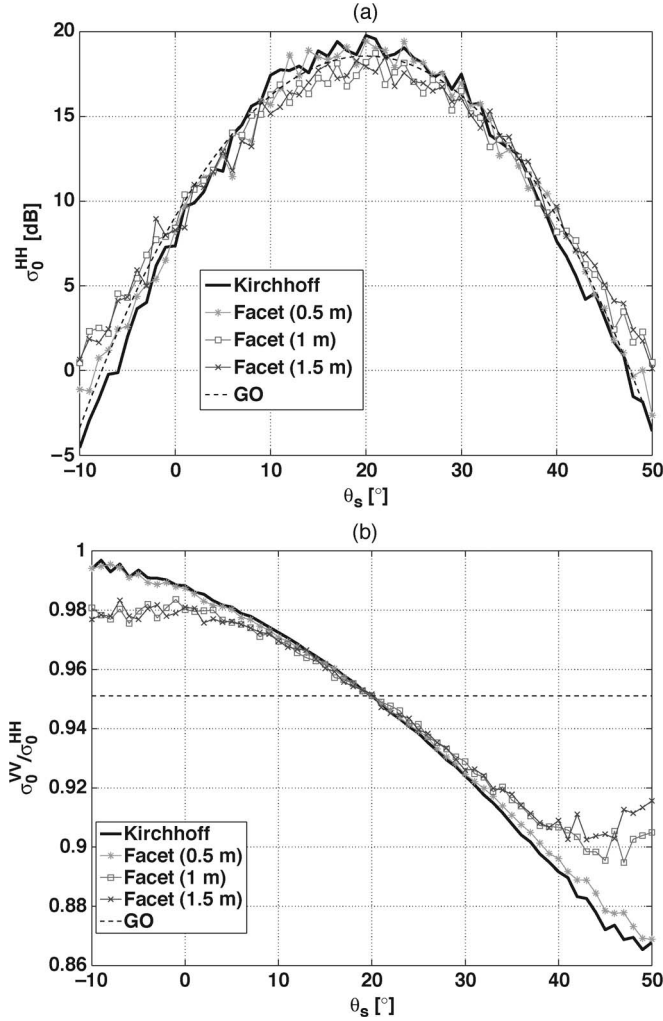
Fig. 4. (Top) Horizontal copolarized NRCS and (bottom) PR plotted against scattering angle for the full KA, the GO, and the FA with three choices of facet size. The results were averaged over 50 sea surface realizations for a wind speed of 4 m/s. The scattering angle value of 20° corresponds to the specular direction.

0.06 m and less than 1.6 m. We therefore present the FA results for three facet sizes (0.5, 1, and 1.5 m) to be compared against the GO and the full KA.

Fig. 4(a) shows the averaged horizontal copolarized (HH) NRCS in decibels calculated using (7) as a function of the scattering angle θ_s^g. The NRCS was averaged over 50 realizations of the sea surface for a wind speed of 4 m/s. The results are shown for an overall angular interval of 60° centered on the specular direction, which is at 20° from the vertical and corresponds to the direction of maximum forward scattering. The average NRCS is shown for HH polarization only, as results for VV polarization were similar.

From Fig. 4(a), we see that the NRCS calculated using the FA is in good agreement with the full KA for all three facet sizes and that they all exhibit oscillations that are comparable with the KA curve. The NRCS from the FA are slightly lower than the KA within 20° of the specular direction (for scattering angles between 0° and 40°) and become slightly higher than the KA further away from the specular direction. As expected, the FA computed with the smallest facet size (0.5 m) gives

the closest results to the KA. The FA results corresponding to 1.5 m facets, close to the upper limit of the facet size condition, differs most from the KA, by approximately 2 dB around the specular point. The patterns and oscillations in the NRCS also seem to become more different from those of the KA curve when the facet size increases. The FA led to a large reduction in computation times compared with the full KA. For facet size of 0.5 m, the FA computations were faster by a factor of almost 600, while for facet size of 1.5 m, the improvement in computation time was by more than 7000. The reduced computation time represents an important benefit of the FA, where larger facets lead to lower computational cost and the ability to handle larger surfaces, while still providing a reasonable level of accuracy compared with the full KA. Fig. 4(a) also shows the NRCS evaluated with the GO through (8). The variance of the Gaussian slopes (MSS) was computed through integration of the Elfouhaily et al. slope spectrum [19] up to the same wave number cutoff as used for the simulation of the explicit surface. The GO results are close to the full KA. GO thus provides a good approximation of the scattering, in an easy to implement method. However, as discussed previously, GO offers only limited means of exploring polarization and the scattering from complex sea surfaces. In order to investigate polarization effects, we use the PR, defined as

$$PR = \frac{\sigma_{\mathrm{VV}}}{\sigma_{\mathrm{HH}}}. \tag{18}$$

Fig. 4(b) shows the PR for the full KA, the FA for three different facet sizes, and the GO, again as a function of the scattering angle. In all cases, the PR is lower than 1, evidence that the scattered HH component is always stronger than the scattered VV component. It is interesting to note that the PR computed with the FA shows sensitivity to polarization similar to the full KA, both showing a decrease of the PR with increasing scattering angles. This indicates that the scattered HH component becomes larger than the scattered VV component as one moves away from the specular direction. The PR exhibits the same behavior around the specular direction for the KA and FA for all the facet sizes. Some differences appear between the KA and FA away from the specular direction, with the smallest facet size showing best agreement with KA over the widest range of angles (as expected). We note also the deterioration in the ability of the FA to match the KA at angles more than 10° from the specular direction when the facet size increases from 0.5 to 1 m. As expected, the PR for the GO shows no variation with respect to the scattering angle and it is simply equal to the ratio of the vertical and horizontal polarization Fresnel reflection coefficients of seawater. Note that the PR for the GO matches the value of the PR for the full KA and the FA in the specular direction.

D. Scattering Results for Different Wind and Wave Conditions

We present the copolarized HH NRCS calculated with the FA for simulated wave fields obtained at two different wind speeds and in the presence of a swell (see Section IV-A). Cross-polarized components of the NRCS (HV and VH) were also computed and analyzed but are not shown, as they display much

lower levels than the copolarized components and no features of interest. The copolarized results are first presented in the form of instantaneous 2-D maps, where each point represents the value for one individual facet. The specular point is located at the center of the maps, and the receiver is located in the specular direction. Here, the facet size is chosen to be 1 m × 1 m, as the computations are now for 500 m × 500 m areas of the sea surface. Fig. 5 shows the instantaneous HH copolarized bistatic NRCS in decibels for the simulated wave fields shown in Fig. 3. It is worth mentioning here that these images do not represent the power scattered from the sea surface, as sensed by a receiver, since they do not account for the phase of the scattered field from each facet. The phase plays a major role when combining the contributions from all facets (as shown later). Nevertheless, these maps are useful to examine the spatial distribution of the scattered power and how the GZ (the area contributing to the forward scattering) looks for different sea conditions and different geometrical configurations. The NRCS in Fig. 5 appears relatively uniform across the surface. This is because we are in a spaceborne configuration and the simulated surface covers only the small central part of the GZ around the specular point, corresponding to a small range of scattering angles away from the specular direction. Interestingly, the NRCS exhibits some wave patterns that show a good degree of correlation with the corresponding wave field, particularly in the high-wind-speed and high-wind-speed-plus-swell cases [Fig. 3(b) and (c)]. The NRCS is larger in the low-wind case [Fig. 5(a)] and decreases for higher wind speed cases [Fig. 5(b) and (c)], which is consistent with our expectations of decreased scattering in the specular direction when the sea gets rougher. Diagonal wave patterns aligned with the swell wave crests can be seen in Fig. 5(c), indicating a detectable influence of this particular swell train on the distribution of the scattered power in the GZ.

Next, we examine the average NRCS for the whole surface, computed by coherently summing the complex scattered fields from all facets and taking into account the phase of the scattered field from each facet. The average NRCS is shown in Fig. 6 for various positions of the receiver over a range of scattering angles up to 30° on either side of the specular direction. Fig. 6 shows the average HH NRCS for simulations at two different wind speeds. The NRCS results were averaged over 50 realizations of the sea surface in order to reduce the variability due to the individual waves in single realizations. The sensitivity of the average NRCS to wind speed is clearly visible. We note again the lower NRCS for higher wind speed in the specular direction and the slower decay away from the specular direction when the surface is rougher. Again, this is consistent with our expectation of increased scattering away from the specular direction at higher wind speeds. The same computation was done also for the wind-sea-plus-swell case [Fig. 3(c)], but the results are not shown as we could not identify any significant difference from the wind-sea-only case for the same wind speed.

E. Scattering Results for Different Polarizations

Here, we investigate the polarimetric signature of the forward scattering by examining the spatial distribution of the
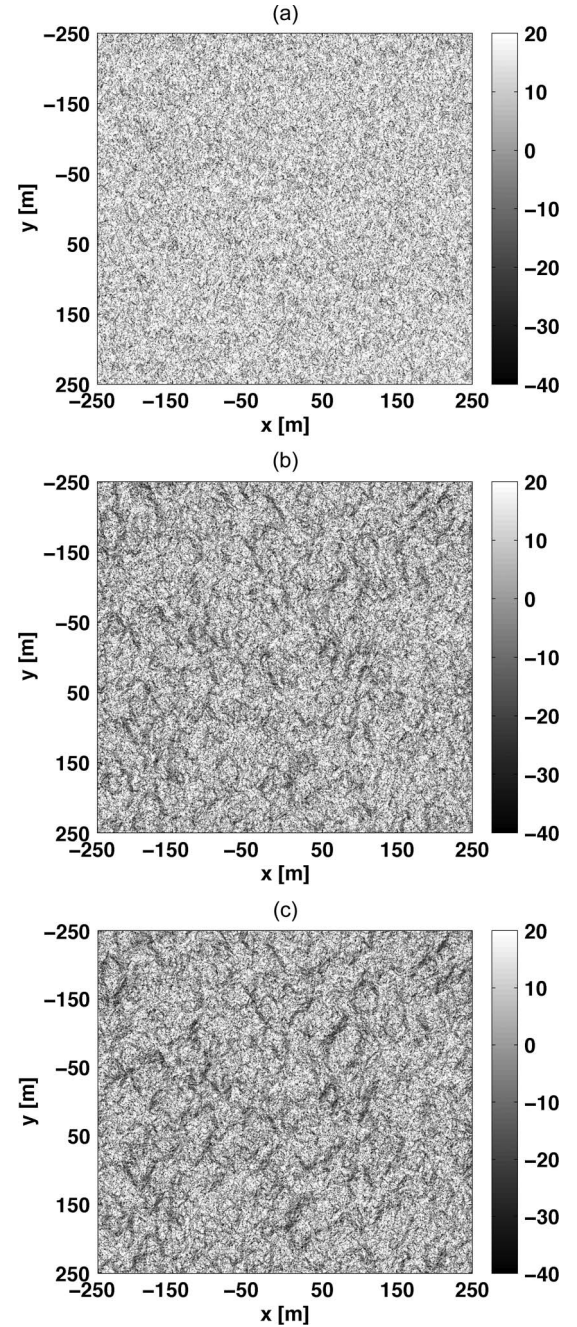
Fig. 5. Spatial maps of instantaneous copolarized HH bistatic NRCS in decibels computed with the FA and a facet size of 1 m^2. Each pixel represents the scattering from a single facet. The three subplots correspond to the simulated wave fields shown in Fig. 3, i.e., (a) wind waves for wind speed of 5 m/s, (b) wind waves for wind speed of 10 m/s, and (c) wind waves for wind speed of 10 m/s plus added swell with amplitude of 1 m, wavelength of 100 m, and direction of 60° clockwise with respect to the x-axis. The wind direction is along the x-axis in all cases.

PR, calculated from the instantaneous NRCS presented in the previous section. Fig. 7 shows the PR for the simulated wave fields shown in Fig. 3. The spatial maps immediately reveal that the PR is clearly correlated with the underlying wave field, the PR exhibiting crests-and-troughs patterns closely matching those of the waves. In Fig. 7(c), the presence and directionality of the swell is easily detected as an oblique pattern across the surface aligned with the line of the swell wave fronts. We see
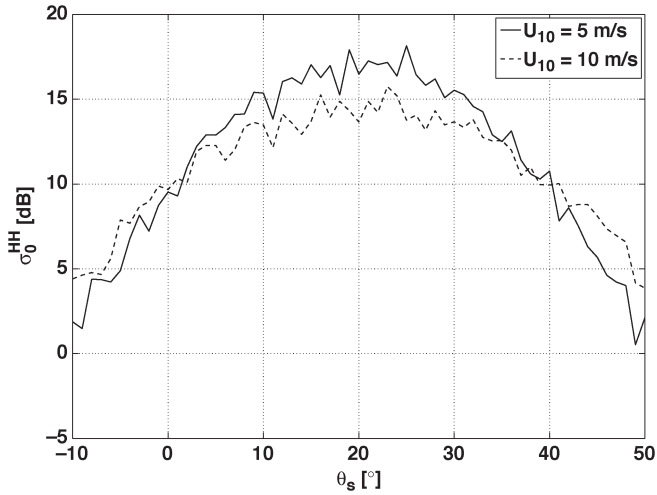
Fig. 6. Average HH NRCS in decibels computed with the FA and a facet size of 1 m² plotted against scattering angle. The specular direction corresponds to the scattering angle value of 20°. Results are shown for simulations at (solid line) 5 m/s and (dashed line) 10 m/s. The results were averaged over 50 realizations of the sea surface.

that the PR is generally less than 1, with marked minima in the troughs of the waves, indicating a stronger HH component for the scattering originating in the troughs of the waves. As for the NRCS, we computed the average PR for a range of scattering angles and different wind speed and wave conditions. We found that the average PR for the different simulated sea states (not shown) exhibits no marked differences, except a long way from the specular direction, where the validity of the FA starts to break down.

F. Delay–Doppler Mapping of the Scattered Power

In this section, we show an example of a noise-free single-look DDM of the scattered power computed using the FA, from a single sea surface snapshot. The sea surface is now a large area of 100 km by 100 km, which is comparable to the size of a typical GZ in a spaceborne GNSS-R configuration. The sea surface has been generated using a resolution of 0.2 m, a cutoff wavelength of 1 m, and a wind speed of 10 m/s. The scattering has been calculated using facets of 1 m by 1 m, and the complex scattered fields from each facet have been coherently accumulated in DD domain, thus taking into account the phase with which each facet scatters. Following the mathematical steps for the GPS-R receiver implementation outlined in [6], the Woodward Ambiguity Function of pseudorandom GPS sequences has been applied to each DD pixel of scattered field to simulate the effect of the GPS-R receiver matched filter. Finally, the resulting complex DDM of scattered field has been converted into a DDM of scattered power by simply taking the squared absolute value. Fig. 8(a) shows the DDM computed from FA in normalized units. For comparison, a DDM of the scattered power computed from the Z-V model is shown in Fig. 8(b). For Z-V, the two components of the MSS have been computed through integration of an Elfouhaily et al. [19] surface wave spectrum for a 10-m/s wind speed, up to the cutoff wavelength of 1 m specified in Section IV-A. Here, we must emphasize that although both FA and Z-V correspond to the same sea-state
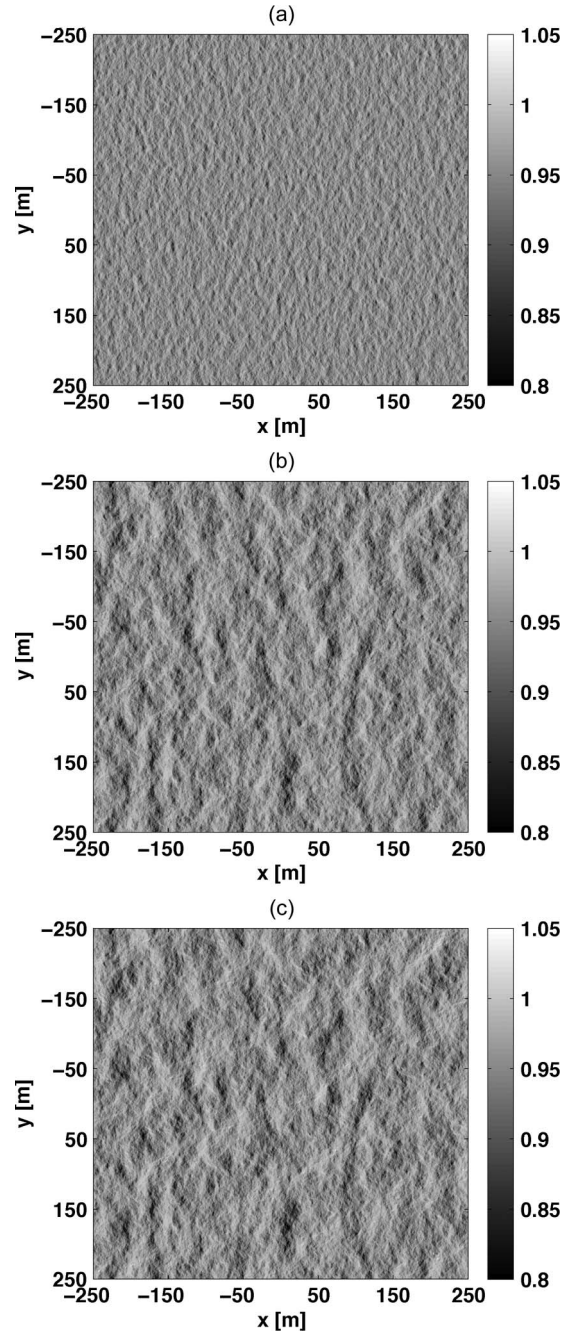


Fig. 7. PR based on the instantaneous VV and HH NRCSs computed with the FA and a facet size of 1 m². Each pixel represents the PR for a single facet. The three subplots correspond to the simulated wave fields shown in Fig. 4(a), i.e., (a) wind waves for wind speed of 5 m/s, (b) wind waves for wind speed of 10 m/s, and (c) wind waves for wind speed of 10 m/s plus added swell with amplitude of 1 m, wavelength of 100 m, and direction of 60° clockwise with respect to the x-axis. The wind direction is along the x-axis in all cases.

conditions, the FA and the Z-V DDM are not exact equivalents, since the Z-V DDM corresponds to a statistical average of the scattered power over an infinite number of looks whereas the FA-DDM represents the distribution of power from a single deterministic sea surface realization. Accordingly, while the FA DDM exhibits the same overall horseshoe shape as Z-V, it also presents a more patchy structure than Z-V. We find (not shown) that the patches occur in different positions in the DD domain for different sea surface realizations, indicating
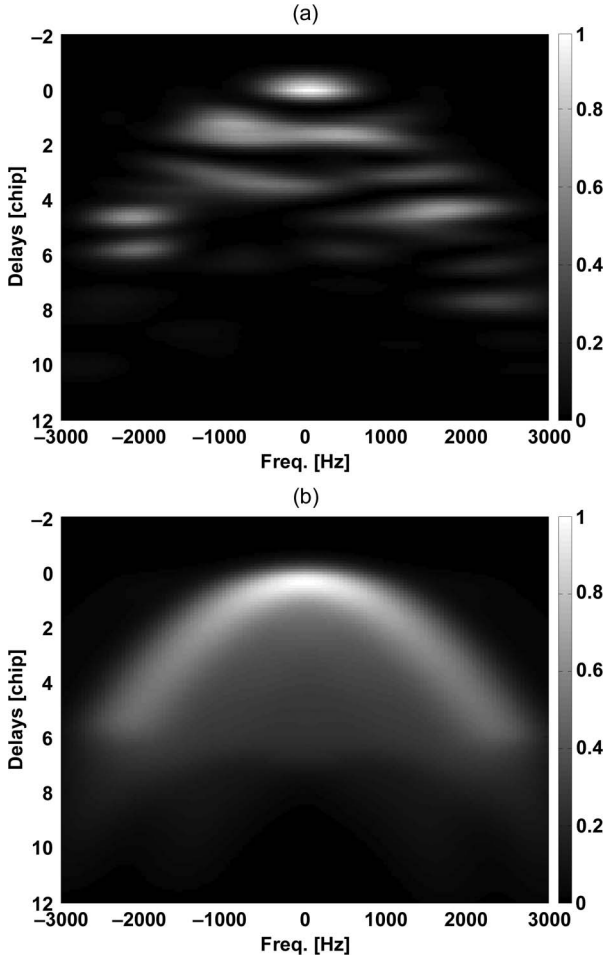
Fig. 8. DDMs for a 100-km^2 GZ and a 10-m/s wind speed, computed using a 50-Hz Doppler resolution and 0.1 chip delay resolution (1 chip $\sim$ 1 μs). (a) DDM computed using FA and 1-m^2 facets. (b) DDM computed using the Z-V model.

that it clearly corresponds to an instantaneous representation in DD space of the scattered power from particular features in each sea surface realization. We also find that, for FA, a considerable amount of scattered power is present both between the branches of the horseshoe and for large delay and Doppler values along the horseshoe, where the Z-V model predicts very weak scattering. The DDMs simulated using the FA therefore exhibits some interesting patterns that show similarities to the measured DDMs on UK-DMC [6]. The response of single-look DDM to different and more complex underlying sea surface conditions will be investigated in more detail in a future paper, together with comparisons with the Z-V DDM after incoherent accumulation of multiple single-look DDMs computed with the FA.

V. CONCLUSION

We have presented a new facet-based approach to model the forward scattering of monochromatic signals at L-band from realistic rough sea surfaces and have illustrated its application to compute DDMs for a spaceborne GNSS-R configuration. Rough ocean surfaces were generated for the cases of wind waves only and of more complex composite wave fields containing both wind waves and swell traveling in different direc-

tions. The electromagnetic scattering was computed through a novel facet-based implementation of the KA, which we call the FA. The method approximates the rough sea surfaces with a large number of small facets, representative of the large-scale roughness of the wave field. The scattered power is calculated for each facet in a closed form, and the facet size is chosen according to specific criteria. The FA scattering results were validated against the full Kirchhoff integral and the GO, which is the model most commonly used in GNSS-R. The FA proves a versatile tool to investigate the relation between the forward scattering and the ocean wave field. With respect to GO, the FA shows more sensitivity to polarization and provides the flexibility to investigate both instantaneous maps of the scattered power fields and average scattered power for different scattering angles. The FA was shown to provide comparable accuracy with that of the full Kirchhoff integral, with the advantage of much lower computational expense, and consequently provides the ability to compute the forward scattering from larger surfaces.

Instantaneous spatial maps of the bistatic NRCS and the PR for three different wind and wave conditions show clear correspondence between the distribution of the scattering and the underlying wave field. The presence of swell traveling in a different direction from the wind is detectable in the spatial distribution of instantaneous NRCS, but its effect is not evident in the average NRCS calculated for the whole surface. The behavior of the average NRCS with respect to wind speed is consistent with increased scattering away from the specular direction as surfaces become rougher as the wind speed increases. As regards polarization, the HH component of the scattered field is consistently larger than the VV component, particularly in the troughs of the ocean waves. Spatial maps of the PR exhibit crest-and-trough patterns strikingly similar to the underlying wave field. Once again, the swell component used in this study and its direction are easily detectable from the spatial maps of the PR. However, the average PR for the whole surface shows little sensitivity to sea state, except in scattering directions far away from the specular direction, where the validity of the FA and the KA is questionable.

An example was presented of a DDM of the scattered power calculated using FA for a large GZ corresponding to a spaceborne GNSS-R scenario. A preliminary comparison with a DDM obtained using the Z-V model for the same sea surface conditions reveals clear differences in overall structure, with the FA-DDM exhibiting interesting patchy features and a broader distribution of the scattered power across the DD domain than seen in Z-V, similarly to the measured DDM from UK-DMC [6].

The proposed facet-based approach has provided interesting insight on the influence of waves on the spatial distribution of the instantaneous scattered power and the PR and some encouraging results when mapping the scattered power in the Delay Doppler domain. The natural next step is to exploit this tool to investigate what characteristics of the wave field have a detectable signature in DDMs. The simulator should help to determine what properties of the ocean surface can be derived from measured DDMs from spaceborne GNSS-R receivers such as UK-DMC. Due to the ability of the FA to

compute the forward scattering for complex surface conditions, defined explicitly through 3-D ocean surfaces, this approach also offers the possibility of analyzing the scattering for more complex combination of linear ocean waves, as well as for ocean surfaces featuring steep nonlinear ocean waves with non-Gaussian statistics.

Finally, this work also revealed some relevant polarization effects in L-band bistatic scattering over the ocean. The polarimetric signature obtained with the FA confirms earlier findings [8] that polarization effects can be reproduced by considering a more comprehensive description of the large-scale scattering, such as provided by the KA. In the future, the facet-based approach could also be enhanced to include a diffuse scattering contribution due to small-scale roughness by considering slightly rough facets. This would lead to a TSM where the large-scale scattering is governed by the deterministic features on the surface and the small-scale scattering is described statistically. The simulator could then be used to ascertain the relative importance of large- and small-scale roughness contributions to GNSS-R signals.

ACKNOWLEDGMENT

REFERENCES

[1] V. Zavorotny and A. Voronovich, "Scattering of GPS signals from the ocean with wind remote sensing applications," *IEEE Trans. Geosci. Remote Sens.*, vol. 38, no. 2, pp. 951–964, Mar. 2000.

[2] J. Garrison, A. Komjathy, V. Zavorotny, and S. J. Katzberg, "Wind speed measurements using forward scattered GPS signals," *IEEE Trans. Geosci. Remote Sens.*, vol. 40, no. 1, pp. 50–65, Jan. 2002.

[3] A. Komjathy, M. Armatys, D. Masters, P. Axelrad, V. Zavorotny, and S. Katzberg, "Retrieval of ocean surface wind speed and wind direction using reflected GPS signals," *J. Atmos. Ocean. Technol.*, vol. 21, no. 3, pp. 515–526, Mar. 2004.

[4] S. Gleason, S. Hodgart, S. Yiping, C. Gommenginger, S. Mackin, M. Adjrad, and M. Unwin, "Detection and processing of bistatically reflected GPS signals from Low-Earth Orbit, for the purpose of ocean remote sensing," *IEEE Trans. Geosci. Remote Sens.*, vol. 43, no. 6, pp. 1229–1241, Jun. 2005.

[5] O. Germain, G. Ruffini, F. Soulat, M. Caparrini, B. Chapron, and P. Silvestrin, "The Eddy experiment: GNSS-R speculometry for directional sea-roughness retrieval from low altitude aircraft," *Geophys. Res. Lett.*, vol. 31, p. L12 306, Nov. 2004.

[6] M. Clarizia, C. Gommenginger, S. Gleason, M. Srokosz, C. Galdi, and M. D. Bisceglie, "Analysis of GNSS-R delay–Doppler maps from the UK-DMC satellite over the ocean," *Geophys. Res. Lett.*, vol. 36, p. L02 608, Jan. 2009.

[7] E. Cardellach and A. Rius, "A new technique to sense non-Gaussian features of the sea surface from L-band bistatic GNSS reflections," *Remote Sens. Environ.*, vol. 112, no. 6, pp. 2927–2937, Jun. 2008.

[8] D. Thompson, T. Elfouhaily, and J. Garrison, "An improved Geometrical Optics model for bistatic GPS scattering from the ocean surface," *IEEE Trans. Geosci. Remote Sens.*, vol. 43, no. 12, pp. 2810–2821, Dec. 2005.

[9] J. Marchan-Hernandez, N. Rodriguez-Alvarez, A. Camps, X. Bosch-Lluis, I. Ramos-Perez, and E. Valencia, "Correction of the sea state impact in the L-band brightness temperature by means of delay–Doppler maps of global navigation satellite signals reflected over the sea surface," *IEEE Trans. Geosci. Remote Sens.*, vol. 46, no. 10, pp. 2914–2923, Oct. 2008.

[10] M. Martin-Neira, M. Caparrini, J. Font-Rossello, S. Lannelongue, and C. S. Vallmitjana, "The PARIS concept: An experimental demonstration of sea surface altimetry using GPS reflected signals," *IEEE Trans. Geosci. Remote Sens.*, vol. 39, no. 1, pp. 142–150, Jan. 2001.

[11] G. Ruffini, F. Soulat, M. Caparrini, O. Germain, and M. Martin-Neira, "The Eddy experiment: Accurate GNSS-R ocean altimetry from low altitude aircraft," *Geophys. Res. Lett.*, vol. 31, p. L12 306, Jun. 2004.

[12] A. Rius, E. Cardellach, and M. Martin-Neira, "Altimetric analysis of the sea-surface GPS-reflected signals," *IEEE Trans. Geosci. Remote Sens.*, vol. 48, no. 4, pp. 2119–2127, Apr. 2010.

[13] C. Zuffada, A. Fung, J. Parker, M. Okolicanyi, and E. Huang, "Polarization properties of the GPS signal scattered off a wind-driven ocean," *IEEE Trans. Antennas Propag.*, vol. 52, no. 1, pp. 172–187, Jan. 2004.

[14] G. Valenzuela, "Theories for the interaction of electromagnetic and oceanic waves—A review," *Bound.-Layer Meteorol.*, vol. 13, pp. 61–85, Jan. 1978.

[15] P. Beckmann and A. Spizzichino, *The Scattering of Electromagnetic Waves From Rough Surfaces*. New York: Macmillan, 1963.

[16] F. Bass and I. Fuks, *Wave Scattering From Statistically Rough Surfaces*. New York: Pergamon, 1979.

[17] F. Ulaby, R. Moore, and A. Fung, *Microwave Remote Sensing, Active and Passive. Vol. II: Radar Remote Sensing and Surface Scattering and Emission Theory*. Reading, MA: Addison-Wesley, 1982.

[18] J. Stratton, *Electromagnetic Theory*. New York: McGraw-Hill, 1941.

[19] T. Elfouhaily, B. Chapron, K. Katsaros, and D. Vandemark, "A unified directional spectrum for long and short wind-driven waves," *J. Geophys. Res.*, vol. 102, no. C7, pp. 15 781–15 796, Jul. 1997.

Maria Paola Clarizia (S'08) was born in Naples in 1983. She received the M.S. degree in telecommunications engineering (*summa cum laude*) from the University of Sannio, Benevento, Italy, in 2007. She is currently working toward the Ph.D. degree in Global Navigation Satellite System Reflectometry (GNSS-R) in the School of Ocean and Earth Science, National Oceanography Centre, Southampton, U.K.

She is also with the Department of Engineering, University of Sannio. Her current research includes GNSS-R data processing, sea surface simulations, and bistatic signal scattering.

Christine Gommenginger received the Diplôme d'Etudes Approfondies in electromagnetics, telecommunications, and remote sensing from the Université de Toulon et du Var/Université de Nice-Sophia Antipolis, Nice, France, and the Ph.D. degree in microwave radar remote sensing of ocean surface roughness at low grazing angles from the University of Southampton, Southampton, U.K.

She has been with the National Oceanography Centre, Southampton, for over 15 years. Her interests are wide-ranging and include active and passive microwave remote sensing of the ocean, understanding interactions of microwave signals with the ocean surface, remote sensing of ocean wind and waves, and new Earth observation technologies. Her recent work includes research in along-track interferometric synthetic aperture radar (SAR), Global Navigation Satellite System Reflectometry, SAR altimetry, salinity from space, and wide-swath ocean altimetry.

Maurizio Di Bisceglie (M'01) received the Dr.Eng. degree in electronic engineering and the Ph.D. degree in electronics and telecommunications from Università degli Studi di Napoli "Federico II," Naples, Italy.

He has been Research Fellow with the and with the University College of London, London, U.K., and is currently an Associate Professor of telecommunications with University of Sannio, Benevento, Italy. His research activities are in the field of statistical signal processing with applications to radar and remote sensing. He was Organizer of the Italian phase of the European AQUA Thermodynamic Experiment (EAQUATE) mission and the Scientific Director of Mediterranean Agency for Remote Sensing and Environmental Control.

Dr. Di Bisceglie was Cochair of the National Aeronautics and Space Administration Direct Readout Conference in 2005.

Carmela Galdi (M'01) received the Dr.Eng. and Ph.D. degrees in electronic engineering from Università degli Studi di Napoli "Federico II," Naples, Italy, in 1992 and 1997, respectively.

During 1993, she was a Software Engineer with Alcatel Italia, Salerno, Italy. She has been with Università degli Studi di Napoli "Federico II" from 1994 to 2000, and in 2000, she joined the University of Sannio, Benevento, Italy, where she is currently a Professor of telecommunications. In 1995, she spent a four-month period for study and research in the Signal Processing Division, University of Strathclyde, Glasgow, U.K. She was a Visiting Scientist at the University College of London, London, U.K., and at the Defence Evaluation and Research Agency, Malvern, U.K. Her research interests are in the field of statistical signal processing, non-Gaussian models of radar backscattering, and remote sensing applications.

Dr. Galdi was in the organizing committee of the IEEE 2008 Radar Conference.

Meric A. Srokosz received the B.Sc. and Ph.D. degrees in mathematics from Bristol University, Bristol, U.K., in 1976 and 1980, respectively.

He has been a Principal Investigator or Coinvestigator on a number of Earth observation missions, including the European Space Agency (ESA)'s ERS-1, ERS-2, and Envisat missions, the National Aeronautics and Space Administration/Centre National d'Études Spatiales Topex/Poseidon and Jason missions, the National Space Development Agency ADEOS and TRMM missions, and most recently, the ESA SMOS mission. Since 2001, he has been the Scientific Coordinator of the U.K. Natural Environment Research Council's Rapid Climate Change (RAPID) program. He is part of the Marine Physics and Ocean Climate Group, National Oceanography Centre, Southampton, U.K. He has over 30 years of experience in the fields of applied mathematics, wave studies, and remote sensing of the oceans. His research interests include rain from altimetry, plankton patchiness using ship and satellite sensors, data assimilation into biological models, altimeter sea-state bias, breaking waves, salinity from space, and sea surface temperature from passive microwave.

Bibliography

Apel, J., 1994. An improved model of the ocean surface wave vector spectrum and its effects on radar backscatter. Journal of Geophysical Research 99(C8), 16269–16291.

Arnold-Bos, A., Khenchaf, A., Martin, A., 2007a. Bistatic radar imaging of the marine environment. part I: theoretical background. IEEE Transactions on Geoscience and Remote Sensing 45(11), 3372–3383.

Arnold-Bos, A., Khenchaf, A., Martin, A., 2007b. Bistatic radar imaging of the marine environment. part II: simulation and result analysis. IEEE Transactions on Geoscience and Remote Sensing 45(11), 3384–3396.

Balanis, C., 1982. Antenna Theory:Analysis and Design. John Wiley and Sons Inc.

Balanis, C., 1989. Advanced Engineering Electromagnetics. John Wiley and Sons Inc.

Barrick, D., 1968. Rough surface scattering based on the specular point theory. IEEE Transactions on Antennas and Propagation 16(4), 449–454.

Bass, F., Fuks, I., 1979. Wave Scattering From Statistically Rough Surfaces. Pergamon Press.

Beckmann, P., Spizzichino, A., 1963. The Scattering of Electromagnetic Waves from Rough Surfaces. Macmillan.

Bian, K., 2007. spaceborne application of GNSS reflectometry for global sea state monitoring. PhD Thesis, University of Surrey.

Bouchereau, F., Brady, D., Lanzl, C., 2001. Multipath delay estimation using a superresolution PN-correlation method. EEE Transactions on Signal Processing 49, 938949.

Brown, G. S., 1979. Estimation of surface wind speeds using satellite-borne measurements at normal incidence. Journal of Geophysical Research 84, 3974–3978.

Cardellach, E., Rius, A., 2008. A new technique to sense non-Gaussian features of the sea surface from L-band bistatic GNSS reflections. Remote Sensing of Environment 112, 2927–2937.

Cardellach, E., Ruffini, G., Pino, D., Rius, A., Komjathy, A., Garrison, J., 2003. Mediterranean balloon experiment: Ocean wind speed sensing from the stratosphere using GPS reflections. Remote Sensing of Environment 88, 351–362.

Cherniakov, E. M., 2008. Bistatic Radar: Emerging Technology. John Wiley and Sons Inc.

Clarizia, M., di Bisceglie, M., Galdi, C., Gommenginger, C., Landi, L., 2009a. Delay superresolution for GNSS-R. Proceedings of IGARSS 2009.

Clarizia, M., Gommenginger, C., di Bisceglie, M., Galdi, C., Srokosz, M., 2012. Simulation of l-band bistatic returns from the ocean surface: A facet approach with application to ocean GNSS reflectometry. IEEE Transactions on Geoscience and Remote Sensing 50(3), 960–971.

Clarizia, M., Gommenginger, C., Gleason, S., Srokosz, M., Galdi, C., di Bisceglie, M., 2009b. Analysis of GNSS-R delay-Doppler maps from the UK-DMC satellite over the ocean. Geophys. Res. Lett. 36.

Corsini, G., Manara, G., Monorchio, A., 1999. A simulation-based approach to radar backscatter from the sea surface. Radio Science 34(5), 1065–1075.

D'Addio, S., Buck, C., Martin-Neira, M., 2008. GNSS-R geometry and coverage. Presentation at workshop on GNSS-Reflectometry.

Donelan, M. A., Pierson, W. J., 1987. Radar scattering and equilibrium ranges in wind-generated waves with application to scatterometry. Journal of Geophysical Research 92(C5), 4971–5029.

Drennan, W. M., Taylor, P. K., Yelland, M. J., 2005. Parameterizing the sea surface roughness. Journal of Physical Oceanography 35, 835848.

Elfouhaily, T., Chapron, B., Katsaros, K., Vandemark, D., 1997. A unified directional spectrum for long and short wind-driven waves. Journal of Geophysical Research 102(C7), 15781–15796.

Elfouhaily, T., Thompson, D. R., Freund, D. E., Vandemark, D., Chapron, B., 2001. A new bistatic model for electromagnetic scattering from perfectly conducting random surfaces: numerical evaluation and comparison with SPM. Waves in Random Media 11, 33–43.

Elfouhaily, T., Thompson, D. R., Linstrom, L., 2002. Delay-doppler analysis of bistatically reflected signals from the ocean surface: Theory and application. IEEE Transactions on Geoscience and Remote Sensing 40(3), 560–573.

Fabra, F., Cardellach, E., Nogues-Correig, O., Oliveras, S., Ribo, S., Rius, A., Belmonte-Rivas, M., Semmling, M., Macelloni, G., Pettinato, S., Zasso, R., D'Addio, S., 2010. Monitoring sea-ice and dry snow with GNSS reflections. Proceedings of IGARSS 2010, 3837 – 3840.

Franceschetti, G., Migliaccio, M., Riccio, D., 1998. On ocean SAR raw signal simulation. IEEE Transactions on Geoscience and Remote Sensing 36(1), 84–100.

Frew, N. M., Bock, E. J., Schimpf, U., Hara, T., Haubecker, H., Edson, J. B., McGillis, W. R., Nelson, R. K., McKenna, S. P., Uz, B. M., Jhne, B., 2004. Air-sea gas transfer: Its dependence on wind stress, small-scale roughness, and surface films. Journal of Geophysical Research 109(C08S17).

Fung, A. K., Lee, K. K., 1982. A semi-empirical sea-spectrum model for scattering coefficient estimation. IEEE Journal on Oceanic Engineering 7(4), 166–176.

Garrison, J., Katzberg, S., Hill, M., 1998. Effect of sea roughness on bistatically scattered range coded signals from the global positioning system. Geophysical Research Letters 25(13), 2257–2260.

Garrison, J., Komjathy, A., Zavorotny, V., S.J.Katzberg, 2002. Wind speed measurements using forward scattered GPS signals. IEEE Transactions on Geoscience and Remote Sensing 40 (1), 50–65.

Germain, O., Ruffini, G., Soulat, F., Caparrini, M., Chapron, B., Silvestrin, P., 2004. The Eddy experiment: GNSS-R speculometry for directional sea-roughness retrieval from low altitude aircraft. Geophys. Res. Letters 31 (L12306).

Gleason, S., 2010. Towards sea ice remote sensing with space detected GPS signals: Demonstration of technical feasibility and initial consistency check using low resolution sea ice information. Remote Sensing 2, 2017–2039.

Gleason, S., Hodgart, S., Yiping, S., Gommenginger, C., Mackin, S., Adjrad, M., Unwin, M., 2005. Detection and processing of bistatically reflected GPS signals from Low-Earth Orbit, for the purpose of ocean remote sensing. IEEE Transactions on Geoscience and Remote Sensing 43 (6), 1229–1241.

Gleason, S. T., 2006. Remote sensing of ocean, ice and land remote sensing using bistatically scattered GNSS signals from low earth orbit. PhD Thesis, University of Surrey.

Gommenginger, C. P., Srokosz, M. A., Challenor, P. G., Cotton, P. D., 2002. Development and validation of altimeter wind speed algorithms using an extended collocated buoy / TOPEX data set. IEEE transactions on Geoscience and Remote Sensing 40(2), 251–260.

Grewal, M., Weill, L., Andrews, A., 2001. Global Positioning Systems, Inertial Navigation and Integration. John Wiley and Sons Inc.

Hasselmann, K., 1966. Feynman diagrams and interaction rules of wave-wave scattering processes. Reviews of Geophysics 4(1), 1–32.

Hasselmann, K., Barnett, T., Bouws, E., Carlson, H., Cartwright, D., Enke, K., Ewing, J., Gienapp, H., Hasselmann, D., Kruseman, P., Meerburg, A., Mller, P., Olbers, D., Richter, K., Sell, W., , Walden, H., 1973. Measurements of wind-wave growth and swell decay during the joint north sea wave project (JONSWAP). Ergnzungsheft zur Deutschen Hydrographischen Zeitschrift Reihe A8(12), 1–95.

Jackson, F. C., Walton, W. T., Hines, D. E., Walter, B. A., Peng, C. Y., 1992. Sea surface mean square slope from ku-band backscatter data. Journal of Geophysical Research 97(11), 411–427.

Johnson, J. T., Shin, R. T., Kong, J. A., Tsang, L., Pak, K., 1998. A numerical study of the composite surface model for ocean backscattering. IEEE Transactions on Geoscience and Remote Sensing 36(1), 72–83.

Khenchaf, A., 2001. Bistatic scattering and depolarization by randomly rough surfaces: application to the natural rough surfaces in x-band. Waves in Random Media 11(2), 61–89.

Kodis, R., 1966. A note on the theory of scattering from an irregular surface. IEEE Transactions on Antennas and Propagation 14(1), 77–82.

Komjathy, A., Armatys, M., Masters, D., Axelrad, P., Zavorotny, V., Katzberg, S., 2004. Retrieval of ocean surface wind speed and wind direction using reflected GPS signals. Journal of Atmospheric and Oceanic Technology 21, 515–526.

Longuet-Higgins, M., 1963. The effect of non-linearities on statistical distributions in the theory of sea waves. Journal of Fluid Mechanics 17, 459–480.

Lowe, S. T., LaBrecque, J. L., Zuffada, C., Romans, L., Young, L., Hajj, G., 2002. First spaceborne observation of an earth-reflected GPS signal. Radio Science 37(1).

Luntama, J. P., Kirchengast, G., Borsche, M., Foelsche, U., Steiner, A., Healy, S., Engeln, A. V., OClerigh, E., Marquardt, C., 2008. Prospects of the EPS GRAS mission for operational atmospheric applications. Bullettin of American Meteorogical Society 89(12), 18631875.

Marchan-Hernandez, J., Camps, A., Rodriguez-Alvarez, N., Valencia, E., Bosch-Lluis, X., Ramos-Perez, I., 2009. An efficient algorithm to the simulation of DelayDoppler Maps of reflected Global Navigation Satellite System signals. IEEE Transactions on Geoscience and Remote Sensing 47(8), 2733–2740.

Marchan-Hernandez, J., Rodriguez-Alvarez, N., Camps, A., Bosch-Lluis, X., Ramos-Perez, I., Valencia, E., 2008. Correction of the sea state impact in the L-band brightness temperature by means of delay-doppler maps of global navigation satellite signals reflected over the sea surface. IEEE Transactions on Geoscience and Remote Sensing 46 (10), 2914–2923.

Marchan-Hernandez, J., Valencia, E., Rodriguez-Alvarez, N., Ramos-Perez, I., Bosch-Lluis, X., Camps, A., Eugenio, F., Marcello, J., 2010. Sea-state determination using GNSS-R data. IEEE Geoscience and Remote Sensing Letters 7(4), 621–625.

Martin-Neira, M., 1993. A Passive Reflectometry and Interferometry System (PARIS): Application to ocean altimetry. ESA Journal 17.

Martin-Neira, M., Caparrini, M., Font-Rossello, J., Lannelongue, S., Vallmitjana, C. S., 2001. The PARIS concept: An experimental demonstration of sea surface altimetry using GPS reflected signals. IEEE Transactions on Geoscience and Remote Sensing 39 (1), 142–150.

Onorato, M., Osborne, A. R., S., S. M. . B., 2001. Freak waves in random oceanic sea states. Physical Review Letters 86(25), 58315834.

Pierson, W. J., Moskowitz, L., 1964. A proposed spectral form of fully developed wind seas based on the similarity theory of S. A. Kitaigorodskii. Journal of Geophysical Research 69(64), 51815190.

Plant, W. J., 1986. Two-scale model for short wind-generated waves and scatterometry. Journal of Geophysical Research 91(10), 735–749.

Plessey, S. G., 1996. Global positioning products handbook.

Rino, C. L., Crystal, T. L., Koide, A. K., Ngo, H. D., Guthart, H., 1991. Numerical simulation of backscatter from linear and nonlinear ocean surface realizations. Radio Science 26(1), 51–71.

Rius, A., Cardellach, E., Neira, M. M., 2010. Altimetric analysis of the sea-surface GPS-reflected signals. IEEE Transactions on Geoscience and Remote Sensing 48 (4), 2119–2127.

Robinson, I., 2004. Measuring the Ocean from Space: the Principles and Methods of Satellite Oceanography. Springer Praxis Books / Geophysical Sciences.

Rodriguez-Alvarez, N., Camps, A., Vall-llossera, M., Bosch-Lluis, X., Monerris, A., Ramos-Perez, I., Valencia, E., Marchan-Hernandez, J., Martinez-Fernandez, J.,

Baroncini-Turricchia, G., Perez-Gutierrez, C., Sanchez, N., 2011. Land geophysical parameters retrieval using the interference pattern GNSS-R technique. IEEE Transactions on Geoscience and Remote Sensing 49(1), 71–84.

Rodriguez-Alvarez, N., X., B.-L., A., C., Vall-llossera, M., E., V., J.F., M.-H., Ramos-Perez, I., 2009. Soil moisture retrieval using GNSS-R techniques: Experimental results over a bare soil field. IEEE Transactions on Geoscience and Remote Sensing 47(11), 3616–3624.

Ruffini, G., Cardellach, E., Rius, A., Aparicio, J., 1999. Remote sensing of the ocean by bistatic radar observations: a review; utilization of scatterometry using sources of opportunity. IEEC Report WP1000.

Ruffini, G., Germain, O., Soulat, F., Taani, M., Caparrini, M., 2003. GNSS-R: Operational applications. Proceedings of Workshop on Oceanography with GNSS-R Reflections.

Ruffini, G., Soulat, F., Caparrini, M., Germain, O., Martin-Neira, M., 2004. The eddy experiment: Accurate GNSS-R ocean altimetry from low altitude aircraft. Geophysical Research Letters 31(L12306).

Sabia, R., Caparrini, M., Camps, A., Ruffini, G., 2007. Potential synergetic use of GNSS-R signals to improve the sea-state correction in the sea surface salinity estimation: Application to the SMOS mission. IEEE Transactions on Geoscience and Remote Sensing 45(7), 2088–2097.

Soriano, G., Guerin, C. A., Saillard, M., 2001. Scattering by two-dimensional rough surfaces: comparison between the method of moments, kirchhoff and small-slope approximations. Waves in Random Media 12, 63–83.

Soulat, F., 2003. sea surface remote sensing with GNSS and sunlight reflections. PhD Thesis, Universitat Politecnica de Catalunya.

Soulat, F., Caparrini, M., Germain, O., Lopez-Dekker, P., Taani, M., Ruffini, G., 2004. Sea state monitoring using coastal GNSS-R. Geophysical Research Letters 31 (L21303).

Spall, M. A., 2010. Effect of sea surface temperaturewind stress coupling on baroclinic instability in the ocean. Journal of Physical Oceanography 37, 1092–1097.

Stosius, R., Beyerle, G., Helm, A., Hoechner, A., Wickert, J., 2010. Simulation of space-borne tsunami detection using GNSS-Reflectometry applied to tsunamis in the indian ocean. Natural Hazards and Earth System Sciences 10, 13591372.

Stosius, R., Beyerle, G., Hoechner, A., Wickert, J., Lauterjung, J., 2011. The impact on tsunami detection from space using GNSS-reflectometry when combining GPS with GLONASS and Galileo. Advances in Space Research 47(5), 843853.

Stratton, J., 1941. Electromagnetic Theory. McGraw-Hill.

Thompson, D., 1988. Calculation of radar backscatter modulations from internal waves. Journal of Geophysical Research 93(12), 371–380.

Thompson, D., Elfouhaily, T., Garrison, J., 2005. An improved Geometrical Optics model for bistatic GPS scattering from the ocean surface. IEEE Transactions on Geoscience and Remote Sensing 43 (12), 2810–2821.

Toffoli, A., Gramstad, O., Trulsen, K., Monbaliu, J., Bitner-Gregersen, E., Onorato, M., 2010. Evolution of weakly nonlinear random directional waves: laboratory experiments and numerical simulations. Journal of Fluid Mechanics 664, 313–336.

Toporkov, J., Brown, G., 2000. Numerical simulations of scattering from time-varying, randomly rough surfaces. IEEE Transactions on Geoscience and Remote Sensing 38(4), 1616–1625.

Tsui, J., 2000. Fundamentals of Global Positioning System Receivers: A Software Approach. John Wiley and Sons Inc.

Ulaby, F., Moore, R., Fung, A., 1982. Microwave Remote Sensing, Active and Passive. Vol. II: Radar Remote Sensing and Surface Scattering and Emission Theory. Vol. II. Addison-Wesley.

Unwin, M. J., Gleason, S., Brennan, M., 2003. The space GPS reflectometry experiment on the UK disaster monitoring constellation satellite. Proceedings of ION-GPS/GNSS.

Valencia, E., Camps, A., Marchan-Hernandez, J., Park, H., Bosch-Lluis, X., Rodriguez-Alvarez, N., Ramos-Perez, I., 2011a. Ocean surfaces scattering coefficient retrieval by DelayDoppler Map inversion. IEEE Geoscience and Remote Sensing Letters 8(4), 750–754.

Valencia, E., Camps, A., Marchan-Hernandez, J., Rodriguez-Alvarez, N., Ramos-Perez, I., Bosch-Lluis, X., 2010. Experimental determination of the sea correlation time using GNSS-R coherent data. IEEE Geoscience and Remote Sensing Letters 7(4), 675–678.

Valencia, E., Camps, A., Rodriguez-Alvarez, N., Ramos-Perez, I., Bosch-Lluis, X., Park, H., 2011b. Improving the accuracy of sea surface salinity retrieval using GNSS-R data to correct the sea state effect. Radio Science 46.

Valenzuela, G., 1978. Theories for the interaction of electromagnetic and oceanic waves: a review. Boundary-Layer Meteorology 13(1), 61–85.

Voronovich, A. G., Zavorotny, V. U., 2001. Theoretical model for scattering of radar signals in ku- and c-bands from a rough sea surface with breaking waves. Waves in Random Media 11, 247–269.

West, B. J., Brueckner, K. A., Jand, R. S., Milder, D. M., Milton, R. L., 1987. A new method for surface hydrodynamics. Journal of Geophysical Research 92(C11), 11803–11824.

Wickert, J., T. S., Beyerle, G., Knig, R., Reigber, C., Jakowski, N., 2004. The Radio Occultation experiment aboard CHAMP: Operational data analysis and validation of vertical atmospheric profiles. Journal of the Meteorological Society of Japan 82(1B), 381–395.

You, H., Garrison, J., Heckler, G., Smajlovic, D., 2006. The autocorrelation of waveforms generated from ocean-scattered GPS signals. IEEE Geoscience and Remote Sensing Letters 3(1), 78–81.

Zakharov, V., 1968. Stability of period waves of finite amplitude on surface of a deep fluid. Journal of Applied Mechanics and Technical Physics 9, 190–194.

Zavorotny, V., Voronovich, A., 2000. Scattering of GPS signals from the ocean with wind remote sensing applications. IEEE Transactions on Geoscience and Remote Sensing 38 (2), 951–964.

Zhang, M., Chen, H., Yin, H. C., 2011. Facet-based investigation on EM scattering from electrically large sea surface with two-scale profiles: Theoretical model. IEEE Transactions on Geoscience and Remote Sensing 49(6), 19671975.

Zuffada, C., Fung, A., Parker, J., Okolicanyi, M., Huang, E., 2004. Polarization properties of the GPS signal scattered off a wind-driven ocean. IEEE Transactions on Antennas and Propagation 52 (1), 172–187.